U.S. DEPARTMENT OF ENERGY | Energy Efficiency & Renewable Energy

DOE/EE-1163

2014

VEHICLE TECHNOLOGIES OFFICE

FY 2014 Annual Progress Report – Electric Drive Technologies Program

CONTENTS

List of Figures

List of Tables

ACRONYMS AND ABBREVIATIONS

3D	three dimensional
ac	alternating current
A	ampere
AEV	all electric vehicle
Al	aluminum
AM	Additive manufacturing
APEEM	Advanced Power Electronics and Electric Motors (program, DOE)
APEEM	Advanced Power Electronics and Electric Machinery (subprogram, ORNL)
AWG	American wire gauge
BCC	body center cubic
BFE	brushless field excitation
CAD	computer-aided design
CAN	controller area network
CVD	chemical vapor deposition
DBC	direct bond copper
dc	direct current
DMLS	direct-melted laser-sintered
DOE	U.S. Department of Energy
DSP	digital signal processing/processor
EMI	electromagnetic interference
EV	electric vehicle
FDM	fused deposition melting
FEA	finite element analysis
FET	field effect transistor
GaN	gallium nitride
HEV	hybrid electric vehicle
HR	high resolution
HSG	hybrid starter-generator
HV	high voltage
IGBT	insulated gate bipolar transistor
INC/CONV	inverter/converter
IPM	integrated power module
IR	insulation resistance
IR	International Rectifier
JBS	junction barrier Schottky
JFE	JFE Steel Corporation
JFET	junction field-effect transistor

K	thermal conductivity
K	degrees Kelvin
MC	Monte Carlo
M/G	motor/generator
MOSFET	metal oxide semiconductor field-effect transistor
MPH	miles per hour
Nd	neodymium
NREL	National Renewable Energy Laboratory (DOE)
OBC	onboard charger
OD	outer diameter
OEM	original equipment manufacturer
ORNL	Oak Ridge National Laboratory
PBA	planar bond-all
PCB	printed circuit board
PCU	power converter unit
PD	power density (peak)
PE	power electronics
PEV	plug-in electric vehicle
PF	power factor
PFC	power factor correction
PI	proportional integral
PID	proportional integral derivative
PM	permanent magnet
PWM	pulse width modulated/modulation
R&D	research and development
rms	root mean square
SBD	Schottky barrier diode
SDSR	sinusoidally driven synchronous reluctance
SEM	scanning electron microscope
Si	silicon
SiC	silicon carbide
SOI	silicon-on-insulator
SP	specific power
SRM	switched reluctance motor
TC	thermal conductivity
TDS	traction drive system
THD	total harmonic distortion
U.S. DRIVE	Driving Research and Innovation for Vehicle efficiency and Energy sustainability (cooperative research effort between DOE and industry partners)

V	volt
Vac	volts of alternating current
Vce	voltage across collector and emitter
Vdc	volts of direct current (operating voltage)
VTO	Vehicle Technologies Office (DOE)
WBG	wide bandgap
ZS	zero sequence
ZSIN	zero sequence impedance network

I. INTRODUCTION

1.0 Introduction

The U.S. Department of Energy (DOE) announced in May 2011 a new cooperative research effort comprising DOE, the U.S. Council for Automotive Research (composed of automakers Ford Motor Company, General Motors Company, and Chrysler Group), Tesla Motors, and representatives of the electric utility and petroleum industries. Known as U.S. DRIVE (Driving Research and Innovation for Vehicle efficiency and Energy sustainability), it represents DOE's commitment to developing public–private partnerships to fund high-risk–high-reward research into advanced automotive technologies. The new partnership replaces and builds upon the partnership known as FreedomCAR (derived from "Freedom" and "Cooperative Automotive Research") that ran from 2002 through 2010 and the Partnership for a New Generation of Vehicles initiative that ran from 1993 through 2001.

Electric Drive Technologies (EDT) subprogram within the DOE Vehicle Technologies Office (VTO) provides support and guidance for many cutting-edge automotive technologies now under development. Research is focused on developing revolutionary new power electronics (PE), electric motor, and traction drive system (TDS) technologies that will leapfrog current on-the-road technologies, leading to lower cost and better efficiency in transforming battery energy to useful work. The research and development (R&D) is also aimed at achieving a greater understanding of and improvements in the way the various new components of tomorrow's automobiles will function as a unified system to improve fuel efficiency through research in more efficient TDSs.

In supporting the development of advanced vehicle propulsion systems, the EDT subprogram fosters the development of technologies that will significantly improve efficiency, costs, and fuel economy.

The EDT subprogram supports the efforts of the U.S. DRIVE partnership through a three-phase approach intended to

- Identify overall propulsion- and vehicle-related needs by analyzing programmatic goals and reviewing industry recommendations and requirements, and then develop and deliver the appropriate technical targets for systems, subsystems, and component R&D activities.
- Develop, test, and validate individual subsystems and components, including electric motors and PE.
- Estimate how well the components and subsystems work together in a vehicle environment or as a complete propulsion system and whether the efficiency and performance targets at the vehicle level have been achieved.

The research performed under this subprogram addresses the technical and cost barriers that currently inhibit the introduction of advanced propulsion technologies into hybrid electric vehicles (HEVs), plug-in HEVs (PEVs), all-electric vehicles (AEVs), and fuel-cell-powered automobiles that meet the goals set by U.S. DRIVE.

A key element in making these advanced vehicles practical is providing an affordable electric TDS. This will require attaining weight, volume, efficiency, and cost targets for the PE and electric motor subsystems of the TDS. Areas of development include

- Novel traction motor designs that result in increased power density and lower cost
- Inverter technologies that incorporate advanced semiconductor devices to achieve higher efficiency while accommodating higher-temperature environments and delivering higher reliability
- Converter concepts that leverage higher-switching-frequency semiconductors, nanocomposite magnetics, higher-temperature capacitors, and novel packaging techniques that integrate more functionality into applications offering reduced size, weight, and cost
- New onboard battery charging electronics that build from advances in converter architectures for decreased cost and size
- More compact and higher-performing thermal controls achieved through novel thermal materials and innovative packaging technologies
- Integrated motor-inverter TDS architectures that optimize the technical strengths of the underlying PE and electric machine subsystems.

The EDT research program conducts fundamental research, evaluates hardware, and assists in the technical direction of the VTO and in setting national policy for future AEVs that addresses the overarching goal of petroleum and greenhouse gas reduction. DOE participates in the U.S. DRIVE Electrical and Electronics Technical Team, evaluates proposals, and lends its technological expertise to the direction of projects and evaluation of developing technologies.

DOE's continuing R&D into advanced vehicle technologies supports the administration's goal to produce a five-passenger affordable AEV with a payback of less than 5 years and sufficient range and fast charging capability to enable average Americans everywhere to meet their daily transportation needs more conveniently and at lower cost by the year 2022.

1.1 EV Everywhere

EV Everywhere, a Clean Energy Grand Challenge, set ambitious, far-reaching goals for the country. Announced by President Obama in March 2012, the initiative focuses on the U.S. becoming the first nation in the world to produce plug-in electric vehicles that are as affordable for the average American family as today's gasoline-powered vehicles within the next 10 years. The strategic investments to meet these goals will:

- Improve the competitive position of U.S. industry and create jobs through American innovation.
- Enhance energy security by reducing our dependence on foreign oil.
- Save money by cutting fuel costs for American families and businesses.
- Protect our health and safety by mitigating the impact of energy production and use on climate change.

EV Everywhere aims to enable American innovators to rapidly develop and commercialize the next generation of technologies to achieve the sufficient PEV cost, range, and charging infrastructure necessary for widespread deployment. A task such as this requires partnership among the private sector, the Federal government, Congress, states and communities, national laboratories, universities, nongovernmental organizations, and individual citizens. In addition to collaborating with outside stakeholders, the DOE VTO is working closely within the Department, with the **Office of Science**, **Office of Electricity**, and **ARPA-e**.

PE and electric motors that make up vehicles' electric drive system are essential to hybrid and plug-in electric vehicles. As such, improvements in these technologies can substantially reduce petroleum consumption in transportation, and help meet national economic, environmental, and energy security goals. HEVs can reduce petroleum use compared to average conventional vehicles by as much as 50%, while plug-in electric vehicles extend these savings even further.

1.2 2014 EV Everywhere / U.S. Drive Accomplishments

Manufacturability of Affordable Non-Rare Earth Magnet Alloys Demonstrated

Compression molding of gas atomized aluminum–nickel–cobalt (Alnico) was identified as the preferred method for producing rare earth free magnets that will reduce the cost of electric traction drive motors.

Ames Laboratory

Ames Laboratory (Ames) led a group of researchers who have identified Alnico magnets as the best near-term candidate to develop alternative rare earth (RE) magnets in permanent magnet (PM) motors for electric drive systems. As part of the Beyond Rare Earth Magnets (BREM) R&D project, Ames has developed a new means of processing Alnico that improves performance through compression molding of gas atomized magnet particles.

The BREM researchers focused on refining Alnico alloys. Alnico 8 and 9 showed the most promise for improvement because of their higher starting coercivity (an important magnetic property), which is believed to be the result of the elongated iron–cobalt (Fe-Co) phase shape anisotropy. Using their in-house gas atomizer, Ames produced a uniform pre-alloy powder with a very spherical shape and a low content of satellite particles. In addition, this powder had excellent flowability and powder packing. Sintering and compression molding, with a binder, were investigated as potential methods to form the powder into bulk magnet shapes.

Compression molding of the gas atomized powder with a polypropylene carbonate binder (see Figure 1-1) was determined to be the preferred method for producing inexpensive bulk magnet shapes. The bulk magnets will require minimum amounts of post-processing, reducing the final product cost.

From these successes, Ames has determined that an improved magnet composition (increased coercivity) can be produced for use in the DOE-funded UQM Technologies Inc. non-rare-earth proof-of-design motor. This improved material will be a variation of Alnico 8.

Additionally, Ames successfully determined the key parameter that leads to increased coercivity: reduced spinodal spacing. Reduction in spinodal spacing is a direct function of the time spent at a specific magnetic annealing temperature. Atomistic modeling also suggested that decreased cobalt concentration in a nano-pattern matrix could boost coercivity, leading to re-design of Alnico 8 alloys to reduce cobalt by 40%, which also cuts product cost.

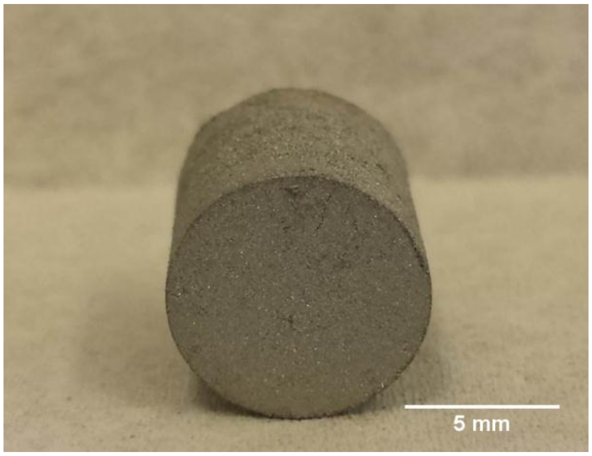

Figure 1-1: Compression molded Alnico 8 prototype magnet made from pre-alloyed gas atomized powder.

Plastic Heat Exchanger Improves Heat Transfer Efficiency and Reduces Inverter Weight

A plastic manifold incorporating jet impingement and surface enhancements increased the coefficient of performance by 17% at 100 kW electrical power and reduced the electric drive vehicle inverter weight by 19%.

National Renewable Energy Laboratory

A novel lightweight plastic heat exchanger prototype (Figure 1-2), incorporating single-phase liquid jet impingement on microfinned surfaces on the module baseplate, was demonstrated in collaboration with UQM Technologies Inc. and Wolverine Tube Inc. At 100 kW electrical power, the new heat exchanger improved the coefficient of performance (COP) by 17%, the specific power by 36%, and the power density by 12% when compared to the channel-flow-based cold plate used in the commercial inverter (baseline UQM PowerPhase®). Performance improvements (Table 1-1) were attributed to two main factors: a 17% decrease in thermal resistance and a 50% reduction in heat exchanger weight (6 kg to 3 kg). With the lower thermal resistance, the dissipation of the heat generated by the power electronic devices increased by 20%. The total inverter weight was reduced from 16 kg to 13 kg (19% reduction).

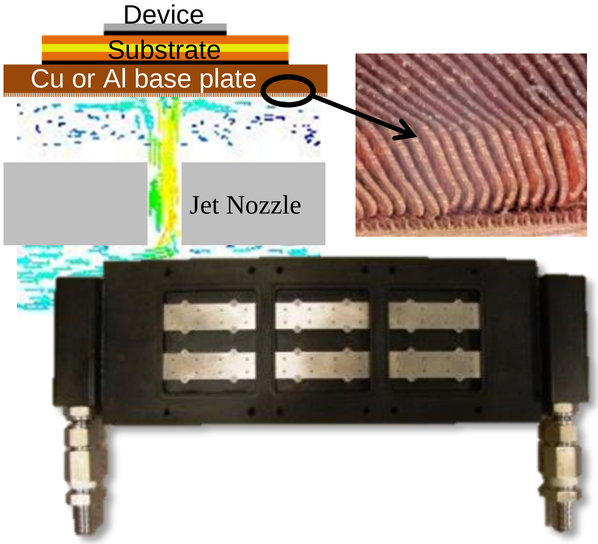

Figure 1-2: Cross-section of the jet impinging on the microfinned enhanced base plate of the PE module stack-up (figure on the top). The plastic manifold with the nozzle inserts is shown on the bottom.

Table 1-1: Table 1: Improvement over the baseline inverter.

Metric	Improvement
Heat dissipation	20%
Weight	19%
COP	17%
Specific power	36%
Power density	12%

At UQM Technologies Inc., scientists conducted full inverter-level experiments using dynamometers with water–ethylene glycol coolant (a 40% to 60% mixture) at 30°C and 10 L/min at 40 to 100 kW electrical power, dissipating 0.9 to 2.2 kW of heat. For the liquid jet impingement-based heat exchanger, the manifold is not part of the thermal pathway. Hence, using mass manufacturing techniques, the manifold can be made of lighter-weight, lower-cost thermal plastic (compared to manifold materials used in current manufacturing techniques). Compared to the channel-flow baseline, jet impingement yielded less variability in the junction temperatures of the power electronic devices (5°C to 7°C lower). The jets provided high localized cooling underneath the devices where the heat fluxes were the highest and the heat transfer was most needed. The microfinned surfaces enhanced heat transfer by providing increased surface area upon which the jets impinged, and created turbulence in the liquid coolant near the surface.

Further efforts to promote adoption include advanced packaging design and integration to improve strategies to attach the power modules to the heat exchanger manifold, reducing risk of leaks. Methods to reduce costs must also be evaluated, and the sequence of applying the microfinned surface enhancements must be determined.

Motor Thermal Management Spurs New Motor Designs

New data for motor thermal management provides designers with critical information needed for modeling and designing motors.

National Renewable Energy Laboratory

Thermal management of motors directly improves power density and reliability; however, thermal management is a significant challenge because the heat transfer and fluid flow are complex. Improved accuracy of motor material thermal properties and convective heat transfer can improve simulation accuracy of motor performance by 20%. National Renewable Energy Laboratory (NREL) motor thermal management expertise enabled more accurate measurements of thermal properties related to lamination stacks and automatic transmission fluid (ATF) cooling. This effort resulted in first-ever detailed motor component thermal data in the open literature, which will enable motor developers to improve motor models and designs.

NREL measured thermal conductivity and inter-lamination thermal contact resistance of multi-layer lamination stacks for a range of motor lamination materials. The through-stack thermal conductivity was between 3% and 9% of the bulk lamination material thermal conductivity. The thermal contact resistance between motor laminations (Figure 1) reduces the through-stack thermal conductivity. The overall thermal conductivity depends on lamination surface profiles, contact pressure, bulk material thermal conductivity, and lamination thickness. The data quantify the difficulty in extracting heat axially through the lamination materials within the motor, which has significant impacts, especially on cooling rotors.

NREL also measured convective heat transfer coefficients with ATF jets (Figure 1) impinging on surfaces representative of motor end-winding wire bundles. Over the tested flow rates, jet impingement on the wire surface resulted in a 10% to 34% increase in the average heat transfer coefficient compared to available data for impingement on flat/smooth surfaces. The project also identified potential degradation in heat transfer, with increasing jet velocity, on the wire surfaces.

NREL's motor thermal management research improves understanding of motor cooling, enabling analysis that supports design of innovative electric motors with improved thermal performance. This capability, knowledge, and data are crucial for original equipment manufacturers and suppliers who require consistent characterization of ATF jets and motor thermal properties for new motor configuration design and development.

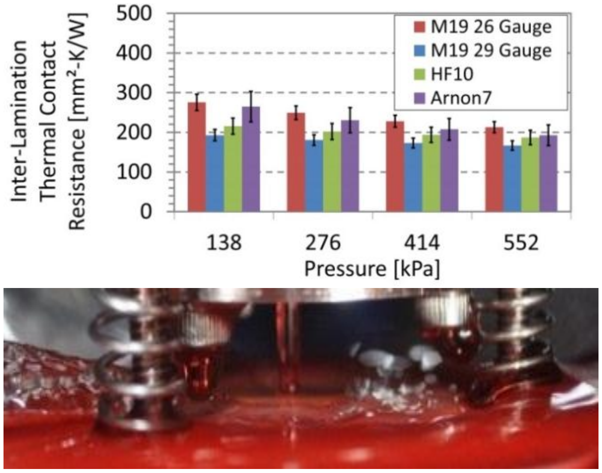

Figure 1-3: Results for inter-lamination thermal contact resistance (top). Picture of the test section for measurement of ATF jet heat transfer coefficient (bottom).

All-SiC Inverter Meets 2015 Performance Targets

Emerging wide bandgap semiconductors offer opportunities for higher power density, higher temperature, and higher frequency operation as well as efficiency and reliability improvements.

Oak Ridge National Laboratory

Emerging wide bandgap (WBG) devices significantly improve PE. Their ability to operate at greater efficiencies over higher temperatures and operational frequencies reduce cooling requirements and minimize passive component requirements.

Oak Ridge National Laboratory (ORNL) developed a 10 kW, all-silicon carbide (SiC) inverter, shown in Figure 1-4, using 1,200 V, 100 A, SiC MOSFET modules. The direct bonded copper (DBC) design and layout were optimized for minimum parasitics and improved performance of the SiC devices.

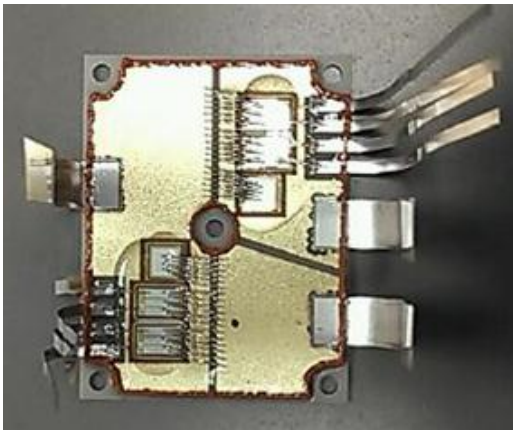

Figure 1-4:1,200 V, 100 A SiC power module.

These modules were used to develop the inverter shown in Figure 1-5. The inverter prototype uses commercially available gate drivers with galvanic isolation up to 3,000 Vrms and integrated over current protection, undervoltage lockout, and temperature feedback features. The modules were mounted on top of a 3-dimensional (3D)-printed, additively manufactured heat sink with thermal grease as the heat transfer medium between the DBC and heat sink.

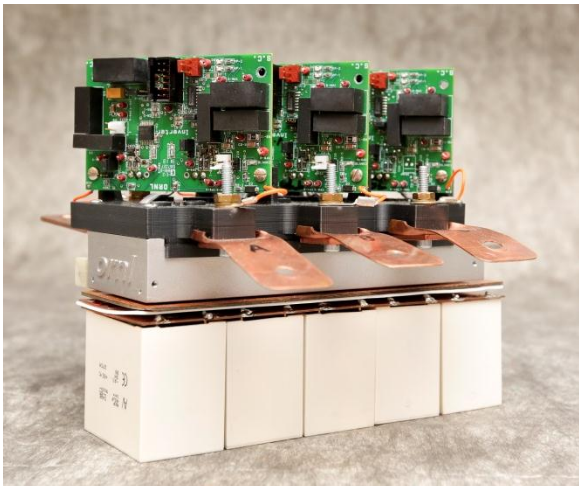

Figure 1-5: 10 kW SiC inverter prototype.

The total volume of the inverter is ~1.5 L and the total weight of the inverter is ~1.76 kgs, not including connectors and housing. The total operating power density and the operating specific power based on the maximum tested conditions are ~13.3 kW/L and ~11.3 kW/kg, respectively (DOE 2015 target: 12 kW/L).

Test results demonstrated successful operation of the inverter with an efficiency of ~99% at 20 kW operating power (380 V, 5 kHz, 60°C coolant temperature, and flow rate of 1.6 gpm).

The additive manufacturing process contributed to several improvements. The specific power increased due to the reduced amount of material required by the innovative versus traditional metal processing techniques. New complex geometries internal to the heatsink were introduced for improving the heat transfer in specific areas for the semiconductor devices.

New System Improves Characterization of Materials

Custom characterization system provides a deeper understanding of magnetization and loss mechanisms in electrical steel; provides information needed for high fidelity electric motor modeling.

Oak Ridge National Laboratory

A newly developed custom magnetic characterization tool observes localized properties in electrical steel. The measurement stage of the characterization system, shown in Figure 1-6, includes excitation coils that apply a magnetic field to a single sheet sample as the local magnetic field on the surface of the sample is measured.

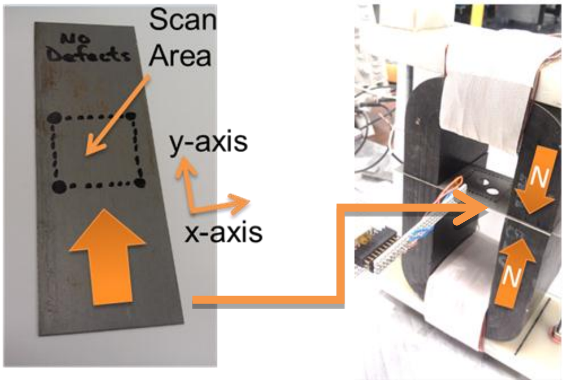

Figure 1-6: Measurement stage of the magnetic material test sample (left) and characterization system (right).

Conventional motor simulation techniques assume that material properties are homogeneous for all of the soft magnetic material. However, many factors impact magnetic properties, including residual stress from stamping or laser cutting. Additionally, stamped or laser cut edges are near the air gap, which is a critical location for the magnetic circuit and operation of the motor.

Characterization of the impact of residual stress upon magnetic properties has revealed significant degradations near areas that have sustained mechanical deformation. Figure 1-7 shows the resulting magnetic field, with a flux density of 1.4 Tesla, after a brief application of laser pulses in five different areas of the sample. Although the disturbed areas are barely visible on the physical sample, five distinct areas are visible in the plot of the scanning results, where the magnetic properties are significantly impacted.

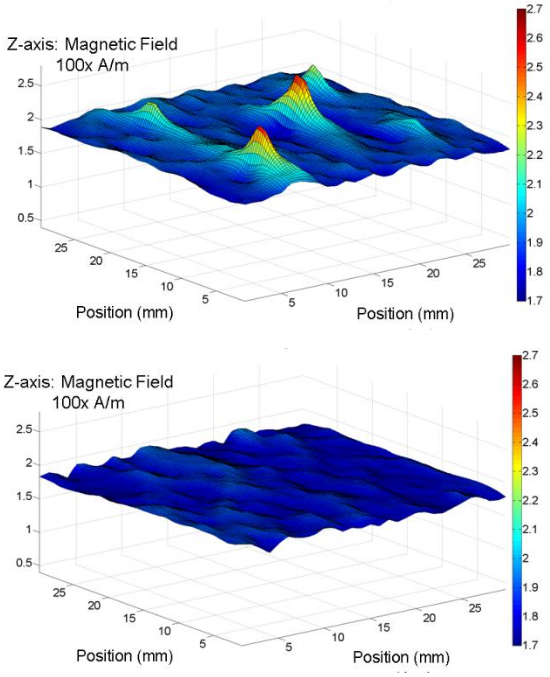

Figure 1-7: Magnetic field results before disturbances (top) and after a brief application of five laser pulses (bottom).

Other test results indicate that stamped edges can have magnetic fields up to five times higher at the deformation zone for a given flux density. Substantial negative impact upon magnetic properties is incurred on the order of millimeters from the site of deformation. These degradations significantly impact motor performance and losses; results indicate that improved modeling of magnetic properties can improve simulation accuracy for torque and power by up to 20%.

Next Generation Wide Bandgap Packaging Improves Inverter Efficiency

Advanced, 3D planar-interconnected SiC power module features innovative packaging; offers comprehensive improvements in performance, efficiency, density, and cost of electronic systems.

Oak Ridge National Laboratory

ORNL is developing WBG automotive PE technologies with advanced packaging technology development to help achieve U.S. DRIVE targets.

The ORNL Packaging Laboratory fabricated an all-SiC 100 A/1,200 V single phase-leg power module using an innovative, planar-bond-all (PBA) packaging technology, shown in Figure 1-8. This innovative approach employs area bonding instead of wire bonding to build multiple layer/multiple component stacks in a two-step process. The module employs the latest industrial SiC power devices and a 3D planar interconnection with double-sided direct cooling (both forced air and liquid).

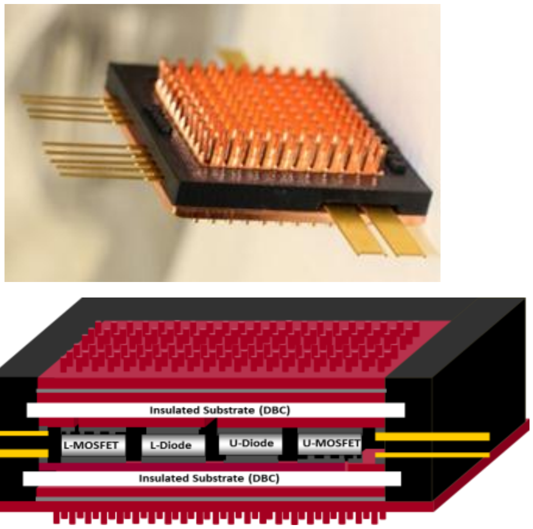

Figure 1-8: ORNL PBA-SiC power module with 3D planar interconnection and double-sided heat sinks.

Figure 1-9 shows a prototype of the PBA-SiC power module integrated with an innovative coolant manifold. Combining the superior attributes of SiC devices with advancements in packaging, the PBA-SiC module reduces electric parasitic parameters by 70%, and specific thermal resistivity by more than 45%, compared to the Toyota Camry module shown in Figure 1-10. These improvements are represented by a four-times larger allowed current density of the SiC device in the module for the same temperature increase. The packaging improvements also allow system operation at high efficiency (50% power loss), resulting in 5 times higher frequency. This is significant for achieving efficiency, power density, and cost targets for power electronic systems in electric drive vehicles.

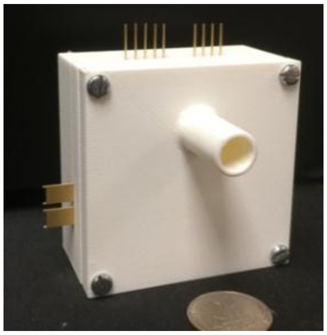

Figure 1-9: Double-sided cooling integrates the PBA power module into a coolant manifold.

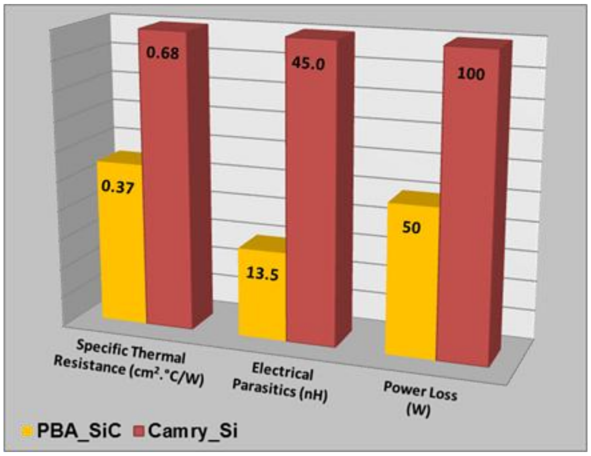

Figure 1-10: Technical relative performance comparison between ORNL PBA-SiC and Toyota Camry Si modules.

1.3 Small Business Innovative Research Grants

Steven Boyd (Technology Manager)

Vehicle Technologies Office
1000 Independence Avenue SW
Washington, DC 20585
Phone: (202) 586-8967
E-mail: steven.boyd@ee.doe.gov

Start Date: October 1, 2012
Projected End Date: September 20, 2013

Objectives

- Use the resources available through the Small Business Innovation Research (SBIR) and Small Business Technology Transfer (STTR) programs to conduct R&D of technologies that can benefit the Advanced Power Electronics and Electric Motors (APEEM) effort within the Vehicle Technologies Program.
- Achieve the four SBIR objectives: (1) to stimulate technological innovation; (2) to increase private sector commercialization of innovations; (3) to use small business to meet federal R&D needs; and (4) to foster and encourage participation by minority and disadvantaged persons in technological innovation.

Accomplishments

- Initiated one Phase I award and two Phase II awards.

✧ ✧ ✧ ✧ ✧

Introduction

The Small Business Innovation Research (SBIR) program was created in 1982 through the Small Business Innovation Development Act. Eleven federal departments participate in the SBIR program and five departments participate in the STTR program, awarding a total of $2 billion to small high-tech businesses. SBIR and STTR are U.S. Government programs in which federal agencies with large R&D budgets set aside a small fraction of their funding for competitions among small businesses only. Small businesses that win awards in these programs keep the rights to any technology developed and are encouraged to commercialize the technology.

A 1982 study found that small businesses had 2.5 times as many innovations per employee as large businesses, while large businesses were nearly three times as likely to receive government assistance. As a result, the SBIR Program was established to provide funding to stimulate technological innovation in small businesses to meet federal agency R&D needs. After more than a decade, the STTR program was launched. The major difference is that STTR projects must involve substantial (at least 30%) cooperative research collaboration between the small business and a non-profit research institution.

Approach

Each year, DOE issues a solicitation inviting small businesses to apply for SBIR/STTR Phase I grants. It contains technical topics in such research areas as energy production (Fossil, Nuclear, Renewable, and Fusion Energy), Energy Use (in buildings, vehicles, and industry), fundamental energy sciences (materials, life, environmental, and computational sciences, and nuclear and high energy physics), Environmental Management, and Nuclear Nonproliferation. Grant applications submitted by small businesses MUST respond to a specific topic and subtopic during an open solicitation.

SBIR and STTR have three distinct phases. Phase I explores the feasibility of innovative concepts with typical awards up to $150,000 for 9 months. Only Phase I award winners may compete for Phase II, the principal R&D effort, with awards up to $1,000,000 over a two-year period. There is also a Phase III, in which non-Federal capital is used by the small business to pursue commercial applications of the R&D. Also under Phase III, Federal agencies may award non-SBIR/STTR-funded, follow-on grants or contracts for products or processes that meet the mission needs of those agencies, or for further R&D.

Results

Phase I Topics for 2014

Below is the text for the Advanced Power Electronics and Electric Machines topic from the 2014 SBIR Phase I Release 2 topics. The full topic release can be found at http://www.science.energy.gov/~/media/sbir/pdf/solicitations/FY13PIR2Topics11912Ver3.pdf

Power electronic inverters and converters are essential for electric drive vehicle operation, and currently add significant cost to these vehicles, therefore limiting their commercialization potential. Improvements in their performance can lead to cost reduction or better utilization of their capabilities in vehicles, as outlined in the U.S. DRIVE partnership Electrical and Electronics Technical Team Roadmap (http://www1.eere.energy.gov/vehiclesandfuels/pdfs/program/eett_roadmap_12-7-10.pdf).

Specifically, improvements are sought for magnetic materials that are used for inductors and magnetic subcomponents in vehicle PE such as inverters, converters, and on-board chargers. Improvements of interest are reduction in size, weight, losses, and cost relative to current state of the art used in production vehicle PE. Materials should be able to withstand operation in a vehicle environment, with ambient temperatures of up to 150°C and no dedicated cooling provided.

Phase I efforts should involve the development and validation of the proposed technology or material with demonstrated performance under simulated operating conditions. In Phase II, the technology should be further advanced and demonstrated through the production of prototype devices.

Phase I Awards Made in 2014

High efficiency, low cost, high-temperature nanocomposite soft magnetic materials for vehicle power electronics

Dr. Timothy Lin

Aegis Technology Inc.

Opportunities exist to use high pressure gas atomization (HPGA) to replace current melt-spinning for making soft magnetic nanocomposite alloy powders containing high moment ▯-CoFe phase. The key to this development is to design advanced soft nanocomposite materials for small, lightweight vehicle PE, by using an innovative low cost HPGA approach to obtain high induction, high temperature soft magnetic nanocomposite materials that have low magnetostrictive coefficients and eddy current, and high operating temperatures over conventional ones.

The project will (1) develop high permeability, large induction, low-loss (hysteretic/eddy current) soft magnetic nanocomposite materials containing high moment α-CoFe, which are capable of operating at high temperatures; and (2) improve mechanical properties and corrosion resistance of these materials with weight reduction and magnetic performance enhancement at higher operating temperatures as a result of reduction in powder size, which can be achieved by lowering the annealing temperature for the crystallization process, because mixtures of amorphous and nanocrystalline powders can be directly obtained by HPGA compared to conventional melt-spinning, which forms amorphous ribbons.

In this Phase I study, Aegis Technology will team with Prof. Anderson of Ames National Laboratory, to develop an innovative class of advanced soft CoFe-based nanocomposite materials. We will further demonstrate an innovative low cost approach (25-30% reduction compared to melt-spinning) in order to produce high permeability, large induction, and low-loss (hysteretic/eddy current) soft magnetic nanocomposite materials with high operating temperatures. The Phase I research will cover material design, processing development, characterization and prototyping, with an aim to identify the underlying technical issues involved with the fabrication and performance of this novel class of soft magnetic nanocomposites.

The successful development of the high permeability, high induction soft magnetic nanocomposite materials with low-loss (hysteretic/eddy current) and high operating temperatures will enable the production of high-efficiency small/lightweight inductors. These proposed soft magnetic nanocomposites will lay the foundation for the next generation of small/lightweight inductors that would have much improved magnetic performance in both permeability and application temperatures with low current losses. Applications for these new magnets are expected for use in electric drive vehicles, aircraft, space vehicles, and weapons power systems. Higher operating temperature soft magnetic nanocomposite materials will enable simpler, lightweight, and more efficient designs for many commercial and military applications.

Phase II Awards Made in 2014

Under the SBIR/STTR process, companies with Phase I awards from FY 2013 are eligible to apply for a Phase II award in FY 2014.Two Phase II awards were made in FY 2014 that resulted in the following project:

Composite Coatings for Low-Cost Motor Windings in Electric Vehicles

Mr. Marvis White

nGimat LLC

Electric vehicles, including hybrids in the nearer term, are the principal transportation technology by which the United States can become independent of foreign oil, can become energy independent overall, and can effect control over greenhouse emissions. For this to become reality electric vehicle costs need to come down and performance needs to improve. For electric vehicle motors, the goals are to reduce manufacturing cost to $4.7/kW by 2020 while improving operating performance, including power density, peak power and operating efficiency.

This SBIR Phase II project will build on the materials and process accomplishments of Phase I, to develop innovative magnet wire insulation for motor windings that results in increased power density and operating efficiency. This will be achieved by developing a wire insulation that has as much as 10 times higher thermal conductivity so that heat can be better dissipated, meaning that the motor will run cooler and therefore more efficiently. In doing so, all other mechanical, thermal and electrical characteristics of the insulation required by standards will be maintained. With better heat dissipation and efficiency owing to high thermal conductivity insulation, dedicated liquid cooling might be eliminated, contributing to smaller, lower-cost electric drives. The proposed advance in magnet wire insulation will result from the incorporation of high thermal conductivity inorganic particles into high performance polymers. The novel insulation is proposed to be applied by the conventional wire enameling method. Electrical, thermal, mechanical, and chemical property measurements according to NEMA standards for magnet wire will be made to insure that all requirements are met or exceeded.

Projections and current market acceptance of hybrid, plug-in, and electric vehicles will create a robust market for motors with the wire insulation being proposed here. In addition to application in EVs, wire insulation technology will also play a key role in larger electric motors that will be used in electric buses and land & marine-based military vehicles. Beyond the traction motor applications mentioned, improved motor/generator systems will also be critical for other energy technologies such as wind turbines.

High Temperature (300°C) Silicon Carbide (SiC)-Based Integrated Gate Drivers for Wide Bandgap Power Devices

Mr. Brett Sparkman

Arkansas Power Electronics International, Inc

SiC power semiconductors have the capability of greatly outperforming Si-based power devices. Smaller switching and on-state losses coupled with higher voltage blocking capability, and especially its high operating temperature make SiC the ideal semiconductor for high performance, high power density power modules. One major factor limiting the switching speed, and thus power loss of these devices, is the parasitic inductance between the gate driver and the switch. The inductance will limit the rise time of the gate current which will limit how fast the gate voltage can increase. This inductance can be minimized by placing the gate driver very close to the power device; however, this increases the ambient temperature of the gate driver up to the maximum junction temperature of the power switch. In addition to this ambient temperature, the gate driver will produce its own losses, increasing the gate driver junction temperature even further. Thus, the full power density advantages of SiC hinge on the successful and reliable realization of this technology at very high temperatures (> 300 °C).

High temperature operation introduces a set of technological barriers. APEI, Inc. researchers have developed solutions to some of these barriers and have proven the feasibility of SiC PE operating at high temperature. A void exists, however, in the full realization of these highly efficient power modules. Currently there are no high temperature integral solutions to meet the particular requirements of driving a SiC field-effect transistor (FET) (e.g., high switching frequency, high voltage transient immunity, high temperature). Approaches with discrete components are large with reduced reliability and added parasitics. The ideal solution is a compact, highly integrated, and flexible gate driver that could be rapidly implemented with its associated switch.

In this project, APEI, Inc. will continue development of its patented high temperature gate driver technology, enabling the next generation of high-efficiency, high power density converters. At the conclusion of Phase II, APEI, Inc. will have designed, fabricated, and tested a high temperature (300°C) SiC application specific integrated circuit (ASIC) gate driver. The fabricated SiC ASIC gate driver will then be integrated into an APEI, Inc. power module, providing for a next generation smart power module solution.

II. RESEARCH AREAS

2.0 Systems, Modeling, and Benchmarking

2.1 Benchmarking EV and HEV Technologies

Tim Burress (Principal Investigator)

Oak Ridge National Laboratory
National Transportation Research Center
2360 Cherahala Boulevard
Knoxville, TN 37932
Phone: (865) 946-1216; Fax: (865) 946-1262
E-mail: burressta@ornl.gov

Burak Ozpineci, ORNL EDT Program Manager
Phone: (865) 946-1329; Fax: (865) 946-1262
E-mail: burak@ornl.gov

Susan A. Rogers, DOE EDT Program Manager
Phone: (202) 586-8997; Fax: (202) 586-1600
E-mail: Susan.Rogers@ee.doe.gov

Start Date: October 2013
Projected End Date: Ongoing

Objectives

- Benchmark hybrid electric vehicle (HEV) and electric vehicle (EV) components.
  - Assess design, packaging, and fabrication innovations in subsystems and components.
    - Determine techniques used to improve specific power and power density and reduce cost.
    - Perform compositional analysis of key components.
  - Examine performance and operational characteristics during comprehensive tests and evaluations.
    - Obtain peak torque and power capability.
    - Identify detailed information regarding time-dependent and condition-dependent operation.
  - Compile information from evaluations and assessments.
    - Identify new areas of interest.
    - Compare results with other EV/HEV technologies and U.S. Department of Energy (DOE) targets.

Technical Barriers

- Integrating custom ORNL inverter-motor-controller with original equipment manufacturer (OEM) components.
  - Optimizing controls for nonlinear motors throughout operation range.
- Intercepting, decoding, and overtaking OEM controller area network signals.
- Adapting nonstandard motor shaft and assembly to dynamometer and test fixture.

Technical Targets

- This project helps with program planning and the establishment and verification of all DOE 2020 targets.

Accomplishments

- Overall: Conducted thorough benchmark assessments and reported on many HEV/EV technologies.
  - 2004 Prius, 2006 Accord, 2007 Camry, 2008 Lexus LS 600h, 2010 Prius, 2011 Hyundai Sonata inverter/motor, 2012 Nissan LEAF inverter/motor, 2012 Hyundai Sonata hybrid starter-generator (HSG), 2013 Nissan LEAF charger, and 2014 Honda Accord (in progress).
- FY 2014
  - Continued and finalized assessments and testing/evaluation of the 2013 Nissan LEAF 6.6 kW on-board charger (OBC).
  - Conducted thorough teardown assessments of 2014 Honda Accord power converter unit (PCU) and transmission/transaxle (includes electric motor and generator).
  - Initiated dynamometer testing of the 2014 Honda Accord inverter and motor.

✧ ✧ ✧ ✧ ✧

Introduction

Automotive manufacturers usually do not publish details about the design, functionality, and operation of EV/HEV technologies, and even published performance specifications need to be verified and clarified. For example, single-value power ratings for motors and inverters are often published; but they do not include information about the power capability throughout the operation range (e.g., versus speed), the duration for which this power can be maintained, the efficiency throughout the operation region, and many other important characteristics. Therefore, ORNL performs teardown assessments to obtain comprehensive information on design, functionality, and subcomponent characteristics. Furthermore, components are completely instrumented and tested in a dynamometer test cell to determine operational characteristics such as performance and efficiency.

These benchmarking activities play an important role in program planning efforts by defining the current state of the art for components and subsystems, defining performance and design metrics for DOE's competitive research and development (R&D) efforts, and identifying technology gaps to provide guidance for future research focus areas. To establish practical targets, the baseline technological status must be obtained from subsystems currently in the marketplace. Therefore, benchmarking cutting-edge technologies in competitive global markets establishes a solid technology baseline for the DOE EDT program. It also assists in determining whether performance goals established for the program are realistically achievable and present sufficient challenge to warrant a robust program.

Benchmarking activities also ensure that the DOE EDT program will not duplicate technical innovations found in commercially available technologies. They provide technical insight, allowing the DOE program to move more rapidly by maintaining awareness of current trends and technical innovations in advancing on-the-road technologies. Findings and results from the benchmarking efforts are detailed in reports and presentations. These publications are frequently cited in technical conference papers and have a high level of recognition among industry, academia, and enthusiasts.

Approach

The general approach for benchmarking HEV and EV components is shown in Figure 2-1. Appropriate components are selected by DOE based on information from the Internet, technical publications, published specifications, and feedback from U.S. automotive manufacturers and suppliers. After benchmarking of the 2012 Hyundai Sonata HSG/inverter and teardown of the 2013 Toyota Camry PCU were completed in FY 2013, initial assessment of the 2013 Nissan LEAF charger began in the latter part of FY 2013. Detailed testing and analysis of the 2013 Nissan LEAF was conducted in the first half of FY 2014. Some research was conducted on the 2014 Honda Accord in the first half of FY 2014, but because of the unavailability of parts, much of the benchmarking effort on the 2014 Accord occurred in the second half of FY 2014. The approach and findings from the 2013 Nissan LEAF charger and 2014 Honda Accord inverter/motor benchmarking are discussed in the following sections.

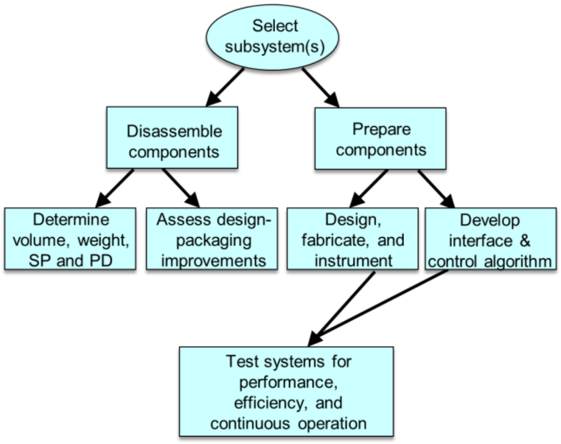

Figure 2-1: General approach for benchmarking components.

Results

2013 Nissan LEAF Charger

With the recent advent of the first mass-produced full EV, the Nissan LEAF, it is important to note that the OBC is a critical component that impacts overall efficiency and the cost of operating the vehicle. The charger requires several power stages and many components, so there are significant associated cost and design requirements. The Nissan LEAF inverter and motor were benchmarked by ORNL in FY 2012 and the results published. The 2012 LEAF includes a 3.3 kW OBC, and the 2013 LEAF upgraded to a 6.6 kW charger, both of which accept ac power in standard forms (i.e., 120 and 240 V). A separate "fast-charging" port is available that accepts dc power from a large off-board charger.

The focus of DOE's EDT program is on components and subsystems; therefore, the entire vehicle was not procured and used during analyses of the LEAF's OBC. Various standards (namely SAE J1772) are in place to regulate charger functionality and impact on grid power quality. Since harmonic analysis for total harmonic distortion and other metrics related to standards requires the entire system, ORNL focused on obtaining design, functionality, and operational characteristics at a detailed subsystem level. Doing so required destructive teardown and invasive investigations to determine the layout and connectivity of all items in the charger. ORNL evaluated the operation of converter stages by implementing custom-developed control algorithms, and some information from FY 2013 is reviewed before detailed results are given.

Design and functionality assessments

The 2013 Nissan LEAF charger is shown on the upper left in Figure 2-2. As received, the mass of the charger was about 16.3 kg, which includes the mass of the external off-white line filter and its support bracket weighing a total of 3.2 kg. The main charger assembly width and length are about 9.9 and 10.9 in., and the height varies from about 3 to 4.5 in., giving a volume of approximately 11.1 L. Using these metrics with a power rating of 6.6 kW, the specific power and power density are 0.4 kW/kg and 0.6 kW/L, respectively. These figures seem quite low, but it should be noted that the charger can operate continuously at a power level of 6.6 kW, and isolation and power quality specifications required by standards ultimately require additional components.

The underside of the charger assembly is also shown in Figure 2-2, where cast (then machined) aluminum channels for liquid cooling with a water ethylene-glycol mixture are visible. The internal compartment includes a control-communication circuit board, a driver and signal conditioning board, a black power module, large passive components for various power stages, and many smaller devices and peripheral passive components. The control board includes a Renesas R5F71476FPV microcontroller, the type of microcontroller used for the Nissan LEAF motor controller.

The block diagram in Figure 2-2 describes the various stages of the OBC and indicates where the associated devices are located in the power module. The corresponding circuit schematic is shown in Figure 2-3 and Figure 2-4. Note that the latter two figures are actually one schematic, but they are separated for image clarity. Also note there is only one 310 V/1 uF and 420 V/2700 uF capacitor in the circuit, but it is shown in both figures as a reference item. After the external line filter, the ac input of the charger is fused and additional filtering (including common mode) is applied with relatively small passive components. A relay remains open until ac voltage has been applied for a certain amount of time, to avoid high in-rush currents by charging the system capacitors through three resistors. The first conversion stage of the charger is a conventional rectifier with four diodes. The next stage is a boosting power factor correction (PFC) stage, which includes three metal oxide semiconductor field-effect transistors (MOSFETs) in parallel for chopping action. It also includes two diodes in parallel to prevent reverse current and to allow energy to be stored in the inductor as the MOSFETs are active. The boosted voltage is regulated to between ~360 and 400 V, and a large 420 V/ 2700 uF electrolytic capacitor is located at the boosted output.

The final stages of the charger, shown in Figure 2-4, include an H-bridge inverter with two MOSFETS for each switch and one small anti-parallel diode for each switch. The inverter drives the primary coil of the large isolation transformer, which has two secondary windings. Output from the two secondary windings is fed to two full-bridge rectifiers, with outputs placed in series and balancing diodes in parallel with each rectifier. In total, ten diodes are located in the final rectification stage. The rectified output is fed through two large inductors, a diode (not located in the power module), a common mode filter, and small passive filters before passing through the output connector that connects to the battery.

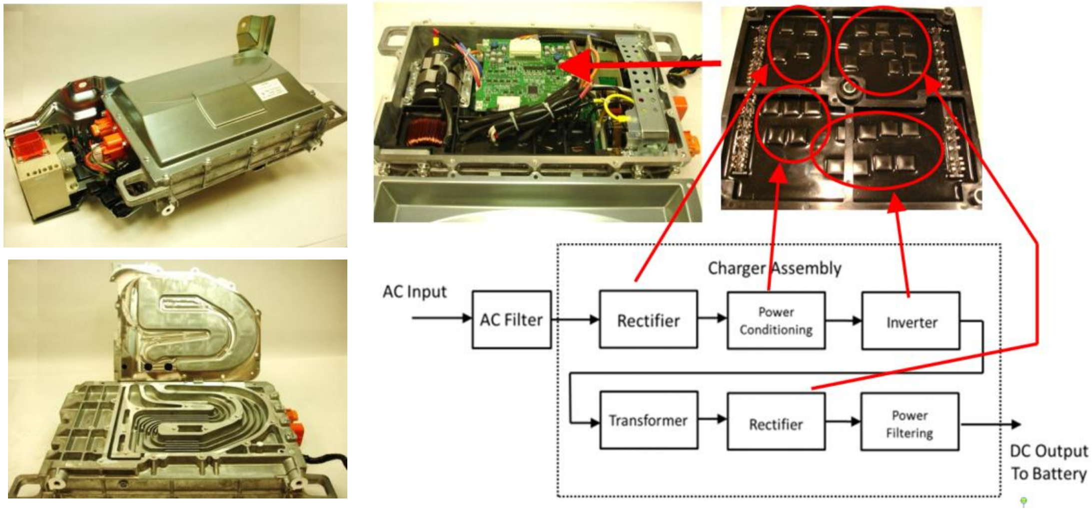

Figure 2-2: Nissan LEAF charger ac input and boost-PFC.

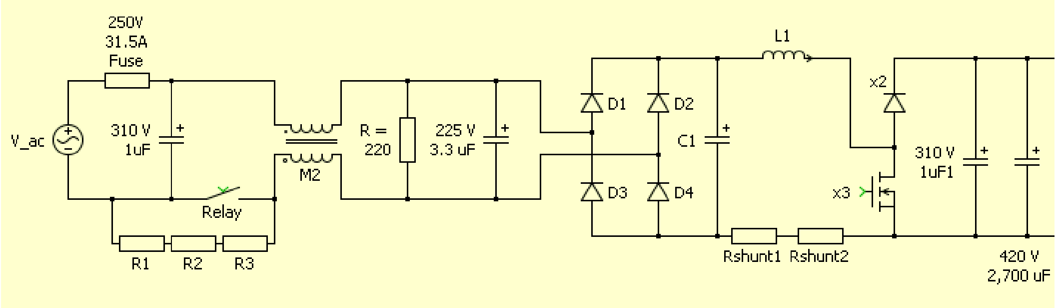

Figure 2-3: Nissan LEAF charger ac input and boost-PFC.

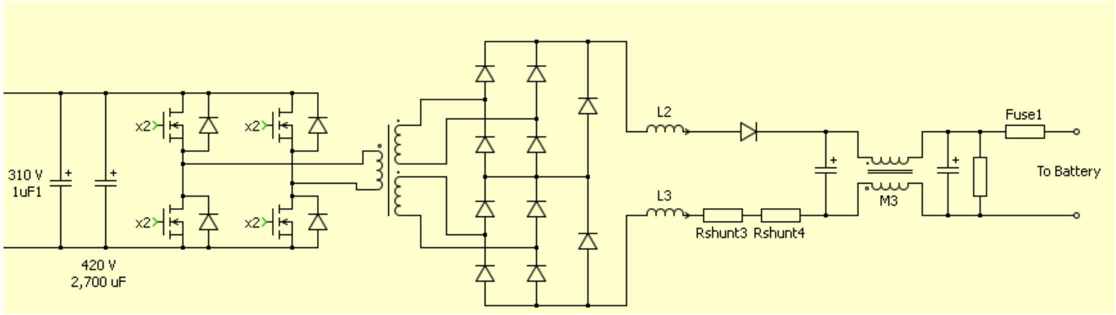

Figure 2-4: Nissan LEAF charger isolation and rectification stage.

The battery voltage varies with the state of charge; therefore, the output voltage of the charger must have a fairly wide range to maintain a constant charging power level and avoid overcharging conditions. It can be roughly estimated that the charger output voltage is in the range of 300–400 V for normal charging conditions.

Testing and characterization

In carrying out basic operational tests, it was discovered that the driver circuitry for the H-bridge inverter is relatively unconventional: the MOSFETs are controlled with only the power isolation transformer, and no additional control signal isolation (i.e., optocoupler) is used. This is possible largely because the H-bridge can be controlled with phase-shift control. Additionally, it appears that the dead-time is generated on the output of the secondary with passive components. The PFC chopper is operated at a frequency of about 30 kHz, and the input current is limited at about 2 Arms.

The image shown in Figure 2-5 displays the operational waveforms of the PFC during testing at a power level of 2.6 kW. The waveforms indicate high power factors with notable stability at the zero crossing, which can be a challenging area in which to maintain stability for PFC operation. The efficiency of the boost-PFC stage at a power level of 3.3 kW is about 92.1 and 96.5%, for 120 and 240 V input voltages, respectively. Similar waveforms are shown in Figure 2-6 for operation at 5.6 kW. For operation at 6.6 kW, the boost-PFC efficiency is about 96.5%. This power level is achievable only at 240 V because of the common residential current availability for 120 V receptacles.

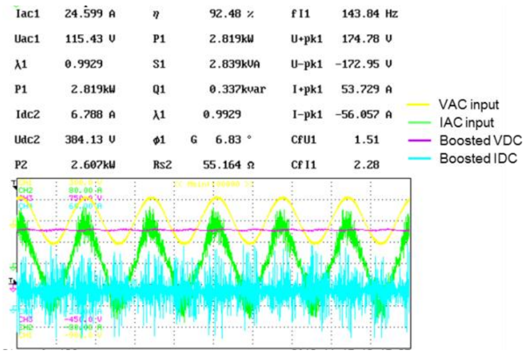
```
Iac1   24.599 A    η          92.48 %     fI1     143.84 Hz
Uac1   115.43 V    P1         2.819kW     U+pk1   174.78 V
λ1     0.9929      S1         2.839kVA    U-pk1  -172.95 V
P1      2.819kW    Q1         0.337kvar   I+pk1   53.729 A
Idc2    6.788 A    λ1        0.9929       I-pk1  -56.057 A
Udc2   384.13 V    φ1    G    6.83 °      CfU1      1.51
P2      2.607kW    Rs2       55.164 Ω     CfI1      2.28
```

Figure 2-5: Power analyzer screenshot during PFC testing at 3.3 kW.

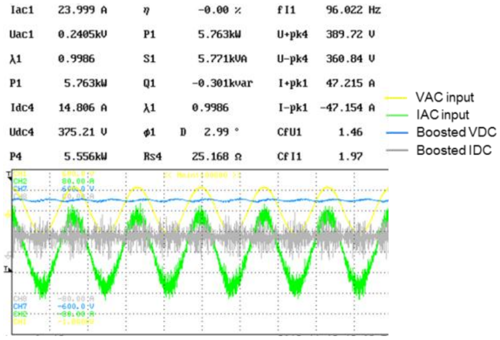
```
Iac1   23.999 A    η          -0.00 %     fI1     96.022 Hz
Uac1   0.2405kV    P1         5.763kW     U+pk4   389.72 V
λ1     0.9986      S1         5.771kVA    U-pk4   360.84 V
P1      5.763kW    Q1        -0.301kvar   I+pk1   47.215 A
Idc4   14.806 A    λ1        0.9986       I-pk1  -47.154 A
Udc4   375.21 V    φ1    D    2.99 °      CfU1      1.46
P4      5.556kW    Rs4       25.168 Ω     CfI1      1.97
```

Figure 2-6: Power analyzer screenshot during PFC testing at 6.6 kW.

The graph in Figure 2-7 indicates the PFC efficiency versus dc output power for 120 and 240 V operation. It is clear that operation at 120 V correlates with efficiencies between 92 and 92.5% over the range of operation. Operation at 240 V correlates with an efficiency of 96 to 96.5% for all power levels above 3 kW. A similar graph is shown in Figure 2-8, where the power factor is plotted versus dc power for 120 and 240 V operation. The power factor is very high for 120 V operation and low power levels, but it quickly drops to about 0.92 as the power increases from about 2.5 to 3.3 kW. Operation at 240 V results in a gradual increase in the power factor from roughly 0.98 at 2.5 kW, approaching 1 near operation at 6 kW.

Test results indicate that the efficiency of the final charger stage is about 94% at 3.3 kW and 120 V and about 95% at 6.6 kW for 240 V operation. This yields a total system efficiency of about 87% for operation at a power level of 3.3 kW and 120 V and about 91.5% for operation at 6.6 kW and 240 V. Since the operation of the charger is largely dependent on battery characteristics and OEM controls, as the charger is operating with the battery pack, ORNL has worked with other organizations that perform full-vehicle assessments to verify and analyze in situ operational characteristics. However, the invasive effort required to obtain this information creates a difficulty: there is some risk of compromising vehicle integrity/value, and most test vehicles are borrowed or will be used in company fleets. Nonetheless, system-level efficiencies are easier to obtain. Argonne National Laboratory performed full-vehicle testing and reports that the 3.3 kW 2012 LEAF charger and EV service equipment have a total efficiency of about 86.3%, which is the efficiency from the ac receptacle to the dc power input to the battery. This is in close agreement with the measurements described above.

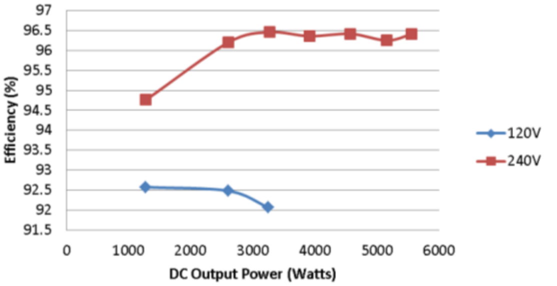

Figure 2-7: Nissan LEAF charger PFC efficiency vs dc power.

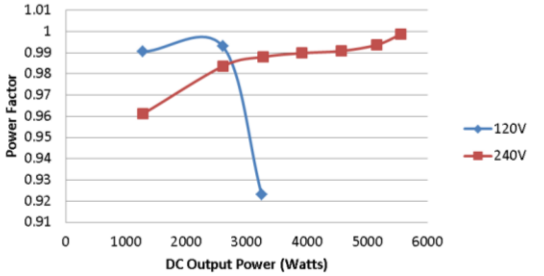

Figure 2-8: Nissan LEAF Charger PFC power factor vs dc power.

2014 Honda Accord PCU and Transmission/Transaxle

Honda was one of the first automotive manufacturers to mass-produce and sell hybrid vehicles in the United States. However, all of the mass-produced hybrid systems have been mild hybrids, with the electric portion of the powertrain operating at a power level of 14 kW or less. For model year 2014, Honda offered a full hybrid powertrain (termed the “Earth Dreams” hybrid system), one without plug-in and one with plug-in capability for recharging the battery. The 2014 plug-in HEV (PEV) had limited production numbers and was largely sold only in California and New York, where tax incentives were higher. The limited number of these vehicles caused significant difficulty and unexpected delays in obtaining PEV parts, of which the OBC was of particular interest. However, 2014 Accord HEV components were also of significant interest, as the motor has the same published power rating of 124 kW for both HEV and PEV powertrains.

Published specifications indicate that the PEV has a 6.7 kWh battery pack, compared with a 1.3 kWh rating for the HEV version, both with a published maximum output of 41 kW. The nominal battery pack voltages for the PEV and HEV are 320 and 259.2 V, respectively. The published engine maximum power rating is 105 kW, and the total system power is reported to be 146 kW, which is the sum of the maximum engine power and the maximum battery power. A detailed teardown and benchmarking analysis of the 2014 Honda Accord hybrid system was conducted, and dynamometer testing began in FY 2014.

The 2014 Accord transmission (Figure 2-9), has a total mass of about 113.5 kg (249.5 lb), quite close to that of the 2007 Camry hybrid transmission mass of 108 kg. This is a good comparison because both passenger vehicles are sedans of similar size and power requirements. As is the case for many hybrid transmissions, there is no torque converter between the internal combustion engine and the transmission. Other than the absence of a torque converter, the transmission mounts to the engine in a conventional manner with a flywheel attached to the spline. Various sections of the transmission are indicated in Figure 2-10, in which the engine input spline shafted is indicated. The gear section is adjacent to the engine mounting location, and it includes the differential gear that drives the left and right drive shafts and ultimately the front wheels. The section that houses the drive motor is located next to the gear section, and the generator section is located next to the motor section on the end of the transmission. The image in Figure 2-11 offers another view of the three primary sections of the transmission, as well as external components such as the motor terminals, resolver connectors, and clutch solenoid valves.

After the end plate of the generator section is removed, the generator is clearly visible, as shown in Figure 2-12. The generator end plate includes a position resolver that has 14 stator teeth, and the generator shaft has a soft-magnetic resolver rotor with four smooth lobes consisting of 8 laminations for position sensing. Also indicated in Figure 2-12 are four tubes used for oil spray cooling of the generator and motor end windings. The image on the right of Figure 2-12 shows one of the tubes after removal. Four groups of two holes are positioned so that they spray the end turns on both sides of the generator and motor. Since the generator is smaller than the motor, the two groupings for the generator are closer together than those for the motor spray holes. After the generator is removed, a clutch located between the generator and the motor is visible (Figure 2-13). The clutch does not have hydraulic activation and is used only as a torque limiter, most likely to mitigate transients and peak conditions when the generator is used to start the engine.

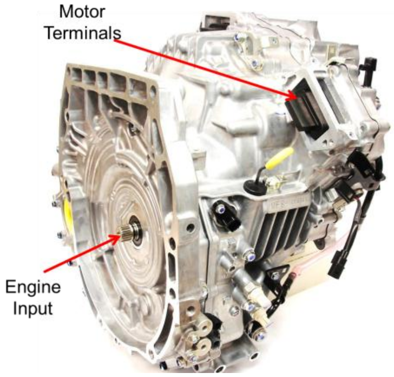

Figure 2-9: 2014 Honda Accord transmission.

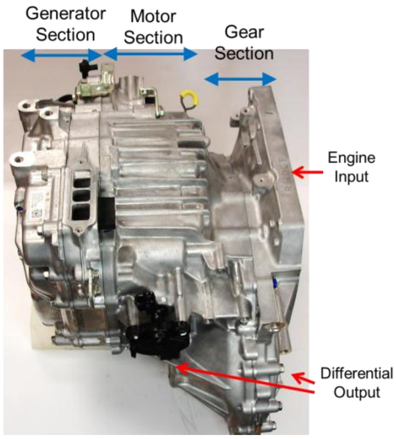

Figure 2-10: Sections of the 2014 Honda Accord transmission.

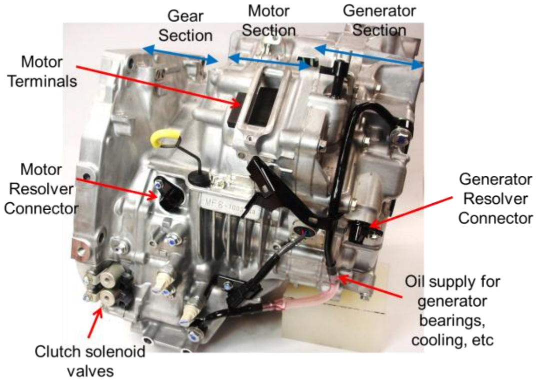

Figure 2-11: Sections and various exterior components of the 2014 Honda Accord transmission.

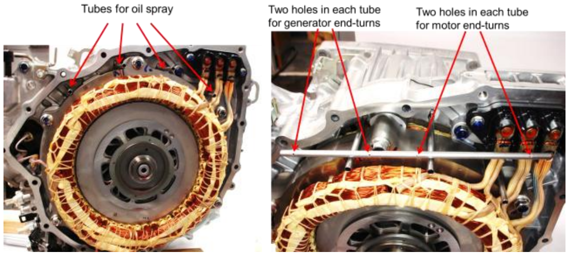

Figure 2-12: 2014 Accord transmission motor and generator oil spray cooling.

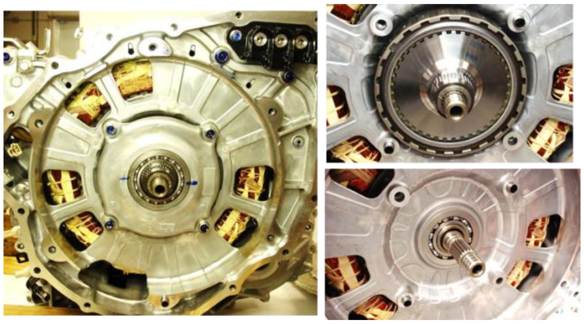

Figure 2-13: 2014 Accord torque-limiting clutch between engine and generator.

One side of the torque-limiting clutch is connected to the generator, and the other side is connected to a long shaft, shown in Figure 2-14, that feeds through the hollow motor rotor shaft and ultimately into the gear section of the transmission. At the end of the long generator clutch shaft, a small helical gear mates with a gear fixed to the splined engine input shaft, which is shown on the left in Figure 2-14. Additional components in the gear section include a large differential gear, a drive gear, an overdrive clutch, and a small motor gear. The image on the right in Figure 2-14 shows the gear section with the generator shaft removed so that the small motor gear is visible. Additionally, the overdrive clutch and engine input spline shaft/gear that mates with the generator shaft have been removed.

During normal operation, the Accord hybrid system operates as a series hybrid, in which power from the engine is absorbed by the generator and passed to the battery and the electric motor for vehicle propulsion. However, at high speeds, the overdrive clutch engages the engine to the drive wheels through a fixed gear ratio. With the overdrive clutch removed, as shown in Figure 2-14, the gear that mates the engine to the drive gear (when the clutch is activated) is visible. The number of gear teeth on each gear is indicated in Figure 2-15. The differential gear has 65 teeth, the driven gear has 39, the drive gear has 49, the clutched generator shaft has 34, the electric motor output shaft has 20, the clutched engine output has 61, and the engine input gear that mates with the generator gear has 66. Neglecting occasional slippage in the torque-limiting clutch, the generator rotational speed is 1.94 times faster than that of the engine.

Considering the OEM tire size, the differential axle rpm is about 13 times the vehicle speed in miles-per-hour (MPH). The total gear ratio from the electric motor to the differential output is 8.38; therefore, the rated motor speed of 14,000 rpm correlates with a vehicle speed of about 128 MPH. The common vehicle speed of 60 MPH correlates with an electric motor speed of about 6500 rpm. When the overdrive clutch is active, the gear ratio from the engine to the differential output is about 2.75, so engine speeds of 2000 rpm and 4000 rpm correlate with a vehicle speed of 66 MPH and 112 MPH, respectively.

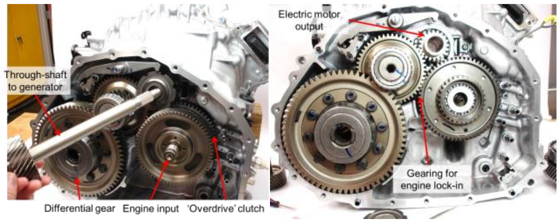

Figure 2-14: 2014 Accord transmission gear section.

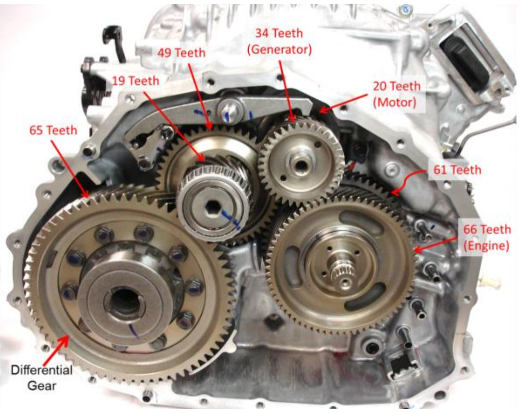

Figure 2-15: 2014 Accord transmission gear section.

The Accord motor and generator stator and rotor laminations appear to be identical—the stator outer diameters are 29.13 cm (11.469 in.), the rotor outer diameters are 19.502 cm (~7.678 in.), and the air gap is about 0.79 mm (0.031 in.). The motor stator stack length is 6.17 cm, which is about 1.64 times the generator stator stack length of 3.762 cm. These metrics and other motor and generator parameters are summarized in Table 2-1. The motor stator and rotor masses are 20.8 and 11.8 kg, respectively, versus the generator stator and rotor masses of 14.4 and 8.3 kg, respectively. Both stators, shown in Figure 2-16, have 48 slots with 8 poles with windings comprising wires that are 18 AWG in size. The motor has 20 wires in parallel for each phase, which split into two parallel paths, each of which has four poles in series before combining at the neutral point. The generator motor has 22 wires in parallel for each phase.

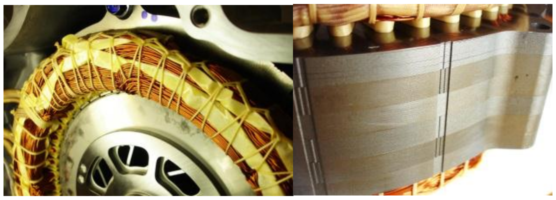

Figure 2-16: 2014 Accord motor stator.

The rotor lamination design for the Accord motor and generator rotor is shown at left in Figure 2-17. The design is similar in principle to the rotor lamination design used in the Toyota Prius (right in Figure 2-17). The inset magnets are in a “V” orientation, and slight dimples are located at the air gap near the tips of the magnets to prevent magnet flux leakage. Both 2014 Accord and 2010 Prius rotor laminations have large holes in the center of the rotor where magnetic flux is not necessary and therefore rotor mass can be reduced substantially. The Accord has a considerably greater amount of material removed from the center section of the rotor, in a pattern that resembles a camera shutter. Another key distinction between the Accord and Prius rotors is the large gap between the magnetic poles of the Accord, along with an oval and a small hole at the tip of each oval. These features help reduce magnet flux leakage and change the magnetic saliency of the rotor, which can modify reluctance torque contributions and potentially yield a more smooth torque profile. The overall NdFeB magnet mass is 0.76 kg for the generator rotor and 1.24 for the motor rotor. A comparison is made in Table 2-1, where a ratio is computed with the magnet mass and the published power rating. This ratio is about 10 for the Accord motor, which is slightly higher than that of the Camry and first-generation Prius, but lower that of the 2010 Prius.

Figure 2-17: 2014 Accord generator rotor lamination (left) and 2010 Toyota Prius lamination (right).

The 2014 Accord PCU, shown in Figure 2-18, includes an inverter for the generator, an inverter for the motor, and a boost converter to boost the battery voltage up to a level of 700 V, depending on driving conditions. The PCU, manufactured by Fuji Electric, has an overall mass of 17.5 kg and a volume of 12.37 L. Various views of the PCU are shown in Figure 2-19, where the dc input connector from the battery and 3-phase output connectors from the motor and generator inverters are visible. An electrical schematic that represents the operation of the PCU is shown in Figure 2-20. The overall functionality of the PCU is nearly identical to that of the Toyota PCU, in that the boost converter operates similarly, and the output of the boost converter supplies a high-voltage dc link for the motor and generator inverters. The PEV version of the Accord has a nominal battery voltage of 320 V and the HEV Accord has a nominal battery voltage of 259 V.

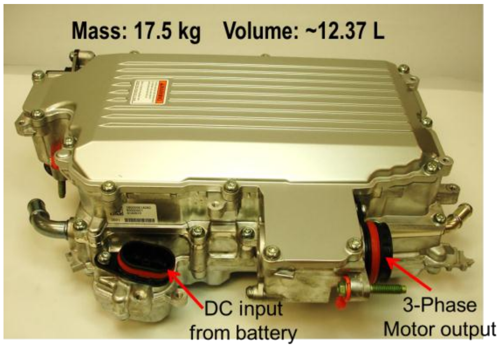

Figure 2-18: 2014 Accord PCU overview.

Table 2-1: Motor and generator design parameters for various HEVs and EVs.

Parameter	Accord G	Accord M	LEAF	2010 Prius	LS 600h	Camry	2004 Prius	Comments
Lamination Dimensions								
Stator OD, cm	29.202	29.134	20.0	26.4	20.0	26.4	26.9	
Stator ID, cm	19.660	19.660	13.10	16.19	13.086	16.19	16.19	
Stator stack length, cm	3.762	6.17	15.1	5.08	13.54	6.07	8.4	
Rotor OD, cm	19.504	19.500	13.0	16.04	12.91	16.05	16.05	
Rotor lamination ID, cm	11.80			5.1	5.3	10.5	11.1	
Rotor stack length, cm				5.0165	13.59	6.2	8.36	
Air gap, mm	0.78	0.8		0.73	0.89	0.73025	0.73025	
Lamination thickness, mm	0.34			0.305	0.28	0.31	0.33	
Mass of Assemblies								
Rotor mass, kg	8.260	11.810	16.432	6.7	11.93	9.03	10.2	Includes rotor shaft.
Stator mass, kg	14.4	20.815		15.99	18.75	18.0	25.9	
Stator core mass, kg	Est			10.36	15.15	12.38	19.05	Laminations only.
Stator Wiring								
Number of stator slots	48	48	48	48	48	48	48	
Stator turns per coil		11?	8	11	7	14	9	
Parallel circuits per phase	2 legs		4 legs	0	2 legs	2 legs	0	
Coils in series per phase	4 per leg		2 per leg	8	4 per leg	4 per leg	8	
Number of wires in parallel	11 per leg	10	15 per leg	12	9 per leg	9 per leg	13	
Wire size, AWG	~18	~18	~20	20	~0.032" ≡ 20	20	19	
Phase resistance at 21°C, ohms			~0.00567	0.077	0.0225	0.023	0.069	Average of phase-to-phase divided by two.
Total mass of stator copper, kg	Est		5.616	4.93	3.59	5.6	6.8	
Slot depth, mm	~28.59	~28.19		30.9	19.25	30.9	33.5	Gap to slot bottom.
Slot opening, mm	~2.037	~2.037		1.88	1.88	1.88	1.93	At air-gap
Magnets (neodymium iron boron [NdFeB])								
Magnet dimensions, mm	26.5x6.28x ~37.62	26.5x6.28x ~61.7	21.3x8.34x2.29 and 28.9x8.36x3.79	49.3×17.88×7.16	66.4×18.7×3.05	60.6×19.1×6.6	83.1×18.9×6.5	
Magnet volume, cm³	6.26	10.27		6.31	3.78	7.63	10.2	
Magnet mass, grams	~47.2	77.50		48	28.1	58	77	
Total mass of magnets, kg	0.755	1.24	1.895	0.768	1.349	0.928	1.232	Entire magnet mass in rotor.
Magnet mass per published power rating (grams/kW)		10.0	23.69	12.8	8.43	8.84	22.4	

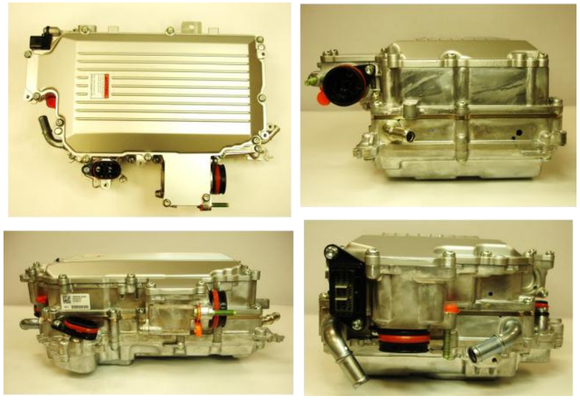

Figure 2-19: Various views of 2014 Accord PCU.

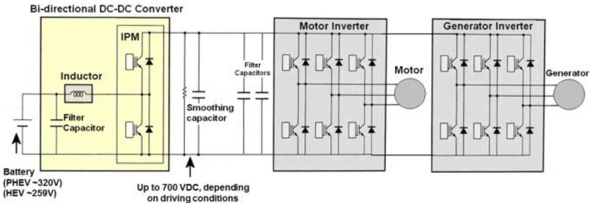

Figure 2-20: Electrical schematic of 2014 Accord PCU.

The bottom compartment of the Accord PCU, shown upside down in Figure 2-21, contains large bulk capacitors and the inductor for the boost converter. The boost inductor is mounted to the bottom of a heat exchanger, and white thermal paste is used to facilitate heat transfer from the inductor. The input from the battery is attached to a filter capacitor and fed through the boost inductor. The capacitor on the dc input from the battery is rated at 410 uF and 370 Vdc. The output of the boost converter passes through a current transducer for feedback control and connects to the input of the power electronics of the boost converter. The power module and control board are located in the top compartment, shown in Figure 2-22.

The output of the boost converter power electronics is directly connected to a dc link bus that connects to the motor inverter and generator inverter power electronics. Both positive and negative high-voltage buses extend the width of the power module, shown in Figure 2-22 and Figure 2-23. This dc link extends from both ends of the power module in the top compartment to the capacitor in the bottom compartment. Several capacitor cells are vertically oriented to form a bulk capacitor rated at 1125 uF and 700 Vdc. There are also two small 700 Vdc, 0.047 uF capacitors attached to the high-voltage dc link. The high-voltage capacitors and the capacitor attached to the battery input are located within one potted module. There is no direct contact between the capacitor module and the heat exchanger.

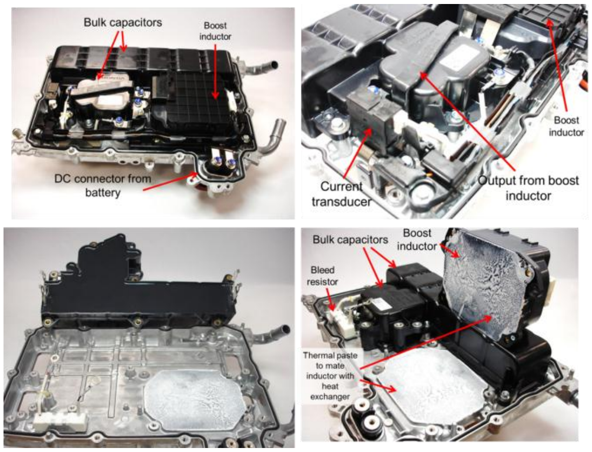

Figure 2-21: Bottom compartment of 2014 Accord PCU.

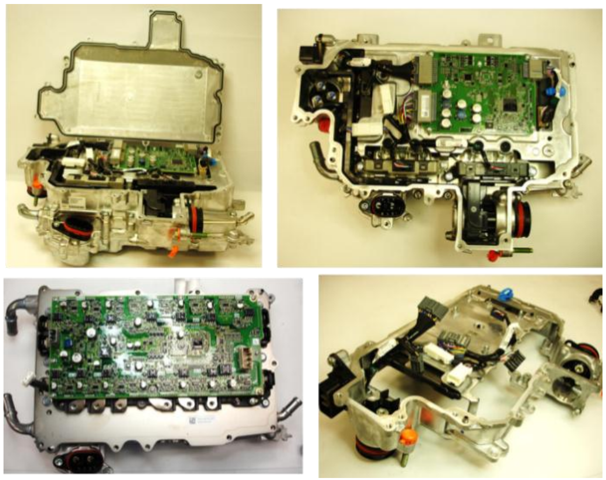

Figure 2-22: Top compartment of 2014 Accord PCU.

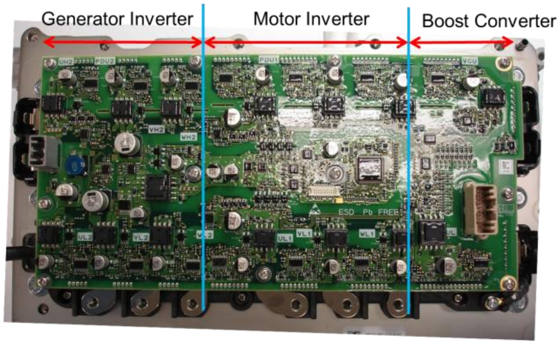

Figure 2-23: Power module and driver board in 2014 Accord PCU.

The control board includes two 32 bit, 32 MHz Renesas microcontrollers (D70F3507M1GJA2) for the control of the electric motor and generator. The board includes a Tamagawa AU6802 resolver to the digital chip to supply and convert analog signals for position feedback. The control board is mounted to a plate that is cast with the housing of the top compartment, as shown at lower right in Figure 2-22. Other benchmarked PCUs use a thinner sheet of metal that mounts to a cast housing. In addition to being used for support, the metal piece also mitigates the impact of electromagnetic interference from the power module on the control circuitry.

A similar 32 bit, 32 MHz Renesas microcontroller is located on the driver board shown in Figure 2-23. The driver board is mounted directly to the power module, and the locations of the power electronics devices for the motor inverter, generator inverter, and boost converter are indicated in Figure 2-23. The generator inverter includes one insulated gate bipolar transistor (IGBT) per switch, yielding a total of six IGBTs and diodes for the generator inverter. The motor inverter uses two IGBTs per switch, so the entire motor contains 12 IGBTs and diodes. Three IGBTs are used on the lower switch of the boost chopper, and only two IGBTs are used in the upper switch of the chopper, which is used during regenerative braking. All previously benchmarked PCUs include that same number of IGBTs for both upper and lower switches of the boost chopper. Current transient requirements for the lower switch and upper diode are more substantial than those of the upper switch; therefore, Honda was able to implement a slightly lower-cost solution for the boost converter power electronics.

The power module is directly integrated with the heat exchanger, as shown in Figure 2-24. Conventional power modules have heat spreaders. A layer of thermal paste is applied to the bottom of the power module and, in the case of many benchmarked PCUs, attached to a heat exchanger that is cast as a part of the housing. However, the Accord PCU has no thermal paste because the heat exchanger is directly integrated with the module, thereby greatly improving the heat transfer from the power electronics devices to the cooling medium. Fine fins, shown on the right in Figure 2-25, are machined on the bottom of the heat sink, which is cooled by a mixture of water and ethylene glycol. The other side of the heat exchanger is part of the bottom compartment, and the flow path of the coolant is indicated on the left in Figure 2-25. Slight indentions are located in the flow path adjacent to the boost inductor, and several fins are located in the flow path below a smaller portion of the boost inductor, by which the coolant passes just before exiting the PCU.

Detailed designs were developed to provide access to the electric motor shaft in the transmission while maintaining the cooling and lubrication functionality used in the original form. This integration requires special attention to detail because high speed and power levels are involved. The electric motor shaft is not normally externally accessible, and unique methods were required to obtain access for dynamometer testing. A custom plate was designed with high-tolerance alignment features and considerations for lubrication. A unique adapter shaft was also designed to adapt the motor shaft to ORNL's dynamometer. The graph in Figure 2-26 shows a comparison of back–electromotive force results, which are considerably lower for the Accord. The 2014 Accord hybrid system is currently being tested to verify performance and to obtain detailed characteristics across the entire operation range of the system.

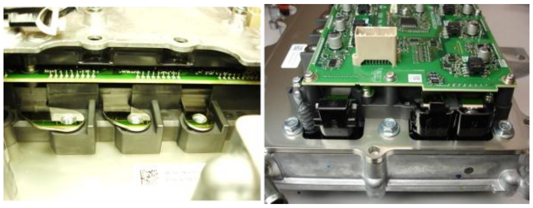

Figure 2-24: Power module and driver board in 2014 Accord PCU.

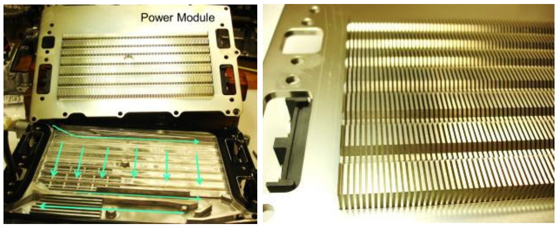

Figure 2-25: 2014 Accord PCU heat exchanger.

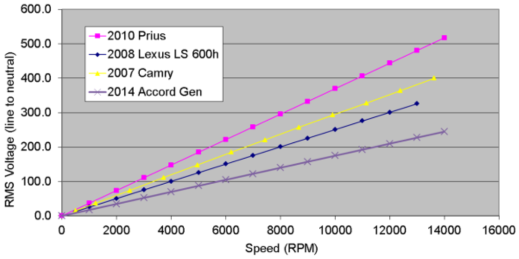

Figure 2-26: 2014 Accord back–electromotive force test results.

Conclusions and Future Directions

Detailed testing of the Nissan LEAF charger indicates that the efficiency of the charger varies greatly depending on the input voltage. For an input voltage of 120 V, the total charger efficiency at 3.3 kW is about 87%, versus an efficiency of about 91.3% for operation at 240 V. Operation at 6.6 kW and 120 V is not possible because of the current limitations of common household receptacles. A charger efficiency of 91.5% was observed for operation at 6.6 kW and 240 V.

The 2014 Honda Accord transmission/transaxle includes a 124 kW electric motor and a generator that absorbs energy from the combustion engine to recharge the battery and to supply energy to the electric motor for vehicle propulsion. For most conditions, the system operates as a series hybrid in that the combustion engine propels the vehicle only through the generator and motor. In some low to medium road load conditions and at high speeds, a clutch locks the engine into the drivetrain with a fixed gear ratio. A comparison of the ratio of magnet mass to published power rating indicates that the Accord motor has a slightly higher ratio than the Camry and first-generation Prius but a slightly lower ratio than the 2010 Prius.

The Accord PCU is very similar in principle to the PCU in the Toyota hybrid systems in that it has a boost converter that supplies the generator and motor inverters. The boosted voltage reaches up to 700 V, which is slightly higher than the boosted voltage of 650 V for the Toyota systems. The power module was directly integrated with the heat exchanger, thereby eliminating the use of thermal paste and greatly increasing heat transfer from the power electronics devices to the coolant medium.

ORNL has integrated custom motor controls with the PCU while maintaining the OEM driver circuitry. Detailed designs were developed to provide access to the electric motor shaft in the transmission while maintaining the cooling and lubrication functionality used in the original form. The 2014 Accord hybrid system is currently being tested to verify performance and to obtain detailed characteristics across the entire operating range of the system.

FY 2014 Publications/Presentations

1. Tim Burress, "Trends and status of on-the-road HEV/EV technologies," IEEE Energy Conversion Congress and Exposition, September 2014.
2. T. Burress, "Benchmarking EV and HEV technologies," 2014 Annual Merit Review and Peer Evaluation Meeting for the DOE Vehicle Technologies Office, Washington, D.C., June 2014.
3. T. Burress, "Benchmarking EV and HEV technologies," Vehicle Technologies Office Advanced Power Electronics and Electric Motors R&D FY 2014 Kickoff Meeting, Oak Ridge, Tennessee, November 2013.

2.2 Assessing Gaps in the North American Supply Chain for Automotive Traction Drive Power Electronics

Christopher Whaling, Principle Investigator
Synthesis Partners, LLC

Richard Holcomb, III, Manager
Synthesis Partners, LLC
11250 Roger Bacon Drive, Suite 2,
Reston, VA 20190
Phone: (301) 706-9034
E-mail: cwhaling@synthesispartners.com

Steven Boyd, DOE Program Manager

Start Date: January 2014
Projected End Date: September 2014

Objectives

Synthesis Partners (Synthesis) was tasked by the Vehicle Technologies Office (VTO), U.S. Department of Energy (DOE) to undertake research to address the following specific questions regarding the North American (NA) supply chain of technologies for traction drive power electronics (PE) for plug-in, hybrid and electric vehicles (PHEV, HEV and EVs):

1. Targeted follow-on primary and secondary research to collect and analyze publicly available information on:
    a. NA PE supply chain company data, trends and growth-related issues
    b. Trends in NA PE company investments over last 5 years
2. Integrated market and technology assessment to address manufacturing process improvements, gaps and constraints that NA PE sources believe to be the highest priority items for VTO consideration
3. Summary assessment of competitive performance and manufacturing cost-basis for WBG-based PE (SiC and GaN) to support follow-on analyses related to NA industrial base expansion activities
4. Roundtable collaborations and other methods and practical steps to support in-depth industry-VTO engagements
5. Initial data collection and analysis on the NA electric motors supply chain

Synthesis' research has focused on traction drive PE, and specifically on inverters. We do not focus on batteries or chargers. A secondary focus for FY14 research was on motors. An overview assessment of WBG cost of manufacturing and an initial description of the NA electric motor supply chain is provided as back-up information to VTO-DOE as part of this deliverable. Please see the final section, Addenda, for other products available from this research.

A partial listing of the key components and their major functions in a representative traction drive inverter is listed in Table 2-2 below for reference:

Table 2-2: Key Power Inverter Components.

Component	Function
Boost converter	"Step up" the voltage from the battery
Busbar	Connect or distribute electricity to multiple devices
Cooling element/thermal management	Maintain operating temperature of power electronics within specified limits
Current sensor	Detect electrical current and generate a signal proportional to it
DC-link capacitor	Act as energy storage and filter for the DC link voltage for the inverter
Driver board	Board on which IGBTs are placed to provide high levels of gate current for short periods of time.
External connector	Connects the inverter to the rest of the vehicle's power systems
Heatsink/cold plate	Passive cooling device that absorbs heat from the power electronics and dissipates it.
Housing	Contains all the other device components and may include integrated cooling channels
IGBT modules	The actual, individual IGBT and associated circuits, typically employed in a multi-IGBT configuration (e.g., "six-pack")
Logic board	Circuits and logic-based processing necessary for control over the system
Microprocessor	The CPUs that enable operation of the system, and which are controlled in certain ways (e.g., through embedded power electronics) to manage correct operation of the system.
MOSFET	Circuit that amplifies or switches the electronic signal.
Smoothing capacitor	Component to decrease variation in the output from AC suppliers

Accomplishments

The FY14 research and analysis effort accessed thousands of secondary sources and hundreds of primary sources during an eight-month timeframe from January to August 2014.

Table 2-3 below provides a detailed summary concerning the secondary sources searched, and Table 2-4 provides statistics on the primary sources accessed during the course of this study period.

Along with the more than 2,000 English-language websites and nearly 9,000 web pages reviewed, Synthesis incorporates an extensive discovery process of key terms, topics and issues over 1,000 Chinese and Japanese language websites.

Table 2-3: Secondary Source Research Statistics.

Research Statistics – Secondary Sources (All sources are English language unless otherwise specified)	
Web sites reviewed	2,000+
WebPages reviewed in depth	6,000+
Companies initially identified and reviewed for relevance	750+
Companies identified for further assessment (possible involvement in NA traction drive PE manufacturing/R&D for xEV passenger vehicle applications)	500+
OEMs	50
Tier 1s	75
Tier 2	75
Tier 3	150
Tier 4	75
Multi-Tier	40
Other (USG Offices, Labs, Universities, Associations, etc.)	35
Japanese and Chinese language Web Sites Reviewed	1,000+
Reviewed in depth	750+
Key documents found	10+

The following table provides an overview of the scope of primary research conducted during the course of this study. Synthesis employed a template of research questions to frame first-time and follow-up in-depth discussions with each of the primary sources. All interviews are maintained in confidence. Each interview is written up by Synthesis, reviewed by the source and only then used as a source of anonymized feedstock for the analysis results in this study.

The primary research approach is not a survey and is not intended to produce statistically significant results. Given the depth and breadth of case-based research, Synthesis is confident that almost all key parties have been contacted and that a broad representation of viewpoints is included. Multiple contacts were frequently made with the same organization and more than one interview was often conducted with different personnel within the same organization, in order to incorporate different, unique perspectives, especially from within large organizations.

Table 2-4: Primary Source Research Statistics.

Research Statistics – Primary Sources (All sources are English language unless otherwise specified)	
Companies vetted for contact	338
OEMs	23
Tier 1	31
Tier 2	60
Tier 3	130
Tier 4	43
Multi-Tier	30
Other	21
Total contacts made (multiple contacts within many organizations)	1,275+
E-mails	725+
Phone Calls	525+
In-Person Conference Contacts	25+
Distribution of in-depth interviews	100%
OEMs	15%
Tier 1s	13%
Tier 2s	22%
Tier 3-4s	24%
Multi-Tier	15%
Others (National Lab, Government Office, Academic, Association, etc.)	11%

Synthesis continues to see significant interest among sources in participating in technical discussions regarding the future of the NA traction drive PE supply chain for PHEV, HEV and EV passenger vehicle applications. There also continues to be interest in providing input to DOE to support effective R&D and other investment decisions.

Synthesis has fielded over 234 requests for copies of prior DOE VTO-sponsored reports, completed by Synthesis. Primary source contacts and others also expressed interest in accessing the results of the current research and learning of DOE VTO viewpoints and decisions that may be partially based on these findings and other market research.

Domestic and transplant (foreign companies that have located significant operations in NA) OEMs, Tier 1s, 2s and 3 suppliers continue to express interest in increasing their participation in this and other DOE-sponsored studies. These companies stated their interest in building information exchanges along the lines of the current research activity. Some transplant OEM executives made specific statements to Synthesis regarding their support of building out the NA supply chain.

The fact that a particular company does not participate in this research does not necessarily mean they are not interested. Most often, companies and sources that could not participate stated that they did not have time but have interest in continued engagement in the future.

Synthesis is committed to continue to engage with all interested parties on the topics reported on in this, past and future reports.

Introduction

This study used a combination of secondary research, covering both English and targeted Chinese and Japanese language sources, in conjunction with in-depth primary source interviews with NA suppliers. This study is not the result of a survey and is not intended to produce statistically significant results.

The key findings in this study are the result of Synthesis' independent assessment of the combination of primary and secondary information collected over approximately eight months, ending in September 2014. The depth and breadth of case-based primary source interviews and secondary sources provides multiple perspectives on the topics identified.

Interviewees, independent experts and DOE personnel were not asked to endorse the conclusions or recommendations contained herein, nor did they review the final draft of the report before its release to the DOE VTO.

Synthesis has made good faith attempts to ensure this study is accurate, up-to-date and as comprehensive. Nonetheless, Synthesis looks forward to working with DOE VTO stakeholders to identify gaps and refinements so that the results of this activity are precise, accurate, and provide the needed inputs for DOE VTO decision-making.

Please note that the following sections provide an abbreviated discussion about selected topics to support the DOE public Annual Report. Additional details and analysis regarding the FY14 work will be made available in an upcoming Synthesis public report.

Approach and Results

1.0 Characteristics of the Automotive PE Supply chain

Synthesis assessed more than 330 companies and organizations which appear to be actively engaged or have the capability to be engaged in NA traction drive PE R&D and/or manufacturing for xEV applications. From that initial list of 330 companies, Synthesis distilled a list of 38 companies (see Table 2-5 below) which are actually engaged or have a very high likelihood of becoming engaged in the near future in NA PE for xEV applications.

The definition of the NA supply chain for automotive traction drive PE includes:

- Automotive suppliers operating in the contiguous United States, Canada and Mexico
- Automotive traction drive PE
  - A sub focus is on PE suppliers that are deemed to have sufficient capability or expertise to become linked to automotive traction drive PE supply chain activities in North America.

For brevity, all of the above information is frequently conveyed by the phrase, "NA-PE Supply Chain."

Companies in the automotive sector are labeled according to their position in the supply chain, which extends from the top OEM, for example Ford or General Motors. OEMs manufacture the final completed product for the consumer market.

The Tier 1 through Tier 4 terms describe the level of the supply chain below the OEM that the company inhabits. Tier 1 companies are direct suppliers to OEMs. Continental, Delphi, Magna International and Denso are Tier 1 companies. Tier 2 companies are direct suppliers to Tier 1 suppliers; for example, Nichicon and SBE Electronics. Tier 3 companies are direct suppliers to Tier 2 companies, and generally supply advanced materials or basic components that are further processed, integrated or assembled into a key component by the Tier 2. For example, Dow Corning, Cree and Fairchild Semiconductor are Tier 3 companies. Tier 4 companies are direct suppliers to Tier 3 companies. These companies are suppliers of basic raw materials, such as ceramics, glass, composites, steel and other specialty materials.

When Synthesis refers to "Others", this means either U.S. Government laboratories and agencies, consultants, engineering firms, associations or other non-profits.

The automotive supply chain is complex and many companies maintain supplier relationships at multiple levels in the supply chain, and are labeled accordingly. This means that some companies represent themselves as being in multiple Tiers at the same time.

Top 38 Companies and Organizations in the NA PE Supply Chain

Table 2-5 below provides a summary list of the 38 companies that are most engaged or which appear most likely to become engaged in the near future in traction drive PE R&D and manufacturing for xEV applications in NA.

Table 2-5: Companies Currently Engaged or Which Appear to Have the Greatest Potential to Become Engaged Soon in Traction Drive PE R&D and Manufacturing for xEV Applications.

Company	Involved in xEV PE today?	Type of Involvement or Product (data is representative, not exhaustive)
Note: "TBD," means included due to likelihood they will become involved in xEV PE R&D and/or NA manufacturing in the near future.		
Alpha Advanced Materials (AAM)	TBD	Semiconductor packaging materials
Amphenol Interconnect Products Corp.	TBD	Busbars and connectors

Company	Involved in xEV PE today?	Type of Involvement or Product (data is representative, not exhaustive)
Analog Devices, Inc.	Yes	Signal processors and amplifiers
Arkansas Power Electronics International, Inc.	Yes	Semiconductor R&D and manufacturer
Bicron Electronics Co.	TBD	Transformers
Bosch Rexroth	TBD	Hydraulic and electric drive systems for industrial and heavy-duty transportation applications
Calsonic Kansei North America, Inc.	Yes	PE R&D and manufacturer
Chrysler	Yes	OEM; PE R&D
Cree, Inc.	Yes	Semiconductor and substrate R&D and manufacturer
Delphi Automotive LLP	Yes	PE R&D and manufacturer
DENSO Manufacturing Tennessee, Inc. (DMTN)	TBD	Denso reports inverter manufacturing started in Maryville, TN in 05/14.
Dow Corning Electronic Solutions	Yes	Substrate R&D and manufacturer
Fabrico	TBD	Insulation for xEV motors and batteries
Fairchild Semiconductor	Yes	Semiconductor R&D and manufacture
Ford Motor	Yes	OEM; PE R&D and manufacturer
Freescale Semiconductor, Inc.	Yes	Semiconductor R&D and manufacturer
Fuji Electric Corp. of N.A.	Yes	Semiconductor R&D and manufacturer
General Motors	Yes	OEM; PE R&D and manufacturer
Hitachi Cable America Inc. (HCA)	TBD	Cables and connectors; compound semiconductors
Hitachi Automotive Systems Americas	TBD	Inverter manufacturer, though no mfg. currently in NA for xEV.
Intersil	TBD	Automotive ICs and power management
IXYS Corp.	Yes	Semiconductor R&D and manufacturer
Kemet Electronics Corp.	Yes	Capacitors
Kongsberg Automotive	TBD	Actuators, seating systems, fuel/hydraulic lines
Magmotor	TBD	DC/DC converter for commercial vehicles
Magna International of America, Inc.	Yes	PE R&D and manufacturer
Methode Electronics, Inc.	Yes	Bus bars, IGBT subsystems for inverters
Mitsubishi Electric USA	Yes	xEV Intelligent Power Unit
ON Semiconductor	Yes	Semiconductor devices
Positronic Industries Inc.	TBD	Connectors
Powerex	Yes	Semiconductor R&D and manufacture
Rinehart Motion Systems	Yes	Power module design and packaging
Rogers Corp.	Yes	Ceramic substrates for inverter
SBE, Inc.	Yes	Capacitors, IGBT modules for inverters
Silicon Laboratories, Inc.	Yes	Signal processors, gate drivers, current sensors
Superior Essex, Inc.	TBD	Communications cables; cables for energy distribution systems
Tesla	Yes	OEM; PE R&D and manufacturer
Toshiba North America	TBD	Inverter manufacturer, though no significant, publicly confirmed mfg. of inverters for xEV in NA

Quantitative Market Research Data and Analysis

Synthesis analyzed public and proprietary quantitative data on the relative position of all major companies in the xEV traction drive inverter supply market space. That analysis produced the following key Charts and analytic results:

- Number of Companies Producing Inverters for OEMs, by Home Country of Inverter Supplier’s HQ
- Number of Vehicles with Traction Drive Inverters Installed by OEMs, by Home Country of Inverter Supplier’s HQ
- Number of xEVs Sold in the United States with Traction Drive Inverters Installed by OEMs, by Home Country of Inverter Supplier’s HQ, 2010-2014 (est.)
- Ranking of Major Inverter Suppliers
    - By Related xEVs Sold in the United States
    - By Related xEVs Produced in N.A. Plants
    - By Related xEVs Sold Globally

The relevant Charts are provided below.

Please note: In the charts below, the home country of an inverter supplier refers to the location of the suppliers' HQ.

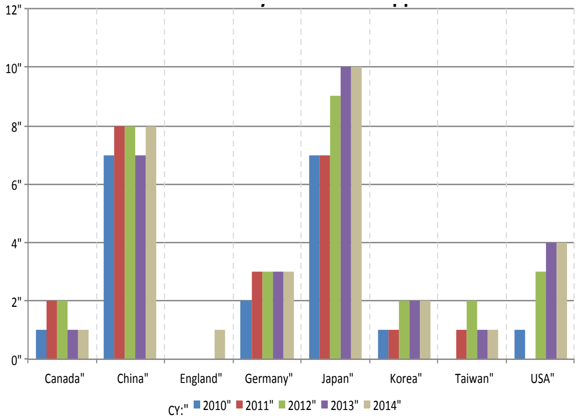

Figure 2-27: Number of Companies Making Inverters for OEMs, by Home Country of Inverter Suppliers' HQ (2010–2014).

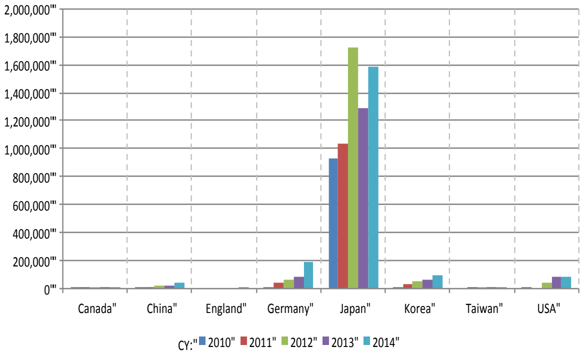

Figure 2-28: Number of xEVs with Traction Drive Inverters Installed by OEMs, by Home Country of Inverter Suppliers' HQ (2010–2014).

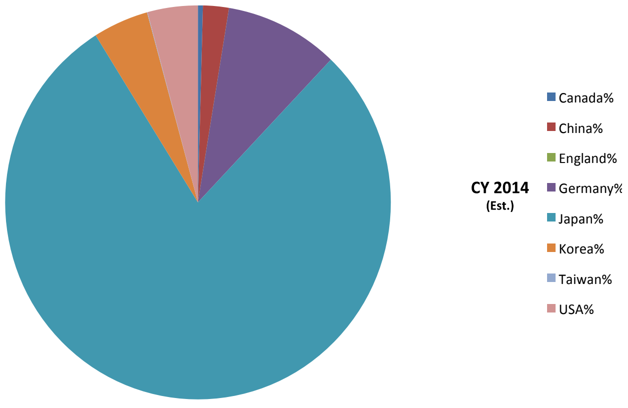

Figure 2-29: Number of xEVs with Traction Drive Inverters Installed by OEMs, by Home Country of Inverter Suppliers' HQ Rounded to Nearest 100 (2010–2014).

Traction Inverter Supplier	Home Country of Supplier	Percentage of xEVs Sold in US with Supplier's Inverter	Percentage of xEVs Produced in NA Plants with Supplier's Inverter
Toshiba	Japan	8.4%	34.8%
Hitachi	Japan	4.8%	26.6%
Denso	Japan	12.8%	25.1%
Keihin	Japan	0.9%	4.6%
Renault/Nissan	Japan	2.3%	3.0%
Toyota	Japan	20.7%	2.7%
Bosch	Germany	0.7%	1.2%
Mitsubishi	Japan	1.1%	0.9%
Magna	Canada	0.2%	0.6%
Tesla Motors	USA	1.8%	0.5%
Hyundai Mobis	Korea	3.5%	0.0%
Continental	Germany	0.4%	0.0%
Meidensha	Japan	0.1%	0.0%
General Motors	USA	0.1%	0.0%

Figure 2-30: Ranking of Suppliers, by Traction Drive Inverter Installations for xEVs Sold in the United States, and Produced in NA Plants, CY2013.

Propulsion Inverter Supplier	Home Country of Supplier	Percentage of Global xEVs Produced with Supplier's Inverter
Toyota	Japan	35.1%
Denso	Japan	21.9%
Mitsubishi	Japan	11.8%
Toshiba	Japan	5.7%
International Rectifier	USA	5.2%
Hyundai Mobis	Korea	4.4%
Hitachi	Japan	4.4%
Continental	Germany	3.3%
Bosch	Germany	1.8%
Meidensha	Japan	1.5%
Calsonic Kansei	Japan	1.1%
Keihin	Japan	0.7%
Renault/Nissan	Japan	0.7%
Edrive	China	0.7%
Siemens	Germany	0.4%
Dajun	China	0.3%
BYD	China	0.2%
Zhongke Shenjiang	China	0.2%
Weiteli	China	0.2%
Unite	China	0.1%
Magna	Canada	0.1%
General Motors	USA	0.1%
Tesla Motors	USA	0.1%
LSIS	Korea	0.1%
Honda	Japan	0.0%
Delta	Taiwan	0.0%
Delphi	USA	0.0%
Nanche	China	0.0%

Figure 2-31: Ranking of Top 28 Suppliers, by Traction Drive Inverter Installations for All xEVs Sold Globally, CY2013.

2.0 Trends in NA PE Company Investments in NA

In this section, Synthesis addresses the level of and trend in investments over the last 5 years, by NA PE companies. For the purposes of this assessment, Synthesis targeted information relative to investments by public and private sector entities in NA traction drive power electronics manufacturing and R&D activities for PHEV, HEV, and EV passenger vehicle applications from 2010–2014.

Approximately 100 companies were reviewed for investment information and approximately 250 contacts made regarding public investment information.

There are a few caveats to consider when interpreting investment trend results, including:

- There are likely company investments that are not reflected in the public information reported here;

- The data presented here is for broad trend analytics, and is not validated for use in drawing company-specific conclusions; and
- The investment data is broken out by company investments related to ARRA/DOE and company investments not related to ARRA/DOE activities.

Key Findings:

The following key findings are covered in the Charts that follow.

- Actual investment on an annual basis for traction drive power electronics applications by any NA-based company is likely well below $10 million.
- By comparison, VTO annual investments of ~$25M in traction drive PE and motors is therefore significant, and a critical driver of activity in the NA PE R&D space in particular.
- Interesting comparisons are possible when comparing company investments that are related to ARRA or DOE funding, against company investments that are not related to ARRA or DOE funding activities.
- In the aggregate, total company investments not related to ARRA or DOE far exceed company investments related to ARRA or DOE funding, for 2010-2016.
- Synthesis identified $2.5Bn in non-ARRA/DOE NA PE company investments, for 2010-2016.
- Synthesis identified $162M in ARRA or DOE-related NA PE company cost-share investments, for 2010-2016.
- There is a severe shortage of Tier 2-3 participation, for 2010-2016, among company investments not related to ARRA or DOE funding.
- The distribution of company investments related to ARRA or DOE for 2010-2016 shows a minor—but very significant for reasons discussed in Synthesis studies—NA Tier 2-3 participation.
- Trends in total investments, including both ARRA/DOE-related and non-ARRA/DOE-related investments show that domestic NA companies were leading by a wide margin pre-2013, in terms of total investments made.
- Trends in total investments, including both ARRA/DOE-related and non-ARRA/DOE-related investments show that transplant companies in NA have been leading by a wide margin since 2013, in terms of total investments made.
- 4 of the 5 U.S. companies (GM, Kemet, Powerex (a 50:50 JV) and Rogers Corp.) specified the level of their traction drive power electronics-specific investments.
- 1 of the 6 transplant companies (Magna) specified the level of their traction drive power electronics-specific investments.
- 6 of the 13 companies identified as making investments since 2010 are transplants and 1 additional is a joint venture with a transplant.
- Approximately 34% of companies on SP's core NA PE R&D and manufacturing list have made investments since 2010.
- More than 60% of the companies listed on SP's core NA PE R&D and manufacturing list are not publicly stating that they are engaged in making investments in NA, in 2010–2016.
- Synthesis concludes that most non-reporting companies (i.e., companies not reporting investments) are either financially constrained and/or waiting for market conditions to improve to make investments.
- Synthesis concludes that it is possible that a very small selection of the non-reporting companies have plans underway which are not publicly reported.

Please see the relevant Charts below:

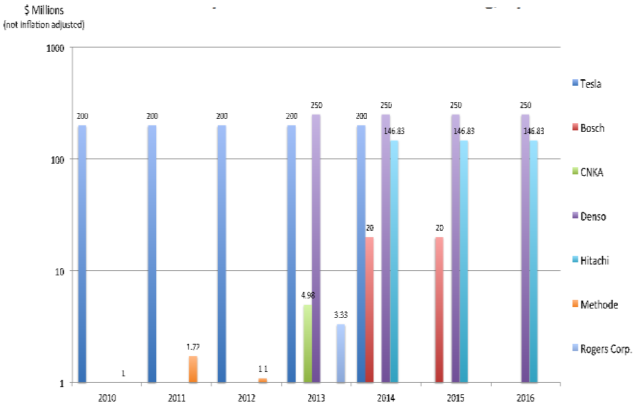

Figure 2-32: NA PE Company-Specific Investments, Not Directly Related to ARRA or DOE Funding, By Year (2010–2016).

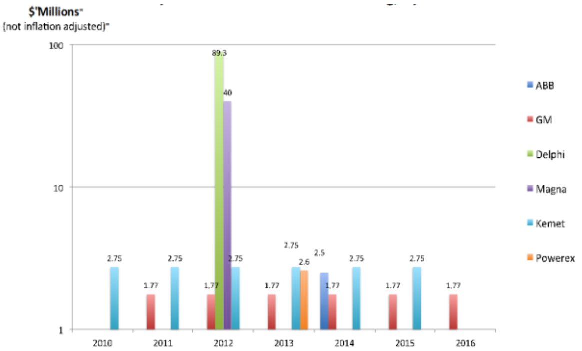

Figure 2-33: NA PE Company-Specific Investments, Directly Related to ARRA or DOE Funding, By Year (2010–2016).

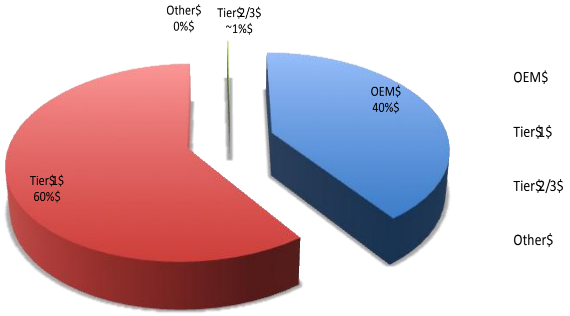

Figure 2-34: Distribution of Total Company Investments, Not Directly Related to ARRA or DOE Funding, By Company Type (2010–2016). Total: $2,492.62M.

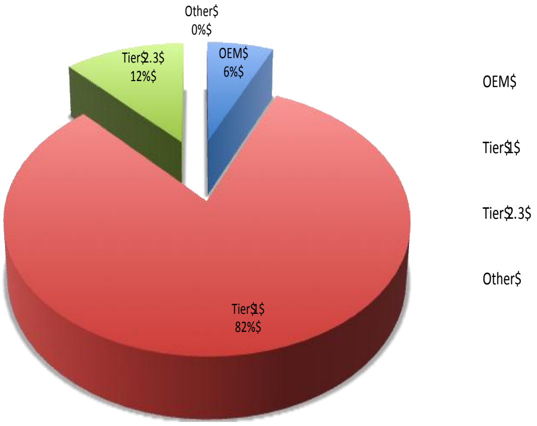

Figure 2-35:Distribution of Total Company Investments, Directly Related to ARRA or DOE Funding, By Company Type (2010–2016). Total: $161.52M.

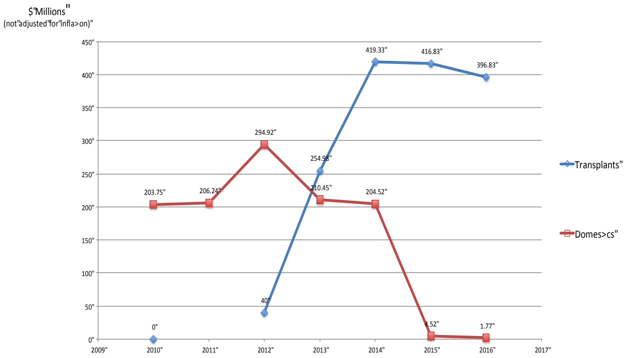

Investments include both ARRA/DOE-related company cost share and non-ARRA/DOE company investments, with estimates for 2015 and 2016. This data covers aggregate NA investments by the core NA PE companies, and does not identify the level of investment in traction drive PE activity specifically.

Figure 2-36: Comparison of Domestic vs. Transplant Total NA PE Company Investments, By Total Investments Identified, By Year (2010–2016).

Conclusions and Future Directions

There is additional information that will be covered in more depth in public report(s), to be made available in 2014/2015. Specifically, the following information will be reviewed in future reports:

1. NA PE Suppliers List and Descriptions (Task 1 deliverable)
2. Anonymized primary source information, including analysis of hundreds of interviewee statements covering 108 gaps and 107 constraints identified (contributes to all Tasks)
3. WBG Cost Analysis Addendum (Task 3 deliverable)
4. Roundtable 1, 2 and 3 results (Task 4 deliverable)
5. Preliminary NA Motors Suppliers List and Initial Motors Supply Chain Analysis Addendum (Task 5 deliverable).

Please contact Mr. Steven Boyd of the Department of Energy or Mr. Chris Whaling of Synthesis Partners, Reston, VA with questions or comments. Thank you.

3.0 Power Electronics R&D

3.1 Power Electronics Packaging

Zhenxian Liang (Principal Investigator)

Oak Ridge National Laboratory
National Transportation Research Center
2360 Cherahala Boulevard
Knoxville, TN 37932
Phone: (865) 946-1467; Fax: (865) 946-1262
E-mail: liangz@ornl.gov

Burak Ozpineci, ORNL EDT Program Manager
Phone: (865) 946-1329; Fax: (865) 946-1262
E-mail: burak@ornl.gov

Susan A. Rogers, DOE EDT Program Manager
Phone: (202) 586-8997; Fax: (202) 586-1600
E-mail: Susan.Rogers@ee.doe.gov

Start Date: October 2012
Projected End Date: September 2014

Objectives

- Develop advanced packaging technologies that exploit the attributes of wide bandgap (WBG) power semiconductors, resulting in comprehensive improvements in the cost-effectiveness, efficiency, and power density of electric drive systems.
  - FY 2014: Develop process technologies and fabricate specific silicon carbide (SiC) power modules for inverter/converter integration with significant advances in performance.

Technical Barriers

- State-of-the-art automotive power modules and power inverters and converter packaging technologies have limitations in electrical performance, cooling capability, thermomechanical properties, and manufacturability. These are barriers to meeting the DOE EDT 2020 targets for cost, efficiency, and density.

Technical Targets

- Develop packaging technologies for advanced WBG power modules with lower thermal resistance, small electric parasitic parameters, and temperature-tolerant capability that can be manufactured efficiently.
- Identify the performance attributes and limits of state-of-the-art WBG power devices in power conversion systems.
- Advance WBG automotive power electronics in electrical performance, cooling efficiency, and thermomechanical capability through highly functional packaging integration.

Accomplishments

- Delivered first-generation SiC integrated power modules (IPMs) for system evaluation, leading to 30% overall volume and weight reductions.
- Developed an integrated cooling SiC 100 A/1200 V phase-leg module that enables 3× current density increases over its conventional silicon (Si) counterpart, resulting from a 35% reduction in the die size; 40 and 80% reductions in conduction and switching power losses, respectively; and a 35% reduction in package thermal resistance.
- Developed an innovative planar-bond-all (PBA) SiC package that
  - integrates double-sided direct cooling that is 40% more efficient
  - realizes 3-dimensional (3D) planar interconnection with a 75% reduction in parasitic electrical inductance and a 90% reduction in resistance
  - incorporates advanced low-cost manufacturing
  - allows converter/inverter system-level functional integration.

✧ ✧ ✧ ✧ ✧

Introduction

WBG power semiconductors, such as SiC and gallium nitride, are known to provide superior power switching features—high current density, low-loss high switching speed, and high operation temperature—compared with their silicon (Si) counterparts. State-of-the-art WBG discrete devices and multi-chip modules are manufactured using technologies that follow packaging schemes used for Si devices. The packaging processes include die attachment and top interconnection, power substrate, power and signal terminals, baseplate, and encapsulation. Specifically, interconnection and die attachment are accomplished by multiple bond wires (from the top of the die) and reflowed solder areas (from bottom of die) onto the power substrate, respectively. In power converter/inverter assembly, the modules need to be attached to a heat sink or cold plate using forced air or liquids for cooling of the semiconductors. In general, a thermal interface material such as thermal grease is usually applied between the modules and the heat sink for good thermal transfer. Although they fulfill well their designed electrical, thermal, and mechanical functions, these hybrid package technologies have limitations in electrical performance, cooling capability, thermomechanical properties, and manufacturability. In particular, they limit the full exploitation of the attributes of WBG semiconductors and, in turn, limit the benefits of WBG power electronics with regard to cost, efficiency, and power density in automotive electric drive systems. These limitations can be characterized by a set of technical metrics such as thermal impedance (resistance and capacitance), electrical impedance (resistance and inductance), thermomechanical properties (power, thermal cycling numbers, and vibration ruggedness), and others. Establishing the relationships between these parameters and the power module performance criteria (e.g., efficiency, reliability, cost, and density) makes it easier to evaluate power module technologies and to identify the shortcomings of existing technologies and develop new concepts. In past years, many techniques in SiC power module packaging, focused on improving these technical parameters, have been developed to promote successfully the adoption of WBG power semiconductors in power electronics.

This project emphasizes the integration of advanced packaging concepts into all-SiC power modules, enabling the exploitation of SiC superior performance. Technical details such as packaging structure and associated packaging process technology were developed. Performance improvements were characterized by experimental measurements; and efficiency, cost, and reliability benefits to power electronics systems were evaluated.

Approach

The target all-SiC power module is a one-phase-leg configuration, composed of SiC metal-oxide-semiconductor field-effect transistors (MOSFETs) and SiC Schottky barrier diodes (SBDs) (see Figure 3-1), which is a basic building block for various automotive power converters and inverters. Power SiC MOSFETs and diodes are commercially available in the form of bare dies, both with ratings of 50 A and 1200 V. The current rating of the power module can be multiplied by paralleling more dies. Figure 3-1 shows the topology for a 100 A, 1200 V phase leg all-SiC power module. The switch units consist of two paralleled bare dies for each switch.

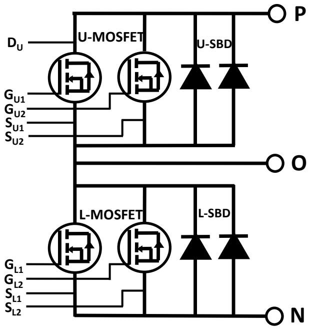

Figure 3-1: Electrical diagram of an all-SiC phase-leg power module (U=upper unit, L=lower unit) with multiple paralleled devices.

Two types of packaging for this module have been successfully prototyped in-house, as shown in Figure 3-2. Figure 3-2(a) presents a photo of this module fabricated using conventional packaging technology (first-gen module). Its structural details are schematically depicted in the cross-sectional view in Figure 3-2(b). It is similar to most industrial SiC power module packages and was built as a baseline to identify the basis packaging parameters. Figure 3-2(c) shows a photo of a second-gen SiC module. It is unique in that it features an integrated direct cooling configuration, schematically depicted in Figure 3-2(d), in which a single cold-base plate replaces the base plate and cold plate in the first-gen package. The cold-base plate used is specially made of a flat copper tube with crisscrossing fins inside. In this module package, the power stage on the direct bond copper (DBC) ceramic power substrate is directly soldered onto the cold-base plate. Thus it not only eliminates the thermal grease and base plate, compared with the conventional power module thermal package scheme, but also realizes integrated, direct cooling.

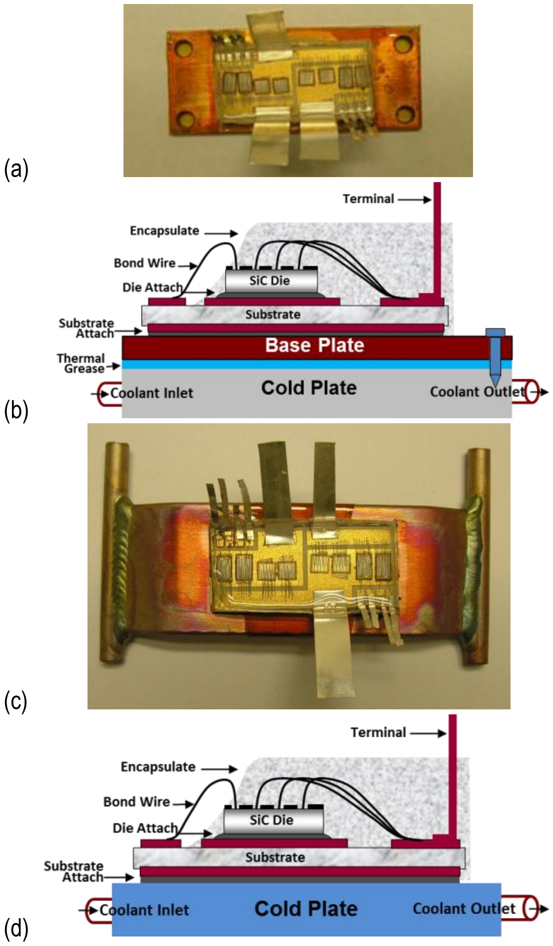

Figure 3-2: Two types of SiC phase-leg power module prototypes: (a) photo of a first-gen module with (b) conventional packaging configuration (cross-sectional view), (c) photo of second-gen module and (d) package with direct cooling from integrating a cold-base plate.

The result of the cooling integration is that the specific thermal resistance of the integrated cooling package is more than 14% lower than that of a conventional (first-gen) package. To assess the effect of this improvement and the advantages of SiC devices over their Si counterparts, four samples with different package/device combinations were prototyped. Silicon insulated gate bipolar transistor (IGBT)/PiN diode dies have the same current and voltage ratings as SiC devices. The improvement resulting from highly efficient integrated cooling can be observed in the increase of allowed current density in the SiC die. With a fixed current density, for example 100 A/cm^2, the difference in the junction temperature ranges from ~36 to 170°C between the SiC/integrated cooling and Si/conventional cooling combinations. The higher temperatures, on the one hand, lead to a significant reduction of the power module lifetime. On other hand, if the maximum operational boundary is set based on temperature limits, the maximum handling current density of a power device for the four combinations increases from 66 to 185 A/cm^2 for a 100°C temperature increase, which can be a case for a coolant temperature of 65°C and a junction temperature of 165°C. These maximum current density values define the minimum die area of the power semiconductors for a designed system current (or power) rating. It is well known that die size is a dominant factor in power module cost. The 3× die area reduction for SiC/integrated cooling combination compared with Si/conventional cooling is significant for reducing the system cost.

In FY 2014, further development of SiC power electronics packaging was focused on two major aspects: (1) the packaging integration of gate drive circuitry and power module to produce IPMs and (2) PBA SiC power module packaging.

A. Integrated SiC Power Module

A prototype SiC IPM was designed to integrate the first-gen SiC power module and a two-channel gate driver board in one package, leading to a smart (or intelligent) SiC power module. Figure 3-3 shows the conceptual schematics of this IPM. The gate drive circuitry on board is assembled closely on top of the power module with transparent silicone gel encapsulation of power devices and interconnection. Such integration not only reduces the part number and increases the power density of the converters but also improves the package performance. The matched interconnection was designed to enable the shortest distance between the output of the gate driver and the input of the power devices. The effects of the tight interconnection can be observed in the lumped electrical element model of a packaging electrical interconnection, as shown in Figure 3-4. It was obtained by employing an electromagnetic simulation tool (MAXWELL Q3D Extractor) that calculates the electromagnetic field and extracts the parasitic components through current conduction paths. The components enclosed within the dashed line are related to the signal pins in a conventional discrete power module assembly. These parasitic components will degrade the signal fidelity from the gate drive to the device, causing undesired voltage and current ringing and limiting the switching speed of SiC devices to far from their maximum regime. In the IPM, these parasitic components were much reduced, making it possible to operate the SiC devices at higher frequency and higher efficiency.

The Si gate drive circuit in this IPM was designed in-house and fabricated specifically. It is based on silicon-on-insulator (SOI) technology, featuring a high operating temperature. A two-channel high-temperature gate drive board was built based on the chip-on-board technique, which also offers the shortest interconnection paths. The experimental results demonstrated the high-temperature operating capability of the gate drive circuitry at up to 200°C.

Furthermore, to promote SiC devices operating at higher temperatures (>200°C), a set of high-temperature packaging materials and associated technologies were used in fabricating this IPM.

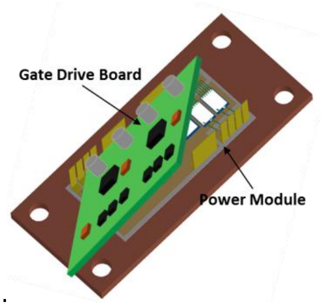

Figure 3-3: Schematics of an integrated SiC power module: the gate drive circuitry on the printed circuit board is closely connected to the power module.

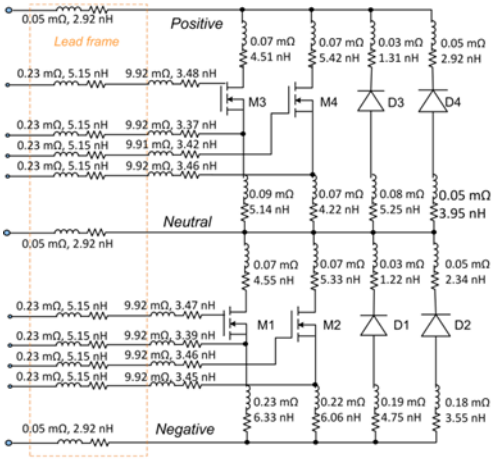

Figure 3-4: Lumped electric element model of packaging interconnections. The area enclosed by the dashed lines is related to the signal terminals.

B Planar-Bond-All SiC Power Module

A PBA is a power module packaging scheme that differs significantly from conventional packaging schemes (first- and second-gen). The key element is that the top interconnections use a planar, larger-area bond to the electrodes on the die instead of multiple tiny wire bonds. This change offers the possibility of integrating many superior packaging concepts into one module package.

B.1 Three-Dimensional Planar Power Interconnection

Figure 3-5 is a schematic of the planar interconnection configuration for the phase-leg power module. The four

MOSFET and four diode dies are sandwiched between two DBC substrates. The electrical interconnection is achieved by conductively bonding these dies from both the top and bottom sides to the copper traces on the two substrates, which are patterned to form circuitry corresponding with the electrode pad layout on the dies. The DBC substrates provide electrical insulation via the internal ceramics (such as aluminum nitride) between two copper layers. This symmetric planar-bonded package offers flexibility in the arrangement of the switch dies. As shown in Figure 3-5, the upper switch pair and lower switch pair in the phase-leg topology are oriented in a face-up/face-down configuration. This makes optimal use of the die's vertical electrode arrangement. Unlike in a traditional wire bond layout, in which all dies are placed in a face-up orientation, the main current flowing loops are also on the X-Y plane of the substrate. However, in the face-up/face-down orientation, the main current flowing loops fall in the X-Z plane of the package. The interconnection between dies is in a 3D planar pattern. The thickness (in Z direction) of the switch die is typically 0.1mm, and its length (X direction) or width (Y direction) is in the range of 10 mm. Thus the length and the enclosed area of the main current loops in the 3D interconnection configuration are reduced dramatically, leading to a significant reduction in electrically parasitic inductance and resistance.

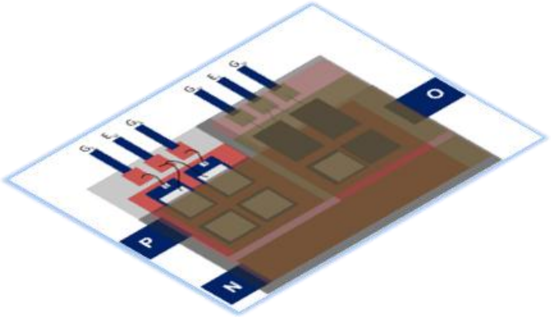

Figure 3-5: Three-dimensional planar power interconnection configuration in PBA SiC phase-leg power module.

The lumped circuit model of such an electrical interconnection is shown in Figure 3-5. The sums of the lumped elements along a main current path from the positive terminal through the upper MOSFET, and then from the lower diode to the negative terminal, are the representative parameters of the package structure. In this planar-bonded power module, the total inductance *L* is 13.58 nH and the total resistance *R* equals 0.25 mΩ. By comparison, the parasitic electrical parameters in a conventional wire-bonded power module are L=53.3 nH and R=2.45 mΩ, respectively.

B.2 Integrated Manufacture Process

In the module structure described, the numerous tiny wire bonds used in conventional packaging are replaced by a few identical planar area bonds. This arrangement makes batch processing possible. For batch processing, a special process method has been developed in which, as shown in Figure 3-6(a), all components are first assembled into a premade jig. The components include the patterned DBC substrates, multiple bare dies and shims, preformed bonding material (such as solder preform), power terminals and signal pins, and so on. The second processing step involves heating the assemblies simultaneously to form the bonds and creating the final package. The simplicity of the process helps reduce costs and improve the manufacturability of the modules. This technology is called PBA, representing the features inherent in the packaging structure as well as the fabrication process.

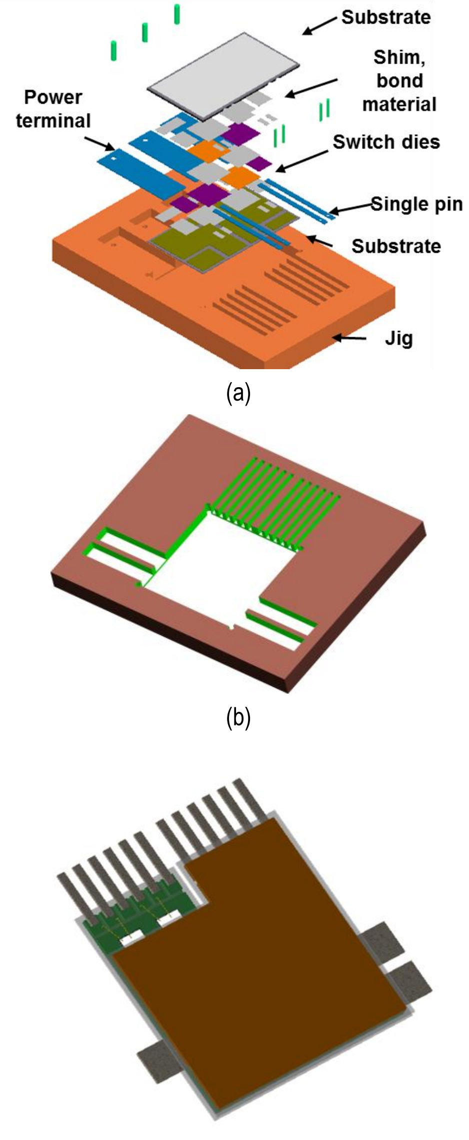

(a)

(b)

(c)

Figure 3-6: Manufacturing process of planar-bond-all packaging: (a) schematic of component assembling, (b) a specific jig for alignment of multiple components, (c) schematic of packaged SiC power module.

Figure 3-6(b) is the schematic of a specific jig designed for assembling PBA SiC power module packaging components. Figure 3-6(c) is a schematic of the PBA SiC power module design. The module body measures 40 ×40 × 2 mm, excluding the terminals and pins. A soldering process is employed to form the planar bonding because of its high electrical conductivity and ease of processing. The special top metallization of the power semiconductor dies required for reliable solder bonding was done during the wafer-level processing. The power terminals (positive, neutral, and negative) and signal pins are also mounted between the two substrates by soldering to form compact input/output connections.

B.3 Double-Sided Integrated Direct Cooling

The planar bond structure allows dual side thermal dissipation paths from both the top and bottom surfaces of the power package.

The internal assembly in Figure 3-7 is an example of an integrated double-sided cooling design, in which two pin-fin base plates made of copper are directly bonded to the power package (Figure 3-6c) from both sides by another soldering process.

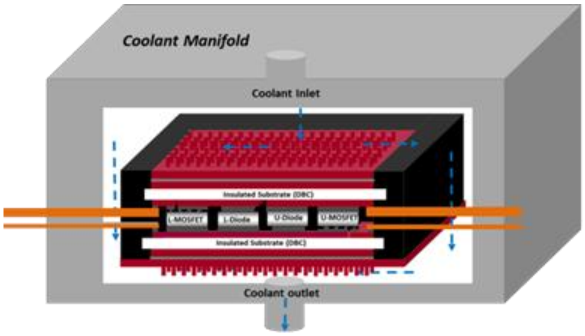

Figure 3-7: Double-sided integrated direct cooling of PBA module (internal) located in a coolant manifold.

The heat generated in the dies can be more efficiently removed by applying double-sided cooling through forced-air or liquid heat transfer. Additionally, direct attachment (bonding) of the heat sink or cold plate leads to further reduction in the thermal resistance, as discussed earlier.

This module can be directly cooled by air. For higher efficiency, forced liquid cooling is employed in most applications. Figure 3-7 shows schematically that the power module is assembled into a special coolant manifold. The manifold provides liquid passageways and allows coolant to pass through the pin fins efficiently.

Results

The benefits gained through the innovative packaging can be demonstrated by the system performance improvements of the prototype modules fabricated in our Advanced Power Electronics Packaging Lab.

A. Integrated SiC Power Module (IPM)

The prototype IPM based on the design in Figure 3-3 is shown in Figure 3-8 as a zoomed-in insert consisting of three parts: a 100 A/1200 V SiC phase-leg module on the bottom, a gate drive board in the middle, and a power supply board on the top. They are assembled to form one building block in a converter. Figure 3-8 presents a photo of a buck converter based on this SiC IPM. The other converter components include a 0.75 mH inductor and a 20 μF capacitor. The equivalent resistive load is around 18 Ω. Figure 3-9 illustrates the waveforms of the converter operating at a switching frequency of 100 kHz, a 600 V dc bus voltage, and a 0.25 duty-cycle.

To evaluate the high-temperature capability of this module, the IPM was mounted on a heat sink that was cooled by natural convection in ambient air at room temperature and heated through device self-heating. The switching frequency was gradually pushed from 10 to 100 kHz to raise the power MOSFET junction temperature above 225°C. Continuous power testing at each switching frequency point was carried out for 30 minutes to reach a steady state. The junction temperature at each step was measured by a method in which the turnoff delay time was used as a temperature sense parameter. Before continuous operation of the SiC MOSFET, a calibration curve of delay time versus junction temperature was obtained under identical operating conditions. For instance, in the SiC MOSFET under test, the delay time = 0.38 Tj + 231.7, where *Tj* was the junction temperature. As shown in the lower section of Figure 3-9, the zoomed-in turnoff transient, the measured turnoff delay time was 320 ns. It corresponds to a junction temperature of 232°C, according to the calibration relationship discussed above.

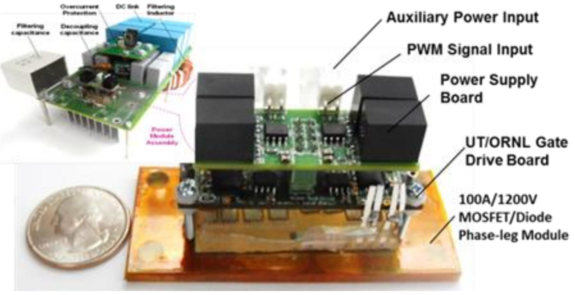

Figure 3-8: A buck converter based on the ORNL SiC integrated power module.

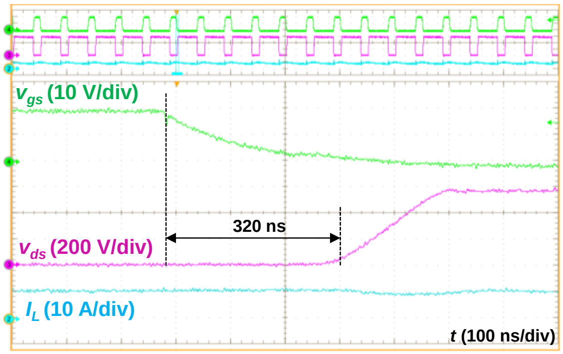

Figure 3-9: Voltage and current waveforms of SiC IPM converter operating at a frequency of 100 kHz, 600 V dc bus voltage, and 0.25 duty cycle.

Even though the SOI Si gate drive chip was operated successfully at 200°C separately, the performance of the IPM at a high ambient temperature (e.g., 150°C) has not yet been evaluated because some of its auxiliary components, such as isolation circuitry and power sources, were not rated for a high-temperature class. In the future, other strategies, such as integrating SOI Si chips and SiC devices, are proposed for further exploitation of the high-temperature features of SiC devices.

B. Planar-Bond-All SiC Power Module

The PBA SiC power module design is illustrated in Figure 3-6(c). The packaging components or/and parts schematically shown in Figure 3-6(a), including two DBC substrates, die shims, bonding foils and power terminals, and signal pins, must be specifically fabricated. The SiC dies are required to have a specific type of metallization on the front surface, different from that for wire-bond interconnections. A specially designed jig, shown in Figure 3-6(b), was fabricated to assist the soldering process. Based on these efforts and intensive process development and optimization, a group of PBA SiC modules were prototyped. Figure 3-10 shows a photo of an exemplary one. The module measures 40 × 40 × 2 mm, excluding the terminals and pins.

Various experimental measurements and multi-physics simulation tools were used intensively to characterize the electrical and thermal performance of the module packaging. They are summarized in the following sections.

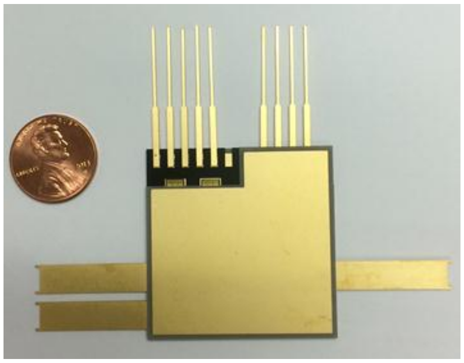

Figure 3-10: Photo of a PBA SiC power module (third-gen package) with dimensions of 40 × 40 × 2 mm, excluding the terminals and pins.

B.1 Electrical Characterization

The electrical performance of power modules can be drastically influenced by their “parasitic” electric parameters (resistance, inductance, and capacitance), adding to SiC’s intrinsic electric parameter network. Parasitic inductances in the current loop will cause a voltage overshoot to be superimposed on the blocking voltages of the devices as they are turned on and off. From the current and voltage waveforms, it was observed that there is only 30 V of overshoot adding to a 600 V bus voltage. This is attributed to the smaller parasitic inductance (13.58 nH for the third-gen package) compared with a 53.3nH inductance in the conventional modules (first- and second-gen). On the other hand, the voltage overshoot is dependent on the switching speed (current decrease slope). The smaller inductance allows the MOSFETs in the PBA module to operate at a higher frequency, an important feature of SiC devices and an effective way to increase the power density of SiC inverters.

The parasitic inductance and resistance also increase the power losses of SiC switches. It has been demonstrated that the PBA module reduces these parasitic-related losses by 75% compared with conventional devices.

B.2 Thermal Characterization

The thermal performance of a power module can be modeled as thermal resistance and capacitance networks. The thermal capacitance determines the transient response of the power module to power dissipation in the switches, and the thermal resistance determines the cooling efficiency.

To implement double-sided cooling on the module shown in Figure 3-10, different configurations were designed based on applying different cooling devices. In one prototype (Figure 3-11), two pin-fin cold plates were added from both sides. As illustrated in Figure 3-7, two cold plates were directly bonded to the back sides of the DBC substrates by reflowed solder. Once the cooling medium, forced air or liquid, goes through the pin fins, the heat generated in the package is efficiently removed because of the low thermal barriers between device and coolant. It can be seen that this design fully fulfills an integrated double-sided-direct cooling scheme, which will exploit efficiently the SiC feature of high current/power density. The effective pin fin array area in the pin-fin cold plate is 38×38 mm. The fin height is 7 mm. The outline of this assembly measures 50 × 50 ×18 mm, excluding terminals and pins.

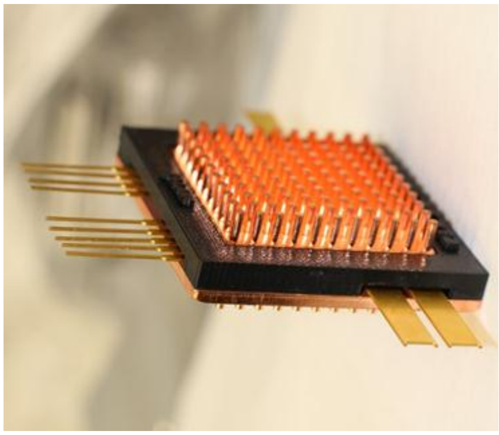

Figure 3-11: Photo of PBA SiC module packaged with integrated double-sided pin fin cold plates.

As illustrated schematically in Figure 3-7, double-sided forced-liquid cooling of this module can be achieved by assembling the module into a specially made coolant manifold. Figure 3-12 presents a final assembly of the PBA module and manifold. The open tube in front is a coolant inlet. The outlet tube is on the back side. The channels inside guide the coolant flow uniformly.

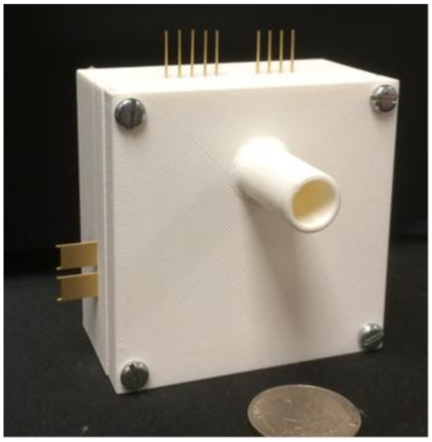

Figure 3-12: Photo of SiC integrated pin-fin PBA power module in a coolant manifold for double sided cooling.

The thermal parameters can be obtained by experimental thermal tests emulating the operation of the power modules. A method of determining junction temperatures was employed that uses the voltage drop of the body diode in the SiC MOSFET as a temperature sense parameter. By analyzing the cooldown temperature curves and input electric power value, the thermal parameters (resistance and capacitance) of the module can be extracted. For a fair evaluation of the thermal performance of a packaging assembly, a specific thermal resistance, $\theta_{ja,sp}$, was taken as a figure of merit, which is a normalized parameter by die area i.e., $\theta_{ja,sp}$ = die area × thermal resistance). Here, the thermal resistance is the sum of those from all thermal stacking elements, including the coolant, the pin-fin substrate, the DBC substrates, and the switch dies.

Figure 3-13 shows the measured specific thermal resistance value of the PBA module with double-sided cooling. For comparison, the specific thermal resistances of the wire-bond package (first-gen) and single-sided cooling package (second-gen) are also presented. The first-gen module, as shown in Figure 3-2(a), was mounted on a cold plate with thermal grease and has a specific thermal resistance of 0.54 cm^2·°C/W; the integrated single-side cooled module (second-gen), as shown in Figure 3-2(c), has a thermal resistance of 0.47 cm^2·°C/W. The double-sided cooling of the PBA module assembly reduces the specific thermal resistance to 0.33 cm^2·°C/W, which is 39% lower than that of the first-gen module assembly.

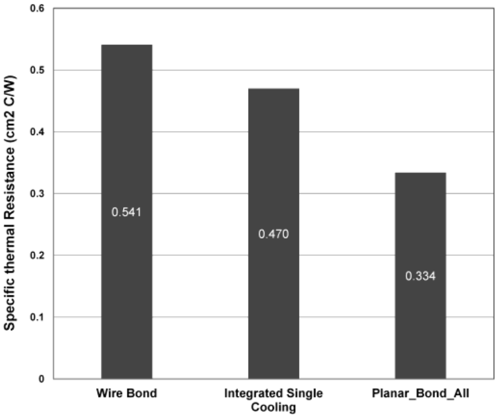

Figure 3-13: Specific thermal resistance and comparison with conventional and single-sided cooling modules.

B.3 Effects on Power Electronics System

The reduction in both parasitic power losses and thermal resistance helps increase the operational current (power) density in the SiC die. This can be seen in the graph of junction temperature versus current density (Figure 3-14). For a 100°C temperature increase, the characteristic current densities of the MOSFET in the module are 145 A/cm^2, 184 A/cm^2, and 220 A/cm^2, respectively, for a (first-gen) conventional cooling configuration, single-sided integrated cooling (second-gen), and double-sided direct cooling (third-gen). The third-gen package increases the current density of the SiC power device by 53%.

Die size is known to be a dominant factor in power module cost. The current density increase from the conventional first-gen package to the third-gen SiC integrated cooling package is significant for reducing the power electronics system cost.

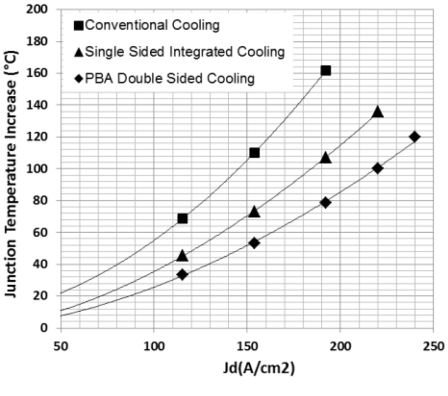

Figure 3-14: Performance of PBA SiC power module: (a) turn-off switching waveforms; (b) specific thermal resistance and comparison with conventional and single-sided cooling modules; and (c) comparison of junction temperature vs current density for different packages.

Conclusions and Future Directions

The advanced packaging technologies successfully developed in FY 2014 include gate drive circuitry integration, 3D planar interconnection, double-sided cooling, and simplified manufacturing processes. The resultant improvements in electrical parasitics and thermal impedance enable the efficient exploitation of WBG power devices. The benefits gained from these innovations are demonstrated by comprehensive upgrades in SiC packaging performance, leading to high-efficiency, high-density system operation beyond the limits of state-of-the-art technologies. These advances result in higher power conversion efficiency (low losses), and improved cost-effectiveness through reductions in power semiconductor size and higher productivity in manufacturing.

Further advancement of WBG automotive power electronics will depend greatly on improvements in power packaging technology through advances in structure, materials, and processing techniques. The focus will be on developing highly integrated functionality for WBG power inverter/converter modules with intelligence and improved operating performance (efficiency, density, and cost). The effort will include (1) incorporating advanced gate drive circuitry into the third-gen package, (2) implementing highly integrated cooling technologies for integrated multi-phase conversion systems, (3) optimizing interconnection layouts and embedding passives for electromagnetic interference containment and sensors; (4) developing processes for temperature-tolerant integrated SiC power module packages.

These advancements will enable considerable strides toward achieving DOE power density and cost targets for power electronics systems in electric drive vehicles.

FY 2014 Publications/Presentations

Publications

1. Z. Liang, P. Ning, F. Wang, and L. Marlino, “A phase-leg power module packaging with optimized planar interconnection and integrated double sided cooling,” *IEEE Journal of Emerging and Selected Topics in Power Electronics* **2**(3), 487–495, September 2014.
2. P. Ning, Z. Liang, and F. Wang, “Power module and cooling system thermal performance evaluation for HEV application,” *IEEE Journal of Emerging and Selected Topics in Power Electronics* **2**(3), 443–450, September 2014.
3. Z. Liang, P. Ning, and F. Wang, “Development of advanced all-SiC power modules,” *IEEE Transaction on Power Electronics* **29**(5), 2289–2294, May 2014.
4. Z. Xu, D. Jiang, M. Li, P. Ning, F. Wang, and Z. Liang, “Development of Si IGBT phase-leg modules for operation at 200°C in hybrid electric vehicle applications,” *IEEE Transaction on Power Electronics* **28**(12), 5557–5567, December 2013.
5. A. A. Wereszczak, T. G. Morrissey, C. Volante, P. Farris, Jr., R. Groele, R. H. Wiles, and H. Wang, “Thermally conductive MgO-filled epoxy molding compounds," *IEEE Transactions on Components, Packaging and Manufacturing Technology* **3**(12),1994–2005 (2013).
6. Z. Wang, X. Shi, L. Tolbert, F. Wang, Z. Liang, D. Costinett, and B. Blalock, “A high temperature silicon carbide MOSFET power module with integrated silicon-on-insulator based gate drive,” *Proceedings of the Fifth IEEE Energy Conversion Congress and Exposition*, Pittsburgh, PA, September 14–18, 2014.
7. B. Guo, F. Wang, P. Ning, E. Aeloiza and Z. Liang, “All-SiC power module for delta-type current source rectifier,” *Proceedings of the Fifth IEEE Energy Conversion Congress and Exposition*, Pittsburgh, PA, September 14–18, 2014.
8. D. DeVoto, P. Paret, and A. A. Wereszczak, “Stress intensity of delamination in a sintered-silver interconnection,” Paper WA26, pp. 190–197 in *Proceedings of IMAPS HiTec*, Albuquerque, NM, May 13–15, 2014.
9. A. A. Wereszczak, Z. Liang, M. K. Ferber, and L. D. Marlino, “Uniqueness and challenges of sintered silver as a bonded interface material,” Paper WA23, pp. 178–187 in *Proceedings of IMAPS-HiTec 2014*, Albuquerque, NM, May 13–15, 2014.
10. A. A. Wereszczak, Z. Liang, M. K. Ferber, and L. D. Marlino, “Uniqueness and challenges of sintered silver as a bonded interface material,” in press, *Journal of Microelectronics and Electronic Packaging* 2014.
11. Z. Zhang, B. Guo, F. Wang, L. M. Tolbert, B. J. Blalock, Z. Liang, and P. Ning, “Impact of ringing on switching losses of wide band-gap devices in a phase-leg configuration,” *Proceedings of IEEE APEC’14*, Fort Worth, TX, March 17–21, 2014.

Presentations

1. Z. Wang, X. Shi, L. Tolbert, F. Wang, Z. Liang, D. Costinett and B. Blalock, “A high temperature silicon carbide MOSFET power module with integrated silicon-on-insulator based gate drive,” presented at the Fifth IEEE Energy Conversion Congress and Exposition, Pittsburgh, PA, September 14–18, 2014.
2. Z. Liang, “Power electronics packaging,” DOE Annual Merit Review, Washington, D.C., June 18, 2014.
3. Z. Liang, “WBG power electronics packaging,” Electrical and Electronics Technical Team meeting, April 16, 2014.
4. Z. Liang, “Integration of cooling function into 3-D power module packaging,” Industrial Session Presentation (invited), APEC’14, Fort Worth, TX, March 17–21, 2014.
5. Z. Liang, “Power electronics packaging,” Kick-off meeting, Oak Ridge, TN, November 5, 2013.

FY 2014 Patents/Disclosures

1. A. A. Wereszczak, “Improved Sintered Silver Joints via Controlled Topography of Electronic Packaging Subcomponents,” U.S. Patent 8,822,036 B1, September 2, 2014.
2. A. A. Wereszczak, D. J. DeVoto, and P. P. Paret, “Perimetric Structure for Improved Reliability in Electronic Device Interconnection,” Invention Disclosure 201303197, DOE S-124,788, October 2013.
3. R. Wiles and A. A. Wereszczak,” Motor Size Reduction via Use of Novel Phase Change Materials,” Invention Disclosure 201303197, DOE S-124,788, October, 2013.
4. Z. Liang, “Integrated Packaging of Multiple Double Sided Cooling Planar Bond Power Modules,” DOE S-number S-124,816, invention disclosure number 201303211, December 5, 2013.
5. Z. Liang, P. Ning, F. Wang, and L. Marlino. “Power Module Packaging with Double Sided Planar Interconnection and Heat Exchangers,” U.S. Patent application publication, US 2013/0020694 A1, January 24, 2013.

3.2 Power Electronics Inverter R&D

Madhu Chinthavali (Principal Investigator)

Oak Ridge National Laboratory
National Transportation Research Center
2360 Cherahala Boulevard
Knoxville, TN 37932
Phone: (865) 946-1467; Fax: (865) 946-1262
Email: chinthavalim@ornl.gov

Burak Ozpineci, ORNL EDT Program Manager
Phone: (865) 946-1329; Fax: (865) 946-1262
E-mail: burak@ornl.gov

Susan A. Rogers, DOE Program Manager
Phone: (202) 586-8997; Fax: (202) 586-1600
Email: Susan.Rogers@ee.doe.gov

Start Date: October 2013
Projected End Date: September 2015

Objectives

- Overall
    - Integrate wide bandgap (WBG) technology and novel circuit architectures with advanced packaging to reduce cost, improve efficiency, and increase power density.
- FY 2014
    - Design, build, and test two 10 kW WBG-based prototypes using advanced packages:
        - ORNL module-based liquid-cooled inverter
        - ORNL optimized air-cooled inverter.

Technical Targets

- Evaluate WBG devices and develop loss models.
    - Acquire, test, and characterize newer-technology WBG power devices, including static and dynamic characterization tests.
- Design, build, and test a 10 kW air-cooled inverter.
    - A 10 kW air-cooled inverter will be designed using silicon carbide (SiC) metal oxide semiconductor field-effect transistors (MOSFETs) and Schottky diodes. The modules developed under the packaging project will be used in building the inverter.
- Design, build, and test a 10 kW liquid-based prototype with advanced packages.
    - Design a 10 kW liquid-cooled inverter using SiC MOSFETs and Schottky diodes. The prototype will be a liquid-based system.

Accomplishments

- Acquired, tested, and characterized SiC MOSFETs, a SiC junction field-effect transistor (JFET), and SiC junction barrier Schottky (JBS) diodes.
- Completed design, build, and testing of an all-SiC 10 kW inverter using a state-of-the-art commercial all-SiC module.

✧ ✧ ✧ ✧ ✧

Introduction

There is an increasing need for higher-temperature operation of power electronics in automotive applications. The ability of components to operate reliably at elevated temperatures can enable cost and weight savings by making it feasible to reduce the sizes of heat sinks and eliminate secondary cooling loops. Additionally, devices capable of increased-frequency operation can reduce requirements for passive components, leading to further reductions in cost, weight, and volume. WBG devices, specifically SiC and gallium nitride semiconductors, are emerging technologies that enable operation at higher temperatures and frequencies, as well as efficiency and reliability improvements. The development of WBG devices promises to help achieve these goals as well as the VTO targets. WBG technology assessment performed under this project will help to determine when a viable market introduction of these devices for automotive use will occur. The independent assessment of devices for the automotive industry is carried out to monitor progress and provide data readily when the need arises.

It should be no surprise that none of the electric drive vehicle traction drive systems on the market can meet cost and efficiency goals. Efficiency is achieved by using lower-loss devices and materials, which tend to be expensive, even as quantity levels increase. A case in point is motor lamination steel, lower-loss grades of which are manufactured using novel processes that add more cost.

Problems associated with power electronics for advanced vehicle applications include:

- Low efficiency at light load conditions for inverters and converters
- Low current density and device scaling issues for high-power converters
- Lack of reliable higher-junction-temperature devices
- High cost of devices and power modules, especially for WBG and advanced silicon (Si) devices
- High number of components for low-voltage electronics (e.g., gate drivers, controllers, sensors)
- Lack of standardized high-power-density, low-cost power modules for scalable and modular power converters

- Substrates that use expensive ceramics for thermal stability and reliability
- Low-cost, low-loss magnetics and high-temperature films for capacitors.

The goal of this research is to reduce the size and weight of power converters to meet the 2015 and 2020 inverter targets. The overall strategy for cost reduction is shown in Figure 3-15. The specific strategy is shown in Figure 3-16. Cost reduction can be achieved by

- Reducing the size and weight of the power inverters to meet the 2015 inverter targets of 12 kW/l and 12 kW/kg.
- Reducing costs by
  - Decreasing the component count by integrating functionality
  - Eliminating the existing liquid cooling loop
  - Cutting manufacturing costs (part count and steps)
  - Reducing the use of high-cost materials, like copper, through bus bar optimization and current reduction.

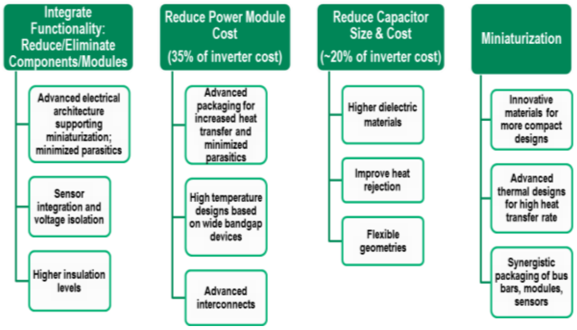

Figure 3-15: Overall strategy to address limitations of the state of the art.

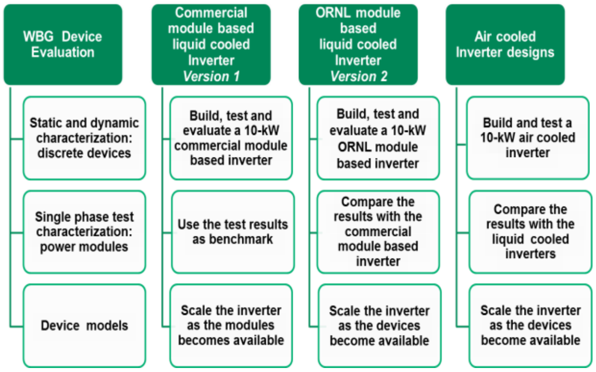

Figure 3-16: Specific strategy to address limitations of the state of the art.

Approach

The overall objective of this project is to design and develop a WBG 30 kW continuous 55 kW peak power inverter. WBG devices offer some distinct advantages over their Si counterparts. Primarily, they can operate at higher junction temperatures. This benefit allows for hotter coolant and smaller heat sinks and can potentially facilitate air cooling without sacrificing performance. Many of the typical components in a commercial inverter cannot withstand the desired operating temperature of WBG devices, i.e., the capacitor and gate driver. Thus the whole inverter must be considered in the development of new high-temperature packages.

The design innovations in this project include the following:

- The design concept uses layers of high-temperature thermal insulating material to separate the low-temperature components from the high-temperature zone.
- It uses the high-temperature operating capability of WBG devices to enable air cooling and uses newer fast-switching Si insulated gate bipolar transistors for high-temperature-liquid designs.
- The innovative heat sink design minimizes thermal resistance.
- The design is optimized for the most frequently operated points.

These new concepts will increase the power density and decrease the volume and weight for electric-base vehicle traction-drive inverters and will achieve the DOE 2020 weight, volume, and efficiency targets.

Results

Device Testing

The new WBG devices acquired this year are 1200 V, 30 A SiC MOSFETs. On-state characteristics and switching energy losses of the devices were obtained over a wide temperature range. All the devices obtained were experimental samples. The static characteristics and switching energy losses of two types of SiC MOSFETs with a TO-247 packaging case are presented and compared. One is a single 1200 V, 30 A SiC MOSFET; the other is a 1200 V, 30 A SiC MOSFET co-packaged with an SiC Schottky barrier diode (SBD). Figure 3-17 illustrates the circuit configuration of the tested devices: M1, Db1, and M2, Db2 are the tested pure SiC MOSFETs and their internal body diodes; Ds1 and Ds2 represent the co-packaged SiC SBD.

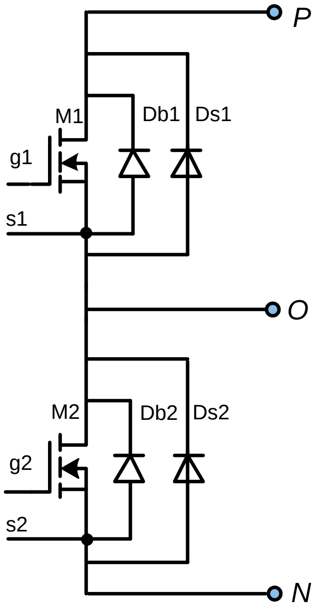

Figure 3-17: Circuit configuration of the tested SiC MOSFETs.

SiC 1200 V, 30 A SiC MOSFET with Schottky diode

The static characteristics of the 1200 V, 30 A SiC MOSFET and the anti-parallel Schottky diode were obtained over a temperature range of 25 to 175°C. The output characteristics of a 1200 V, 30 A SiC MOSFET at +20 V Vgs for different operating temperatures are shown in Figure 3-18. The on-state resistance and transconductance of the SiC MOSFET present a positive temperature coefficient, which is beneficial for device paralleling operation.

The forward characteristics of the co-packaged SiC SBD were obtained at +0 V of get bias, as shown in Figure 3-19. Similar to an Si Schottky diode, the built-in potential of the device is reduced and the equivalent resistance becomes larger at higher temperatures.

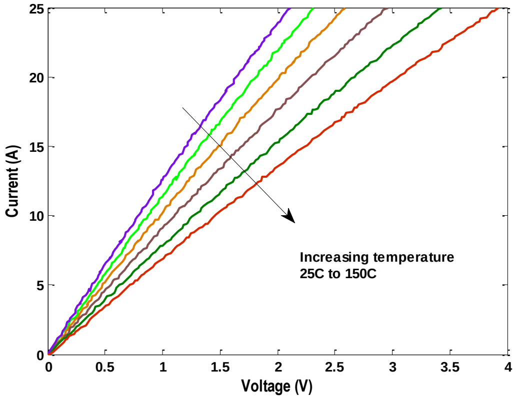

Figure 3-18: The i-v curves of a 1200 V, 30 A SiC MOSFET.

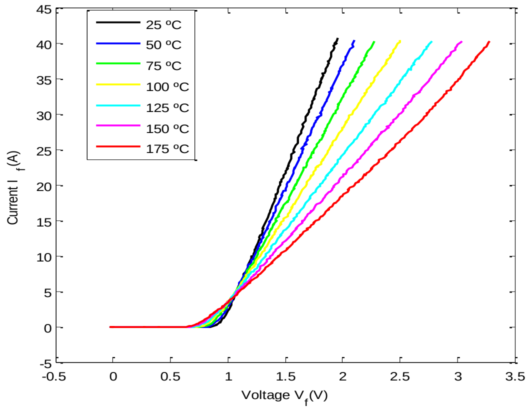

Figure 3-19: The i-v curves of the co-packaged SiC SBD.

The turn-on and turn-off energy losses of the MOSFET and the Schottky diode were obtained using a double-pulse circuit with a load inductance of 360 µH, as shown in Figure 3-20. The co-packaged anti-parallel diode was used as the clamping diode in the circuit. The gate driver used for this testing was a commercial gate driver chip.

The data were obtained at 600 Vdc for various currents at 25 and 175°C. As can be observed, the turn-on, turn-off, and total energy losses increase with an increase in current. With a rise in temperature, the turn-on energy loss decreased as a result of a faster switching speed, whereas the turn-off energy loss increased as a result of a slower switching speed. The net result was that the total switching energy loss became somewhat lower at higher temperatures.

The reverse recovery loss of the SiC SBD during the off transient was also evaluated with different current and temperature levels (Figure 3-21). Compared with the SiC MOSFET, the energy losses of the SiC SBD were negligible since there was almost no reverse recovery phenomenon for the SiC SBD.

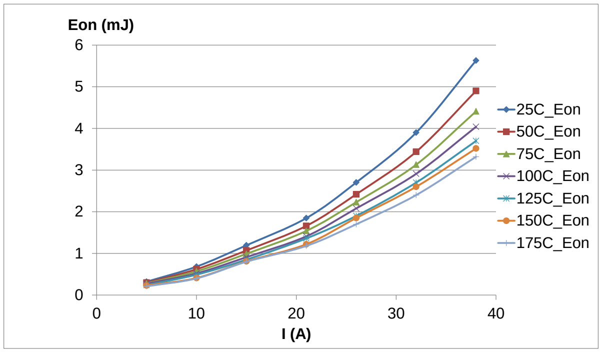

(a) Turn-on loss

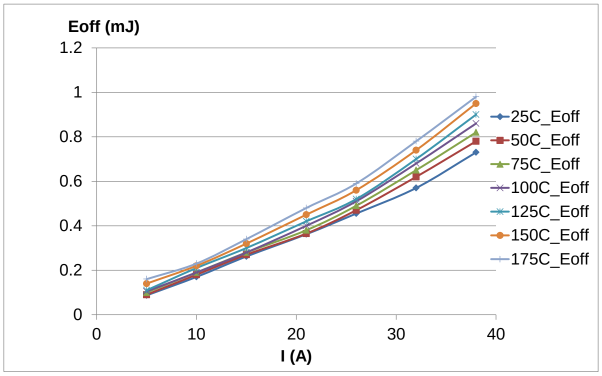

(b) Turn-off loss

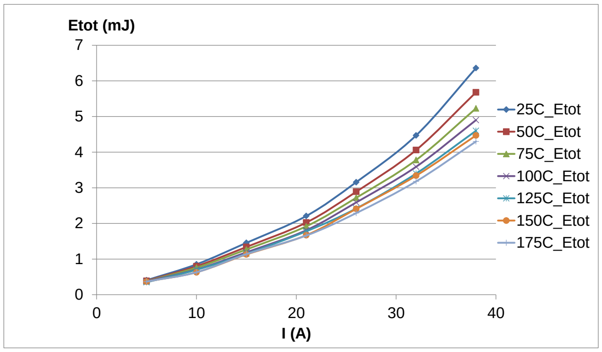

(c) Total loss

Figure 3-20: Energy losses of 1200 V, 30 A SiC MOSFET with SiC SBD at 600 V.

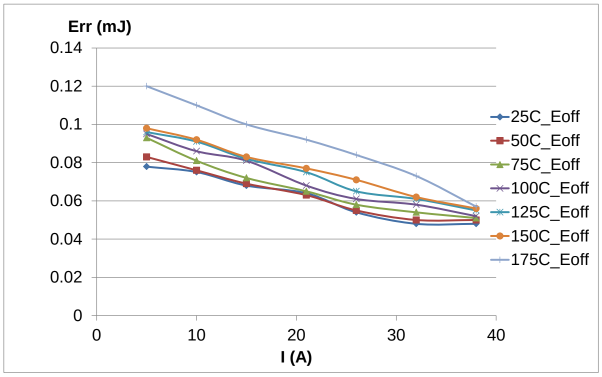

Figure 3-21: Energy losses of the co-packaged SiC SBD at 600 V.

SiC 1200 V, 30 A SiC MOSFET without Schottky diode

Similarly, the static characteristics of the 1200 V, 30 A SiC MOSFET without a Schottky diode were obtained over a temperature range of 25 to 175°C. The output characteristics of the 1200 V, 30 A SiC MOSFET are shown in Figure 3-22 with a gate voltage of +20 V. The output characteristics remained nearly the same as those of the SiC MOSFET with the SiC SBD, since the SiC MOSFET dies are the same.

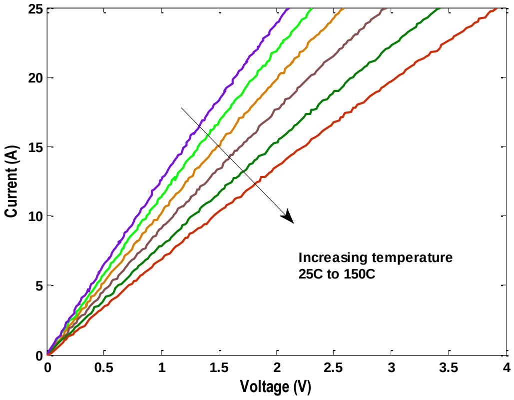

Figure 3-22: The i-v curves of a 1200 V, 30 A SiC MOSFET.

The forward characteristics of the body diode are shown in Figure 3-23. With a rise in temperature, the built-in potential decreased as a result of the increase in intrinsic concentration. However, unlike in the SiC SBD, the bulky resistance of the body diode presents a negative temperature coefficient, which may cause a thermal runaway issue during parallel operation. Another issue for the body diode is its high built-in voltage, resulting in much higher conduction losses compared with the SiC SBD.

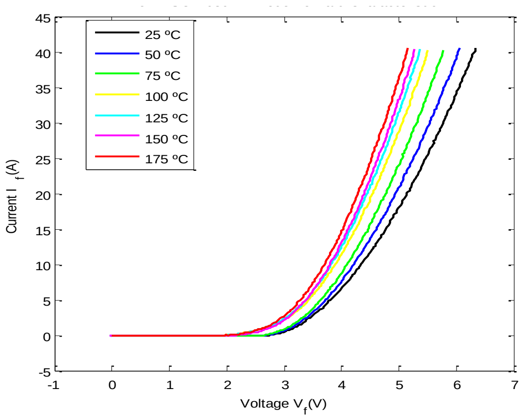

Figure 3-23: The i-v curves of the body diode of the SiC MOSFET.

The turn-on and turn-off energy losses of the SiC MOSFET without a SiC SBD were obtained under the same testing conditions (600 V, 25 to 175°C), as shown in Figure 3-24. Compared with the SiC MOSFET with a co-packaged SiC SBD, the total energy loss was a little lower because of a smaller equivalent junction capacitance across the drain to source terminals.

The reverse recovery loss of the body diode of the SiC MOSFET during the off transient was also evaluated at different current and temperature levels (Figure 3-25). The energy loss of the body diode was somewhat higher than that of the SiC SBD because of the more severe reverse recovery phenomenon; however, it was still negligible.

WBG Inverter Design and Development

Device packages able to withstand high temperatures are required to take advantage of the high-temperature operating capability of WBG devices. Various organizations are working on high-temperature packaging for high-temperature devices. Several high-temperature packages, which include discrete device packages for power modules, have been reported in the past several years. Novel packaging concepts focus primarily on improving the existing packages or on designing new packages using new materials and or processing techniques for better reliability and performance. Even though the novel packages enable the devices to work at higher temperatures, theoretical advantages such as the current density of WBG devices are not realized because of the interconnects needed for the power module to access the device terminals. In addition, the novel designed packages need further development to be used in full systems.

Other factors that limit the system designers from reaping the benefits of WBG technology are the low-voltage electronics and the passive components. This is because even though the packages and the power devices can handle high temperatures, the low-power electronics that drive the power devices, Si-on-insulator (SOI) -based technologies, are limited to a maximum temperature of 200°C. Si-based electronics are limited to 125°C operating temperatures. Although SOI-based electronics can work at up to 200°C, they

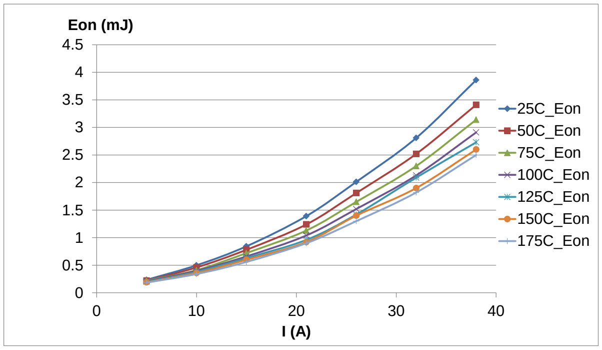

(a) Turn-on loss

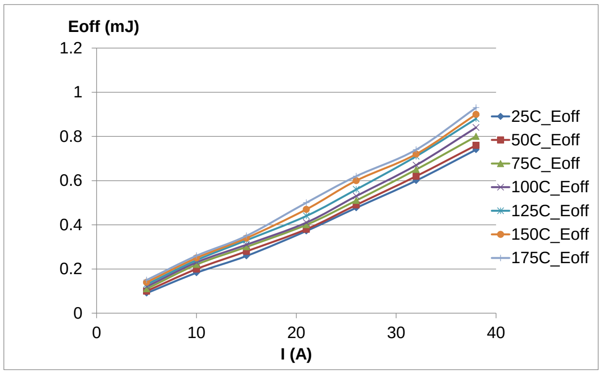

(b) Turn-off loss

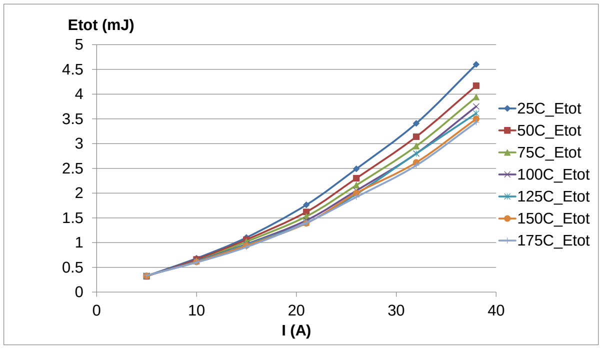

(c) Total loss

Figure 3-24: Energy losses of 1200 V, 30 A SiC MOSFET without SiC SBD at 600 V.

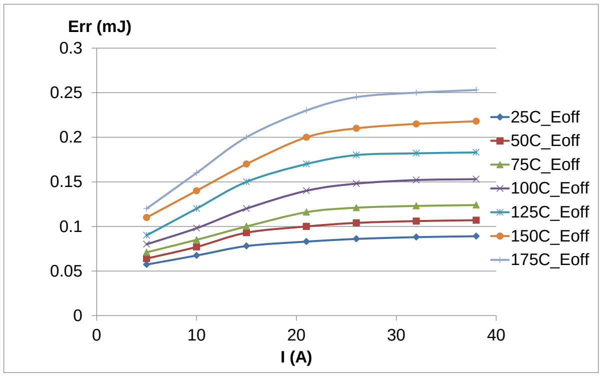

Figure 3-25: Energy losses of the body diode of the SiC MOSFET.

are expensive. High-temperature (over 200°C) electronics have been reported as being feasible; however, they have not been built to demonstrate their performance capabilities. It could be many years before a logic-level high-temperature transistor can be built. This time lag creates a void in the power module industry, especially for intelligent power module products, which include the electronics inside the module.

Similarly, the passive components in an inverter have a low operating temperature and cannot be operated in close proximity to high-temperature WBG devices. This situation leads to an increase in the volume and a reduction in the power density of the system. High-temperature passive components are currently being developed to address the high-temperature-operation requirement. However, as with the electronic components, they will be much more expensive than the low-temperature components.

To address these problems, a system-level approach for packaging design needs to be developed. Complex 3-dimensional packaging structures with integrated interconnects can reduce the required assembly steps and increase the power densities of power electronic systems. Recent advancements in additive manufacturing (AM) promise an exciting future trend for WBG technology to make inroads into the power electronics industry. AM techniques enable the development of complex 3-dimensional geometries that will result in size and volume reductions at the system level by integrating low-temperature components with high-temperature active devices and reducing the material needed to build the heat exchangers in inverters. ORNL has developed expertise in AM in the last few years. ORNL's PEEM team recognized the potential of this technology for power electronics system packaging and took the first step toward achieving a completely printed inverter concept.

A 10 kW all SiC inverter incorporating an aluminum-based printed power module with an integrated cooling system and a printed plastic lead frame was built using AM techniques. This is the first inverter prototype built using AM. This paper presents the design and development of the inverter and characterization of a high-temperature 1200 V, 100 A all-SiC module. The module development was presented in the FY 2013 VTO annual report. The inverter development and testing are discussed in the following sections.

Inverter Design

Overall design

The current required for a 10 kW inverter can be calculated to be approximately 37 A peak current per phase, assuming the battery voltage to be 350 Vdc with a square mode of operation and a power factor of 0.6. This operating condition represents the worst-case scenario for peak power through the inverter, required to drive the motor. The dc bus capacitors were designed to handle a maximum rms ripple current (~90 A). The capacitors used in this design are not a brick type but are smaller individual capacitors connected in parallel to ensure better cooling and to reduce costs. The cost reduction results from their being off-the-shelf components as opposed to custom-designed brick capacitors with integrated bus bars. A total capacitance of 200 uF was obtained with five 900 V, 40 uF capacitors. The dc bus bars for this inverter were laminated and designed with inserts for each individual capacitor.

The power loss of the 1200 V, 100 A devices (two 50 A SiC MOSFETs and two 50 A diodes) was calculated using the test data obtained through device characterization, as shown in Figure 3-26 and Figure 3-27. The loss per device was calculated as a function of power factor, operating voltage, peak current through each device (37/2=~16.5 A per switch), switching frequency, and modulation index. It can be clearly seen that for M=1, the maximum loss for a 175°C maximum junction temperature design was ~30 W. The loss through the diode for M=1 was approximately 16 W. The total loss per switch was ~46 W. This number set the design specifications for the heat removal system for the entire inverter at an operating junction temperature of 175°C maximum. The total loss for the inverter was simply six times the loss per module, which is approximately 276 W. It should be noted that for different values of M and different power factors, the losses would vary between the MOSFET and the diodes. Based on the simulated values, the average efficiency of this inverter is estimated to be around 98–99% over a wide range of operating conditions. A CAD model of the overall inverter design is shown in Figure 3-28.

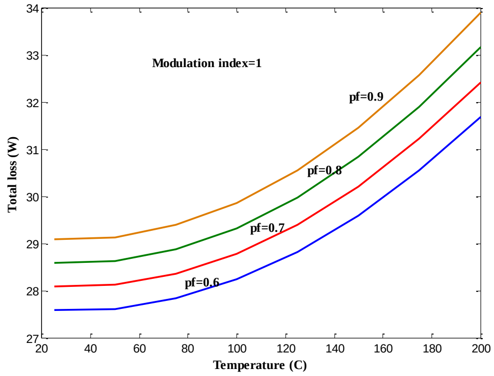

Figure 3-26: Loss per switch in a 1200 V, 100 A SiC MOSFET module at 350 Vdc, 37 A,10 kHz, and M=1.

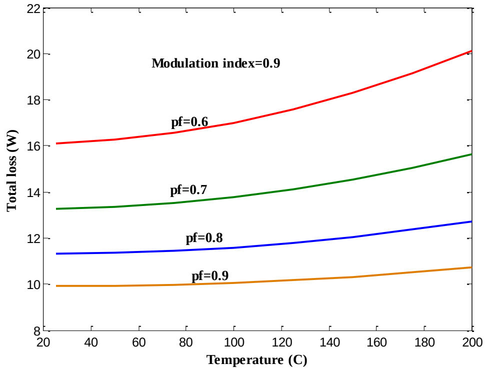

Figure 3-27: Loss per switch in a 1200 V, 100 A SiC diode module at 350 Vdc, 37 A,10 kHz, and M=0.9.

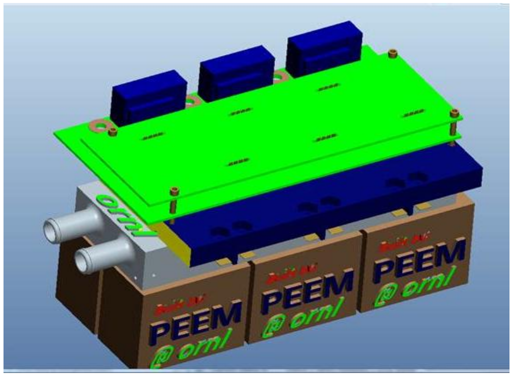

Figure 3-28: CAD model of the inverter design.

Gate driver design for the module

The gate driver boards were individually designed for each phase leg with separate gate drivers for upper and lower switches (Figure 3-29). Commercially available gate driver chips from Rohm were used in this inverter. The gate driver has galvanic isolation at up to 3000 Vrms, integrated overcurrent protection under voltage lockout, and temperature feedback features. One important feature of this gate driver is that it has miller clamp protection, which is very important for fast-switching devices like SiC MOSFETs. This feature prevents the upper and lower switch from faulting through switching transients.

Figure 3-29: Gate driver board for a single-phase power module.

The driver can provide a peak output current of 5 A with a maximum output resistance of 1 Ω. The maximum rise time is 45 ns for a capacitive load of 10 nF with VCC=24 V, according to the data sheet specifications. Each switch in the phase leg was designed for a gate voltage of 25 V (+20 V to −5 V). The devices were switched with an external gate resistance of 4 Ω to ensure fast turn-on and turn off switching. The peak current required was slightly higher than 6 A, and a buffer stage was added to the output of the gate driver to handle it. The over-current protection circuit was designed using the desaturation detection feature of the gate driver chip. The gate driver protection features were designed and tested using a single-phase test bed.

Cooling system design

The cooling system for this prototype is single-sided cooling for the power module substrates. The heat sink is not a simple conventional structure but capitalizes on AM capabilities to build complex internal structures for better heat transfer capability throughout the unit. This design was used because it allows lower-temperature components to be placed as close to the high-temperature devices as physically possible to achieve two goals: (1) reduce electrical parasitics and (2) reduced volume and mass of the overall system package. AM (using printed metals) will allow optimized design for heat transfer in the smallest possible package.

With AM, complexity is basically free, so any shape or grouping of shapes can be imagined and modeled for performance. The heat sink used for this inverter is a complex unit made using a direct-melted laser-sintered (DMLS) process, which incorporates flow paths inside the heat sink that allow a complex geometry around the heat-generating paths. Figure 3-30 shows an x-ray of the internal structure of the printed power module. The x-ray confirms that there are no clogged channels inside the module with unremoved powder or bridged metal structures. Since this is still a maturing technology, it is very important to understand the material properties and compare them with those of conventional aluminum alloys to further improve or optimize the design. A material analysis was performed on the AM power module and compared with analysis results for a regular 6061 aluminum alloy. Figure 3-31 and Figure 3-32 show materials analysis results for AM aluminum compared with 6061 aluminum. The results show that the strength of the AM alloy is very similar to that of the 6061 alloy.

Figure 3-30: Cross-section view of AM model heat sink and x-ray of that view.

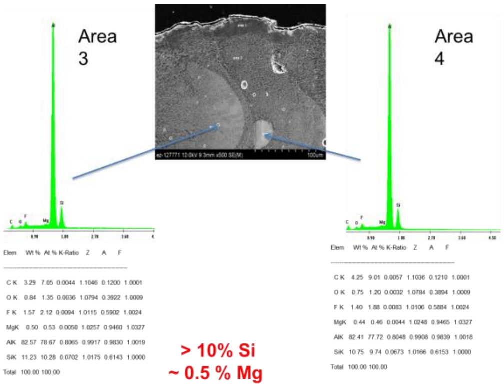

Elem	Wt %	At %	K-Ratio	Z	A	F
C K	3.29	7.05	0.0044	1.1046	0.1200	1.0001
O K	0.84	1.35	0.0036	1.0794	0.3922	1.0009
F K	1.57	2.12	0.0094	1.0115	0.5902	1.0024
MgK	0.50	0.53	0.0050	1.0257	0.9460	1.0327
AlK	82.57	78.67	0.8065	0.9917	0.9830	1.0019
SiK	11.23	10.28	0.0702	1.0175	0.6143	1.0000
Total	100.00	100.00				

Elem	Wt %	At %	K-Ratio	Z	A	F
C K	4.25	9.01	0.0057	1.1036	0.1210	1.0001
O K	0.75	1.20	0.0032	1.0784	0.3894	1.0009
F K	1.40	1.88	0.0083	1.0106	0.5884	1.0024
MgK	0.44	0.46	0.0044	1.0248	0.9465	1.0327
AlK	82.41	77.72	0.8048	0.9908	0.9839	1.0018
SiK	10.75	9.74	0.0673	1.0166	0.6153	1.0000
Total	100.00	100.00				

Figure 3-31: Material composition of AM aluminum ($AlSi_{10}Mg$).

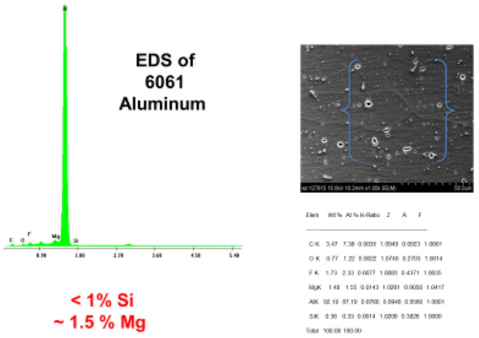

Elem	Wt %	At %	K-Ratio	Z	A	F
C K	3.47	7.38	0.0035	1.0949	0.0923	1.0001
O K	0.77	1.22	0.0022	1.0740	0.2700	1.0014
F K	1.73	2.33	0.0077	1.0893	0.4371	1.0035
MgK	1.48	1.55	0.0143	1.0261	0.9050	1.0417
AlK	92.19	87.19	0.8768	0.9948	0.9560	1.0001
SiK	0.36	0.33	0.0014	1.0206	0.3826	1.0000
Total	100.00	100.00				

Figure 3-32: Material composition of 6061 aluminum.

Additional test results in Figure 3-33 show thermal conductivity comparisons between conventional 6061 aluminum, which is used on many ORNL prototype heat sinks, and the typical AM aluminum alloy used in DMLS, AlSi$_{10}$Mg. ORNL will pursue the development of an aluminum alloy material that works well in the DMLS process and has improved thermal performance. At lower temperatures, 6061 aluminum has a significantly better thermal conductivity than does the AM aluminum, but the conductivity of the two becomes close to equal around 150°C, which is near the center of this inverter's operating range. It would be beneficial to improve the performance in the 100–150°C range for this application.

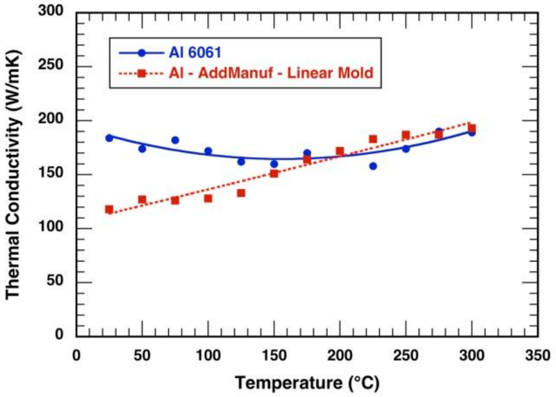

Figure 3-33: ORNL test results for thermal conductivity for AM aluminum sample (AlSi$_{10}$Mg) vs conventional 6061 aluminum.

Inverter Assembly and Testing

The final power module assembly is shown in Figure 3-34. The direct-bonded copper substrates were directly mounted to the printed module enclosure using spring pressure and thermal grease as the heat transfer medium from the lower side of the direct-bonded copper substrates. The lead frame was built using a plastic printer at the ORNL Manufacturing Demonstration Facility. The bolt holes in the lead frame served as the strain relief structure for the power leads from the substrates. The plastic lead frame also provided the support for the gate driver printed circuit boards and the control board through integrated plastic stand-offs. The material for this first prototype was made using fused deposition melting (FDM) and is common ABS plastic; it can be replaced on the next prototype with an FDM plastic that has a temperature rating near 200°C. The gate driver leads were soldered to flexible wires and were connected to the gate driver boards. The total volume of the inverter is ~1.5 L. (9.2 × 9.1 × 17.8 cm).

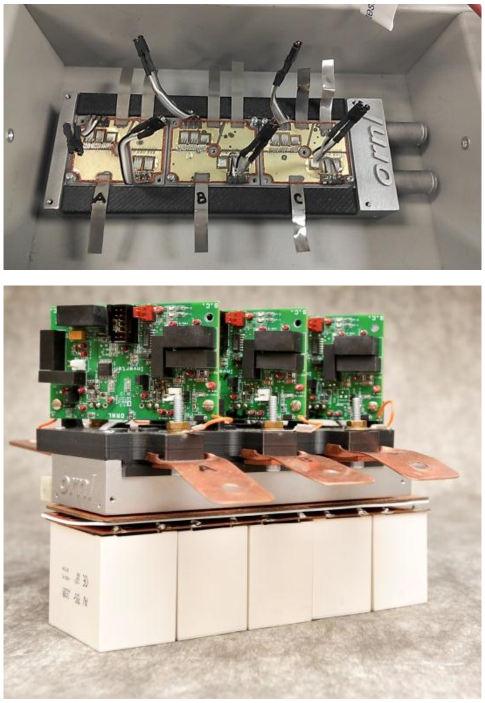

Figure 3-34: Final assembled inverter and the power module prototype.

The experimental test setup is shown in Figure 3-35. The test equipment used for this experiment included a Tektronix DPO 7104 1 GHz, TEK differential probe P5205 with 100 MHz bandwidth, and a Tektronix 404 XL current probe. A PZ4000 power analyzer from Yokogawa was used for the power measurements. The neutral point connection from the three-phase resistive load was used for the power measurement setup in the power analyzer. For this test, the dc-link voltage was fixed at a nominal operating voltage (350 V) to the maximum bus voltage (450 V). The load resistance was set to the minimum value, and changing the modulation index controlled the current. The coolant was set at 20°C at a flow rate of 1.5 gpm. The open-loop frequency of operation and the pulse width modulation frequency were fixed, and the current command was varied for a particular dc-link voltage. The command current was increased in steps without exceeding the power rating of the inverter or of the load. The coolant temperature was changed to 60°C, and data were recorded for a wide range of current and switching frequencies. The experimental waveforms for 350 and 450 V operation are shown in Figure 3-36.

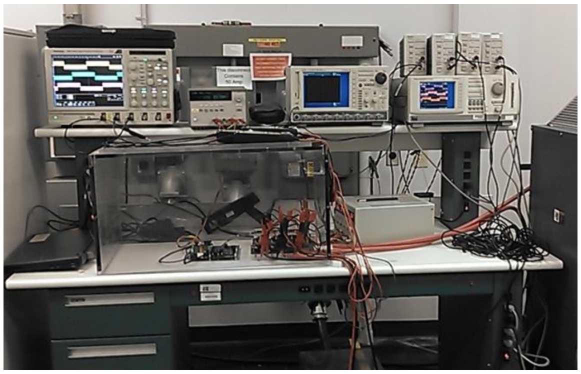

Figure 3-35: Experimental setup for evaluating inverter performance.

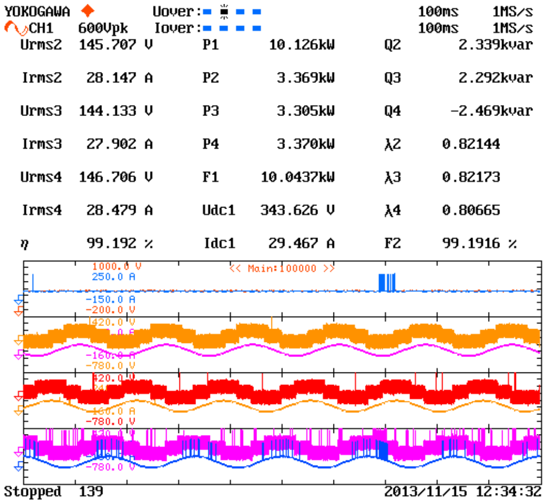

```
YOKOGAWA ◆        Uover:■ ■ ■ ■                    100ms     1MS/s
 CH1     600Vpk   Iover:■ ■ ■ ■                    100ms     1MS/s
  Urms2  145.707 V      P1       10.126kW    Q2       2.339kvar

  Irms2   28.147 A      P2        3.369kW    Q3       2.292kvar

  Urms3  144.133 V      P3        3.305kW    Q4      -2.469kvar

  Irms3   27.902 A      P4        3.370kW    λ2     0.82144

  Urms4  146.706 V      F1      10.0437kW    λ3     0.82173

  Irms4   28.479 A      Udc1    343.626 V    λ4     0.80665

  η       99.192 %      Idc1     29.467 A    F2     99.1916 %
```

```
Stopped   139                                 2013/11/15 12:34:32
```

(a)

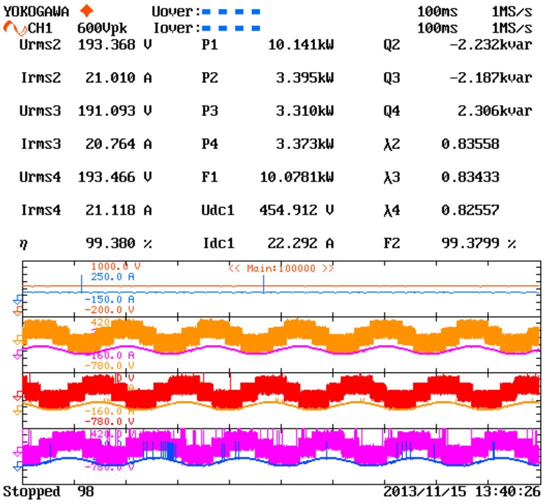

```
YOKOGAWA ◆        Uover:■ ■ ■ ■                    100ms     1MS/s
 CH1     600Vpk   Iover:■ ■ ■ ■                    100ms     1MS/s
  Urms2  193.368 V      P1       10.141kW    Q2      -2.232kvar

  Irms2   21.010 A      P2        3.395kW    Q3      -2.187kvar

  Urms3  191.093 V      P3        3.310kW    Q4       2.306kvar

  Irms3   20.764 A      P4        3.373kW    λ2     0.83558

  Urms4  193.466 V      F1      10.0781kW    λ3     0.83433

  Irms4   21.118 A      Udc1    454.912 V    λ4     0.82557

  η       99.380 %      Idc1     22.292 A    F2     99.3799 %
```

```
Stopped   98                                  2013/11/15 13:40:26
```

(b)

Figure 3-36: Experimental waveforms of 10 kW SiC inverter. (a) Screen shot of 350 V dc-link operation; (b) screen shot of 450 V dc-link operation.

The plot of efficiency vs output power for several operating conditions is shown in Figure 3-37. Inverter efficiencies were higher at the 450 V than at the 325 V operating condition, as expected. Figure 3-38 shows that the inverter efficiency did not change much as the switching frequency increased. The overall inverter efficiency was ~99% for different operating conditions. The total operating power density based on the test conditions for the inverter was ~7 kW/L, and the designed power density was much higher. This inverter can be further pushed to a higher operating power by increasing the dc-link voltage and current, and a power density at least four times greater can be realized.

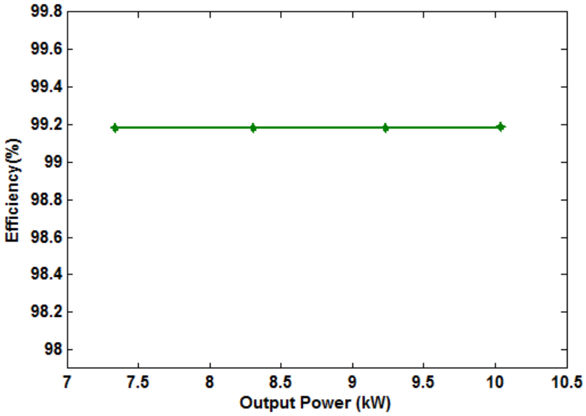

Figure 3-37: Inverter efficiency vs. output power.

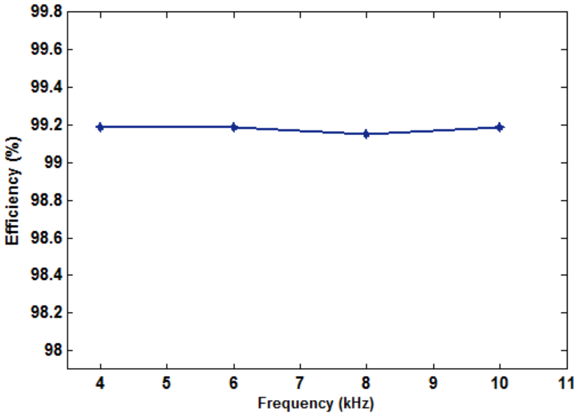

Figure 3-38: Inverter efficiency vs. switching frequency.

Air-cooled inverter

ORNL worked with the National Renewable Energy Laboratory (NREL) to develop an air-cooled inverter to further optimize the thermal design. The air-cooled inverter developed in FY 2013 was redesigned using thermal simulations from NREL. The initial inverter size was reduced by 33% through fin design optimization. A balance-of-plant analysis is currently being conducted to establish the feasibility of air cooling at the system level. The new module design has been fabricated and tested for heat transfer. The design was modified by ORNL and redesigned with 1200 V, 100 A MOSFET and Schottky diodes. The module and the inverter assembly are shown in Figure 3-39 and Figure 3-40.

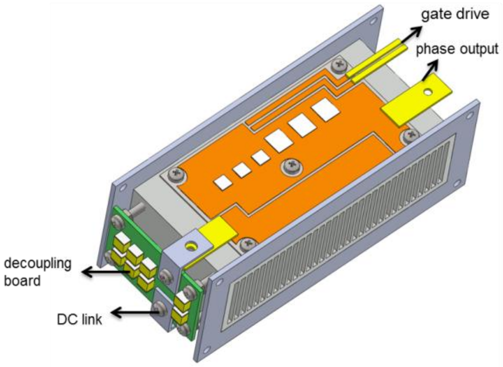

Figure 3-39: Air-cooled inverter module layout.

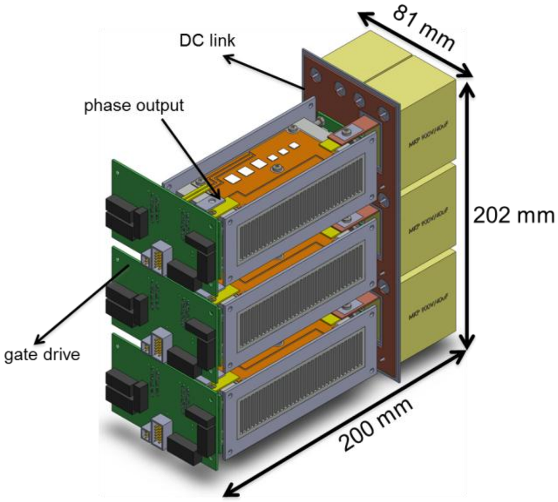

Figure 3-40: Air-cooled inverter design layout.

Conclusion and Future Directions

WBG device evaluation will continue until the technology transitions to industry. Design, development, and testing of a SiC inverter with a printed power module AM heat sink was presented. The total operating power density of the laboratory prototype inverter is ~7 kW/L and the average operating efficiency of the inverter for a wide range of operating conditions is around 99%. However, based on the design, the power density can potentially be four times greater for higher power with the same power module. This prototype is the first inverter built using AM techniques. The material analysis showed there is no issue with the strength of the AM material compared with that of Al-6061. It was also shown that there is no compromise in the performance of the inverter because of the different material used. From ORNL’s perspective, this is the first step toward realizing a full inverter built using AM techniques

The inverter test results obtained this year will be used as a benchmark for next-generation higher power inverters to be built using ORNL’s WBG package. The results obtained show that if the inverter is scaled to 30 kW, it will meet the 2020 VTO targets. They also show that WBG technology will aid in achieving U.S. DRIVE targets for volume, efficiency, power density, and system costs.

3.3 Innovative Technologies for dc-dc Converters and On-board Chargers

Gui-Jia Su (Principal Investigator)

Oak Ridge National Laboratory
National Transportation Research Center
2360 Cherahala Boulevard
Knoxville, TN 37932
Phone: (865) 946-1330; Fax: (865) 946-1262
Email: sugj@ornl.gov

Burak Ozpineci, ORNL EDT Program Manager
Phone: (865) 946-1329; Fax: (865) 946-1262
Email: burak@ornl.gov

Susan A. Rogers, DOE EDT Program Manager
Phone: (202) 586-8997; Fax: (202) 586-1600
Email: Susan.Rogers@ee.doe.gov

Start Date: October 2013
Projected End Date: September 2016

Objectives

- Overall project objective:
  - Develop low-cost, high-efficiency, high-power-density all-wide bandgap (WBG) dc-dc converters and on-board chargers (OBCs). The aim is to reduce charger converter cost by 50% and weight and volume by a factor of 2 compared with the state of the art and provide charger efficiency of more than 96%.
- FY 2014 objective:
  - Design, build, and test a 6.6 kW silicon carbide (SiC) isolation converter.
  - Characterize gallium nitride (GaN) devices for OBC and dc-dc converter designs.

Technical Barriers

- Reducing OBC and dc-dc converter cost, weight, and volume.
- Achieving high efficiency.
- Overcoming the limitations of existing semiconductor and magnetic materials to address charger and converter cost, weight, volume, and efficiency targets.

Accomplishments

- Characterized 1200 V/100 A SiC switch phase-leg modules developed in FY 2013 for use in the development of a 6.6 kW OBC prototype.
- Completed design and fabrication of a 6.6 kW isolation converter using the ORNL-designed SiC phase-leg modules and planar ferrite cores.
- Completed tests of the 6.6 kW SiC-based isolation converter that showed a measured peak efficiency of 99.0%.
- Tested and characterized 600 V GaN switches for use in OBC converter designs.
- Completed tests of a baseline 5.8 kW Si-based integrated charger that integrates the segmented traction drive, 14 V dc-dc converter, and high-voltage battery charger dc-dc converter. It showed a peak efficiency of 94.6% when charged from a 240 V source and 92.0% when charged from a 120 V source.

✧ ✧ ✧ ✧ ✧

Introduction

The stand-alone OBCs that currently dominate plug-in electric vehicles (EVs) are not cost-effective and have performance limitations that stem from the large component counts of the topologies and limitations in existing semiconductor and magnetic materials. The result is a plateau in charger and converter performance because (1) silicon (Si) switches constrain switching frequencies to less than 100 kHz at power levels of several kilowatts, and (2) inductors and transformers based on soft ferrite magnetic materials further limit power density and efficiency because of low saturation flux densities (~0.38 T) and high core losses at high frequencies. The limitations in switching frequency and material properties result in bulky and expensive passive components—including ac filter capacitors, inductors, and transformers—in currently available OBCs. And passive components contribute more than 30% to the charger cost in state-of-the-art Si-based technology.

As a result, OBCs:

- Add significant cost (~$106/kW)
- Have low power density and specific power numbers (e.g., the 2012 Nissan LEAF 6.6 kW OBC: 0.41 kW/kg, 0.66 kW/L)
- Are relatively inefficient (85–92%)
- Are unidirectional (can charge the battery but are incapable of vehicle-to-grid support, a highly desirable function in future smart grids).

Emerging WBG devices, including SiC and GaN and advanced soft magnetic materials, are poised to offer significant improvements in ac-dc and dc-dc converters. Their ability to operate with enhanced efficiency over higher frequencies and temperatures minimizes passive component requirements and reduces cooling demands, providing opportunities for revolutionary strides in power conversion.

This project is targeted at leapfrogging existing Si-based charger technology to address charger and converter cost, weight, volume, and efficiency requirements. It proposes to overcome the limitations of existing semiconductor and magnetic materials by using WBG devices, advanced magnetic materials, and novel integrated charger topologies and control strategies to significantly increase power density, specific power, and efficiency at lower cost.

Approach

The strategy to address the limitations of state-of-the-art OBCs and dc–dc converters is multifold:

- Push the envelope on functional integration of the traction drive, 14 V dc-dc converter, and OBC.
- Take up the challenge of introducing WBG materials, specifically GaN, into automotive applications to determine what performance, packaging, cost, and efficiency benefits can be gained.
- Perform analysis, modeling, and simulation that lead to a functional prototype meeting VTO OBC specific power, power density, and efficiency requirements while significantly reducing the current cost levels.
- Design, build, test, and demonstrate prototypes.
- Work with U.S. DRIVE to develop insights and lessons learned from the automotive community pertinent to dc-dc converters and OBCs.
- Collaborate with industry stakeholders, universities, and other national laboratories to maximize the impact of this work.

Three technical approaches are being pursued. First, integrated bidirectional WBG OBCs will be developed that (a) provide galvanic isolation; (b) provide an integrated function for dc-dc conversion of high voltage to 14 V; (c) use soft switching at the dc-dc stage to reduce electromagnetic interference (EMI) and improve efficiency. Figure 3-41 shows an integrated dc-dc converter and charger architecture consisting mainly of an ac filter, a WBG front active converter, a dc bus capacitor, and a WBG isolation converter. The isolation converter integrates the functions for charging both the high-voltage traction battery and the 14 V battery for vehicle accessory loads. It includes high-frequency transformers and dc filters as well as WBG switches.

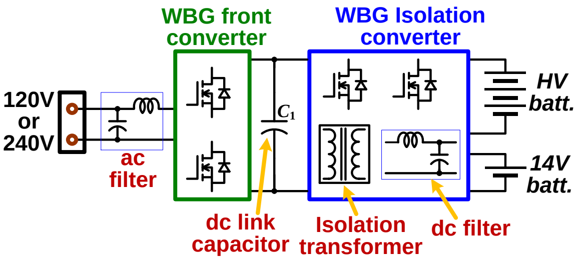

Figure 3-41: An integrated dc-dc converter and charger architecture.

Second, increasing power density and specific power without compromising efficiency is aggressively pursued by exploiting high switching frequency with WBG devices (especially GaN switches) and using advanced soft magnetic materials (nanocomposites) to drastically reduce the cost, weight, and volume of the ac and dc filters and isolation transformer. Because the availability of WBG power modules is limited, SiC and GaN devices are purchased or obtained directly from device vendors and tested, characterized, and packaged for use in converter design and prototype development. Prototypes will be built and tested first using SiC devices—for which wafer processing and device fabrication technologies have advanced to the stage that SiC metal oxide semiconductor field-effect transistors (MOSFETs) and other switches are available commercially—and then GaN switches as that technology matures and devices with high current ratings become available.

Third, further integration with traction drive systems is employed to reduce the component count for OBCs. For instance, WBG traction drive inverters and motors will be operated as the active front converter and used to replace the ac filter inductor, significantly reducing OBC cost, weight, and volume.

Finally, a control strategy for the isolation converter has been developed to shrink the bulky dc link capacitor. Without the control, this bulky capacitor is necessary to filter out the large voltage ripple— with twice the grid supply frequency—inherent in single-phase ac-dc converters. The proposed control strategy enables a 60% reduction in the ripple current and thereby a significant size reduction in the bulky dc link capacitor in the front ac-dc converter.

Figure 3-42 shows the integrated isolation converter topology selected through simulation. It consists of a dual H-bridge phase shift dc-dc converter and a 14 V buck converter coupled through a high-frequency transformer. One H-bridge is connected to the high-voltage traction battery and the other to the active front ac-dc converter. Sharing of the transformer (for galvanic isolation) and other switch components between the OBC and the 14 V converter leads to substantial cost, weight, and volume savings for the OBC compared with a stand-alone counterpart. Other features of the integrated charger include these:

- It provides bidirectional power flow and thus can offer additional desired functions, such as vehicle-to-grid and vehicle-to-home applications.
- It can charge the 14 V battery from the grid in addition to normal operation from the high-voltage traction battery.
- It uses the parasitic capacitance of the switches and the transformer leakage inductance to achieve zero-voltage switching for EMI noise reduction and efficiency improvement.
- The dual H-bridge converter enables the OBC to charge the battery over a wide range of voltages by providing a voltage buck and boost function through phase shift and duty ratio control.

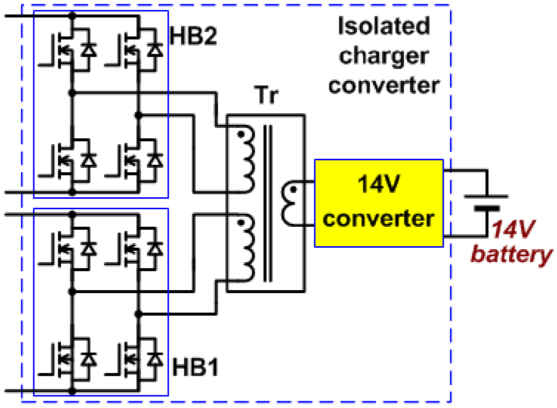

Figure 3-42: Isolated charger converter topology.

Figure 3-43 shows an example of the proposed integrated architecture, in which an OBC is integrated into an electrical drive system based on the segmented traction drive topology. Specifically, it consists of a high-voltage (HV) battery, a segmented traction drive system, two sets of contact switches (CS_1 and CS_2), and an isolated charger converter. The segmented traction drive system is formed by splitting the switches of the inverter/converter (INV/CONV) and the stator windings of the motor/generator (MG) into two groups and connecting each group of switches and windings to form a drive unit. The major benefit of the segmented traction drive is the significant (>60%) size reduction of the dc bus capacitor enabled by interleaved switching by the two drive units [1].

The neutral points of the two stator winding groups (N_1 and N_2) are brought out to a charging port through a third contact switch (CS_3). In addition, as in a stand-alone charger, a filter of common mode and differential mode is usually needed to filter out switching harmonics and common mode noises to meet power quality standards and safety regulations. The differential mode filter is typically realized with a capacitor and an inductor connected across and in series, respectively, with the charging port. One advantage of the integrated charger is that the motor is used as the filter inductor (as described later), thus eliminating the external filter inductor altogether or significantly reducing its inductance if the motor leakage inductance is not sufficient.

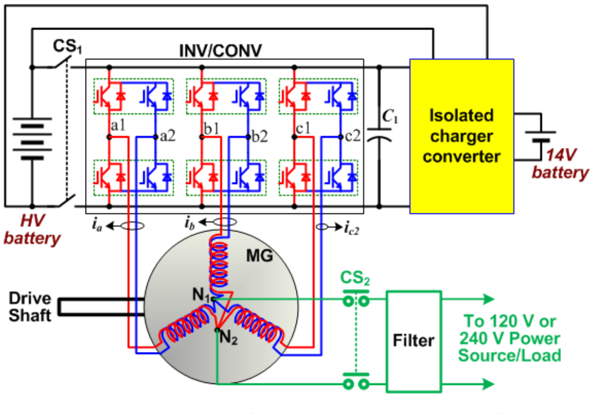

Figure 3-43: An example of the proposed integrated OBC based on the segmented traction drive topology.

The drive system operates in one of the three modes: (1) providing the propulsion force for driving the vehicle (propulsion mode), (2) charging the HV battery (charging mode), or (3) supplying power to external loads (sourcing mode).

In the propulsion mode, contact switch CS_1 is closed and CS_2 is open, connecting the HV battery to the drive units while disconnecting the charging port from the drive units. The two drive units operate with interleaved switching to reduce the dc bus ripple current, and thus the required size for the dc bus capacitor, and to control the speed and/or torque of the MG according to the amount of power required to propel the vehicle. Two current sensors, i_a and i_b, that measure the combined current of phases *a* and *b*, respectively, are used in the motor control. In the meantime, the H-bridge, HB2, and 14 V converter operate to charge the 14 V battery from the HV battery.

In the charging mode, contact switch CS_1 is open and CS_2 is closed, disconnecting the HV battery from the drive units while connecting the charging port to the drive units. All the switch legs in each INV/CONV of each drive unit collectively function as a single switch leg. The MG functions as an inductor, which is made possible by the motor's zero sequence (ZS) impedance network (ZSIN). Together, the two drive units form a single-phase front converter to regulate the dc bus voltage and perform power factor correction, drawing power from the external source. A third, smaller current sensor, i_{c2}, is used to sense the grid current for use in the controller of the front converter. Moreover, the H-bridge, HB1, operates off the dc bus and supplies, through the transformer, a high-frequency voltage to HB2, which converts the high-frequency voltage to a dc voltage to charge the HV battery. If needed, the 14 V converter can also convert the high-frequency voltage to a dc voltage to charge the 14 V battery. In this mode, the motor functions as a coupled inductor; and the ZS current will not generate a rotating air-gap flux and thus will not produce any torque.

In the sourcing mode, the power flow is reversed from that in the charging mode. The two drive units form a single-phase inverter to supply external loads or the utility grid. In this mode, the H-bridges operate to supply dc power from the HV battery to the single-phase inverter, which in turn converts the dc power to ac power to the external load. If needed, the 14 V converter can be activated to charge the 14 V battery.

During operation in the charging and sourcing modes, the motor is used as a filter inductor that is the ZS network. The grid current splits into three equal parts, and each part flows in each branch of the motor ZS network; therefore, the currents do not produce air-gap flux or generate any torque in the motor.

Figure 3-44 shows a control block diagram for INV/CONV1 and INV/CONV2. The purpose of these control blocks is twofold: to maintain a constant dc bus voltage at a commanded level of V_{dc}^* and maintain a near-sinusoidal grid current with a near-unity power factor (or a commanded value for reactive power compensation) and a low harmonic distortion factor. The dc bus voltage control loop is implemented with a proportional integral (PI) regulator, which generates a portion of the amplitude (I_s^*) of the current command, i_s^*, for the grid current control loop. The other part of the amplitude of the current command is provided by a feed-forward compensation determined by the battery charging power command, P_{bat}^*, modified by a feed-forward gain, ***k**ff*. The battery charging power command is generated in the charger converter controller and is described below. The current regulator, GI, can be a simple gain block of a relatively high value; and a sine-triangle comparator can be used to generate pulse width modulated (PWM) gating signals for the two INV/CONVs. It was found, however, that hysteresis control yields better performance in terms of lower switching losses and current harmonic contents, and it was thus employed in the test setup.

As shown in Figure 3-44, low pass filters (LPFs) are used in the feedback paths to remove the high-frequency components in the sensed voltages and currents. Since only a portion of the grid current is directly measured with the smaller current sensor, i_{c2}, the grid current can be computed—assuming the grid current is shared evenly among the three leads—by

$$\boldsymbol{i}_s = 3\boldsymbol{i}_{c2}, \qquad (1)$$

where $\boldsymbol{i}_{c2}$ is half-phase *c* motor current. Note the three-phase structure of the INV/CONVs and ZSINs enables the use of interleaved switching to reduce switching losses.

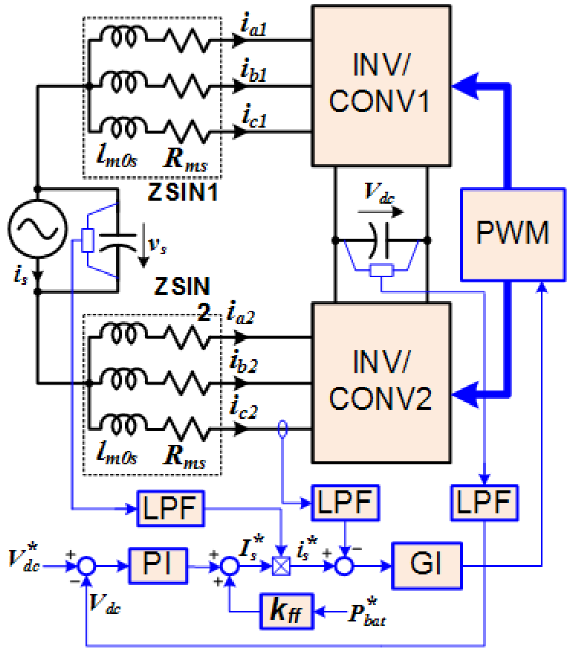

Figure 3-44: Control block diagram for INV/CONV1 and INV/CONV2.

Figure 3-45 shows a control block diagram for the charger converters, HB1 and HB2. The purpose of this control is to maintain a constant battery terminal voltage at a commanded level of V_{bat}^* in the CV charging mode or a constant current at a commanded level of I_{bat}^* in the CI charging mode. A software switch, **S**VI, is used to select the charging mode according to the state of charge of the battery. Again, a PI controller is used to regulate the battery voltage or current. Because of the significantly smaller dc bus capacitor in the segmented inverter, the dc bus voltage, *V*dc, will fluctuate to a greater degree during operation in the single-phase charger mode. To prevent it from causing a large ripple component in the battery charging current, the PI output is divided by the high-frequency component of *V*dc, obtained with a band-pass filter (BPF) and then fed to the PWM block, which controls the duty cycles. It also regulates the phase shift between the two H-bridges, if needed.

In addition, the battery charging power command, P_{bat}^*, is computed by

$$P_{bat}^* = \begin{cases} V_{bat}^* I_{bat}, \text{ in CV charging mode} \\ I_{bat}^* V_{bat}, \text{ in CI charging mode} \end{cases}, \qquad (2)$$

where ***V**bat* and ***I**bat* are the measured battery terminal voltage and current. As mentioned, P_{bat}^* is used in the feed-forward compensation in the grid current control loop to improve the dynamic response of the dc bus voltage loop.

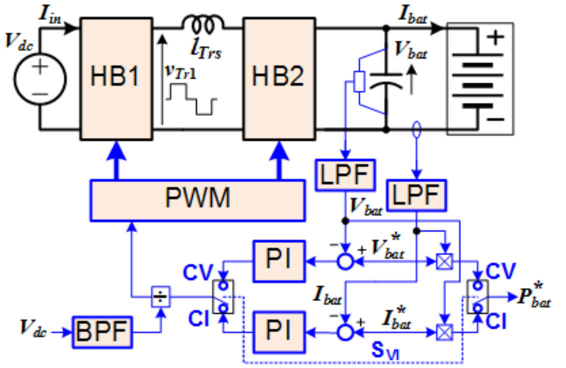

Figure 3-45: Control block diagram for HB1 and HB2.

An Si-based 5.8 kW prototype consisting of an electrical drive system and an isolation converter was built to test the charging function and verify the selected topology. The isolation converter and the experimental results will serve as the baseline for comparison with WBG-based prototypes being developed under this project. The drive system consists of a segmented inverter rated at 55 kW and a commercial, off-the-shelf, induction motor rated at 14.9 kW, 230 Vrms, 45.4 Arms. The motor has two poles and two sets of stator windings with all leads accessible. Figure 3-46 shows photos of the inverter and test motor. The 55 kW segmented inverter was fabricated with two pieces of 600 V/300 A six-pack of intelligent IGBT modules and two film dc bus capacitors, each rated at 500 V and 200 µF. These components are mounted on a 6×7 in. (15.24 × 17.78 cm) water-cooled cold plate.

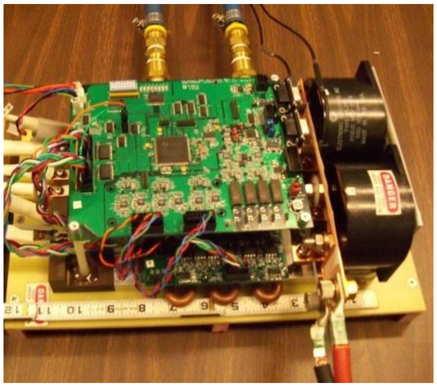

(a) Segmented inverter

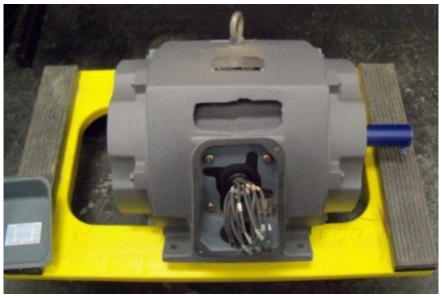

(b) Induction motor

Figure 3-46: Photos of the traction drive inverter and motor used in the integrated charger tests.

Because of its relatively low power rating, the measured ZS resistance of the motor is quite large. The plots in Figure 3-47 show the measured ZS resistance and inductance of the test motor at 60 Hz. The ZS inductance, decreasing from 1.9 to 1.1 mH as the currents increases from 5 to 30 A and the motor cores saturate, is sufficient for the inductor-capacitor filter. Because of its relatively low power rating, the measured ZS resistance of the motor is quite large, around 315 mΩ, compared with those of production EV/hybrid EV motors. For example, the measured ZS resistance of the Toyota Camry motor is 10.75 mΩ. The high-resistance test motor will have a significant impact on the measured charger system efficiency in the following test results.

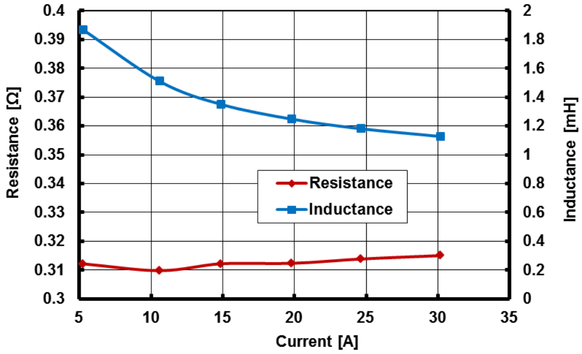

Figure 3-47: Measured ZS resistance and inductance of the test motor.

The charger converter prototype is rated at 5.8 kW and was fabricated using Si power MOSFETs and a planar transformer that has two HV windings and one 14 V printed circuit board (PCB) winding using heavy copper traces. The parasitic capacitances of the MOSFETs are used for zero voltage switching. Figure 3-48 is a photo of the charger converter prototype. All the components are mounted on an aluminum cold plate with a foot print of 6×7 in. Gate driver PCBs are then mounted directly over the MOSFETs to eliminate wire connections between them. In addition, a control PCB using a TI TMS320F1208 fixed-point digital signal processor (DSP) controller located on the top is used to implement the dc bus voltage, grid current, battery charging voltage, and current control blocks.

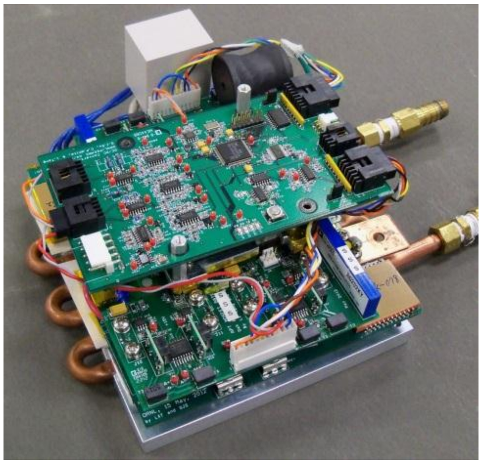

Figure 3-48: Photo of the 5.8 kW Si-based charger converter.

Results

Si-based isolation converter and charger system tests

The charger converter and the segmented traction inverter and test motor were combined to create an integrated OBC, and the whole charging system was tested successfully with a resistive load bank at both 120 and 240 V grid voltages. Representative waveforms are included here to illustrate the operations of the integrated charger. Figure 3-49 and Figure 3-50 show typical operating waveforms of the system with a 120 V input voltage and charging power of 1.0 kW and 2.9 kW, respectively. Figure 3-51 and Figure 3-52 give waveforms of the system with a 240 V grid voltage and charging power of 3.3 and 5.8 kW, respectively.

Figure 3-53 plots measured and estimated system efficiencies of the integrated charger. The estimated efficiency numbers are computed using a ZS resistance of 22 mΩ and considering only the differences in the copper losses. The maximum measured efficiency is 92.9% at a grid voltage of 240 V and 87.0% at 120 V, with respective estimated maximum efficiencies of 94.6 and 92.0%. The fast drop in the measured efficiencies as the input current increases illustrates the impact of the copper losses in the high-resistance motor. It is thus reasonable to expect higher efficiency numbers with production EV/hybrid EV motors, which have much lower stator resistances.

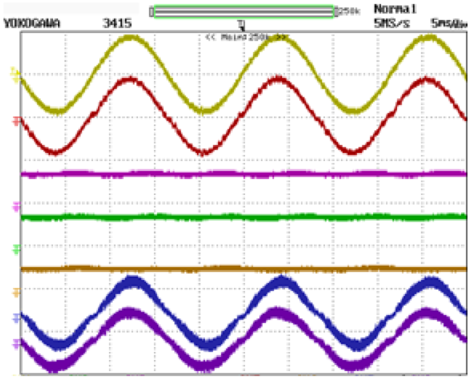

Figure 3-49: Waveforms of the charger system with 120 V input and 2.9 kW charging power. From top, grid voltage (v_s, 200 V/div, CH1), grid current (i_s, 50 A/div, CH5), dc bus voltage (V_{dc}, 500 V/div, CH3), charging voltage (V_{bat}, 500 V/div, CH2), charging current (I_{bat}, 20 A/div, CH6) and motor phase *a1* and *a2* currents (i_{a1}, CH7, i_{a2}, CH8, 20 A/div).

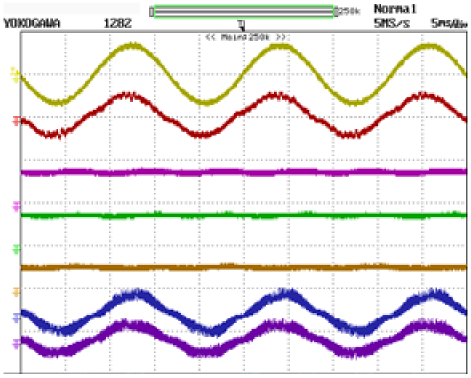

Figure 3-50: Waveforms of the charger system at 240 V input and 3.3 kW charging power. From top, grid voltage (v_s, 500 V/div, CH1), grid current (i_s, 50 A/div, CH5), dc bus voltage (V_{dc}, 500 V/div, CH3), charging voltage (V_{bat}, 500 V/div, CH2), charging current (I_{bat}, 20 A/div, CH6) and motor phase *a1* and *a2* currents (i_{a1}, CH7, i_{a2}, CH8, 20 A/div).

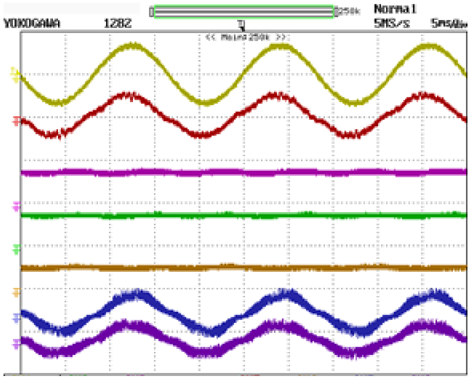

Figure 3-51: Waveforms of the charger system at 240 V input and 3.3 kW charging power. From top, grid voltage (v_s, 500 V/div, CH1), grid current (i_s, 50 A/div, CH5), dc bus voltage (V_{dc}, 500 V/div, CH3), charging voltage (V_{bat}, 500 V/div, CH2), charging current (I_{bat}, 20 A/div, CH6) and motor phase *a1* and *a2* currents (i_{a1}, CH7, i_{a2}, CH8, 20 A/div).

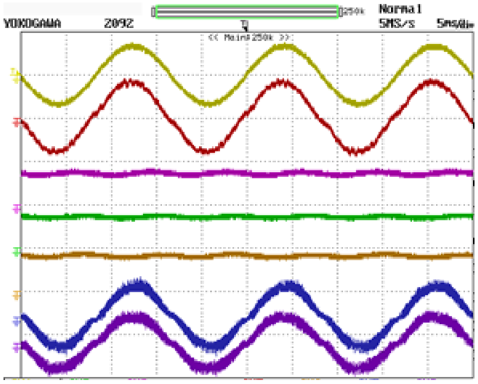

Figure 3-52: Waveforms of the charger system at 240 V input and 5.8 kW charging power. From top, grid voltage (v_s, 500 V/div, CH1), grid current (i_s, 50 A/div, CH5), dc bus voltage (V_{dc}, 500 V/div, CH3), charging voltage (V_{bat}, 500 V/div, CH2), charging current (I_{bat}, 20 A/div, CH6) and motor phase *a1* and *a2* currents (i_{a1}, CH7, i_{a2}, CH8, 20 A/div).

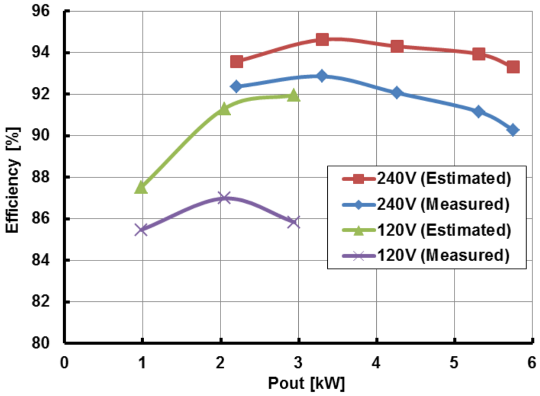

Figure 3-53: Measured and estimated charger system efficiencies at grid voltages of 120 and 240 V.

GaN device tests

For use in high-voltage charger converter designs, 600 V GaN switches manufactured by International Rectifier (IR) and packaged by Delphi were tested and evaluated for static and switching performance. A test board for characterizing the IR GaN switches was designed and fabricated. The test circuit (Figure 3-54) is flexible and can be reconfigured for double-pulse tests to measure switching losses and test loads in a half-bridge configuration for efficiency measurement. The IR devices are packaged in a cascade connection of a normally-on GaN high-electron mobility transistor fabricated on an Si substrate, and a low-voltage Si MOSFET, which makes them operate as normally-off switches.

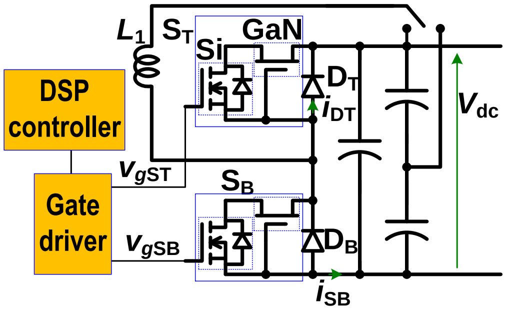

Figure 3-54: IR 600 V GaN switch test circuit.

Figure 3-55 plots typical I-V curves for the IR/Delphi 600 V medium-size GaN switches measured with a curve tracer. The medium-size GaN field-effect transistor has a package size of 1.7×3.1cm and a typical R_{dson}=17 mΩ, translating to a specific on resistance of 89.6 mΩ/cm^2. In comparison, the similarly rated Infineon CoolMOS IPW60R041C6 has a package size of 2.1×1.6 cm and R_{dson}=41 mΩ, resulting in a specific on resistance of 137.8 mΩ/cm^2.

Double-pulse tests were performed with the top switch, S_T, kept off or switched complementarily. Figure 3-56 shows double-pulse test results with S_T kept off and V_{dc}=300 V. Measured switching losses were 275.8 µJ for turn-off and 69.5 µJ for turn-on.

After the double-pulse tests, further experiments were carried out by operating the IR GaN switches in a half-bridge inverter with an inductor load at a dc bus voltage of 320 V and switching frequencies of 100–300 kHz. Figure 3-57 shows typical operation waveforms at a switching frequency of 150 kHz. The estimated efficiency is about 98.5% at 1.8 kVA.

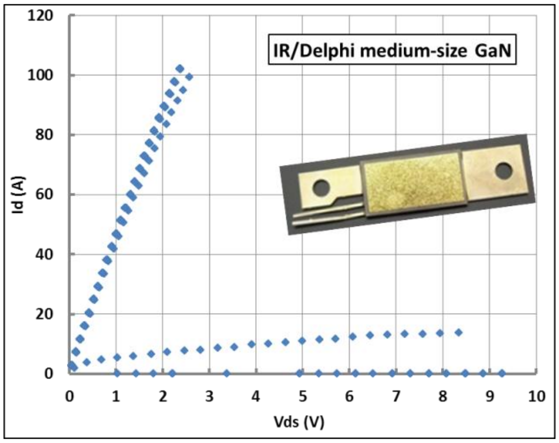

Figure 3-55: Typical I-V curve for IR/Delphi 600 V medium-size GaN switch.

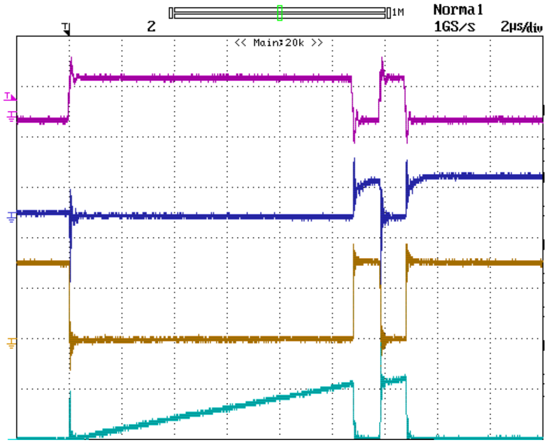

Figure 3-56: Double-pulse test results with S_T kept off. From top, v_{gSB}, 10 V/div; i_{DT}, 50 A/div; v_{DSB}, 200 V/div; i_{SB}, 50 A/div; 2 us/div.

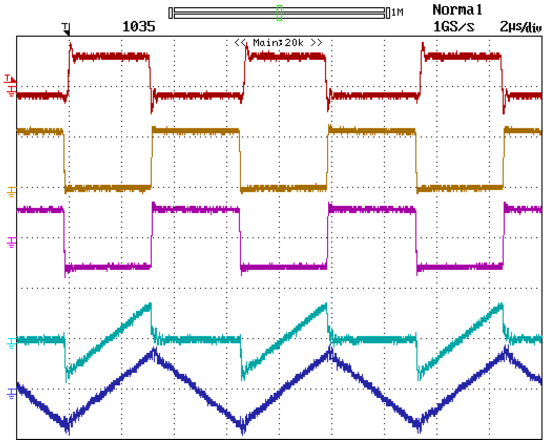

Figure 3-57: IR GaN switch operation waveforms in a half-bridge inverter with an inductor load. From top, v_{gSB}, 20 V/div; v_{DSB}, 300 V/div; v_{out}, 300 V/div; i_{SB}, 100 A/div; i_{L1}, 100 A/div; 2us/div.

6.6 kW SiC-based isolation converter

SiC switch phase-leg modules rated at 1200 V/100 A were fabricated on ORNL-designed direct bond copper substrates using Cree SiC MOSFETs and Schottky barrier diodes and characterized using a Tektronix curve tracer (Figure 3-58).

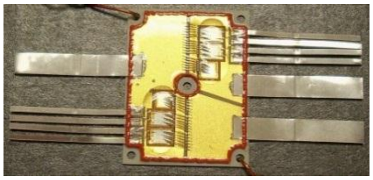

(a) Assembled SiC MOSFET module

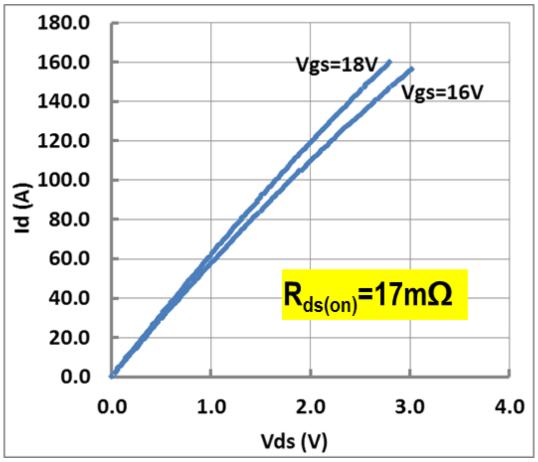

(b) Static characteristics

Figure 3-58: SiC switch phase-leg modules.

Incorporating the results from the simulation study, a power circuit design for a 6.6 kW isolation converter using the ORNL-designed SiC phase-leg modules and planar ferrite cores was completed and a prototype fabricated. Figure 3-59 is a photo of the isolation converter. It comprises a primary switch PCB and its gate driver board, a secondary switch PCB and its gate driver board, a 14 V converter board, a DSP control board (top), and a planar transformer assembly. All the components are mounted on a 7×5 in. heat exchanger.

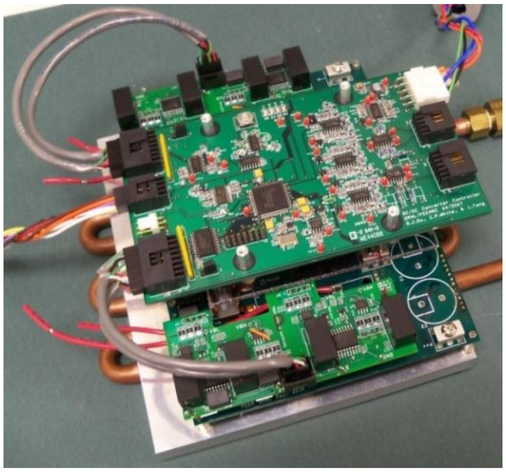

Figure 3-59: Photo of a 6.6 kW SiC isolation converter.

The DSP control board is based on a TI TMS320F2809 chip, which enables high-resolution (HR) PWM (180 ps vs 10 ns for HRPWM-incapable chips) for the more accurate duty/phase shift control that is needed for high-switching-frequency operation. Converter control code was developed that uses the chip's HRPWM hardware for accurate phase shift control under high-switching-frequency operation with WBG devices.

The SiC-based isolation converter prototype was tested with a resistive load bank. Figure 3-60 is a photo of the test setup. A programmable dc power supply was used to power the isolation converter. Operating waveforms were recorded with a digital oscilloscope; and input and output voltages, currents, and power were measured with a digital power meter. Figure 3-61 gives typical operating waveforms, in which V_{dc}, V_{bat}, v_{Tr1}, v_{Tr2}, I_{bat}, and I_{in} are input dc voltage, output dc voltage, transformer primary voltage, transformer secondary voltage, output dc current, and input dc current, respectively.

Figure 3-60: Test setup for the 6.6 kW SiC-based isolation charger converter.

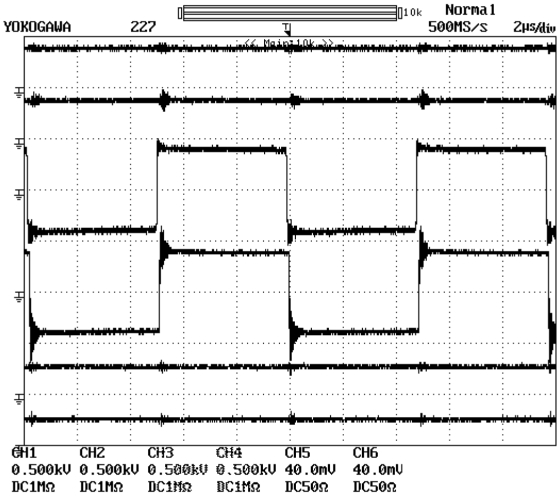

Figure 3-61: Isolation converter operating waveforms showing, from top, input dc voltage, V_{dc}, 500 V/div; output dc voltage, V_{bat}, 500 V/div; transformer primary voltage, v_{Tr1}, 500 V/div; transformer secondary voltage, v_{Tr2}, 500 V/div; input dc current, I_{in}, 40 A/div; and output dc current, I_{bat}; 40 A/div.

Figure 3-62 plots measured isolation converter efficiency vs output power. The efficiencies are greater than 97% for output power levels up to 6.66 kW, and the maximum value is 99.0%.

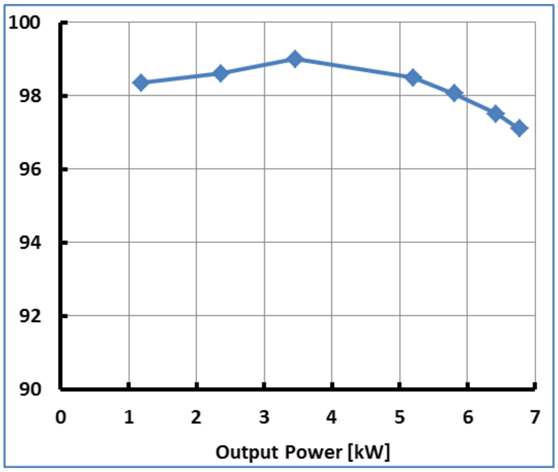

Figure 3-62: Measured efficiency of the 6.6 kW SiC-based isolation charger converter.

Conclusions and Future Directions

This project is aimed at leapfrogging existing Si-based charger technology to address charger and converter cost, weight, volume, and efficiency. It proposes to overcome the limitations of Si semiconductor and magnetic materials by using WBG devices, including SiC and GaN; using advanced magnetic materials; and employing a novel integrated charger architecture and control strategy.

ORNL has developed a new integrated OBC and dc-dc converter architecture that integrates the segmented traction drive, 14 V dc-dc converter, and HV battery charger dc-dc converter. The new topology significantly reduces the number of components (power circuit components alone are reduced by 47%, not counting savings in gate driver and control logic circuits). ORNL has built and tested a 5.8 kW Si-based prototype employing the new topology, which showed a peak efficiency of 94.6% when charged from a 240 V source and 92.0% when charged from a 120 V source. Test results validated the new integrated charger and dc-dc converter architecture and provided a baseline for measuring the benefits of WBG counterparts. ORNL also developed a control strategy for the charger isolation converter to reduce the battery ripple current inherent in single-phase ac-dc converters. Simulation results show the control strategy reduces the ripple current by 60%, enabling a corresponding reduction of the bulky dc link capacitor in the active front end converter.

Emerging GaN devices fabricated on Si substrates are poised to offer significant improvements in charger and dc-dc converters at a cost comparable to that of Si devices. Their enhanced switching speed and reduced switching and conduction losses may enable these switches to minimize passive component requirements, a major driver of cost, weight, and volume in charger and dc-dc converters. ORNL has characterized both low-voltage (<200 V) and high-voltage (600 V) GaN switches and collected valuable design data for hardware development of OBCs and dc-dc converters.

Incorporating the simulation results, ORNL has designed, fabricated, and tested a 6.6 kW isolation converter using the ORNL-designed SiC phase-leg modules and planar ferrite cores. Test results demonstrated efficiencies of greater than 97% with a peak value of 99.0%.

Future work will be directed at designing, building, and testing prototypes for a 6.6 kW SiC OBC, a 6.6 kW GaN isolation converter and OBC, and a 2 kW GaN 14 V converter.

FY 2014 Publications/Presentations

1. G. J. Su and L. Tang, “A new integrated onboard charger and accessory power converter for plug-in electric vehicles,” pp. 4790–4796 in *Proceedings of the 6th IEEE Energy Conversion Congress and Exposition (ECCE 2014)*, Pittsburgh, September 14–18, 2014.
2. G. J. Su, “Innovative technologies for dc-dc converters and on-board chargers,” presented at the DOE Vehicle Technologies Program Advanced Power Electronics and Electric Motors R&D FY 2014 Kickoff Meeting, November 5–7, 2013.
3. G. J. Su, “WBG converters and on-board charger,” presented at the 2014 DOE Hydrogen and Fuel Cells Program and Vehicle Technologies Program Annual Merit Review and Peer Evaluation Meeting, June 16–20, 2014.

References

1. G. J. Su and L. Tang, “A segmented traction drive system with a small dc bus capacitor,” pp. 2847–2853 in Proceedings *of the 4th IEEE Energy Conversion Congress and Exposition (ECCE 2012)*, Raleigh, North Carolina, September 16–20, 2012.
2. Datasheet: http://www.infineon.com/cms/en/product/mosfets/power-mosfets/n-channel-mosfets-coolmos-tm-500v-900v/IPW60R041C6/productType.html?productType=*db3a304426e7f13b0127f2050dcb45ac*.

3.4 Cost-Effective Fabrication of High-Temperature Ceramic Capacitors for Power Inverters

U. (Balu) Balachandran (Principal Investigator)

Argonne National Laboratory
9700 S. Cass Avenue
Argonne, IL 60439
Phone: (630) 252-4250; Fax: (630) 252-3604
Email: balu@anl.gov

Susan A. Rogers, Program Manager
Phone: (202) 586-8997; Fax: (202) 586-1600
E-mail: Susan.Rogers@ee.doe.gov

Steven Boyd, Program Manager
Phone: (202) 586-8967; Fax: (202) 586-1600;
E-mail: Steven.Boyd@ee.doe.gov

Subcontractors:
Delphi Electronics & Safety Systems
2151 E. Lincoln Road, Kokomo, IN 46904

Sigma Technologies International
10960 N Stallard Place, Tucson, AZ 85737

Pennsylvania State University
201 Old Main, University Park, PA 16802

Start Date: October 2013
Projected End Date: September 2016

Objectives

- Develop an efficient, cost-effective process for fabricating compact, high-temperature, Pb-La-Zr-Ti-O (PLZT)-based DC-link capacitors for advanced power inverters in electric drive vehicles.

Technical Barriers

This project addresses the overall size, cost, and high-temperature operability barriers of the presently used polymer-based capacitors in automotive power inverters. Current DC bus capacitors occupy a significant fraction of volume (≈35%), weight (≈23%), and cost (≈23%) of the inverter module, cannot tolerate temperatures >85°C, and suffer from poor packaging, and inadequate reliability. Traditional capacitor architectures with conventional polymer-based dielectrics cannot adequately meet all of the performance goals for capacitance density, weight, volume, and cost. There is a need for the development of capacitors that has potential to reduce size, weight, and cost, concomitant with increased capacitance density and high temperature operation.

Technical Targets

- Achieving APEEM targets for capacitance density, weight, volume, and cost requires a dielectric material that has high permittivity, shows good performance at high temperature, can be packaged in an architecture with high volumetric efficiency, and exhibits benign failure.
- Technical targets of this project is to develop an economically attractive fabrication process to make PLZT-based dielectric films with permittivity (k) that is ≈30 times that of presently used polymer-based film capacitors over the temperature (-40°C to +140°C), voltage (450 V nominal) and frequency (≈10 kHz) ranges required for automotive power electronics.

Accomplishments

- Demonstrated in a previous project that a spin-coating process produces PLZT films that satisfy high-temperature and volumetric efficiency requirements for advanced capacitors; however, the spin-coating process is not practical for mass production of large area capacitors.
- Aerosol deposition, a high-rate, room-temperature film deposition process, is being developed at Argonne to reduce the PLZT capacitor's cost.
- Developed solution chemistry and synthesized and characterized PLZT submicron powders required for high-rate deposition process.
- Deposited ≈8-μm-thick PLZT film on aluminum metallized polyimide films using AD process in significantly shorter time (≈10 min. vs. 5 days by spin-coating process).
- Measured mean breakdown voltage of 860 V on ≈8-μm-thick PLZT capacitor fabricated on metallized polyimide film using AD process.
- Demonstrated graceful failure mode by self-clearing method in single layer PLZT films.
- Established materials cost targets to meet the APEEM requirement.
- Published three papers in peer reviewed international journals, presented results at seven scientific conferences, awarded on patent, and published two patent applications in FY14.

✧ ✧ ✧ ✧ ✧

Introduction

Capacitors are essential for carrying out a host of functions in pulse power and power electronics applications such as pulse discharge, filtering, voltage smoothing, coupling, de-coupling, DC blocking, power conditioning, snubbing, electromagnetic interference suppression, and commutation in power electronics. They are a critical component of power inverter modules within electric drive vehicles (EDVs) and their performance directly affects fuel efficiency and battery life. Capacitors occupy ≈35% of the inverter volume and account for ≈23% of the weight in current designs. Thus, even if all other components in an inverter are reduced significantly, the capacitor requirement is a serious impediment to achieving the required volume and weight reduction. In addition, the use of high-temperature coolants further exacerbates the situation because existing film capacitors lose their capability to absorb ripple currents at elevated temperatures, necessitating the addition of extra capacitors. Increasing the volumetric performance (capacitance per unit volume) of DC bus capacitors is required, and their maximum operating temperature also must be increased to assure reliability requirements. Ceramic capacitors have the greatest potential for volume reduction; they could be as small as 35% of the volume of a polymer-based capacitor currently used in EDVs. Ceramics offer high dielectric constants and breakdown fields and, therefore, high energy densities. They also can tolerate high temperatures with a low equivalent series resistance (ESR), enabling them to carry high ripple currents even at elevated temperatures, although the capacitance may vary strongly with temperature.

Driven by the increasing demand for passive power electronics with improved performance, high reliability, and reduced size and weight, much attention has been paid to the so-called “film-on-foil” technology, in which ceramic films deposited on metal foils are embedded into a printed circuit board (PCB). Our research [1–4] had shown that the lead lanthanum zirconate titanate ($Pb_{0.92}La_{0.08}Zr_{0.52}Ti_{0.48}O_3$, PLZT) films deposited on base metal foils possess excellent dielectric properties even at high temperatures, which are promising for high power applications such as inverters in electric drive vehicles. Use of base-metal foils reduces the cost of the capacitor. The PLZT-based capacitors significantly reduces component footprint, improves device performance, provides greater design flexibility, and offers an economic advantage for commercialization. This technology will achieve the high degree of packaging volumetric efficiency with less weight.

In power electronics, capacitors with high capacitance are required to work under high voltages. This requirement imposes the additional challenge of fabricating thicker (>5 µm) films. However, due to the well-known critical thickness effect, per-layer thickness that can be achieved by conventional sol-gel method is generally limited to ≈0.1 µm, thus making the conventional method less attractive to industry when thicker films are needed to meet the operation voltage requirement. The spin-coating process is simply impractical on an industrial scale. A high-rate aerosol deposition (AD) process being developed at Argonne can produce thick PLZT films with desirable high voltage properties at significantly shorter time. AD process can produce dense ceramic films at room temperature without the needs for high temperature sintering; thus making the process amenable for depositing the PLZT films on variety of substrates such as polymer, glass, and metal foils. Therefore, it is a cost-effective method for manufacturing ceramic film capacitors for power inverters in electric drive vehicles.

In this project, the team will collaborate to develop a high-rate, economically attractive AD manufacturing process to produce PLZT-based DC-link capacitors with dielectric properties suitable for power inverter applications. In this report, some of the results obtained on PLZT films prepared by the spin-coating process that are relevant to the development of high-rate AD process are also included.

Our R&D efforts focus on examining the underpinning issues of PLZT capacitor performance and reliability, making dense and thicker films, fabricating high-voltage-capable PLZT capacitors defined by the inverter application requirements, establishing robust fabrication protocols that are commercially and economically viable, and transferring the technology to Sigma Technologies for manufacturing.

Approach

Develop high-rate deposition process to economically make high-dielectric constant, high-temperature, low-cost ferroelectric PLZT dielectric films on thin metal and polymer substrates. Ferroelectric ceramics possess high dielectric constants, breakdown fields, and insulation resistance. With their ability to withstand high temperatures, they can tolerate high ripple currents at under-the-hood conditions. High-dielectric constant materials significantly reduce component footprint, improve device performance, provide greater design and packaging flexibility, achieve high degree of volumetric efficiency with less weight, and offer an economic advantage. A high-rate, room-temperature deposition process, aerosol deposition (AD), has been identified as an economically attractive process to make PLZT-based capacitors. PLZT capacitors made by AD process were evaluated to provide feed-back for process optimization. Future effort will be focused on optimizing the AD process parameters to fabricate high-voltage capable thicker PLZT films with uniform thickness and transfer the AD process to Sigma Technologies’ roll-to-roll deposition system, fabricating a DC-link capacitor using roll-to-roll produced films, and demonstrating a DC-link capacitor with an automotive power inverter.

Results

In our previous project we developed a core technology for fabricating PLZT on metallized silicon and $LaNiO_3$ (LNO) buffered Ni foils by a chemical solution deposition (CSD) process [5]. CSD precursor solutions were synthesized and films were deposited by spin coating. Platinized silicon (PtSi) substrates were cut from premium-grade <100> oriented silicon wafers of ≈375-μm-thick silicon with 500-nm-thick thermally oxidized silicon dioxide coated with 20-nm-thick titanium and 200-nm-thick platinum. High purity (99.98% pure) nickel substrates of 25-mm-square and 0.4-mm-thick were polished by chemical-mechanical planarization (CMP) process and coated with ≈0.4-μm-thick LNO buffer prior to the deposition of PLZT by CSD. The detailed procedures were reported elsewhere [5,6].

Figure 3-63 shows the 2θ X-ray diffraction (XRD) patterns measured on ≈2-μm-thick PLZT films deposited on LNO/Ni and PtSi substrates. The patterns indicate that both samples are well crystallized without preferred orientation. All peaks can be indexed accordingly (JCPDS 56-0900). The use of LNO buffer layer effectively reduces the crystallization temperature and facilitates the formation of pyrochlore-free PLZT phase [7,8]. The LNO also compensated for the roughness of the Ni foil and provided a smooth interface for the PLZT film to grow on. Diffraction peaks from the nickel substrate and the LNO buffer film can be identified from the diffraction pattern shown in Figure 3-63a. The small peak at 2θ ≈36° on the XRD pattern for PLZT grown on PtSi (Figure 3-63b) is from Cu-K$_\beta$ diffraction of Pt (111). No crack or delamination was observed from microscopic analysis [5]. A close look at the two diffraction patterns in Figure 3-63 revealed that the PLZT peaks in Figure 3-63a shifted to lower angle compared to those peaks for the same index shown in Figure 3-63b. With the regular θ-2θ scan configuration, diffraction patterns are taken on these crystallites with the diffraction plane parallel to the substrate surface. According to Bragg's equation, a peak shift to lower 2θ angle indicates an expansion of d-spacing in the out-of-plane direction, which is a result of compressive strain in the in-plane directions that are parallel to the substrate surface. Residual stress analysis by XRD indicated compressive stress in the PLZT grown on LNO-buffered nickel substrate, and tensile strain in the PLZT grown on PtSi substrate, as a result of the difference in the coefficients of thermal expansion (CTE).

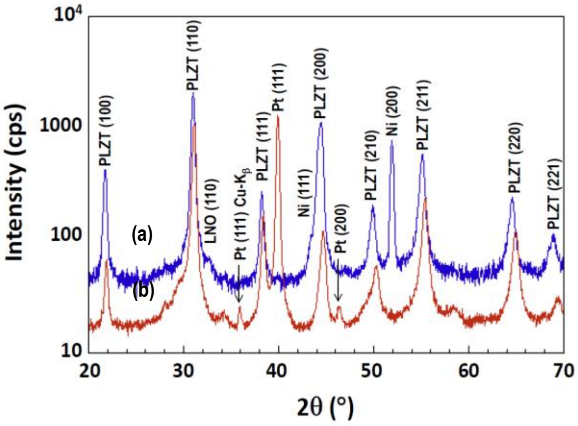

Figure 3-63: XRD patterns of PLZT deposited on (a) LNO/Ni and (b) PtSi substrates.

To determine residual stress in the PLZT films grown on LNO-buffered nickel and PtSi substrates, we measured XRD patterns with various tilt angles. Such residual stress in the PLZT films can be determined from XRD data collected under various tilt angles using the following equation [9],

$$\sigma_{\phi} = \left(\frac{E}{1+\nu}\right)_{(hkl)} \cdot \frac{1}{d_{\phi 0}} \cdot \frac{\partial d_{\phi\psi}}{\partial \sin^2 \psi} \qquad (1)$$

where E and ν are Young's modulus and Poisson ratio of the thin film, $d_{\phi 0}$ and $d_{\phi\psi}$ are the lattice d-spacing in a stress-free sample and d-spacing measured in a stressed sample that was tilted at angle ψ, respectively. Young's modulus E = 72 GPa and Poisson ratio ν = 0.30 [10,11] were used in calculation of residual stress in the PLZT films. We collected XRD patterns at various rotation angles (ϕ = 0°, 45°, and 90°) and observed no measurable difference. This finding indicates that crystallites in the polycrystalline films are randomly oriented. Figure 3-64 shows lattice d-spacing as a function of sin2θ measured using XRD data on PLZT films grown on LNO/Ni and PtSi substrates. Data obtained from PLZT (211) and (220) diffraction peaks are plotted in Figure 3-64a and Figure 3-64b, respectively. Slopes determined from linear fitting to the data were plugged into Eq. 1 to determine the residual stresses in the PLZT films. We measured compressive stress of ≈370 MPa and tensile stress of ≈250 MPa, respectively, for ≈2-μm-thick PLZT films grown on LNO buffered Ni and PtSi substrates. Our measurements of residual stresses are in good agreement with those reported for PZT films [10].

Figure 3-65a shows the dielectric constant and loss as a function of bias field measured at room temperature for samples of PLZT grown on LNO/Ni and PtSi substrates. The data conformed to butterfly-shaped curves, which are typical for ferroelectric materials measured below the Curie temperature. At zero bias, a dielectric constant of ≈1300 and dielectric loss of ≈0.06 were measured for PLZT grown on LNO/Ni substrate, and a dielectric constant of ≈1350 and dielectric loss of ≈0.05 were found for samples deposited on PtSi substrates. Since both samples have PLZT films of the same thickness (≈2 μm) but grown on different substrates, they exhibit different field-dependent change, i.e., "tunability," which can be expressed as,

$$\eta = \left[1 - \frac{\varepsilon_r(E)}{\varepsilon_r(0)}\right] \times 100\% \qquad (2)$$

where ε_r(E) is the dielectric constant in the presence of an external field E. We observed a tunability of ≈55% and ≈40% at room temperature under 100 kV/cm applied field for PLZT deposited on LNO/Ni and PtSi substrates, respectively.

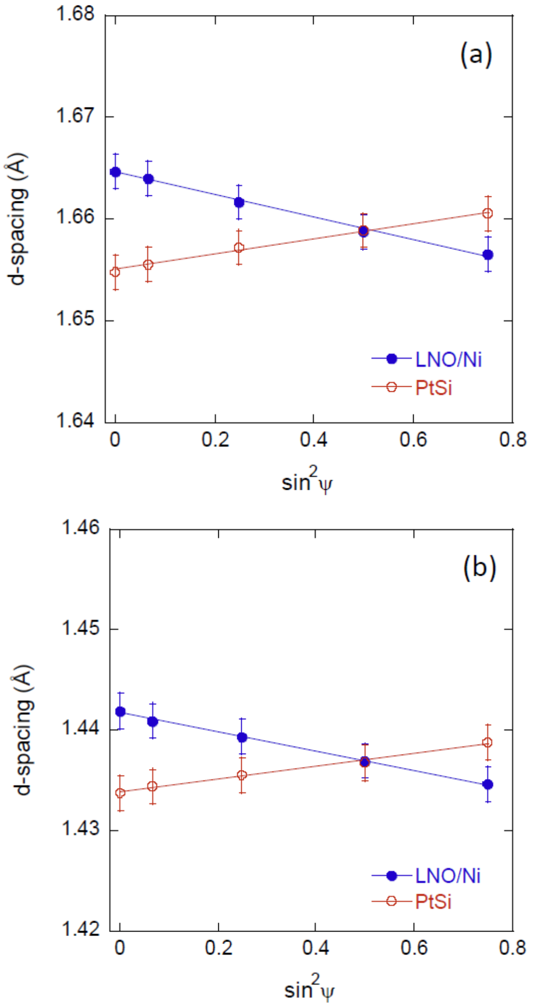

Figure 3-64: Lattice d-spacing as a function of sin$^2\psi$ measured from (a) PLZT (211) and PLZT (220) diffraction peaks.

The difference in tunability can be attributed to difference in residual stress for PLZT films deposited on different substrates. Because the dipoles in PLZT film under compressive stress have better tendency of getting aligned in the out-of-plane direction, the dipole momentum exhibits greater change collectively under a specific small change in applied field (or near zero-field); but under high applied field, dipoles are more clamped and dipole momentum is more difficult to change. This is also the reason why we measured sharper peaks in the butterfly curve of dielectric constant as a function of applied field for PLZT deposited on LNO/Ni substrate and broader peaks for PLZT on PtSi substrate. Figure 3-65b shows the dielectric constant and loss measured as a function of frequency for PLZT deposited on LNO/Ni and PtSi substrates. The dielectric constant decreases while dielectric loss increases with increasing frequency above 10^5 Hz for both samples. No obvious differences were observed between the PLZT films deposited on LNO/Ni and PtSi substrates even though they have different stress levels.

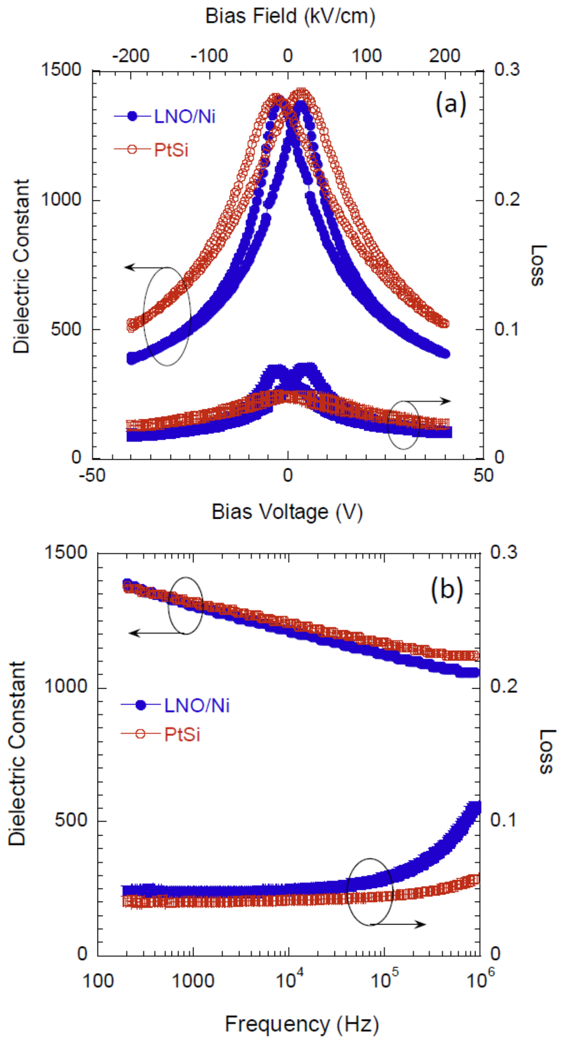

Figure 3-65: (a) Field and (b) frequency dependent dielectric properties of PLZT films deposited on LNO/Ni and PtSi substrates.

Figure 3-66 shows the polarization-electric field (P-E) hysteresis loops measured at room temperature on ≈2-μm-thick PLZT films deposited on LNO/Ni and PtSi substrates. Both samples were coated with Pt top electrodes and measured using a field sweeping period of 10 ms (frequency of 100 Hz). From the P-E loop with a maximum applied voltage of 50 V (corresponding to an electric field of 250 kV/cm), we measured a remanent polarization (P_r) of ≈23.5 μC/cm^2 and ≈7.4 μC/cm^2, and coercive electric field (E_c) of ≈25.6kV/cm and ≈21.1 kV/cm, for PLZT films grown on LNO/Ni and PtSi substrates, respectively. Even though PLZT films deposited on LNO/Ni substrates exhibit comparable coercive field compared to those grown on PtSi substrates, they display substantially higher remanent polarization. This difference in P-E loops can be attributed to the residual stress in PLZT films. Lee et al. [12] reported that both remanent polarization and saturation polarization decrease with an increase in tensile residual stress and increase with an increase in compressive stress (decrease in tensile stress), as in-plane compressive stress is beneficial to dipole alignment along the out-of-plane direction that is parallel to the applied field. Our experimental results revealed similar trend.

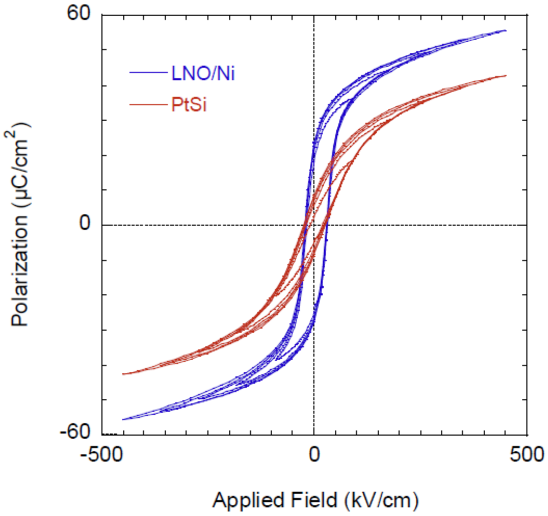

Figure 3-66: P-E hysteresis loops measured at room temperature on PLZT films deposited on LNO/Ni and PtSi substrates.

Sub-coercive field amplitude sweeps were performed as a function of frequency to investigate domain wall movements in the PLZT films deposited on LNO/Ni and PtSi substrates. The real part of permittivity (ε') increases with increasing AC field amplitude and decreases with increasing frequency. It exhibits good linear dependence on the logarithm of frequency, as shown in Figure 3-67, indicating that extrinsic factors such as motions of defect charge species and domain wall movement are the contributing factors to the polarization under low applied AC field. To quantitatively assess the contribution of the extrinsic effect on permittivity, we fitted ε' as a function of oscillation field amplitude E_0. As shown in Figure 3-67 insets, data measured at three frequencies (1 kHz, 10 kHz, and 100 kHz) fit well to the Rayleigh law [13],

$$\varepsilon' = \varepsilon'_{init} + \alpha' \cdot E_0 \tag{3}$$

where ε', ε'_{init}, α', and E_0 are the real permittivity, initial (zero-field) permittivity, irreversible Rayleigh coefficient, and the applied AC oscillation field amplitude, respectively. It is worth noting that ε'_{init} consists of a combined reversible and intrinsic component to permittivity. The corresponding Rayleigh parameters derived from least square fitting of the experimental data to Eq. 3 are summarized in Table 3-1 for PLZT deposited on LNO/Ni and in Table 3-2 for PLZT deposited on PtSi substrate, respectively.

Table 3-1: Rayleigh parameters of ≈2-μm-thick PLZT films deposited on LNO/Ni substrates.

Frequency (kHz)	α' (cm/kV)	ε'_{init}	$\alpha' / \varepsilon'_{init}$ (cm/kV)
1	35.2	1294	0.027
10	26.9	1214	0.022
100	18.6	1136	0.016

Table 3-2: Rayleigh parameters of ≈2-μm-thick PLZT films deposited on platinized silicon substrates.

Frequency (kHz)	α' (cm/kV)	ε'_{init}	$\alpha' / \varepsilon'_{init}$ (cm/kV)
1	14.8	1413	0.010
10	13.1	1318	0.010
100	10.7	1242	0.009

The ratio of irreversible to reversible contributions to dielectric nonlinearity ($\alpha' / \varepsilon'_{init}$) that we measured for ≈2-μm-thick PLZT deposited on PtSi substrates is in agreement with the reported literature values of 0.011 to 0.027 cm/kV for ≈2-μm-thick PZT films grown on PtSi substrates [13–15]. Bintachitt et al. investigated the nanoscale and mesoscopic disorder and associated local hysteretic responses in polycrystalline ferroelectric films and reported that large-scale collective domain wall dynamics, as opposed to motion of noninteracting walls, underpins Rayleigh behavior in disordered ferroelectrics [15]. Bastani et al. reported the effect of PZT film thickness on dielectric nonlinearity [14]. They found the existence of a critical film thickness ≈50 nm below which the extrinsic contributions to the dielectric response are almost completely suppressed. Dielectric nonlinearity increases with film thickness because of increased interaction and collective movement of the domain walls [15]. The ratio of irreversible to reversible contributions we measured for PLZT deposited on LNO buffered Ni substrate is about twice as much higher than observed for PLZT deposited on PtSi substrates. This difference can be attributed to their difference in strain states; PLZT grown on LNO/Ni bears ≈370 MPa compressive stress while PLZT on PtSi endures ≈250 MPa tensile stress. Compressive strain in PLZT films leads to enhanced polarization alignment and increased interaction among domain walls; therefore, strengthened collective motion of domain walls under AC oscillation field.

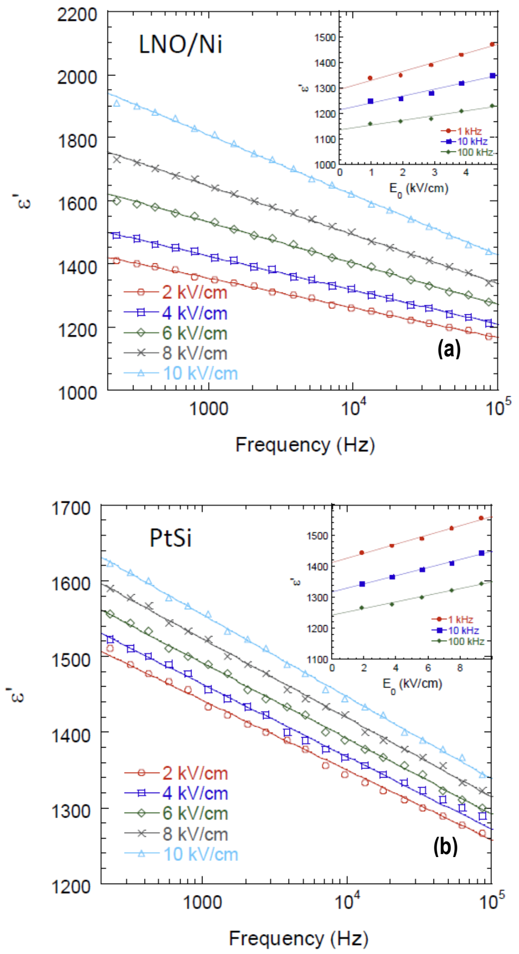

Figure 3-67: Frequency dependent dielectric constant of PLZT films deposited on (a) LNO/Ni and (b) PtSi substrates measured with various oscillation signal amplitudes; data plotted as function of oscillation signal amplitude are shown in corresponding insets.

Figure 3-68 shows the Weibull plot of breakdown field strength obtained at room temperature from 30 capacitor samples of PLZT deposited on LNO/Ni and another 30 capacitor samples of PLZT deposited on PtSi substrates. The solid straight line is a least-square fitting to the two-parameter distribution function [16,17]. We measured mean breakdown field strengths of 2.6 MV/cm and 1.5 MV/cm for PLZT grown on LNO/Ni and PtSi, respectively. Figure 3-68 inset illustrated the correlation between residual stress and PLZT film breakdown strength. Breakdown strength increases with decrease in tensile stress (or increase in compressive stress). When an electrical potential is applied between the top and the bottom electrodes, the electrostrictive strain causes expansion in the longitudinal direction (same direction as the applied electric field) and contraction in the radial direction (film in-plane direction). This condition leads to reduction in the overall compressive stress and/or addition in the overall tensile stress in PLZT films that are subjected to the applied field.

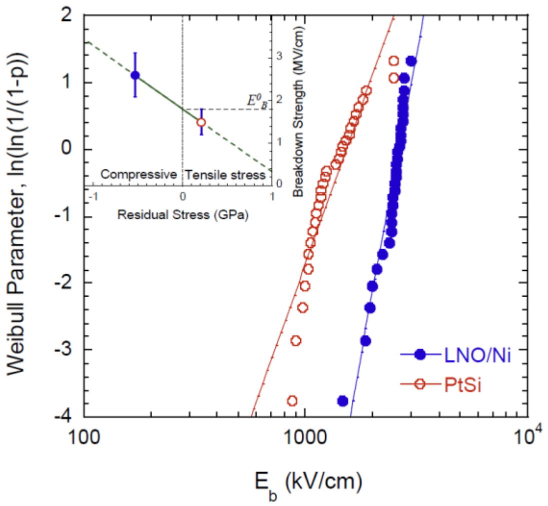

Figure 3-68: Weibull plot for breakdown field strength of PLZT deposited on LNO/Ni and PtSi substrates, inset illustrated the correlation between breakdown strength and residual stress.

A “stress-free” breakdown strength (E_B^0) can be defined to facilitate the understanding of breakdown strength characteristics in PLZT films that are enduring residual stresses. When there is a preexisting tensile residual stress in a PLZT film, such as the one grown on a PtSi substrate, it needs less additional tensile strain to reach the threshold strain value that will cause dielectric breakdown. Therefore, this sample bearing residual tensile stress needs only an electric field of E_B^0 - ΔE_1 (with $\Delta E_1 > 0$) to reach the breakdown threshold value. For PLZT grown on LNO/Ni substrate, due to the existing compressive stress, additional field strength ΔE_2 is required to compensate the residual compressive strain. In other words, for the film to reach the threshold tensile strain level value that will cause dielectric breakdown, a total electric field of E_B^0 + ΔE_2 (with $\Delta E_2 > 0$) must be applied. For this reason, we observed higher mean breakdown strength in PLZT films deposited on LNO/Ni compared to those deposited on PtSi substrates. This difference in breakdown strength is a direct result of the difference in residual stresses in these two types of samples. As illustrated in Figure 3-68 inset, E_B^0 can be determined from the intersection between the solid line to the vertical line going through residual stress of zero. E_B^0 , known as stress free breakdown strength, was found to be ≈1.8 MV/cm for the ≈2-μm-thick PLZT films grown by chemical solution deposition process. The stress coefficient of breakdown strength, determined from the slope of the solid line, was found to be -0.15 V·m/N. Therefore, it is beneficial to have a compressive residual stress in ferroelectric PLZT films for applications requiring high breakdown field strength.

The research done in this phase of the project demonstrated that the dielectric constant of spin-coated PLZT film is ≈30 times that of the currently used polypropylene-based materials over the temperature, voltage and frequency ranges required for automotive power electronics. PLZT's temperature capability also meets or exceeds the temperature requirement for today's automotive environment; however, the spin coating process requires over thirty depositions, more than thirty annealing steps, and many hours to produce a simple 3-µm-thick PLZT coating suitable for a capacitor. The spin-coating process is simply impractical on an industrial scale. Therefore, effort was focused on developing a high-rate deposition process. We have identified aerosol deposition (AD) as a high-rate deposition process to fabricate PLZT films. During AD, PLZT particles are accelerated toward the substrate and, if their speed exceeds a critical value, the particles consolidate upon impact without additional heating of the substrate. Because AD is done without heating the substrate, flexible materials such as polymers, plastics, thin metal foils, glass, etc. can be used as the substrate. By using flexible substrates, PLZT-based capacitors can be produced in a wound configuration, which would allow EDT's requirement of benign failure to be engineered for the capacitor.

Recent work at Argonne demonstrated that a ≈8-µm-thick PLZT film can be prepared in about 10 minutes by AD process. Sample of similar thickness deposited by spin-coating process would take about five days to make. A photograph of the aerosol deposition system at Argonne is shown in Figure 3-69.

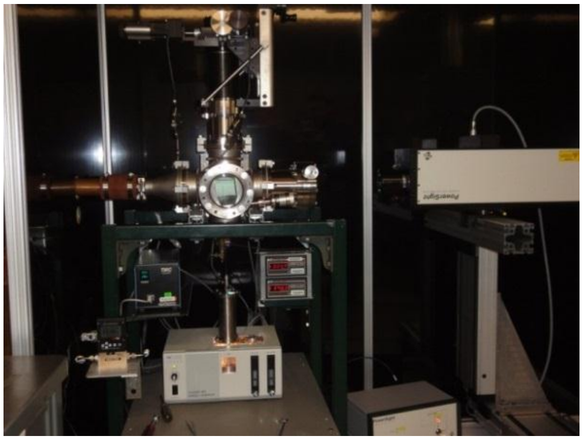

Figure 3-69: Photograph of the aerosol deposition system at Argonne National Laboratory.

Figure 3-70 shows photographs of an aluminum metallized polyimide sheet (Figure 3-70a) and a ≈8-µm-thick PLZT film deposited by AD process on aluminum metallized polyimide film (Figure 3-70b). This ≈8-µm-thick PLZT film was deposited at room temperature in about 10 minutes.

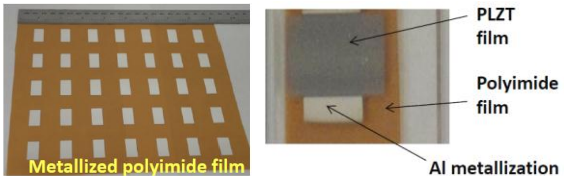

(a) (b)

Figure 3-70: Photographs of (a) metallized polyimide film and (b) PLZT film deposited on metallized polyimide by AD process.

The PLZT powder was prepared using an aqueous solution made from Ti citrate and nitrates of Pb, La, and Zr. Concentrations of the cations are in the range 0.1-2.0 moles/liter. A fuel [e.g., citric acid ($C_6H_8O_7$), glycine ($C_2H_5NO_2$), or hydrazine (N_2H_4)] is added to the nitrate solution. Ammonium nitrate is added to the solution to adjust the fuel to oxidant ratio, which affects the combustion characteristics (i.e., the peak temperature during combustion and the speed of combustion). Fuel to oxidant ratios in the range 2:1 to 1:2 are used in the preparation of the PLZT powder used for aerosol deposition. The solution is heated to drive off water and initiate combustion. In order to prevent segregation of individual components as the water is removed, the fuel/nitrate solution is either poured into a beaker that is pre-heated on a hot plate or sprayed as a fine mist into a furnace that is pre-heated to 300–900°C. After synthesis, the PLZT powder is milled with ZrO_2 media in a volatile solvent (e.g., isopropyl alcohol) to produce the desired particle size. XRD pattern of the as-prepared powder is shown in Figure 3-71.

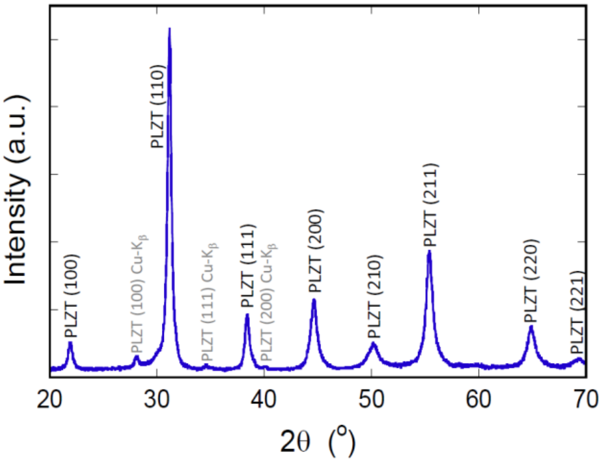

Figure 3-71: X-ray diffraction pattern of PLZT powder used in the AD process.

SEM image of the surface of a PLZT film deposited by AD process is shown in Figure 3-72. Average particle size of the ceramic powder used for aerosol deposition is ≈500 nm, as shown in Figure 3-73. However, during the deposition, only those particles floated by gas stream are carried to the nozzle in the deposition chamber. Particles reaching the aerosol nozzle are typically smaller in size than those in the original powder [18]. This is likely due to the fact that transferred particles collide inside transport line, and thus smaller particles are produced before arriving at the deposition nozzle. As shown in the SEM image (Figure 3-72), PLZT particles of ≈200 nm are observed on the top surface of the PLZT film made by AD process.

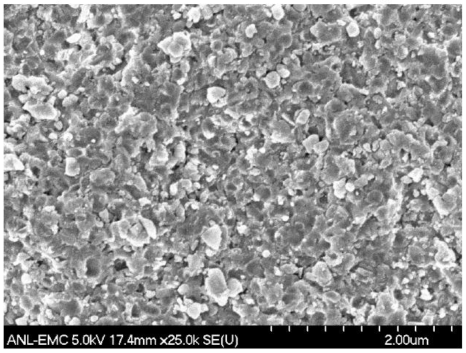

Figure 3-72: Surface view SEM image of the PLZT film deposited by AD process.

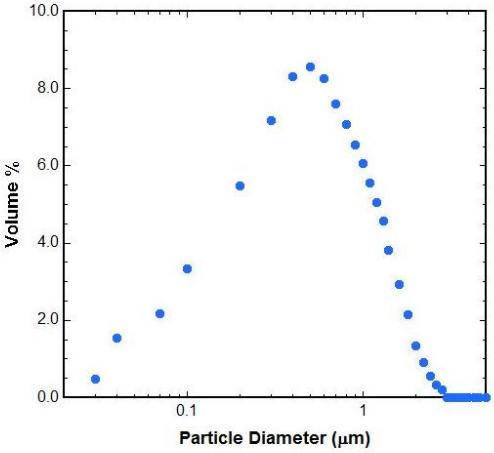

Figure 3-73: Particle size distribution of the powder used for deposition of PLZT films by AD process.

Figure 3-74 shows cross-sectional view SEM micrograph of a ≈8-μm-thick PLZT film deposited on PtSi substrate by AD process. As show by the cross-sectional SEM, the highly dense and uniform ceramic film is made of close-packed particulates that collided at high speed and fused together upon arrival at the substrate surface. The as-deposited film is polycrystalline, as illustrated by the X-ray diffraction pattern in Figure 3-75. Unlike the amorphous films made by CSD process which require high temperature annealing to form the desirable crystalline structure to offer good dielectric properties, the as-deposited AD films already exhibit excellent dielectric properties that are suitable for many applications.

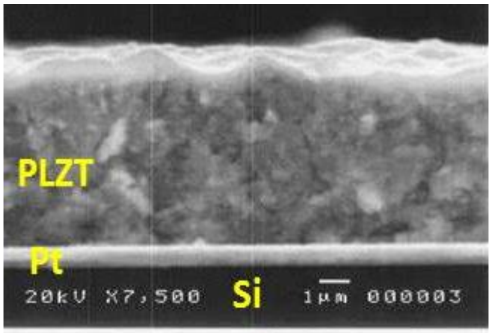

Figure 3-74: Cross-sectional view SEM image of PLZT film deposited by AD process.

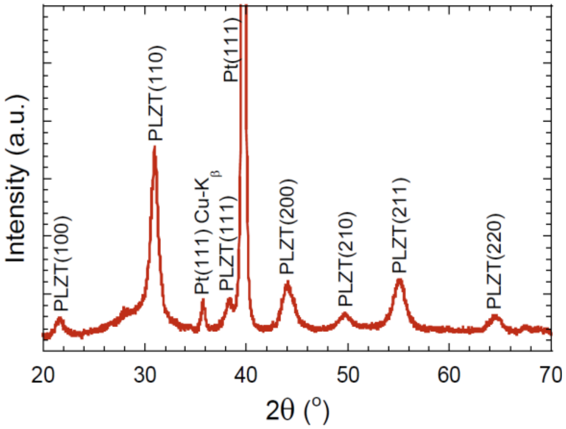

Figure 3-75: X-ray diffraction pattern of a ≈3-μm-thick PLZT film grown on PtSi substrate by AD process.

Figure 3-76 shows frequency dependent dielectric property measured on a ≈8-μm-thick PLZT film grown on aluminum metallized polyimide film by AD process. As shown in the figure, both dielectric constant and dielectric loss decrease slightly with increasing frequency from 100 Hz to 100 kHz. At room temperature and 10 kHz, we measured dielectric constant of ≈82 and dielectric loss of ≈0.016.

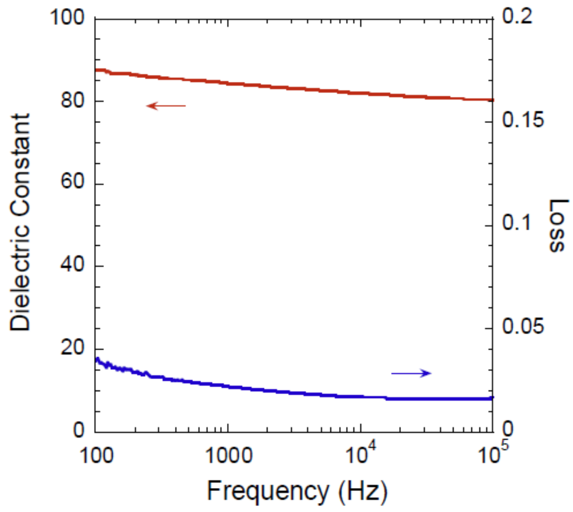

Figure 3-76: Frequency dependent dielectric properties of a ≈8-µm-thick PLZT film deposited on aluminum metallized polyimide film by AD process.

Figure 3-77 shows the dielectric properties measured at room temperature as a function of applied bias field for a ≈8-µm-thick PLZT film capacitor grown by AD process on aluminum metallized polyimide film. Dielectric constant exhibits weak dependence while dielectric loss is nearly independent of bias field. With 300 V bias, we measured dielectric constant of ≈80 and loss <0.02 at room temperature. This dielectric constant value, under high electric field, is more than 30 times higher than that of the polymer dielectrics (dielectric constant of ≈2.2) that are currently used in power inverters. Our results demonstrate the great potential of PLZT-based capacitors meeting EDT power inverter specifications.

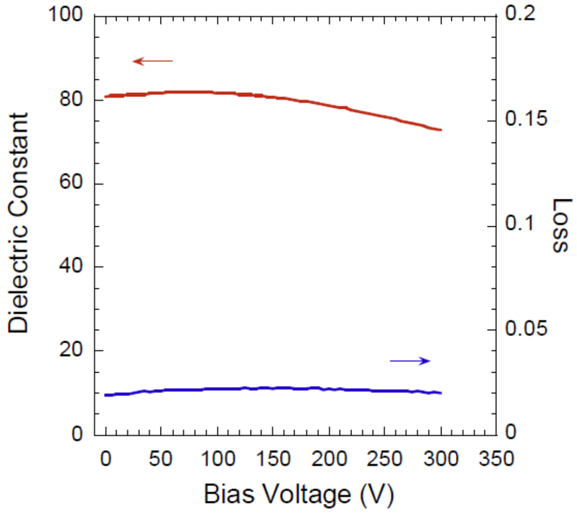

Figure 3-77: Field dependent dielectric properties of PLZT film capacitor deposited by AD process.

Figure 3-78 shows the polarization-electric field (PE) hysteresis loop measured at room-temperature for a ≈8-µm-thick PLZT film capacitor deposited on aluminum metallized polyimide film by AD process. It exhibits paraelectric behavior. A recoverable energy density of 5.9 J/cm was observed from the hysteresisloop measurements, as shown by the shaded area in Figure 3-78.

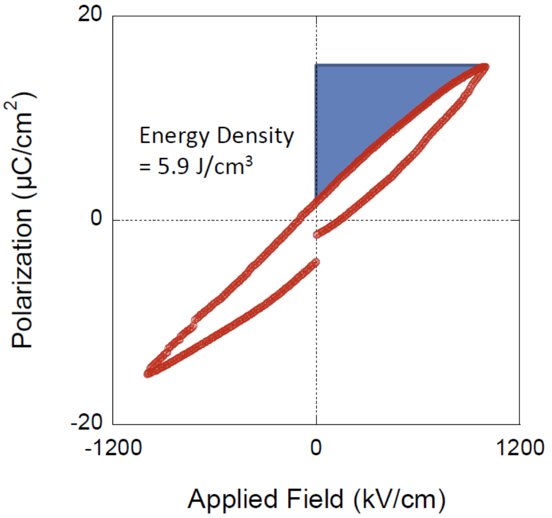

Figure 3-78: PE hysteresis loop of a ≈8-µm-thick PLZT film capacitor deposited on aluminum metallized polyimide film by AD process.

Figure 3-79 shows the dielectric properties measured at frequency of 10 kHz as a function of temperature for a ≈8-µm-thick PLZT film capacitor deposited by AD process on aluminum metallized polyimide film. Both the dielectric constant and dielectric loss increase with increasing temperature. It is worth noting that dielectric loss tanδ <0.015 at subzero temperatures and ≤ 0.01 at -55°C were observed for PLZT capacitors grown on aluminum metallized polyimide films, indicating that PLZT-based film capacitors are suitable for applications with a broad temperature range from-55°C to above 150°C.

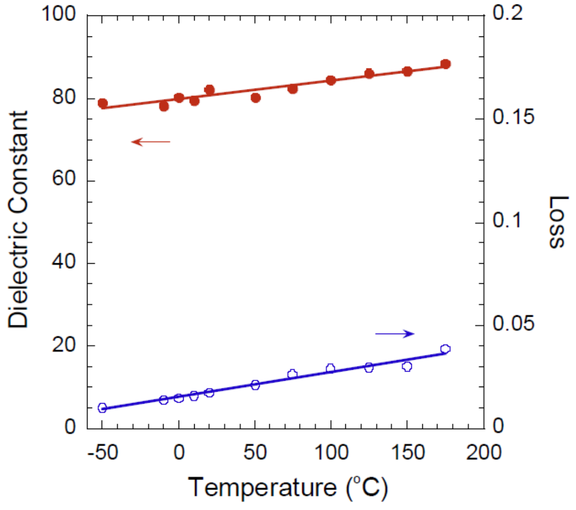

Figure 3-79: Temperature dependent dielectric property of ≈8-µm-thick PLZT film deposited on aluminum metallized polyimide film by AD process.

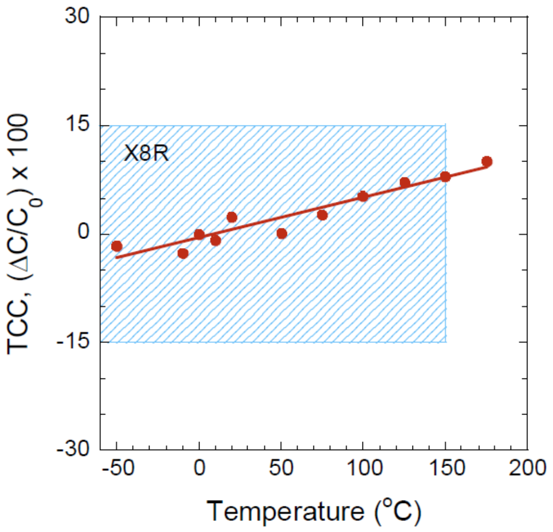

Figure 3-80: Temperature coefficient of capacitance (TCC) as function of temperature measured on a ≈8-µm-thick PLZT film on aluminum metallized polyimide film by AD process.

Figure 3-80 shows temperature coefficient of capacitance (TCC) measured for a ≈8-µm-thick PLZT film deposited by AD process on aluminum metallized polyimide films. Temperature variation property of the PLZT film capacitor fabricated by AD process exceeds the X8R requirement (−55/+150, $\Delta C/C_0$ = ±15%) as highlighted by the shaded area; this again indicates that the PLZT-based film capacitor deposited by aerosol deposition process presents desirable temperature properties that meet EDT power inverter specifications. From the slope of the linear fitting to the experimental data, we observed temperature coefficient (α) of 560 x 10^{-6} K^{-1} for PLZT films deposited on metallized polyimide sheet.

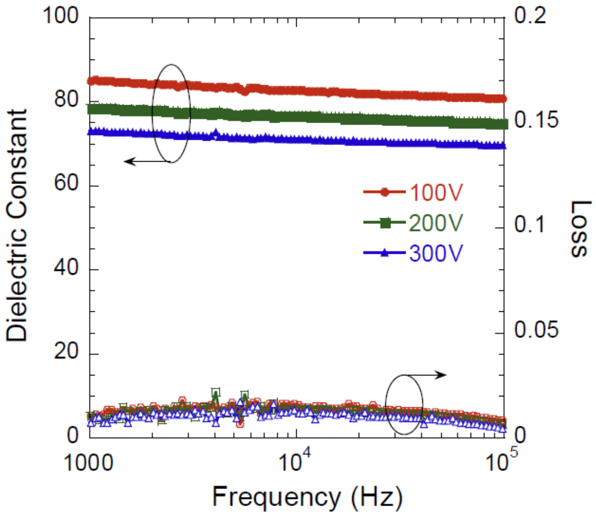

Figure 3-81: Frequency dependent dielectric properties of PLZT film deposited on metallized polyimide film.

Figure 3-81 shows dielectric properties of a ≈8-µm-thick PLZT film deposited on metallized polyimide film by AD process as a function of frequency at 100, 200, and 300 V bias voltages. Data showed linear dependent of capacitance on logarithm of frequency. Dielectric constant and loss decreases slightly with increase in bias voltages.

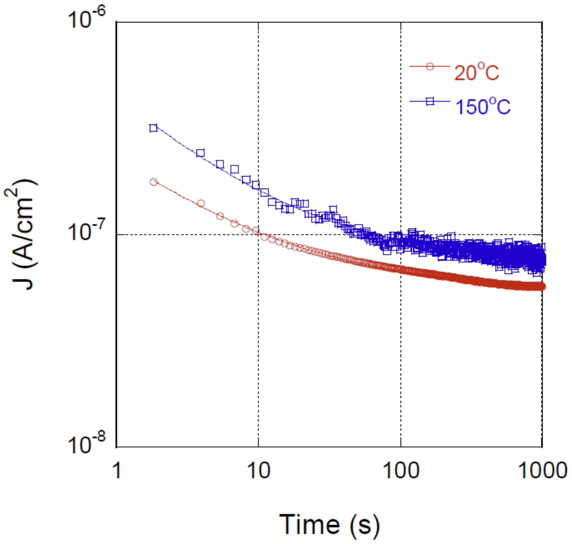

Figure 3-82: Time relaxation current density of PLZT film deposited on metallized polyimide film by AD process.

Figure 3-82 shows time relaxation current density measured at 20 and 150°C for a ≈8-µm-thick PLZT film deposited on metallized polyimide film by AD process. We measured steady state leakage current density ≈5.4 x 10^{-8} and ≈7.3 x 10^{-8} A/cm^2 at 20 and 150°C, respectively.

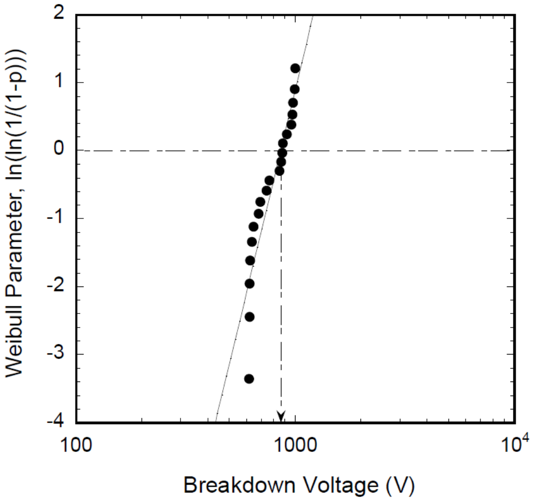

Figure 3-83: Weibull analysis of breakdown strength of PLZT deposited on aluminum metallized polyimide substrates.

Figure 3-83 shows the Weibull plot of dielectric breakdown strength measured on ≈8-µm-thick PLZT film capacitors deposited on aluminum metallized polyimide films by AD process. We measured mean breakdown voltage of 860 V at room temperature. Our results demonstrated that PLZT film capacitors produced by aerosol deposition process not only meet EDT specification for power inverter applications but also provide a method for cost-effective manufacturing of high-temperature capable capacitors.

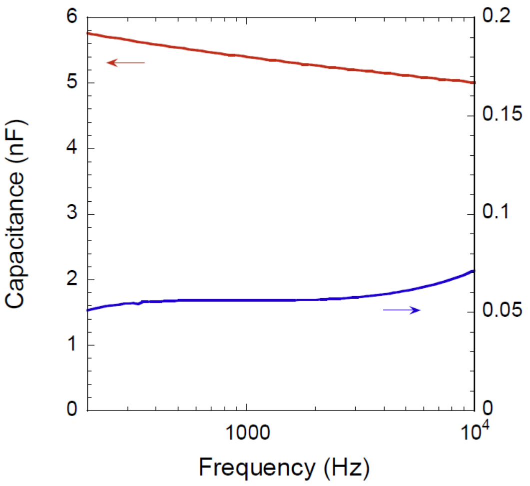

Figure 3-84: Frequency dependent capacitance and dielectric loss of a large area PLZT film deposited on aluminum metallized polyimide substrate.

Figure 3-84 shows the capacitance and dielectric loss of a large area (0.5 cm x 1.0 cm) PLZT film measured at room temperature as a function of frequency. This sample was used for the benign failure clearing test.

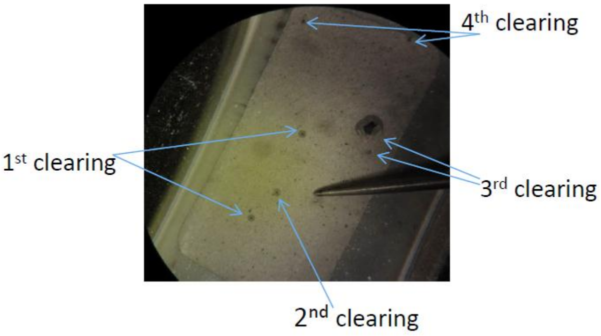

Figure 3-85: Photograph of a large area PLZT film on aluminum metallized polyimide film after fault clearing test.

Figure 3-85 shows a photograph of a large area PLZT film after four fault clearing events. This is a ≈8-μm-thick PLZT film deposited on aluminum metallized polyimide film with large area top electrode (1 cm x 0.5 cm). The first clearing occurred at 145 V, as shown in Figure 3-86a. Point defects induced high conduction faulty spots caused evaporation of portions of the top electrode as shown in Figure 3-85 (1st clearing).

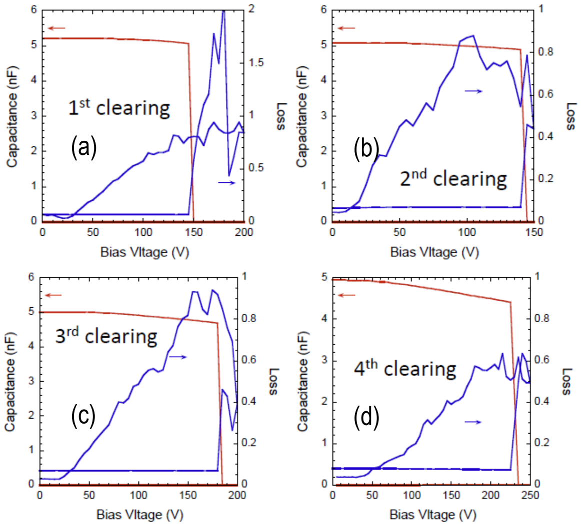

Figure 3-86: Dielectric properties as a function of applied bias voltage of a large area PLZT film on aluminum metallized polyimide film during fault clearing test.

Following the 1st clearing, the sample was subjected to increasing bias voltage until the second clearing occurred. Capacitor and dielectric loss of the capacitor were monitored during the application of bias voltage. Data were plotted in Figure 3-86b. Coincidently, a second clearing occurred at 145V again, resulting in additional removal of part of the top electrode as shown in Figure 3-85 (by 2nd clearing). After the first two clearing tests, the total capacitance reduced by ≈4.5% while the clearing voltage increased ≈28% from 145 V to 185 V as shown in Table 3-3.

Table 3-3: Summary of dielectric properties observed during fault clearing test.

Clearing Sequence	Capacitance (nF)	Dielectric loss tanδ	Clearing Voltage (V)
1	5.20	6.98%	145
2	5.14	6.85%	145
3	5.02	9.06%	185
4	4.95	8.15%	235

Subsequently, the 3rd clearing and the 4th clearing were conducted on the sample (as shown in Figure 3-86c and Figure 3-86d). We observed increased clearing voltage of 185 V and 235 V, respectively. Dielectric properties measured during the clearing tests were summarized in Table 3-3. After four clearing tests, the remaining capacitance is >95% of the initial value and the breakdown strength increased by >62%.

Conclusions and Future Directions

During FY 2014, we focused our effort on developing a wet-chemical route to synthesize PLZT powders suitable for AD process and deposit thick PLZT films on PtSi and metallized polyimide substrates. The AD technology allows deposition of dense ceramic films at room temperature with high deposition rate. We have shown that the AD process can be used to fabricate dense PLZT film capacitors with superior volumetric and gravimetric properties without the need for high temperature annealing. The properties measured show that the PLZT-based ceramic film capacitors have great potential to meet the EDT goals. We successfully fabricated ≈8-μm-thick PLZT films by AD process on aluminum metallized polyimide films. Preliminary characterization of PLZT on metallized polymer film capacitors fabricated by AD process revealed high dielectric constant, low dielectric loss, weak-dependence on field, high recoverable energy density, and suitable for high field and high temperature operation. The AD process offers the greatest potential for producing low-cost, reliable, high temperature operational, compact and light-weight capacitors for power electronics. Defect clearing events result in increased breakdown strength and minimal loss in capacitance density. Focus of our FY 2015 effort is to optimize the AD process parameters to deposit thick PLZT films with uniform thickness and integrate the AD process into a roll-to-roll coating system.

FY 2014 Publications/Presentations

1. U. Balachandran, B. Ma, T.H. Lee, S.E. Dorris, “Ferroelectric PLZT films deposited on base-metal foils for power inverters in electric drive vehicles,” Presented at the 23rd IEEE International Symposium on Applications of Ferroelectric (ISAF), International Workshop on Acoustic Transduction Materials and Devices (IWATMD) Piezoresponse Force Microscopy Workshop (PFM), State College, PA, May 12–16, 2014.
2. U. Balachandran, M. Narayanan, Z. Hu, C.Y. Park, T.H. Lee, S.E. Dorris, B. Ma, “High-dielectric constant, high-temperature ceramic capacitors for power inverters,” Presented at the 143rd Annual Meeting of TMS, Technical Symposium: Advanced Materials for Power Electronics, Power Conditioning, and Power Conversion II, San Diego, CA, February 16–20, 2014.
3. U. Balachandran, B. Ma, S. Garner, P. Cimo, “Development of flexible glass capacitors for power inverters in electric drive vehicles,” Presented at the 13th Annual Flexible & Printed Electronics Conference, Phoenix, AZ, February 3–6, 2014.
4. M.R. Fairchild, R.S. Taylor, C.W. Berlin, C. Wong, B. Ma, U. Balachandran, “Thin-film high voltage capacitors on ultra-thin glass for electric drive vehicle inverter applications,” *Presented at SAE 2014 World Congress & Exhibition*, SAE Technical Paper 2014-01-0417, April 2014.
5. B. Ma, M. Narayanan, S. Liu, Z. Hu, U. Balachandran, “Development of PLZT film-on-foil capacitors with high energy density,” Proceedings of Dielectrics 2013, IOP Publishing, *Journal of Physics: Conference Series* **472**, 012004, 2013.
6. U. Balachandran, B. Ma, T. H. Lee, S. E. Dorris, “Development of ceramic dielectric films for power inverters in electric drive vehicles,” Presented at the International Union of Materials Research Societies – International Conference in Asia (IUMRS-ICA), Bangalore, India, Dec. 15–20, 2013.
7. Z. Hu, B. Ma, R.E. Koritala, U. Balachandran, “Temperature-dependent energy storage properties of antiferroelectric $Pb_{0.96}La_{0.04}Zr_{0.98}Ti_{0.02}O_3$ thin films,” *Appl. Phys. Lett.* **104**, 263902, 2014.
8. Z. Hu, B. Ma, S. Liu, M. Narayanan, U. Balachandran, “Ceramic dielectric film capacitors fabricated on aluminum foils by chemical solution deposition,” *Materials Research Bulletin* **52**, 189–193, 2014.
9. Z. Hu, B. Ma, S. Liu, M. Narayanan, U. Balachandran, “Relaxor behavior of ferroelectric PLZT thin films with different Zr/Ti ratios,” *Ceramics International* **40**, 557–562, 2014.
10. U. Balachandran, B. Ma, T. H. Lee, S. E. Dorris, “Development of ferroelectric PLZT films for power inverters in electric drive vehicles,” Presented at the International Union of Materials Research Societies – International Conference in Asia (IUMRS-ICA 2014), Fukuoka, Japan, Aug. 24–30, 2014.
11. B. Ma, U. Balachandran, S. Chao, S. Liu, M. Narayanan, “Method for Fabrication of Crack-Free Ceramic Dielectric Films,” U.S. Patent No. 8,647,737 B2, issued 02/11/2014.
12. B. Ma, U. Balachandran, S. Liu, “Method of Making Dielectric Capacitors with Increased Dielectric Breakdown Strength,” U.S. Patent Application 2013/0335882 A1, published 12/19/2013.
13. B. Ma, M. Narayanan, U. Balachandran, S. Chao, S. Liu, “Method for Fabrication of Crack-Free Ceramic Dielectric Films,” U.S. Patent Application 2014/0120736 A1, published 05/01/2014.

References

1. B. Ma, M. Narayanan, S.E. Dorris, U. Balachandran, "Method for Fabrication of Ceramic Dielectric Films on Copper Foils," U.S. Patent Application 2010/0302706A1, published Dec. 2, 2010.
2. U. Balachandran, D. K. Kwon, M. Narayanan, B. Ma, "Development of PLZT Dielectrics on Base Metal Foils for Embedded Capacitors," *J. European Cer. Soc.,* **30**, 365, 2010.
3. B. Ma, M. Narayanan, U. Balachandran, Dielectric "Strength and Reliability of Ferroelectric PLZT Films

Deposited on Nickel Substrates," *Materials Letters*, **63**, 1353, 2009.

4. U. Balachandran, M. Narayanan, S. Liu, B. Ma, "Development of Film-on-Foil Ceramic Dielectrics for Embedded Capacitors for Power Inverters in Electric Drive Vehicles," *Jpn. J. Appl. Phys.* **52**, 05DA10, 2013.
5. B. Ma, D.-K. Kwon, M. Narayanan, U. Balachandran, "Chemical Solution Deposition of Ferroelectric Lead Lanthanum Zirconate Titanate Films on Base-Metal Foils," *J. Electroceram.* **22**, 383–389, 2009.
6. K.D. Budd, S.K. Dey, D.A. Payne, "Sol-Ggel Processing of $PbTiO_3$, $PbZrO_3$, PZT, and PLZT Thin Films," *Proc. Br. Ceram. Soc.* **36**, 107, 1985.
7. C. K. Kwok, S. B. Desu, "Pyrochlore to perovskite phase transformation in sol-gel derived lead-zirconate-titanate thin films," *Appl. Phys. Lett.* 60 (1992) 1430–1432.
8. Q. Zou, H. E. Ruda and B. G. Yacobi, "Improved dielectric properties of lead zirconate titanate thin films deposited on metal foils with $LaNiO_3$ buffer layers," *Appl. Phys. Lett.* **78** (2001) 1282–1284.
9. P. S. Prevéy, "X-ray Diffraction Residual Stress Techniques," in *Metals Handbook*, Metals Park, OH, American Society for Metals (1986) 380–392.
10. R. J. Ong, D. A. Payne, N. R. Sottos, "Processing effects for integrated PZT: Residual Stress, thickness, and dielectric properties," *J. Am. Ceram. Soc.* **88** (2005) 2839–2847.
11. G. A. C. M. Spierings, G. J. M. Dormans, W. G. J. Moors, M. J. E. Ulenaers, P. K. Larsen, "Stress in $Pt/Pb(Zr,Ti)O_3/Pt$ thin-film stacks for integrated ferroelectric capacitors," *J. Appl. Phys.* **78** (1995) 1926–1933.
12. J. Lee, C. Park, M. Kim and H. Kim, "Effect of residual stress on the electrical properties of PZT films," *J. Am. Ceram. Soc.* **90** (2007) 1077–1080.
13. N. Bassiri-Gharb, I. Fujii, E. Hong, S. Trolier-McKinstry, D. V. Taylor, D. Damjanovic, "Domain wall contributions to the properties of piezoelectric thin films," *J. Electroceram.* **19** (2007) 49–67.
14. Y. Bastani, T. Schmitz-Kempen, A. Roelofs, N. Bassiri-Gharb, "Critical thickness for extrinsic contributions to the dielectric and piezoelectric response in lead zirconate titanate ultrathin fil," *J. Appl. Phys.* **109** (2011) 014115.
15. P. Bintachitt, S. Jesse, D. Damjanovic, Y. Han, I. M. Reaney, S. Trolier-McKinstry, S. V. Kalinin, "Collective dynamics underpins Rayleigh behavior in disordered polycrystalline ferroelectrics," *Proc. Natl. Acad. Sci. U.S.A.* **107** (2010) 7219–7224.
16. W. Weibull, "A statistical distribution function of wide applicability," *J. Appl. Mech.* 18 (1951) 293–297.
17. L. A. Dissado, "Theoretical basis for the statistics of dielectric breakdown," *J. Phys. D: Appl. Phys.* 23 (1990) 1582–1591.
18. Y. Imanaka, H. Amada, F. Kumasaka, N. Takahashi, T. Yamasaki, M. Ohfuchi, C. Kaneta, "Nanoparticulated Dense and Stress-Free Ceramic Thick Film for Material Integration," *Adv. Eng. Mater.* 15 (2013) 1129–1135.

3.5 High Temperature DC Bus Capacitor Cost Reduction & Performance Improvements

Angelo Yializis (Principal Investigator)

Christopher Hohmann, Program Manager
Sigma Technologies International Group
10960 N Stallard Place
Tucson, AZ 85737
Phone: (520) 575 8013; Fax: (520) 575 8013
E-mail: chohmann@sigmalabs.com

Subcontractor:
Delphi Automotive Systems, LLC
2151 East Lincoln Road M/C: CTC 1E
Kokomo, IN 46902

Subcontractor:
Oak Ridge National Laboratory

Start Date: October 1, 2013
Projected End Date: April 30, 2016

Objectives

- Reduce the cost, size and weight of the DC-link capacitor by >50%.
  - Increase durability in high temperature environments.

Technical Barriers

The performance and lifetime of capacitors available today degrade rapidly with increasing temperature (ripple current capability decreases with temperature increase from 85˚C to 105˚C). Therefore, today's capacitors are typically twice the size (up to 40% of the inverter's volume) and too costly (up to 30% of the inverter's cost).

Technical Targets

- For Phase 1 the GEN 1 targets will be:
  - A PML capacitor that will have a rating of 800 μF / 400 Vdc / 650$V_{transient}$
  - Designed for a 30 kW continuous, 55 kW peak (30 seconds) inverter
  - Operating temperature: -40°C to +140°C
  - Projected volume: < 0.2L
  - Dissipation factor: < 0.01 up to 160°C
  - Ripple current: 130A_{rms} continuous
  - Energy density: > 3X today's PP caps, or >1 J/cc
  - Cost: < $30 (with direct cost < $15)
  - Benign failure mechanism.

Accomplishments

- Selection of optimized PML dielectric for 800 μF / 400 Vdc / 650 $V_{transient}$ GEN1 Capacitor
  - Dissipation and capacitance stability over -40°C to +160°C

✧ ✧ ✧ ✧ ✧

Introduction

The proposed project focuses on process development and scale-up to produce application-specific DC-link capacitors for automotive inverter applications. In Phase I of the program (2013–2014), the development work addresses optimization of the polymer dielectric formulation and thickness, to produce GEN 1 capacitors with a rating of 800 μF / 400 Vdc / 650$V_{transient}$. GEN 1 will demonstrate operation at -40°C to 140°C, a benign failure mode, direct cost <$15 and 3 times reduction in volume and weight, compared to today's baseline polypropylene (PP) capacitors. A significant part of the Phase I effort was to scale up process steps to allow manufacture and assembly of an adequate number of parts for the various test protocols and to meet the Phase I deliverables. In the Phase II effort (2015–2016), GEN 2 capacitors will be produced that will further decrease capacitor volume by optimizing the polymer dielectric thickness and increasing the dielectric constant. GEN 2 capacitors will be packaged, integrated into a Delphi inverter and long-term reliability tests will be performed to confirm the target specifications have been met.

Approach

Sigma has developed a solid state Polymer-Multi-Layer (PML) capacitor comprising 1000s of radiation cured polymer dielectrics and Al electrodes to form a large area nanolaminate (Mother Capacitor) that is segmented into individual capacitors.

- Having a prismatic shape with low ESL and ESR
- Operating temperature range of -40°C to 140°C
- Dissipation Factor (DF) < 0.01
- Amorphous high breakdown strength dielectrics
- Dielectric constants in the range of 3.0 < k < 6.2
- Benign failure mode
- Low-cost materials and process

This PML technology is a transformational and potentially disruptive technology in the following ways:

- Liquid monomer and Al wire are converted in a single step into Mother Capacitor material.
- Eliminates film manufacturing and metallizing by outside suppliers.
- Capacitor manufacturer has opportunity to innovate and create application-specific products with different polymer dielectric properties.

Results

2014 activities for Phase 1 of the project consisted of the following 5 tasks:

- Task 1 – Program Management
- Task 2 – Optimize PML Dielectric for 800 μF / 400 Vdc / 650 $V_{transient}$ GEN1 Capacitor
- Task 3 – DC-Link Capacitor Prototype Line
- Task 5 – Package PML DC-Link Capacitor
- Task 6 – Preliminary Cost and Commercialization Plan.

A brief summary of progress to date and future plans for each of these tasks follows.

Task 1 – Program Management

Sigma Technologies and Delphi have worked closely together over the first phase of the project. There have been monthly review meetings involving Sigma and Delphi as well as correspondence via email and phone calls. All quarterly Research Performance Progress Reports and other reporting requirements have been submitted on time to the DOE.

Future work for this task will be a continuation of the monthly meetings and completion of DOE reporting requirements as required.

Task 2 – Optimize PML Dielectric for 800 μF / 400 Vdc / 650 Vtransient GEN1 Capacitor

A polymer dielectric has been selected that meets both the cost, process and dielectric performance criteria.

Figure 3-87 and Figure 3-88 show that the GEN1 dielectric formulation meets and exceeds the targeted 140°C capacitance and dissipation factor stability. Multilayer capacitors produced with this dielectric formulation show that GEN1 PML capacitors have an energy density that is > 3X that of metallized PP.

These monomers have a relatively low cost and are projected to meet the < $15 total direct cost requirement. These costs are expected to be reduced significantly when purchased in high volume with a long term contractual obligation.

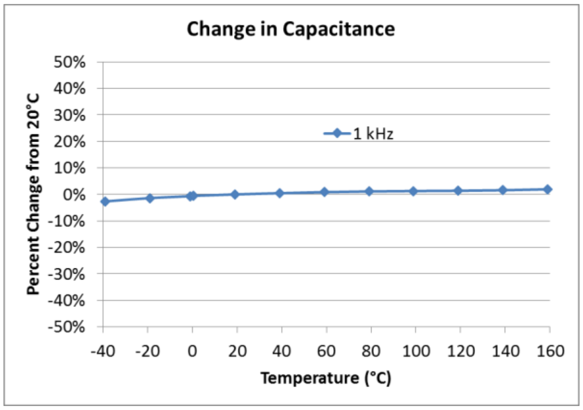

Figure 3-87: Capacitance Stability vs. Temperature.

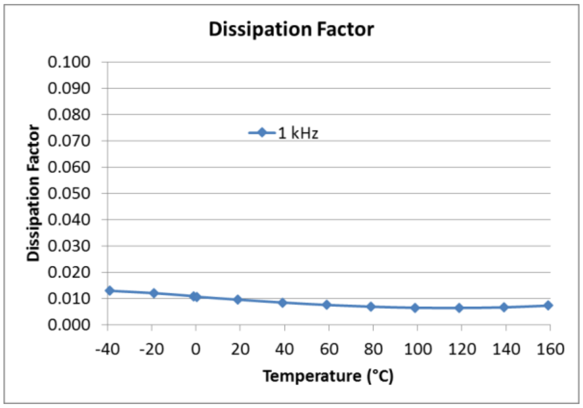

Figure 3-88: Dissipation Factor Stability vs. Temperature.

Task 3 – DC-Link Capacitor Prototype Line

Most pilot equipment used to produce PML capacitors have been upgraded, including the following:

- PML Capacitor Mask and Evaporator Nozzle
- Monomer feed controls
- Dicing sawsaw
- Various equipment used to terminate the capacitors.

Equipment improvements have had a significant positive impact on the ability of the DC-link Capacitor Prototype Line to produce capacitor samples in a timely and repeatable manner, enabling process optimization to continue toward achieving the project goals.

Future work will consist of completing the modifications and improvements to the system and verifying the operation of all components.

Task 5 – Package DC-Link Capacitor

Delphi has been working with Sigma to define and document the dielectric material properties and capacitor design. The material and construction properties are being provided to ORNL to develop a thermal-mechanical model of the DC-link capacitor. Delphi is also developing capacitor specifications and testing requirements for the PML DC-link capacitors.

Delphi will continue to work with Sigma to evaluate the final dielectric formulation and document the material and construction properties of the GEN1 PML capacitors. In particular, the focus will shift toward applying those materials and construction techniques to the fabrication of DC-link capacitors for Delphi. Using PML capacitor GEN1 samples, Delphi will conduct packaging experiments to define an optimum capacitor package that combines environmental protection and electrical and thermomechanical requirements. Capacitor and package material properties and design shall be provided to ORNL to refine and verify their thermomechanical model of the DC-link capacitor.

Task 6 – Preliminary Cost and Commercialization Plan

Preliminary direct cost analysis shows that the project PML capacitor cost is in line with the program objectives. Sigma is working closely with a major U.S.-based manufacturer of materials and components that actively supplies products to the automotive industry and other markets where Sigma capacitors can have commercial impact. Sigma is planning to use its strategic partner's distribution network to commercialize the PML capacitors in several application areas that include mass transportation/rail, PV and wind energy, pulsed power, and LED lighting.

Future activity will include refinement of the cost model as well as detailed analysis of specifications and cost of competitive products.

Conclusions and Future Directions

Extending Sigma's PML lower voltage capacitor technology to meet the higher voltage, higher capacitance and temperature requirements of electrified vehicles would enable a step-change in inverter size and cost, by reducing the inverter's DC-link capacitor size and cost by 50% or greater. The achievements to date have further improved our confidence that the targeted aggressive advancements should be feasible, with completion of the scaling up of the primary manufacturing process, assembly and testing of the capacitor building blocks planned for the balance of Phase 1.

FY 2014 Publications/Presentations

1. 2014 DOE APEEM FY14 Kickoff Meeting Presentation.
2. 2014 DOE Annual Merit Review Meeting Presentation.

3.6 High Performance DC Bus Film Capacitor

Daniel Tan (Senior Materials Scientist)
GE Global Research Center

Susan Rogers, Program Manager
DOE Technology Development
Phone: (202) 586-8997; Fax: (202) 586-1600
E-mail: Susan.Rogers@ee.doe.gov

Steven Boyd, Program Manager
DOE Technology Development
Phone: (202) 586-8967; Fax: (202) 586-1600
E-mail: Steven.Boyd@ee.doe.gov

Subcontractor:
Delphi Automotive Systems, LLC

Start Date: October 2013
Projected End Date: September 2016

Objectives

- Develop high-temperature, thin polymer films, and a scalable process for manufacturing the films to meet the performance, size and cost targets of the DC bus capacitor for electric vehicle inverters.

Technical Barriers

There is no commercially available capacitor film which meets DOE targets for electric vehicle inverter capacitors, in terms of improved temperature rating (>140 °C), small volume (<0.6L), and low cost ($30). A key challenge is the low cost manufacture of a very thin capacitor quality film with high dielectric strength and performance at high temperature.

Technical Targets

- Achieve temperature stability and cost effectiveness by extruding polyetherimide (PEI) films with high dielectric strength for higher energy density and greater design freedom for vehicle systems.
- Scale up production of PEI films of 3–5 μm in thickness, with minimal film wrinkling and thickness variability.
- Develop nanocoating process on thin PEI films for enhanced dielectric strength.
- Qualify film properties in terms of thermal, dielectric and mechanical characteristics.

Accomplishments

- Investigated melt extrusion processes of PEI and evaluated the physical and dielectric properties of films.
- Eliminated wrinkling issue of thin films associated with extrusion process through working with film extrusion manufacturers.
- Developed a new film extrusion process assisted with a carrier. Produced >500 meter long roll of 5 μm thick film.
- Extruded 3–4 μm thick PEI film up to 250 meter in length with satisfactory thickness uniformity.
- Identified 2 vendors capable of roll-to-roll nanocoating.
- Demonstrated enhanced dielectric strength on nanocoated PEI films.
- Qualified PEI films with: dielectric strength of >500 kV/mm, dielectric loss of <0.003 at 1 kHz, thickness variation of ≤+/-10%, mechanical strength of equivalent or better than polypropylene films, and shrinkage of zero up to 180ºC. These are consistent and acceptable film properties suitable for capacitor application.
- Met milestones for Go/No go decision points.

✧ ✧ ✧ ✧ ✧

Introduction

To enable broader adoption of efficient and affordable electric vehicles, the DOE has defined a need for less-expensive, more-efficient, smaller, and lighter power electronics and electric machines for electric traction systems. Capacitors are an essential element of such systems, but current commercial capacitor technology imposes significant costs and design constraints on such systems. For example, BOPP film capacitors being used in current inverter design are the one of the most expensive and largest components in inverter systems, and contribute to a large under-hood footprint due to energy density limitations, and the need for thermal management as a result of limited operating temperature (<125°C).

The DOE has defined performance targets for capacitors with improved thermal capability and energy density, as well as cost targets which would enable broad adoption of such capacitors by industry.[1] Development of high-dielectric strength, low loss, thermally stable and sufficiently thin dielectric films is a key technology for meeting these capacitor performance targets.

Unlike other approaches utilizing inorganic dielectrics or high dielectric loss polymers, GE is pursuing a high temperature polymer with a moderate dielectric constant and low dielectric loss [2–6]. GE has actively led the development of Polyetherimide (PEI) film for conversion to high temperature capacitor applications [7–8]. A glass-transition temperature of about 217°C and dielectric strength of >500 kV/mm makes it an ideal candidate to meet the DOE's DC bus capacitor performance goals. PEI films are produced by melt extrusion and commercialized in various thicknesses above 13 μm.

GE's past research and development has repeatedly confirmed the superior dielectric, mechanical, and thermal performance of PEI film for film capacitor applications. A primary technical challenge for commercial use is the melt extrusion of very thin PEI films (<10 μm), with consistent thickness and no wrinkling during extrusion, winding, or subsequent conversion.[9] Meeting these goals for a film scale-up process will enable reduced system volume, weight and cost, increased thermal stability, and improved design freedom for electrical vehicle systems as envisioned by DOE.

Approach

GE will leverage a melt extrusion process to produce high temperature amorphous PEI films in the quality and scale needed for capacitor fabrication. GE will work with film manufacturers to improve processing parameters and winding capabilities, in order to produce wrinkle-free 3–5 μm PEI films with minimal thickness variability. GE will work with film coating companies to deposit scalable nanocoating and metallization layers on PEI film to achieve higher dielectric strength and graceful failure characteristics. A selected capacitor manufacturing facility will be used to make and test the capacitors required under this contract. In the first phase, GE will determine the proper PEI resin, develop the extrusion process(es) for high quality films, and evaluate film dielectric, mechanical and thermal properties. Success in the film scale-up and qualification based on prototype capacitors will lead to continued development and delivery of high performance packaged capacitors in the second phase.

Results

Polymer film extrusion is a relatively mature technology. For years, thin films of polypropylene (PP) have been produced by melt extrusion followed by biaxial stretching, in order to yield very thin biaxially-oriented polypropylene (BOPP) films with good properties for wound film capacitors. The semi-crystalline nature of PP provides the melt-strength and physical properties required for thickness reduction by biaxial stretching. Unlike the semi-crystalline nature of PP, PEI is an amorphous material with a high glass transition temperature (217°C). This results in very significant differences in the rheological and melt-flow properties of the two polymers. PEI film extrusion equipment has more stringent requirements for heating and process control. If the film extrusion process is not properly designed and controlled, the resulting PEI film can exhibit wrinkles, thickness variation, and surface defects, with these challenges increasing as the target film thickness decreases. Due to these challenges, a very limited number of film manufacturers have the equipment and skill to extrude PEI films thinner than 25 microns.

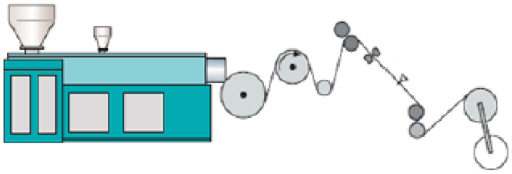

Figure 3-89: Schematic of extruder and winding process flow.

Leveraging the experiences and understanding of molecular weight, rheology and types of PEI resin, GE extruded PEI films of various thicknesses and evaluated film properties. Figure 3-89 shows a schematic drawing of a conventional melt extrusion process that is the focus of the program for production of high quality PEI films.[10] The historical progress made in PEI film development over the past ten years is shown in Figure 3-90. In order to further reduce film thickness to the desirable gauge, GE has established collaborative efforts with Japanese and U.S. film manufacturers to leverage their extrusion facility and resources for engineering PEI film of 3-10 μm in thickness.

First quarter: Extrusion of thinner films is known to become progressively more difficult, as this requires faster winding speed and better extrusion process control. Higher winding speed leads to thinner films, however, more film non-uniformities may arise as well. Figure 3-91 shows an example of minor winkles in one engineering film roll, which were observed in the end of a small roll of 7 μm film.

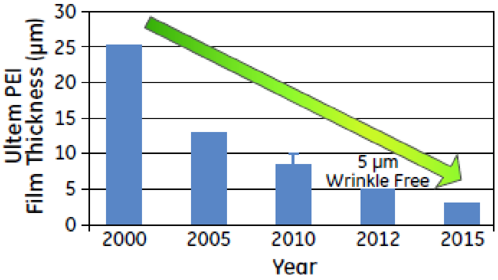

Figure 3-90: Historical progress in PEI film development and evaluation.

Figure 3-91: Image of a PEI film roll with wrinkles and crease.

In order to minimize the wrinkles associated with free-standing films, the team explored a different mechanism of extruding PEI films. Making use of a carrier, the wrinkles commonly seen in conventional extrusion of thinner films were minimized. The team started with a pilot extruder, and qualified two carrier materials that have appropriate adhesion and delamination capability.

Second quarter: Following the success in the extrusion of 7–10 μm film, process control was improved to produce 5 μm film rolls on a scale-up level. Three different PEI resins characteristic of different molecular weight and additives were studied. Two types of resins were demonstrated to extrude to 5 μm film. Figure 3-92 shows the microscopic image of a film roll with 650 mm in width and 650 meter in length. The physical properties of the larger rolls was shown to be good with a thickness variation of <+/-10%. The film thicknesses were measured using a Filmetrics optical analyzer. Continued efforts on the extrusion process will be made toward consistent PEI film rolls with minimal thickness variation and defects.

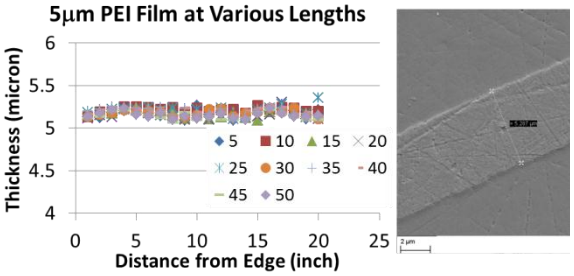

Figure 3-92: Thickness variation and Scanning electron microscope images of 5 μm PEI film.

In parallel, GE worked with a U.S. manufacturer scaling up the carrier-assisted extrusion process for 5μm PEI film. Extrusion processing parameters were established and validated for two different carriers. Surface condition of the carriers was determined to provide appropriate wettability, adhesion and delamination for the high temperature PEI films. 10” wide rolls of more than 500 meter in length were produced; however, thickness variation is yet to be reduced.

Third quarter: GE discussed film specification with a Japanese film manufacturer, aiming at the extrusion of 5 and 3 μm PEI films. Their modified winding mechanism involves regular features on the chill roll, which effectively eliminates film wrinkles. Engineering grade PEI film rolls of 5 μm in thicknesses were reproduced in >500-meter lengths, yet continuous efforts are needed for consistent production of long rolls. For 3 μm film, small sample films, on the order of size of a piece of letter paper, were provided to GE to demonstrate the feasibility of free-standing thin films. These films exhibit good dielectric properties, low thickness variation (<+/- 5%) and no wrinkle issues.

On the other film process development path, a carrier-assisted film extrusion process for the high temperature polymer received extensive investigation. GE studied the effect of extrusion temperature, cooling roll temperature, nip roll pressure, carrier surface adhesion, carrier line speed and die lip gap on the film quality. Wrinkle-free 5 μm PEI film rolls were confirmed to be reproducible. The root causes for the thickness non-uniformity in the outer range of the web were studied and identified to be limitations for in-process control of die lip spacing. Thickness variation was reduced to +/-10% only in the center area (6” wide) of the film web as shown in the lower graph of Figure 3-93. One side of the die gap is not stable and the uniform thickness control is not attainable as shown by the shaded data in Figure 3-93.

Dielectric properties of the thin films were measured as a function of temperature and frequency using a broadband dielectric spectrometer from Novacontrol GmbH. Figure 3-94 shows the complex dielectric responses of 5 μm thick PEI film that was produced in free-standing extrusion mechanism. Tensile and tear strength of the films were also tested. Film shrinkage was tested as a function of ageing temperature. The results show film properties meeting the program’s performance targets for the capacitor application. Chemical analyses were performed on films from both extruding facilities, which confirmed the consistent use of the same PEI resin without involving other additives.

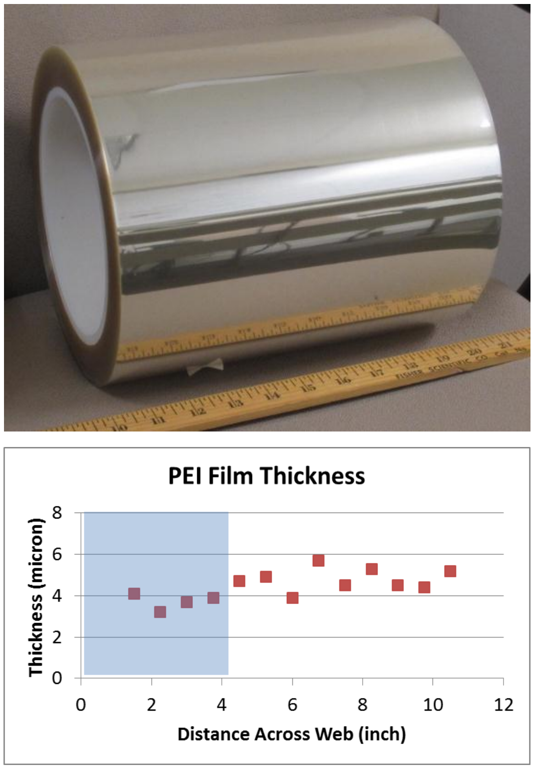

Figure 3-93: Thickness variation and image of a film roll with a carrier.

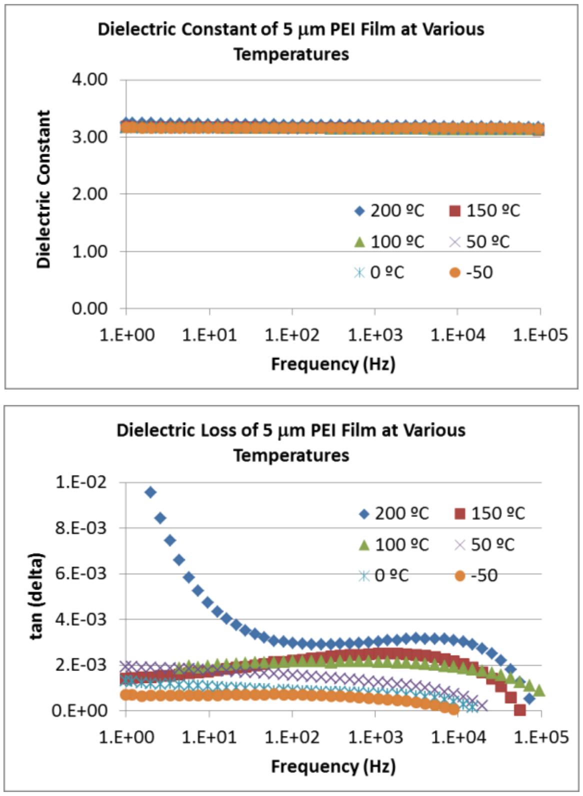

Figure 3-94: Dielectric response of a 5 µm PEI film produced in carrier-assisted extrusion trials.

The polymer film must survive the winding and conversion processes involved in capacitor manufacturing. Tensile and tear strength are the mechanical properties of interest. PEI films of >25 µm are known to be strong and useful in the capacitor winding process. For films thinner than 10 microns, these properties were also studied on an Instron 4202 Universal Tensile Instrument using the ASTM D638 standard test method for tensile properties of plastics. The thin films are challenging to handle during the sample preparation and tests, yet 15 samples were tested to obtain representative results. These results are as good as or better than polypropylene film, which confirms the mechanical strengths of PEI films being suitable for capacitor manufacturing.

The tear resistance of PEI films was also tested by cutting a notch in a strip of film using the ASTM D1004 test standard for plastic film and sheeting (Graves Tear). The average resistance value for the specified tear propagation is 0.131 lbs, which is the same as that for a 50 µm PEI film (http://ultem.de/downloads/brochure_01.pdf). In comparison with propylene film, the tear resistance of commercial polypropylene films of the same thickness was tested to be the similar value.

A strip of 28.7 mm long PEI film was placed on a Kapton sheet and exposed at different temperatures to test the dimensional stability of the films. By measuring the length change of the strip samples after ageing, film shrinkage was determined as shown in Figure 3-95. No length change was measurable when ageing at temperatures below 180ºC. Even at 205 ºC, the film only shrinks less than 2%. Therefore, this material is dimensionally stable for high temperature capacitor applications.

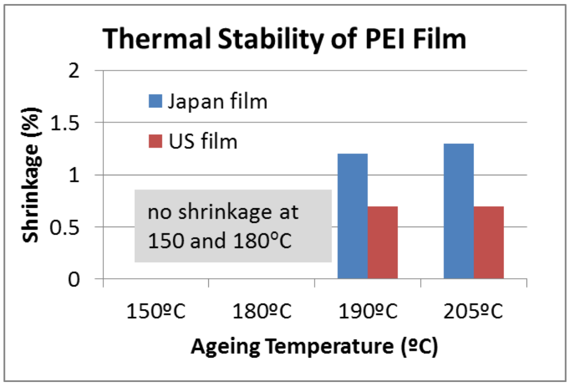

Figure 3-95: Film length shrinkage of 5 µm films aged at four different temperatures.

Fourth quarter: Film scale-up improvement, cost model analysis, and nanocoating effect on dielectric strength were made in this period. The team has identified that the most critical process aspect of achieving the DOE goals is availability of thinner films without wrinkles and thickness variability. Figure 3-96 shows why the development of thinner film is essential. A 3–4 µm thick PEI film is good enough to meet the volume requirement of an inverter.

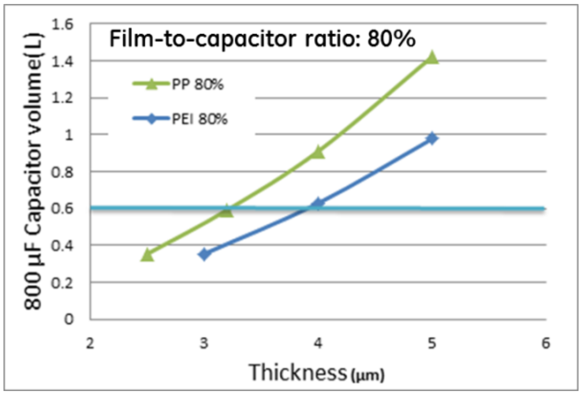

Figure 3-96: Thickness dependence of the volume of an 800µF capacitor made of PEI and PP films.

So far, extrusion parameters have been tuned to eliminate wrinkles and to reduce thickness variation. The team has also demonstrated the reduction of film thickness from 5 microns down to 3 microns in rolls as wide as 620 mm. Free-standing and wrinkle-free films of various thicknesses were extruded as shown in Figure 3-97. A trial run of a 3 µm film roll 250 meters in length was produced. The thickness variation across the web of 3 µm film was shown in Figure 3-98, where film thickness variation is within +/-5%.

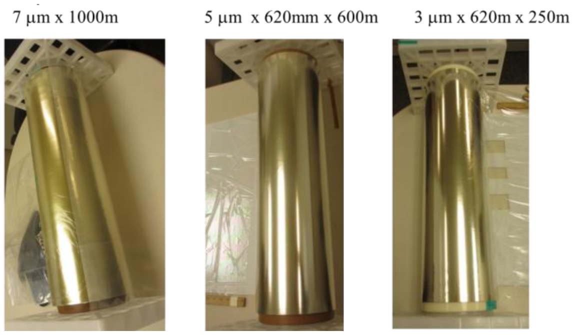
7 µm x 1000m 5 µm x 620mm x 600m 3 µm x 620m x 250m

Figure 3-97: A summary of film rolls produced using a conventional melt extrusion.

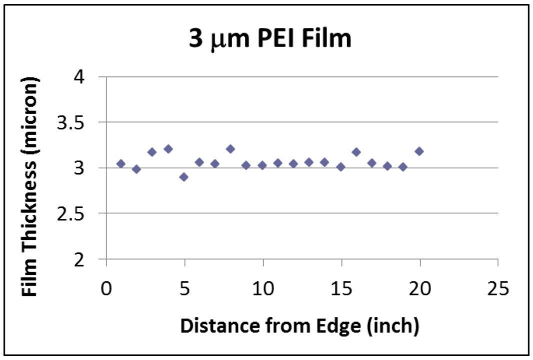

Figure 3-98: Thickness variation across the film web for a 3 µm PEI film.

Carrier-assisted PEI films of 5 µm were reproduced as well. The dielectric strengths were measured using a DC mode set up following ASTM D149 (method A) using a ball-plane electrode configuration in the GE Global Research Lab. The sample was immersed into insulation oil and dc voltage was applied at a ramp rate of 500 V/s until the sample failed. Modulus results were obtained using a thermomechanical analysis (TMA) spectrometer. Table 3-4 summarizes the test results for both free-standing and carrier-assisted films (shape factor of Weibull breakdown strength distribution is 5–15).

Table 3-4: Dielectric and physical properties of various films.

Extruded PEI Film	Thickness Uniformity	Breakdown Strength	Film Roll Length
Free 10µm	<+/-10%	630 V/µm	>2000 m
Free 7µm	<+/-10%	570 V/µm	>2000 m
Free 5µm	<+/-10%	560 V/µm	>500 m
Free 3µm	<+/-10%	510 V/µm	>250 m
Carrier 5µm	~+/-10%	582 V/µm	>500 m

Tear resistance of 3 µm PEI films was tested, despite the handling difficulties previously noted for 5 µm film testing. Figure 3-99 shows the test results for PEI films and the comparison with polypropylene (PP) of the same thickness. The variation in the results is primarily related to sample preparation and handling. The tear resistance for PEI film is 0.32 lbs on the average, which is higher than the measured tear resistance of PP films as shown between the two dashed lines. So, the material itself has the reliable strength for the subsequent winding process in consideration of the success in handling of 3 µm PP. However, at these thicknesses good control of the film slitting process is necessary, to prevent defects at the film edge which may allow tear initiation during film conversion.

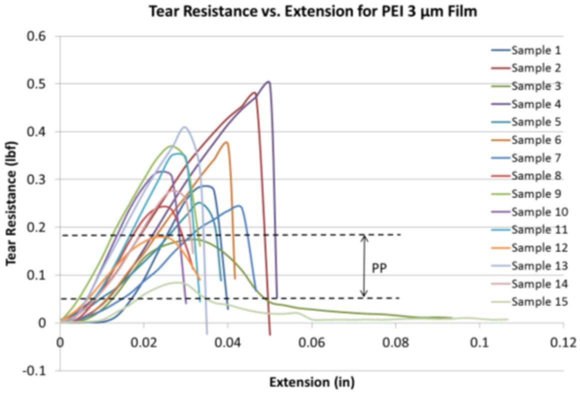

Figure 3-99: Tear resistance results for fifteen samples of 3 µm films. The tear resistances of PP films of the same thickness are shown between the two dash lines.

Cost model: A PP film of 2.5–3 µm in thickness is estimated to be about $10/kg according to capacitor manufacturers. Today, a polypropylene capacitor of 800 µF required for an inverter is about $80, higher than the DOE's target. GE understands that the PEI resin is at least 3 times more expensive than polypropylene resin. Even using a cost effective melt extrusion process, PEI film remains more expensive. The initial cost estimate of a 5 µm PEI film under development was made using engineering batches. Given a unit price of $1.4 per linear meter, PEI film costs about $100/kg. Because of higher dielectric constant for PEI (3.2 vs 2.2 for PP) and thinner gauge of film, less film usage will reduce size & weight of film for a capacitor as well as cost. Our calculation shows that a capacitor of 800 µF only needs 0.364 kg film and a volume of <0.6L. Assuming the annual production of electric vehicles is 500,000, the need for PEI film is ~364,000 kg (2 capacitors for 2 inverters). The cost need for PEI film will be less than $30/kg, which is possible to achieve and to be verified after rolling into mass production. In addition, utilizing higher temperature film (200˚C vs 105˚C) brings improved reliability/durability and reduced thermal management requirements, which can enable reduce costs at the system level. Utilizing existing capacitor manufacturing infrastructure may also lower cost via improved throughput and effective use of packaging materials because of the high temperature nature of PEI film.

Nanocoating: A preliminary effort was initiated investigating nanocoating feasibility and resource availability. The purpose of nanocoating on thin polymer films to achieve higher dielectric strength and reliability under high voltage. By using a lab scale sputtering deposition method, an increase in the dielectric strength of 5 µm thick PEI films was demonstrated with a thin inorganic coating as shown in Figure 3-100. Although batch coating of films is readily accomplished using sputtering, chemical vapor deposition or e-beam deposition, roll-to-roll processing of very thin polymer films is a significant challenge. We identified three coating vendors who are able to perform roll-to-roll coating services on polymer substrates. This provides the foundation for more extensive investigation of thin film roll-to-roll coating in the second year of Phase 1.

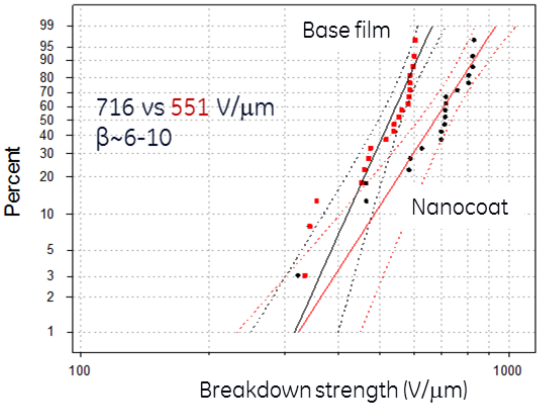

Figure 3-100: Dielectric strengths under DC mode for base PEI films and nanocoated films of 5 µm in thickness.

Conclusions and Future Directions

During the first budget period, the GE team focused on the extrusion processes using a conventional extrusion-winding process and a carrier to produce wrinkle free PEI films. This extensive effort gives the team a broader technical scope for film process and performance evaluation. The conventional melt extrusion process was proven to be reliable and reproducible for free-standing PEI films with 620 mm in width. Additional engineering effort will support a commercially scalable route to large scale rolls that can be used for this program. Use of a carrier to support the very thin extruded film has the potential to improve the ease of handling and yield associated with various capacitor manufacturing steps, and the resulting process cost savings may help to offset the initial material cost of the carrier. With free-standing film of thinner gauge, film yield rate needs to be improved.

Wrinkle-free 5 μm PEI film rolls of >500 meter in length were also produced on a carrier with a thickness variation in the center area (6” wide) of the film web controlled at +/-10%. However, the thickness and its non-uniformity could not be further reduced due to die control limitations on the development extruder. An extrusion die incorporating modern in-line feedback thickness control using a similar carrier-assisted mechanism is expected to meet the PEI film quality targets.

The thin PEI films were characterized in terms of dielectric properties, mechanical properties, thermal properties and chemical analyses. The test results meet the program targets required for capacitor applications. The cost of extruded films was estimated based on the raw PEI resins and the film processes. The cost model will need to be refined as the film process development progresses toward a commercial-scale process.

FY 2014 Publications/Presentations

1. Daniel Tan, DOE APEEM Annual Merit Review; ape 060 High Performance DC Bus Film Capacitor; June 17, 2014.
2. Daniel Tan, Lili Zhang, Qin Chen, and Patricia Irwin, “High Temperature Capacitor Polymer Films" Journal of Electronic Materials, DOI: 10.1007/s11664-014-3440-7, 2014.

References

1. Advanced Power Electronics and Electric Motors Program. DOE EERE Vehicle Technologies Office, 2008.
2. U. Balachandran, M. Narayanan, S. Liu, B. Ma, Development of film-on-foil ceramic dielectrics for embedded capacitors for power inverters in electric drive vehicles, *Jpn. J. Appl. Phys.* ***52****, 05DA10, 2013.*
3. M. Manoharan, C. Zou, E. Furman, N. Zhang, D. Kushner, S.Zhang, T. Murata, and M.Lanagan. "Flexible Glass for High Temperature Energy Storage Capacitors." Energy Technology 1: 5-6, 313–318, 2013.
4. Numbering List S. Fries-Carr, S. Adams and J. Weimer, R.L.C. Wu, H. Kosai, K. Bray, T. Furmaniak, E. Barshaw, S. Scozzie and R. Jow, SAE Technical Paper 2004-02-3216, Power Systems Conference, Nevada, 2004.
5. Shihai Zhang, Chen Zou, Xin Zhou, Douglas Kushner, “High Temperature Polymer Capacitor Film with High Dielectric Constant” 2011 CARTS USA, March 28–31, 2011, Jacksonville, FL. http://strategicpolymers.squarespace.com/capacitors2011. Strategic Polymer Sciences Inc.
6. K.W. Browall, M.W. DeVre, S.M. Gasworth, C.W. Reed, S.J. Rzad, “High Energy Storage Capacitors for Pulse Power”, ARL-CR-150, Contract DAAL01-91-C-0149, 1994.
7. Q. Tan, P.C. Irwin, Y. Cao, Advanced Dielectrics for Capacitors, IEEJ Transactions on Fundamentals and Materials, 11, 11532–1159 Vol 126 (2006).
8. D. Tan, Q. Chen, Y. Cao, P. Irwin, S. Heidger, “Polymer Based Nanodielectrics for Capacitors”, EMA 2010, Orlando, FL, (2010).
9. Bruce Mixer, High Temperature Inverter—Delphi Automotive S, Advanced Power Electronics and Electric Motors Program. DOE EERE Vehicle Technologies Office (2013).
10. Giles, H. F., Wagner, J. R. and Mount, E. M., *“Extrusion: The Definitive Processing Guide and Handbook”*; William Andrew Publishing (2005).

3.7 Next Generation Inverter

Zilai Zhao (Principal Investigator)

General Motors Corporation
777 Joslyn Avenue, Mail Code: 483-720-450
Pontiac, MI 48340
Phone: (248) 326-5304
E-mail: zilai.zhao@gm.com
mailto:cashtiani@ENERDEL.com

Subcontractors:
Hitachi, Delphi, Infineon, HRL, Panasonic, AVX, Freescale, Oak Ridge National Laboratory, and National Renewable Energy Laboratory

Start Date: 2011
Projected End Date: 2016

Objectives

- Develop the technologies and the engineering product design for a low cost highly efficient next generation power inverter capable of 55kW peak/30kW continuous power.
- The Inverter is to improve the cost of the power electronics to $3.30/kW produced in quantities of 100,000 units, and the power density to 13.4kW/l, and a specific power of 14.1kW/kg to meet the DOE 2020 goals

Technical Barriers

Traction inverter cost is the key barrier to economic viability of electric traction drives. Achieving the cost goals though must be done simultaneously with increasing efficiency, decreasing mass and volume, and maintaining reliability. Current materials used in today's inverters for automotive applications are expensive and require multiple processes to be performed to construct a complete inverter. Additionally because of instability in the EV/HEV market, commitment from the supplier base is difficult because the cost of introducing new technologies and their validation are high.

Technical Targets

- The Inverter is to improve the cost of the power electronics to $3.30/kW produced in quantities of 100,000 units, and the power density to 13.4kW/l, and a specific power of 14.1kW/kg to meet the DOE 2020 goals.

Accomplishments

- Detailed design based on modified conventional module including:
  - Integrated power stage
  - Gate drive and control PCBA.
- Initial build:
  - 5 early prototype built and tested to full current.
- Process development:
  - Die and substrate attach in one operation
  - Press-fit connection for power and signals\
  - Low cost Al cooling manifold fabrication
  - Final assembly.
- Test asset build started.
- Long duration engineering testing started.

✧ ✧ ✧ ✧ ✧

Introduction

The goal of this Cooperative Agreement is the development of a Next Generation Inverter. The key goal is to reduce the production cost of a traction drive inverter while still making improvements in mass, volume, and reliability/durability. Traction inverter cost is a key barrier to economic viability of electric traction drives. This program is divided into four budget periods: technology assessment, technology development, technology build, and non-destructive confirmatory testing. The technology assessment phase includes the investigation through experimentation and evaluation of all key elements of the inverter. Technology development includes the concept and breadboard, and a final detailed design of the inverter. Technology build includes the procurement, fabrication of components, and the assembly of the inverter. Non-destructive confirmatory testing includes environmental test setup, electrical verification, temp/vibe characterization and margining, and test support at a national lab. The National Energy Technology Laboratory (NETL) awarded GM a Cooperative Agreement in October 2011. Budget period 3 started on January 16, 2014. Since all engineering tasks scheduled for Budget period 3 had been completed ahead of schedule, we requested to start Budget period 4 immediately.

Approach

Engage with Tier 1, 2, and 3 suppliers along with National Labs to co-develop technology that reduces cost and increases efficiency, without increasing volume or mass. An Inverter design will be done that ensures modularity and scalability of the inverter to meet all vehicle applications. This dictates that packaging will fit in all vehicle applications and have these additional characteristics:

- Consistent electrical parameters and mechanical structure
- Has to adhere to global manufacturing processes
- Has to provide adequate cooling for the capacitor
- Has to have low inductance.

Then demonstrate technology to verify feasibility and cost. Multiple units will be built and tested over the complete automotive operating envelop.

Results

Design Selection

Technology evaluation and testing was conducted in the first phase of this project, which was concluded in FY13. Highlighted in earlier project reports, three types of power semiconductor packaging technologies, Conventional (gel and lead frame), Transfer Molded and Encapsulated, were evaluated. While each technology offers its own path to achieve the performance and power density targets, the manufacturing processes, for the module itself and the inverter architecture built around the module, vary significantly. As stated in our approach, electrical and mechanical consistency and adhesion to global manufacturing processes are critical. That is, the processes need to be mature enough and deployable globally by the time the inverter and key components manufacturing lines have to be built for 2020 production start.

The conventional gel and lead frame construction was the technology chosen for the inverter we would design, build and test in Phase 2, which was started in FY13.

The conventional gel and lead frame packaging has the following advantages:

- Relatively mature manufacturing processes, which can be improved to lower cost and increase product performance.
- Highly efficient single-sided can be achieved.
- Can be adapted to work with wide band-gap power devices.
- Offers scalability.

Other technologies evaluated in Phase 1 include film capacitor, wide bad-gap power semiconductor, power circuit interconnection and cooling mechanism.

Our design is also guided by the following principles to achieve low cost and scalability:

- Minimize material usage to lower BOM cost.
- Scalable without significant additional tooling cost.
- Manufacturing process can be developed for high volume production launch in 2020.

Phase 1 work yielded the following technology/ architecture features in the demonstration inverter we design, build and test in Phase 2. Figure 3-101 depicts an exploded view of the Next Generation Inverter.

- Closed aluminum coolant manifold
- Power semiconductors and substrates directly attached to coolant manifold
- Film capacitor built into coolant manifold frame, removing capacitor housing and providing better cooling
- Press-fit pins for signal and power circuit interconnection
- One piece lead frame for power semiconductor packaging
- One piece bus bar to route DC and AC current
- Gate drive and control circuit on one printed circuit board assembly (PCBA).

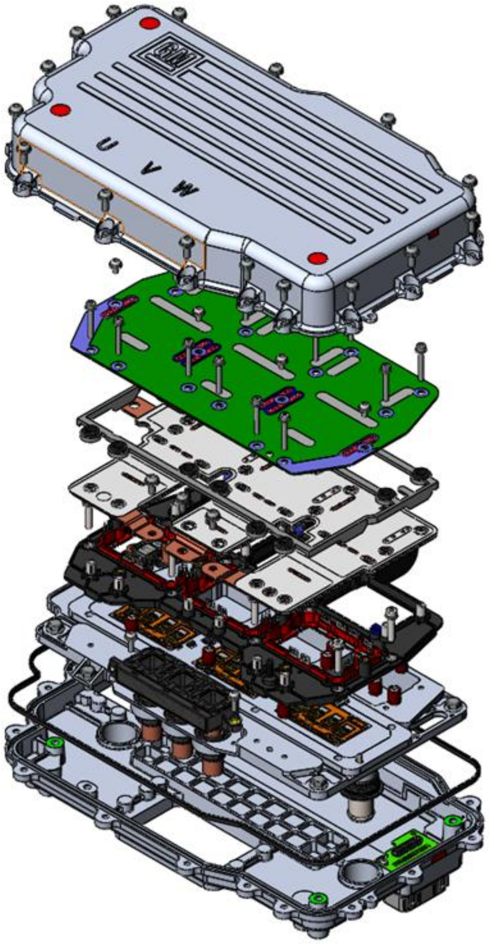

Figure 3-101: Next Generation Inverter Exploded View.

Detailed Design and Process Development

Detailed design started in late FY13. General Motors designed the overall architecture of the inverter, power stage and control/gate drive board. Key components were designed with cooperation from sub-contractors.

Five initial prototypes were built in early FY14 to verify the concept. Maximum phase current was reached on inductive load with two of the five units while the other three units showed various degrees of deficiency. This was traced back to build quality.

As part of the plan, General Motors and sub-contractors were engaged in further development of manufacturing processes prior to building the units for confirmatory tests.

The intention of the process development is to ensure the design can be built with high quality and provide a path for high volume production beyond the Cooperative Agreement.

The processes we focused our attention on are:

- Die and substrate attach, cleaning and wire-bonding
- Press-fit pins.

Die and Substrate Attach

These joints are required to have minimum thermal resistance throughout the life of the module. The complex internal geometry of the coolant manifold was one of the barriers to achieve a good joint. The targeted specifications for the joints are:

- Individual void ≤ 0.5%; total void ≤ 2% for both layers
- Thermal shock (-50C to 150) cycles ≥ 1000, delamination < 20%.

Additionally, it is desirable to form both joints in one reflow step.

We explored different soldering techniques. For the initial prototypes, an existing conductive heating vacuum oven was used. Despite efforts in optimizing oven operating parameters and solder compositions, the result is not satisfactory.

- While the voids in the substrate to manifold joint were pretty low, we could not get consistent results in the die to substrate joint (Figure 3-102).
- The time above liquidus was too high, typically over 5 minutes.
- Cycle time was very slow: typically 17 minutes for the die to substrate joint + 45 minutes to cool the chamber, and 45 minutes for the substrate to manifold joint + 45 minutes of chamber cooling.

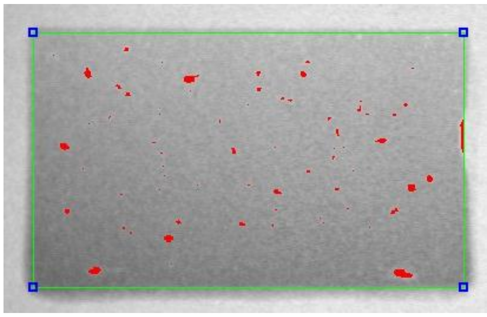

Figure 3-102: Die Attach X-Ray Image – Conductive Heating Oven.

Condensation soldering technique was then introduced to tackle this issue. Figure 3-103 shows the Condensation Reflow Oven operation. This reflow method allows the whole part to uniformly heat up, therefore making single reflow for both joints easier to achieve.

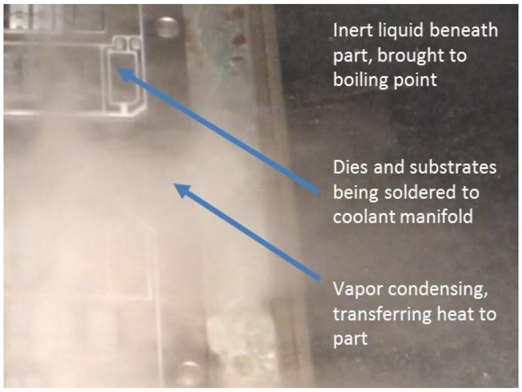

Figure 3-103: Condensation Reflow Oven Operation.

Overall voiding is very low in both joints as demonstrated in the first tries but river voids between the substrate and manifold are now a problem. See Figure 3-104.

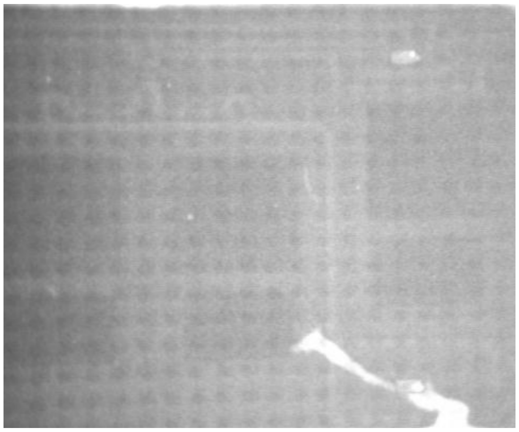

Figure 3-104: “River Void” in Substrate to Manifold Joint.

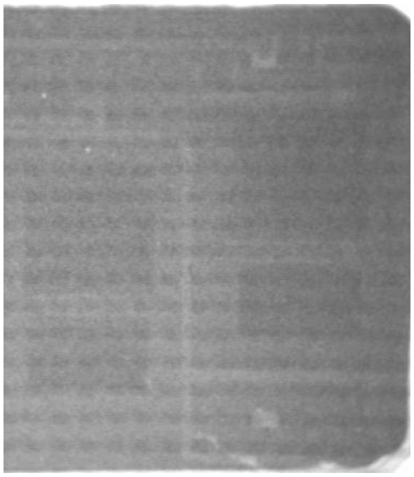

Figure 3-105: X-Ray Image of Good Solder Joints.

Parameters of the reflow operation were adjusted to improve the solder joints. Some of the parameters are:

- Heating ramp rate
- Pre-vacuum
- Time above liquidus

- Rate of vacuum
- Degree of vacuum
- Cooling ramp rate.

This effort resulted in high quality joints and relatively high yields, about 80%. While the yield needs to be much higher in high volume production, we are confident that this is the right path.

After reflow, the soldered substrates and dies must be cleaned to remove flux residue. Ultrasonic wire bonding is then used to connect the dies to the substrates. While these are industry standard processes, we spent effort to adapt the exiting processes to the new reflow and part geometry. As pointed out in the next section, bonding to insert-molded press-fit pin's landing pad proved to be a challenge. Together with the material optimization discussed in the next section, we adopted plasma cleaning to ensure a high quality bond.

Press-Fit Pins

Press-fit pins provide reliable joints between circuits and the multiple connections can be made with one short operation. While it has been widely used in signal connections in automotive electronics modules, its application in power circuits only exists in industrial application so far.

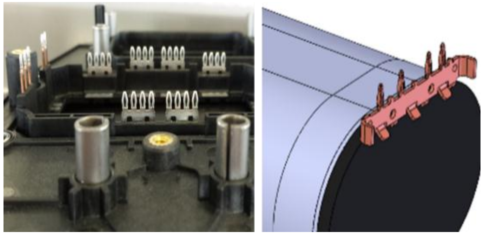

Figure 3-106: Press-fit Pins in Lead Frame and Film Capacitor.

In the Next Inverter Design, press-fit pins are used to connect:

- Power stage lead frame to DC and AC bus bars
- Power stage lead frame to Control/Gate Drive board
- Film capacitor bobbins to DC bus bars.

Fixtures and operation parameters were developed to press the bus bars and control/gate drive boards on to the lead frame. It is important to ensure the integrity of the components and solder joints on the PCB during this operation. Strain gauges were installed to monitor the deformation of the board during experimental operation. The keep-out areas were then optimized based on the result.

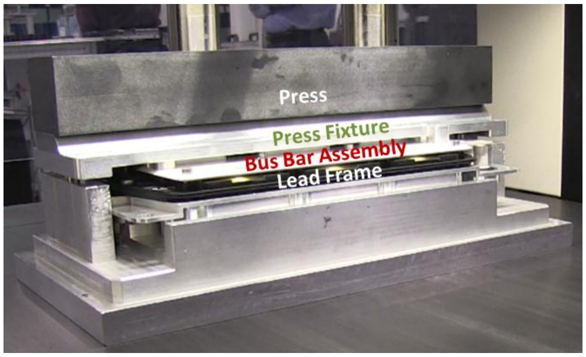

Figure 3-107: Pressing Bus Bar Assembly onto Lead Frame.

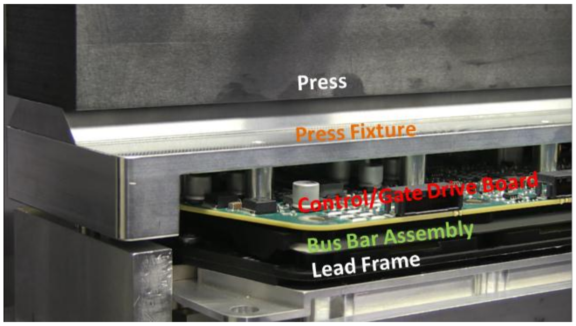

Figure 3-108: Pressing Control/Gate Drive Board onto Lead Frame.

Another aspect of the press-fit pins in the lead frame is that aluminum wire must be ultra-sonic bonded to the other end of the pins (landing pad). Various surface materials were tested. We achieved the best result with Al inlay method.

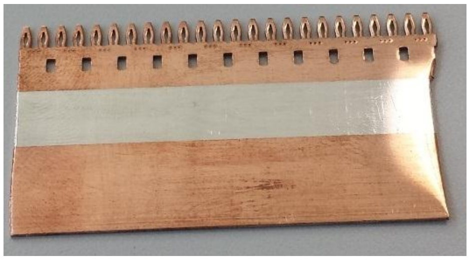

Figure 3-109: Press-Fit Pins with Al inlay, prior to Plating.

ENGINEERING TESTS

At the time of writing, units for engineering tests are being built. Six units have been delivered to our test lab and characterization test conducted to verify that they meet the design specification at the beginning of life (BOL). Total of 16 units will be built for the following tests:

- Fast power cycle
- Intermittent operation life
- High temperature and vibration
- Vibration fatigue life
- Power temperature cycling
- Infrared thermal survey
- High temperature high humidity
- Dyne performance test.

These tests are a subset of design validation tests General Motors requires from a production program. The results will give us indication whether the Next Generation Inverter can be ready for high volume production in 2020.

Conclusions and Future Directions

All tasks of Next Generation Inverter project have been progressing well. We were able to develop key manufacturing processes along with the chosen design. In FY15 we will carry out the engineering tests listed in the previous section. In addition to evaluating the inverter's performance against the stated targets, we will have solid data to best estimate the cost for this design.

After engineering tests, we will build the final units for delivery to DOE. We will also provide final cost estimate of this inverter. The manufacturing processes we studied and develop will make the cost model more accurate.

In parallel with the testing, we will continue to evaluate other technologies to enhance the inverter's performance, widen its scalable range and/or lower its costs. Some of these technologies are:

- Over molded power bus bar assembly
- Pressureless sintering
- Pick and place process for thin dies
- 3-D X-ray to evaluate solder joints on complex coolant manifold
- Replacing Si devices with wide band-gap devices to further increase the inverter's power density

FY 2014 Publications/Presentations

1. DOE Annual Merit Review Vehicle Technologies Program June 17, 2014.
2. DOE Vehicle Technologies Program Kickoff November 18, 2014.

3.8 Advanced, Integrated, Modular, and Scalable Wide Bandgap (WBG) Inverter R&D for Electric Traction Drive Vehicles

Kraig J. Olejniczak (Principal Investigator)

APEI
535 W. Research Center Boulevard
Fayetteville, AR 72701
Phone: (479) 443-5759, ext. 8393
E-mail: kolejni@apei.net

Ty R. McNutt, Ph.D., APEI Program Manager
Phone: (479) 443-5759, ext. 8170
E-mail: tmcnutt@apei.net

Partners:
Toyota Research Institute of North America (TRINA), GaN Systems, National Renewable Energy Laboratory (NREL)

Subcontractor:
University of Arkansas (UofA) National Center for Reliable Electric Power Transmission (NCREPT)

Start Date: October 2013
Projected End Date: September 2015

Objectives

The objectives of this R&D project are to:

- Develop two independent 55 kW traction drive designs (one SiC based and one GaN based) to showcase the performance capabilities of WBG power devices—namely high efficiency, increased gravimetric and volumetric density through high operating junction temperature capability.
- Demonstrate a substantial cost reduction from the die level to the system level.
- Optimize proven productized high temperature WBG power modules for increased manufacturability and reduced cost.
- Integrate existing APEI high temperature silicon-on-insulator (HTSOI) application-specific integrated circuit (ASIC) designs as a means to procure low-cost, high-reliability, high-temperature control circuitry.
- Apply advanced system-level packaging techniques to completely eliminate a vehicle's secondary cooling loop system, utilize 85°C rated capacitors, reduce the number of interconnects, and enable increased system reliability;
- Demonstrate design robustness and reliability through extended testing of subsystems and systems under realistic application-specific operating conditions.
- Complete a cost and manufacturing analysis to aid in the commercialization effort.

The goals of this research are to **reduce traction inverter size** (≥ 13.4 kW/L), **weight** (≥14.1 kW/kg), and **cost** (≤$182 / 100,000) while maintaining 15-year reliability metrics.

Technical Barriers

The following technical barriers have been identified and are listed in decreasing risk order:

- Unit cost: ≤ $182 unit cost / 100,000
- Ambient operating temperature: [-40 to +140°C]; and
  - A reduction in the upper limit of the ambient operating temperature range would significantly increase the candidate parts count within the designer's library.
- Weight: ≤ 3.9 kg (≤ 8.6 lbs.), largely due to cold plate.

Technical Targets

The Area of Interest 12, Advanced, Integrated, Modular, and Scalable Wide Bandgap (WBG) Inverter R&D for Electric Traction Drive Vehicles, inverter targets are summarized in Table 3-5 and Table 3-6 below.

Table 3-5: AOI 12 Inverter Targets

Requirement	Target
Continuous power output (kW)	30
Peak power output for 18 seconds (kW)	55
Weight (kg)	≤ 3.9
Volume (L)	≤ 4.1
Efficiency (%)	> 93
Unit Cost for quantities of 100,000 ($)	≤ 182
Operating voltage (V dc)	200–450; nominal: 325
Power factor of load	> 0.8
Maximum current per phase (A rms)	400
Precharge time – 0 to 200 V dc (sec)	2
Output current ripple – peak to peak (% of fundamental peak)	≤ 3
Maximum switching frequency (kHz)	20
Current loop bandwidth (kHz)	2
Maximum fundamental electrical frequency (Hz)	1000
Minimum isolation impedance-input and phase terminals to ground (MΩ)	1
Minimum motor input inductance (mH)	0.5
Ambient operating temperature (°C)	-40 to +140

Table 3-6: AOI 12 Thermal Management Subsystem Targets

Requirement	Target
Coolant inlet temperature (°C)	105
Maximum coolant flow rate (liters/min.)	10
Maximum coolant pressure drop (psi)	2
Maximum coolant inlet pressure (psi)	20

Accomplishments

- APEI completed the design, built, and performed initial testing of a 55 kW SiC inverter using state-of-the-art 25 mΩ SiC MOSFETs and 50 A SiC SBDs within APEI's HT-3201 power module.
- GaN Systems completed the design, to APEI's specification, of a 650 V, 100 A, enhancement-mode GaN HEMT power device.
- APEI completed a design to insert the high-current GaN HEMT power device into the HT-3000 series power module.
- TRINA has designed and fabricated an ultra-high performance cold plate with a heat transfer coefficient of ~ 35,000 W/m^2-K while meeting the targets in Table 3-6.

✧ ✧ ✧ ✧ ✧

Introduction

Widespread industry and consumer adoption of automotive electric traction drive vehicles promises to substantially decrease transportation costs, reduce environmental pollution and greenhouse gas emission, reduce reliance on non-renewable fuels, and increase energy independence from unstable foreign sources. In contrast to internal combustion powered vehicles, electric traction drive vehicles (either hybrid-electric or fully electric) are more energy efficient through the use of advanced energy storage systems, power electronics, and electric motors. However, several challenging technological and economic barriers exist presently which limit mass adoption of these electric drivetrain vehicles—many in the area of vehicular onboard power electronics. Specifically, dramatic reductions in subsystem cost, volume, and weight coupled with simultaneous improvements in power throughput, energy efficiency, operating temperature capability, and lifetime are needed to spur true competition in the automotive propulsion world.

The traction inverter is the power electronic heart of all electric traction systems and is responsible for converting stored DC electrical energy (typically in a battery) into precisely controlled three-phase AC power, allowing the electric motor to accelerate or decelerate the vehicle. Present-day traction inverters are simply too expensive, too heavy, and too bulky to penetrate the mass consumer automotive market—ultimately limiting the vehicle customer base to a moderately high-end subset of the population and necessitating additional economic incentives.

This DOE program seeks to advance the development and demonstration of next-generation WBG automotive traction inverter systems which directly address the barriers listed above. APEI, TRINA, GaN Systems, NREL, and the UofA NCREPT project team will develop two completely independent traction inverter systems in this program: one designed around the latest commercially available SiC power MOSFETs, and the other designed around emerging Gallium Nitride (GaN) power HEMTs, to meet and exceed the program specifications listed above. The team will develop both SiC and GaN inverter systems in parallel paths in order to make direct technological and system-level performance comparisons. This program will also explore advanced packaging and active cooling techniques to enable the use of widely-available 85°C-rated DC link capacitors in this 140°C ambient application.

Approach

This program will develop two 55 kW WBG traction inverters. In both cases, APEI will design "inside out"—from the power devices inside the power module to the outside world—to optimize the local and global system performance. This will be done specifically by:

- Using the highest current-carrying SiC MOSFET (1200 V, 25 mΩ) commercially available in the industry;
- Using the highest current-carrying, enhancement- mode GaN HEMT (650 V, 14 mΩ) available in the industry; and,
- Packaging them inside the highest current-carrying, smallest form factor, lightest weight, and highest performing commercially available WBG power module in the industry. The HT-3000 is shown in Figure 3-110.

Figure 3-110: HT-3000 series WBG power module.

This half-bridge power module is capable of up to 1200 V and 1000 A operation depending on the power devices used and system design constraints. The housing is made from a high-temperature packaging material, capable of 250°C operation, allowing it to accept all presently available WBG devices such as SiC BJTs, JFETs, MOSFETs, and GaN HEMTs.

Results

Design Cycle 1

In this section, the design work during Budget Period 1 is presented.

APEI's SiC-Based HT-3201 Power Module

Assuming a 7 SiC MOSFETs and 6 SiC SBDs per switch position, an ambient/case temperature of 25°C, a coolant loop of 105°C, a maximum junction temperature of 200°C, and a cold plate with a heat transfer coefficient, *h*, of ~ 35,000 W/m^2-K, then the maximum power dissipation for this module is estimated to be ~1710 W with a temperature distribution shown in Figure 3-111. The thermal resistance from junction to case is computed as 0.107 °C/W.

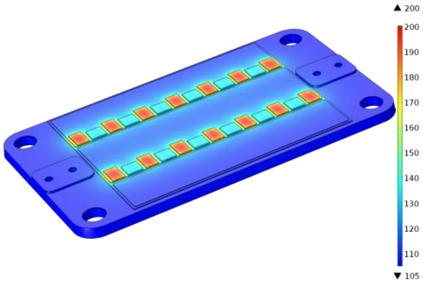

Figure 3-111: Temperature profile for the APEI HT-3201 power module with an estimated maximum power dissipation of 1710 W.

The 400 A (R_G = 5 Ω) turn-on and turn-off switching waveforms for the HT-3201 are shown in Figure 3-112.

Here, Channel 1 (yellow) is the (inverted) low-side source-drain current of the half bridge sensed across a 2.475 mΩ low inductance resistor. Channel 2 (cyan) is the 600 V bus voltage. Channel 3 (magenta) is the low-side drain-source voltage. And lastly, Channel 4 (green) is the gate signal. The resulting turn-off and turn-on energy losses are easily computed from the data acquisition of the waveforms shown in Figure 3-112. Numerical integration of the instantaneous power *p*(*t*) at turn-off and turn-on result in switching energy losses of approximately 9 mJ and 12 mJ, respectively.

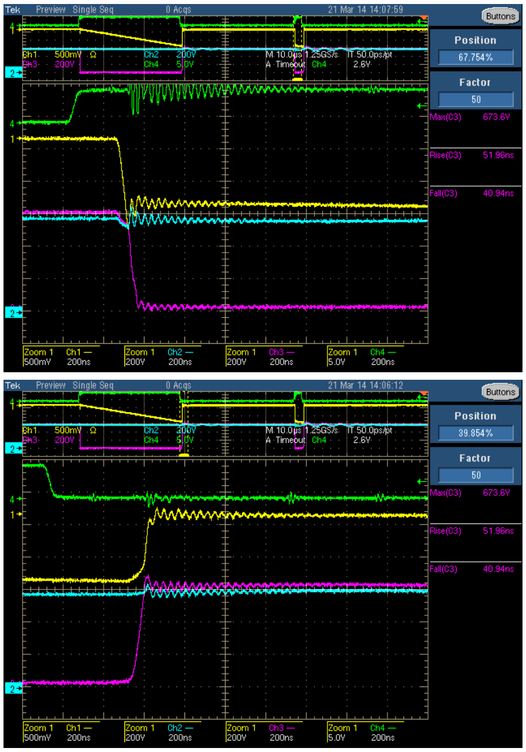

Figure 3-112: HT-3201 turn-on (top) and turn-off (bottom) switching waveforms. (Bus voltage = 600 V, (Inverted) Current = 400 A).

APEI's GaN-Based HT-3000 series power module

The APEI GaN-based HT-3000 series power module design is based on GaN Systems GS66540C device shown in Figure 3-113. This is a 650 V, 14 mΩ, enhancement-mode GaN HEMT power device which is rated for 100 A of current at 25°C. With a case temperature of 100°C, the current is derated to 70 A. Assuming 4 GaN HEMTs per switch position, an ambient/case temperature of 25°C, a coolant loop of 105°C, a maximum junction temperature of ~150°C, and a cold plate with a heat transfer coefficient, *h*, of ~ 10,000 W/m^2-K, then the maximum power dissipation for this module is estimated to be 580 W with a temperature distribution shown in Figure 3-114. The thermal resistance from junction to case is computed as 0.092°C/W. While packaging of the

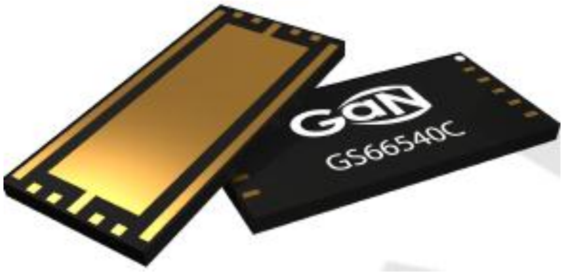

Figure 3-113: GaN Systems GS66540C GaN HEMT power device in the GaNPX™ package. (Courtesy of GaN Systems)

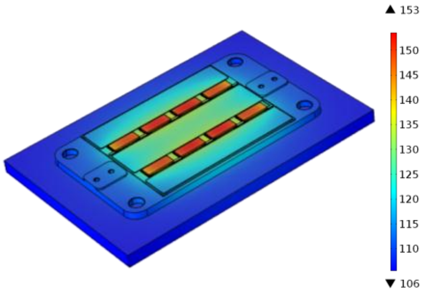

Figure 3-114: Temperature profile for the APEI's GaN-based HT-3000 power module with an estimated maximum power dissipation of 580 W.

C40 progresses, APEI is using GaN Systems' GS66508P for process development. This is a 650 V, 52 mΩ, enhancement-mode GaN HEMT device which is rated for 30 A of current at 25°C. With a case temperature of 100°C, the current is derated to 20 A. Using 5 GS66508P devices per switch position, 150 A capability can be realized at 25°C and 100 A at 100°C. The package is shown in Figure 3-115.

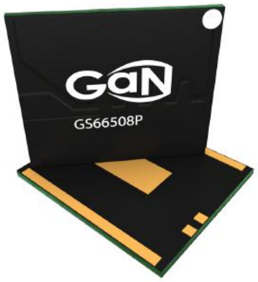

Figure 3-115: GaN Systems 650 V, 52 mΩ, GaN HEMT in their GaNPX package. APEI is using this package for process development while the C40 package is finalized. (*Courtesy of GaN Systems*)

Once static characterization was completed, the 40 A (RG = 49.9 Ω, albeit a conservative value) turn-on and turn-off switching waveforms for the GS66508P devices were obtained as shown in Figure 3-116. Here, Channel 1 (yellow) is the source-drain current of the device sensed across a 2.475 mΩ low inductance resistor. Channel 2 (cyan) is the drain-source voltage. Again, the resulting turn-on and turn-off energy losses are easily computed from the data acquisition of the waveforms shown in Figure 3-116. Numerical integration of the instantaneous power p(t) at turn-on and turn-off result in preliminary switching energy losses of approximately 750 μJ and 170 μJ, respectively.

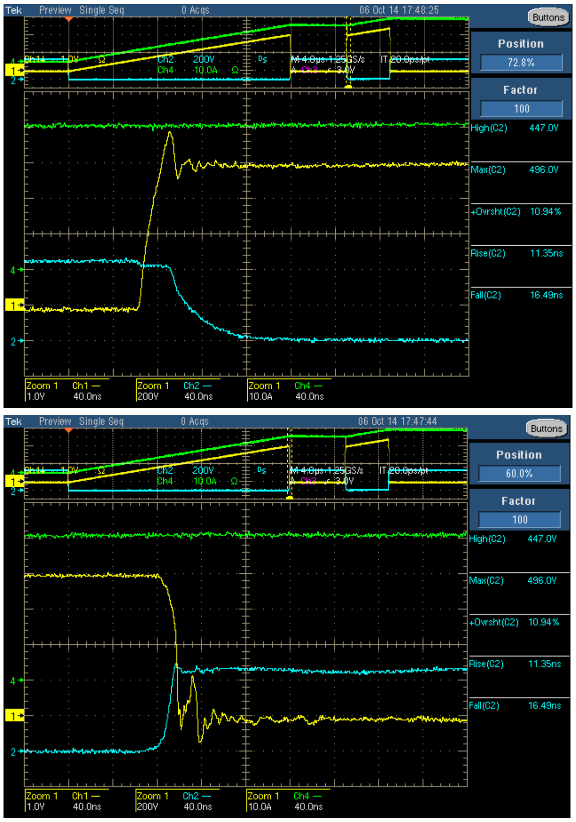

Figure 3-116: GaN Systems GS66508P power HEMT turn-on (top) and turn-off (bottom) switching waveforms. (Bus voltage = 450 V, Current = 40 A).

System Packaging Metrics

The program targets are now discussed below based on the present status of the Design Cycle 1 WBG inverter.

AOI 12 Target 1: Continuous power output, 30 kW

APEI will over-deliver on the 30 kW continuous output power target for the SiC inverter. Three-phase, low-power dynamometer testing is underway with high-power dynamometer testing to be complete by the end of Budget Period 1, January 15, 2015. The GaN inverter capability can only be conjectured at this time based on the GS66508P device performance. The GS66540C is expected to arrive by the end of 2014 or Q1 of 2015.

The APEI WBG inverter is fully modular. Success in market insertion is based on an "optimized" level of integration (i.e., not too much and not too little) among the dc/dc converter, required EMI filters, and inverter based on the particular application. Clearly, APEI seeks a design which not only satisfies this program but also is commercializable.

The APEI WBG inverter is fully scalable. Providing the die will fit within the module switch positions, power levels from 55 kW to 120 kW and beyond are possible leveraging the same optimally designed power module. Of course, adjustments must be made in other subsystems like the enclosure, cold plate (whether COTS or custom), bussing, dc bus capacitance, etc.

AOI 12 Target 2: Peak power output, 55 kW for 18 seconds

APEI will over deliver on the 55 kW peak for 18 seconds output power target for the SiC inverter. Three-phase, low-power dynamometer testing is underway with high-power dynamometer testing to be complete by the end of Budget Period 1, January 15, 2015. Again, the GaN inverter capability can only be conjectured at this time based on the GS66508P device performance. The GS66540C is expected to arrive by the end of 2014 or Q1 of 2015. The cold plate design (i.e., COTS vs. custom) and performance (heat transfer coefficient, *h*) will impact the maximum peak power capability performance.

AOI 12 Target 3: Weight, ≤ 3.9 kg

The weight of the Design Cycle 1 WBG inverter is presently 5.6 kg with a COTS cold plate contribution of 1300 g. Viewing Figure 3-117 below, the three components contributing the most to the total weight are: the enclosure, the cold plate, and the bussing. The enclosure, now a HT plastic weighing 1117 g, will more than double in weight by switching to a standard Al alloy (i.e., 2414 g). The existing *h* = ~ 20,000 W/m-K COTS cold plate weighs in at 1300 g. A high-performance, custom- designed cold plate with an approximate *h* = ~ 35,000 W/m-K is estimated to weigh 1561 g and 962 g with lightweighting materials used. The bussing, current sensors, and miscellaneous hardware weigh in at 1271 g. The present copper bussing could be lightweighted by again switching to an aluminum alloy. This could reduce the bussing weight by 50–70% depending on the required ampacity.

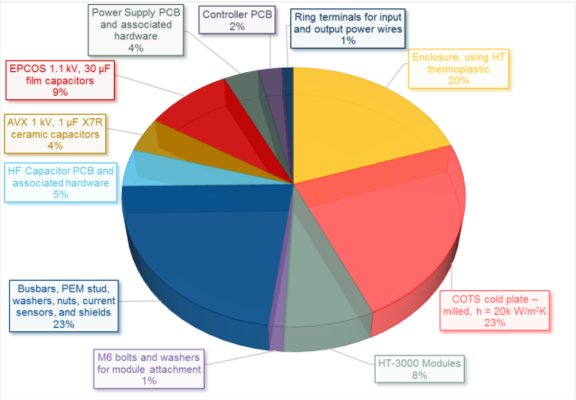

Figure 3-117: Percent weight distribution of the Design Cycle 1 WBG inverter.

AOI 12 Target 4: Volume, ≤ 4.1 liters

The internal and external volumes of the Design Cycle 1 WBG inverter are 4.08 and 4.25 liters, respectively. Total component volume is approximately 1.5 liters. Viewing Figure 3-118 below, the three components contributing the most to the total volume are: the cold plate, the DC bus capacitors, and the power modules. Air accounts for 64% of the total volume. Design Cycle 2 will focus on minimizing the total volume by minimizing the required number of DC bus capacitors and eliminating as much air space as possible.

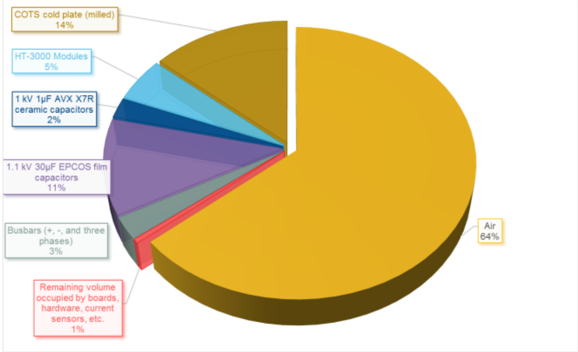

Figure 3-118: Percent volume distribution of the Design Cycle 1 WBG inverter.

AOI 12 Target 5: Efficiency, > 93%

The WBG inverter efficiency, for both the SiC- and GaN-based designs, will surpass the 93% peak efficiency target at many points within the traction motor's torque versus speed space. This assumes a 105°C cooling loop. Peak efficiencies greater than 99% are possible, and expected, based on loading and DC bus voltage levels.

Figure 3-119, APEI's peak efficiency target is bounded by the blue polygon whose base lies on the *x*-axis from 10 to 40 kW. The operating points under light loading are of specific interest to APEI and will be interrogated in detail using the UofA NCREPT high-power dynamometer test bed. The SiC- and GaN-based inverter efficiencies will be directly compared (i.e., operating point by operating point) to that of a commercial silicon IGBT-based inverter over the entire custom traction motor's design space.

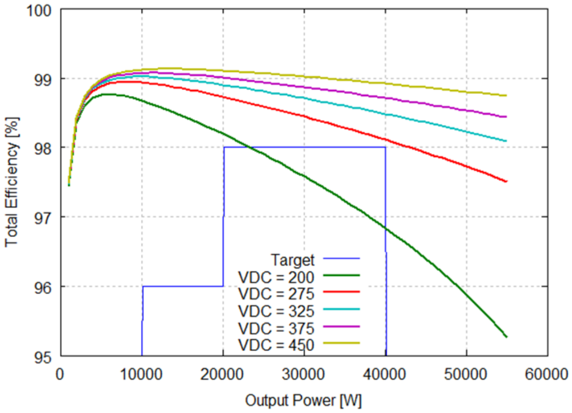

Figure 3-119: Estimated WBG inverter efficiency versus output power for various DC bus voltage levels.

AOI 12 Target 6: Unit Cost in Quantities of 100,000

The unit cost of < $182 in quantities of 100,000 has been identified by APEI as a technical barrier above. This target is difficult to achieve based on the technical trade-offs required by the designers using limited parts which satisfy *both* temperature and 15-year reliability targets of the system. In general, parts are priced higher when rated beyond > 85°C. This is true for military- and automotive-grade parts.

Preliminary WBG inverter BOM analysis estimates the unit cost at approximately $2181 using pricing information available from online resources. In many cases, the pricing was not available at the 100,000 unit level; thus, pricing was taken from the highest volume provided. This preliminary unit cost excludes the three (3) APEI power modules. “Big ticket” items include: power modules, bus bars, custom magnetics, gate driver IC, high frequency capacitors, custom connectors, high temperature DSP controller, cold plate, and high performance TIM. Further refinement will be done in Budget Periods 1 and 2.

AOI 12 Target 7: Operating Voltage

The DC bus voltage is 200 to 450 V, nominal 325 V. The APEI target for a GaN-based inverter is 200–450 V. The APEI target for a SiC-based inverter is 200–650 V. The SiC inverter uses Cree 1200 V, 25 mΩ, 90 A @ T_{case} = 25°C; 60 A @ T_{case} = 100°C. The GaN-based inverter (Design Cycle 1): utilizes GaN Systems, 650 V, 52 mΩ, 30 A @ T_{case} = 25°C; 20 A @ T_{case} = 100°C. The GaN-based inverter (Design Cycle 2) will utilize GaN Systems, 650 V, 14 mΩ, 100 A @ T_{case} = 25°C; 70 A @ T_{case} = 100 °C.

AOI 12 Target 8: Displacement Power Factor

The load power factor target is > 0.8 leading or lagging. APEI will satisfy this target power factor.

AOI 12 Target 9: Maximum Current Per Phase, 400 A rms

Figure 3-120 shows a simulation of the junction and case temperatures for the HT-3201 power module assuming 7 SiC MOSFETs, 6 SBDs, 10 μΩ contact resistance per bolt, and a 0.01°C/W cold plate.

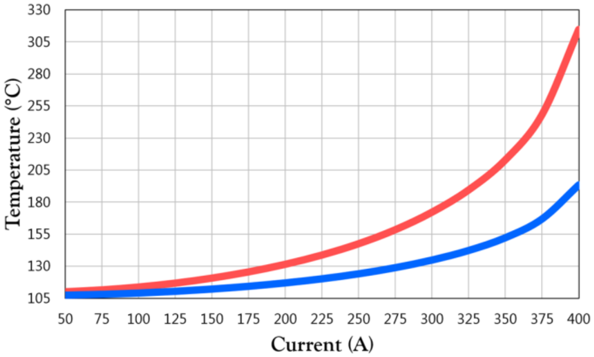

Figure 3-120: Junction (red) and case (blue) temperatures versus current.

See Figure 3-112 for 400 A rms switching. The HT-3201 power module has been demonstrated operating at 50 kHz, 400 A rms with a coolant temperature up to 125°C.

AOI 12 Target 10: Pre-charge Time; 0 to 200 V Within 2 seconds

This target is normally achieved via a soft-charge circuit. Usually a resistor “pre-charge” circuit in parallel with either a relay or solid-state switch is used. When the inverter uses small IGBTs instead of resistor to limit power going to the capacitors, it is referred to as an active soft charge. The main goal is to restrict the inrush current going to the DC link capacitors.

In the APEI case, a programmed DC power supply is used to ramp the voltage with a dv/dt = 100 V/s. Proper sequencing of the inverter is used and required.

AOI 12 Target 11: Output Current Ripple – Peak to Peak; ≤3% of Fundamental Peak

The output current ripple is independent of the power being transferred; i.e., $i_{ripple} = f(L, v_{ripple})$ at the load. Large values of the frequency modulation ratio, $m_f = f_s / f_1$, where f_s is the switching frequency and f_1 is the modulating frequency, will result in the current ripple being significantly lower compared to a square-wave inverter. Switching at high frequencies (e.g., > 20 kHz), the motor inductance will smooth the current to minimize the output current ripple.

AOI 12 Target 12: Maximum Switching Frequency & AOI 13 Current Loop Bandwidth

Controller testing to date has shown that a current rise time for the responses in both i_D and i_Q are less than ¼ millisecond. This corresponds to a current loop bandwidth of 4 kHz. There is almost no overshoot indicating a well-damped response. Switching is at 20 kHz; the entire control loop also runs at a 20 kHz update rate. On the APEI inverters, switching will remain at 20 kHz, but by using a double-update mode, the controller will run at 40 kHz which will only further improve the current loop bandwidth.

The APEI controller board has been running the full controller at 40 kHz using ~57% of the CPU time available. This indicates that faster switching is possible. Single- vs. double-update would result in a switching frequency of 60 kHz. Running the controller once for every two (2) PWM cycles can increase the switching frequency up to 120 kHz. Through code optimization, the controller should be able to run faster than a 60 kHz update rate leading to a > 120 kHz switching frequency and current loop bandwidth on the order of > 10 kHz.

AOI 12 Target 14: Maximum Fundamental Electrical Frequency is 1000 Hz

The controller was tested and easily able to synthesize a modulating frequency of 1000 Hz based on the high switching frequencies discussed previously.

AOI 12 Target 15: Minimum Isolation Impedance-Input and Phase Terminals to Ground is > 1 MΩ

APEI has measured the isolation impedance of its Design Cycle 1 WBG inverter and in all cases it is > 200 MΩ which is the limitation of our measurement equipment.

AOI 12 Target 16: Minimum Motor Input Inductance

The traction motor under test must possess an inductance greater than 0.5 mH. The custom-designed Baldor/ABB PMSM has an input inductance > 0.5 mH.

AOI 12 Target 17: Ambient Operating Temperature

The ambient operating temperature is specified to be -40 to +140°C. As stated in the Technical Barriers section above, APEI has identified this target as one of three with the highest risk in the project. To date, APEI has generated a BOM for its Design Cycle 1 WBG inverter. The parts selected are all rated 125°C and above except one. On the gate driver power supply board, one adjustable voltage reference shunt is rated at 85°C; however, an alternate part exists with a 125 °C rating but at a higher cost.

The one component which poses the biggest challenge is selection of the DC link film capacitors. The main issue here is the tension that exists among the following three variables: cost, maximum temperature rating, and electro-thermal-mechanical performance at 85°C. APEI chose to seek and use film capacitors rated at 105°C because they will have a nonzero ripple current at 85°C, are commercially available and have defendable pricing in quantity, and have the best overall performance when accounting for the following concerns:

- Voltage blocking capability as a function of temperature
- Capacitance stability as a function of temperature and voltage
- Equivalent impedance
- Footprint
- Volume
- Weight
- RMS ripple current @ 85°C
- ESR / losses
- ESL / resonant frequency
- Insulation resistance
- Thermal resistance from core to case
- Reliability data / life expectancy.

Design and Fabrication of a Low-Power Dynamometer Test Bed for Embedded Controller Testing

To minimize project risk when testing the APEI WBG inverters driving the Toyota-emulating 75 HP PMSM, a low-power dynamometer (LPD) was constructed as shown in Figure 3-121. Initially, this LPD was driven using the commercially available Texas Instruments HVMC kit. This combination has allowed testing over a wide range of speeds and torques including the high-speed flux-weakening region where control is more difficult. Next, the APEI inverter is tested on the LPD to ensure correct operation of the controller and protections. Additionally, any time changes are made to the controller firmware, the new version will be regression tested using the LPD prior to running on the UofA NCREPT high-power dynamometer.

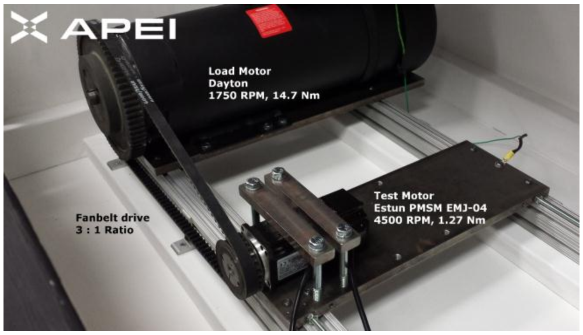

Figure 3-121: APEI low-power dynamometer: UUT and load motor.

The LPD test motor is a 400 W PMSM (Estun Model EMJ-04) coupled with a fan belt to a Dayton 2.5 kW DC permanent magnet load motor. The output of the load motor is attached to an Avtron load bank to provide a variable-torque load. A LabVIEW-based data acquisition system is under construction to record the voltages and currents in this system. This makes use of a NI PXI chassis equipped with two multifunction data acquisition cards (Type PXI-6233) and a CANopen card (Type PXI-8531). This combination will allow a unified LabVIEW application to both collect data and issue commands to the inverter over the CANbus interface. Figure 3-122 shows the risk-mitigating LPD setup.

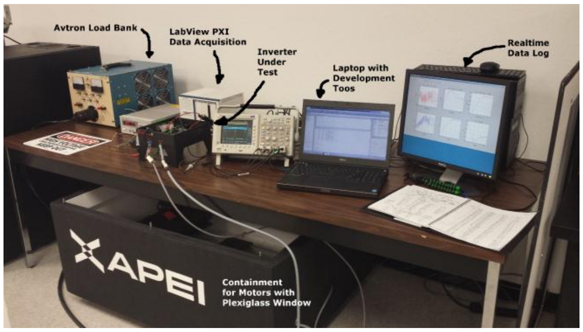

Figure 3-122: APEI low-power dynamometer setup for embedded controller testing.

Design and Fabrication of a High-Power Dynamometer Test Bed for WBG Inverter Testing

A one-line diagram and photos of the integrated test bed are shown in Figure 3-123, Figure 3-124, and Figure 3-125. The permanent installation of the ABB drive (sitting on its wooden shipping base) is planned during Budget Period 2 of this project.

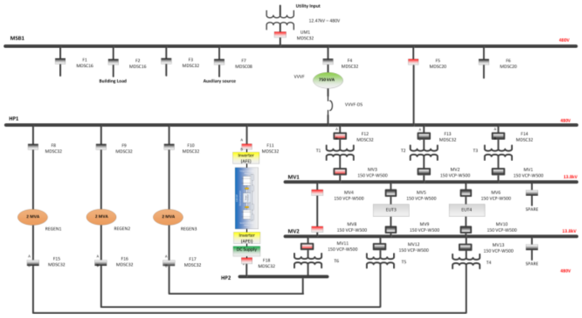

Figure 3-123: One-line diagram showing the dynamometer's placement within the UofA NCREPT's power system.

Figure 3-124: The completed dynamometer installation.

Figure 3-125: The motors, sensors, and dynamometer frame.

The design of the initial prototype traction inverter was optimized for high power density, high performance, and low cost. SolidWorks® was used to design the traction inverter system. For the analysis of the system, COMSOL Multiphysics® was utilized to model some of the key thermal and electrical characteristics of the systems such as the bus bar inductance as well as the internal temperature of the system. Figure 3-126 shows the complete design rendering of the traction inverter system. The heart of the system is three half-bridge HT-3000 modules connected in a six-pack configuration. High current, low inductance bus bars were design to connect the power modules to external connectors, DC capacitors, and control boards. Different bus bar schemes were evaluated in terms of ease of assembly, cost, and performance (i.e., inductance).

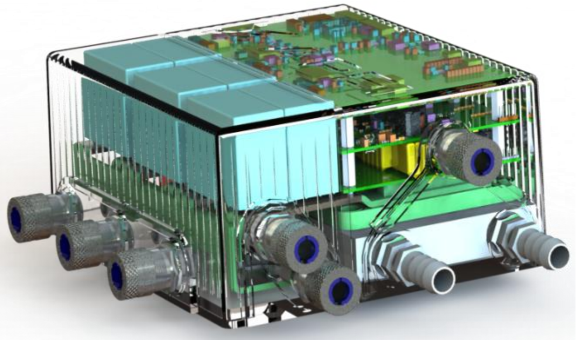

Figure 3-126: A rendered CAD image of the DOE VTP inverter assembly with a transparent enclosure.

Three approaches consisting of a laminated scheme, a simple powder coat design with copper pillar connections to the HF capacitor PCB, and an additional simple powder coat design with copper rail connections for the HF capacitor board were analyzed. The different designs can be seen in Figure 3-127. In terms of cost, the simple powder coat designs initially seem to be the best choice. For assembly, all of the options are very similar with the laminated scheme being slightly easier to assemble since it comes as one unit. The main issue with a single bus structure is tolerance stack-up. If the tolerances of the components are greater than the tolerance of the laminated process then the bolt holes will not align. In most cases, this can be achieved by reducing the tolerance of components but, unfortunately, this comes with a cost.

It was highly desirable to model the inductances associated with each bussing design. Figure 3-128 shows the inductance of each of the bus bar designs as a function of frequency. As expected, the laminated bussing design has a lower inductance over frequency compared to the simple powder-coated designs, which is smaller by 1 nH. At this point in the design cycle, this additional inductance of 1 nH should have a minimal effect on the electrical performance. However, the research team at APEI is working on a higher performance design that has demonstrated a simulated inductance in the 1.5–2 nH range.

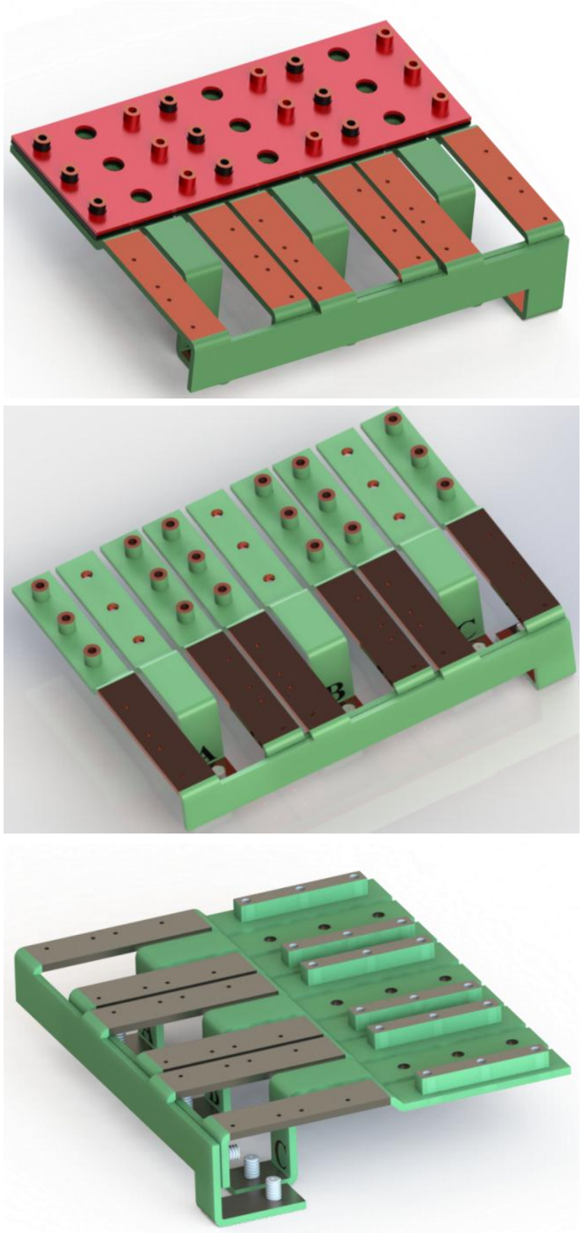

Figure 3-127: Rendered CAD images that show three different bus bar designs which include (top) a laminated bussing approach and non-laminated approaches that use (middle) vertical pillars and (bottom) copper bar connections to allow for a low-inductance connection to the HF capacitor PCBs in the stack-up above.

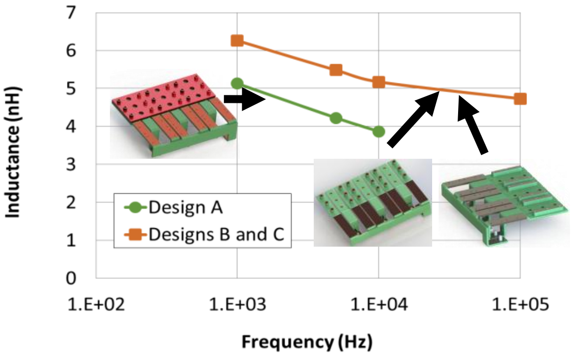

Figure 3-128: A comparison of the inductance as a function of frequency for the different bussing designs.

Figure 3-129 shows the assembled traction inverter with and without the enclosure lid. For size demonstration purposes, the enclosure was 3D printed. The APEI/Toyota/NREL research team is presently investigating different enclosure materials which include aluminum, high temperature plastic, and a high temperature plastic composite material. APEI will evaluate the cost vs. performance benefits for each option. The present weight and volume is 5.62 kg and 4.32 L, respectively.

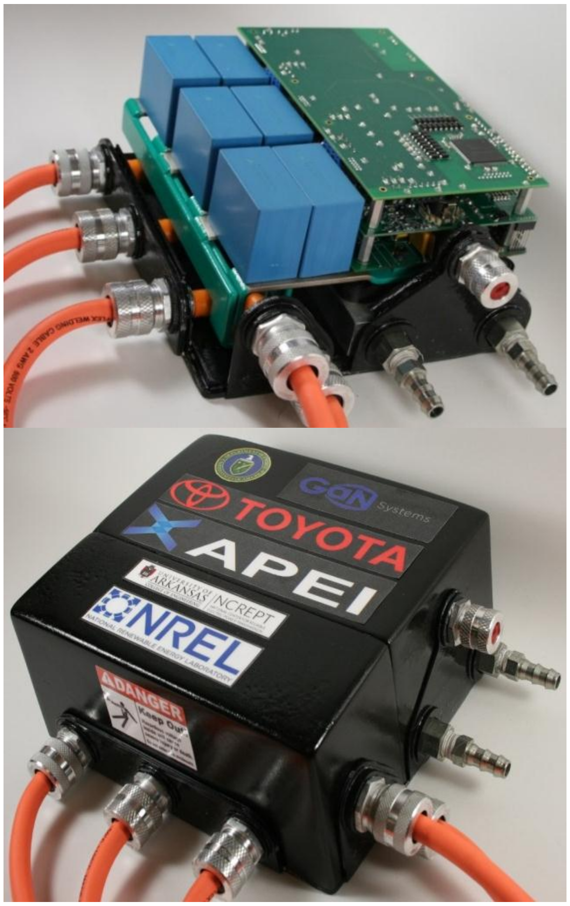

Figure 3-129: The assembled DOE VTP inverter without (top) and with (bottom) the enclosure lid.

Conclusions and Future Directions

This annual report provides an overview on the work performed to date by the APEI team during Budget Period 1 which will end on January 15, 2015.

The future direction of this project is moving on to Design Cycle 2 for the SiC-based inverter, testing of the Design Cycle 1 SiC-based inverter, packaging of the Design Cycle 1 GaN-based inverter, and preparing for SiC-based inverter testing in a high ambient environment (i.e., up to 140°C).

FY 2014 Publications/Presentations

1. Adam Barkley, “Advanced Low-Cost SiC and GaN Wide Bandgap Inverters for Under-the-Hood Electric Vehicle Traction Drives,” FY14 VTO Kickoff Meeting, ORNL, Oak Ridge, TN, November 5–7, 2013.
2. Kraig Olejniczak and Ty McNutt, “Advanced Low-Cost SiC and GaN Wide Bandgap Inverters for Under-the-Hood Electric Vehicle Traction Drives,” Technical Kickoff and Review Meeting, U.S. Department of Energy, Washington, D.C., February 27, 2014.
3. Dr. Brandon Passmore, “Three-Dimensional Packaging for Wide Bandgap Based Discrete and Multi-Chip Power Packages,” Paper IS1-5-7, APEC, Fort Worth, TX, March 18, 2014.
4. Ty McNutt and Kraig J. Olejniczak, General overview of APEI and SiC motor drives, (via teleconference), 21st Century Truck Partnership, April 22, 2014.
5. Kraig J. Olejniczak, “Advanced Low-Cost SiC and GaN Wide Bandgap Inverters for Under-the-Hood Electric Vehicle Traction Drives,” U.S. Department of Energy Vehicle Technologies Office Annual Merit Review and Peer Evaluation Meeting, Washington, DC, June 16-20, 2014.
6. Kraig J. Olejniczak, “Advanced Low-Cost SiC and GaN Wide Bandgap Inverters for Under-the-Hood Electric Vehicle Traction Drives,” U.S. Department of Energy Vehicle Technologies Office On-Site Project Review Meeting, Fayetteville, AR, September 24, 2014.
7. Kraig J. Olejniczak, Ty R. McNutt, Brandon Passmore, Chad O’Neal, “Manufacturing Low-Cost High-Voltage SiC Power Modules,” NIST/DOE Workshop on High-Megawatt Direct-Drive Motors and Front-End Power Electronics, Gaithersburg, MD, September 4, 2014.
8. Kraig J. Olejniczak, “Advanced Low-Cost SiC and GaN Wide Bandgap Inverters for Under-the-Hood Electric Vehicle Traction Drives,” (via teleconference), Electrical & Electronics Technical Team, USCAR, September 25, 2014.

3.9 High-Temperature Air-Cooled Power Electronics Thermal Design

Scot Waye *(*Principal Investigator*)*

National Renewable Energy Laboratory (NREL)
Transportation and Hydrogen Systems Center
15013 Denver West Parkway
Golden, CO 80401
Phone: (303) 275-4454
E-mail: scot.waye@nrel.gov

Susan A. Rogers, DOE Technology Development Manager
Phone: (202) 586-8997
E-mail: susan.rogers@ee.doe.gov

Sreekant Narumanchi, NREL Task Leader
Phone: (303) 275-4062
Email: sreekant.narumanchi@nrel.gov

Start Date: FY11
Projected End Date: FY14

Objectives

The overall project objective is to develop and apply air-cooling technology to improve power electronics thermal management design and influence industry, enhancing system performance to help meet the U.S. Department of Energy (DOE) Electric Drive Technologies (EDT) Program power electronics technical targets for weight, volume, cost, and reliability. This overall objective includes the following:

- Develop and demonstrate commercially viable, low-cost air-cooling solutions for a range of vehicle applications and assess their potential for reducing the cost and complexity of the power electronics cooling system.
- Enable heat rejection directly to ambient air, simplifying the system by eliminating liquid coolant loops, thereby improving weight, volume, cost, and reliability.
- Collaborate with Oak Ridge National Laboratory (ORNL) to demonstrate the feasibility of using a high-temperature, air-cooled inverter to achieve DOE technical targets.
- FY 14 objectives included:
  - Prototype and test optimized heat exchanger. Improve models based on test results. Down select best design for prototype module
  - Test baseline and optimized heat exchangers. Extrapolate results to inverter level, including balance-of-inverter components and balance-of-system metrics
  - Within electrical topology constraints, test module-level heat exchanger design for thermal performance. Results will feed into improved design and future high-temperature, air-cooled inverter demonstration with ORNL.

Technical Barriers

The use of air as a coolant has several benefits, drawbacks, and challenges. Air is free, it does not need to be carried, it is benign (no safety or environmental concerns), and it is a dielectric. As a heat transfer fluid, however, it has a number of drawbacks. Air has a low specific heat, low density, and low conductivity. These make it a poor heat transfer fluid and cause a number of design challenges. To reject the high power densities required by electric-drive power electronics using the heat transfer coefficients achievable with air, large increases in wetted area are needed. When increasing the wetted area, spreading resistance, fin efficiency, weight, volume, and cost need to be considered. Due to the low specific heat, larger mass flows of air are required to remove the heat. This can lead to parasitic power issues, especially coupled to the pressure loss of extended surfaces. This requires careful consideration of the system coefficient of performance. Depending on the location of the inverter, environmental loads and ducting to better air sources may need to be considered. Location can also affect the need for noise suppression for the prime mover (blower/fan). For example, the Honda system incorporated a silencer [1] because the inverter was located in the passenger compartment. To push heat transfer performance higher, small-channel heat exchangers can be used, but filtering must be addressed. If needed, filtering can add pressure drops and maintenance issues may need to be addressed.

Technical Targets

The 2015 and 2020 DOE EDT Program technical targets for power electronics are applicable for a 30-kW continuous and 55-kW peak power inverter.

Accomplishments

- Shifted modeling efforts that optimized heat exchanger geometries to experimental efforts.
- Tested baseline and optimized sub-module heat exchangers for maximum junction temperatures of 150°C to 300°C.
- Extrapolated results to inverter scale.
- Target heat load of 2.7 kW was dissipated at various flow rates for each of the configurations.
- Combining optimized heat exchanger with other inverter components (excluding housing), estimated power density and specific power exceeded 2015 technical targets.
- Module-level heat exchanger tested with one-side and two-side heat generation, dissipating 150 kW to 450 kW of heat with maximum junction temperatures of 150°C to 300°C.

✧ ✧ ✧ ✧ ✧

Introduction

All commercially available electric-drive vehicles, with the notable exception of the low-power Honda system, use liquid-cooled power electronics systems. All the heat from a vehicle, however, must ultimately be rejected to the air. For liquid-cooled systems, heat from the power electronics is transferred to a water-ethylene glycol coolant via a heat exchanger and then pumped to a separate, remote liquid-to-air radiator where the heat is rejected to the air. Air cooling has the potential to eliminate the intermediate liquid-cooling loop and transfer heat directly to the air.

Eliminating the intermediate liquid-cooling loop using direct air cooling of the power converter can reduce system complexity and cost by removing or reducing the pump, coolant lines, remote heat exchanger, remote heat exchanger fan, and coolant. To realize these gains, however, effective system-level design of the direct air-cooled system heat exchanger, fan, and ducting is needed. Decoupling the inverter/converter from the liquid cooling system also has the potential to provide increased flexibility in location. Honda took advantage of this benefit by placing its 12.4-kW power electronics system behind the rear seat of the vehicle cabin and integrating it closely with the battery thermal management system [1].

As power electronics semiconductor and electronic packaging technology advances, higher allowable junction temperatures will further expand the feasible designs and benefits of direct air-cooled power electronics. Currently, silicon insulated gate bipolar transistors have a maximum allowable junction temperature between 125°C and 150°C [2,3] that may be extended to 175°C in the future [3], while advanced semiconductor technologies such as silicon carbide (SiC) and gallium nitride allow operation above 200°C [4–6] and may also improve the inverter efficiency at lower temperatures [5].

The Honda system is a mass-produced, commercially available solution. It is low power, however, with a peak power delivery of 12.4 kW [1]. The electric Mini-E uses an air-cooled AC Propulsion drive system. This has a 50-kW continuous, 150-kW peak power, but does not meet DOE technical targets and the volume of production is low [7]. Toshiba Corporation is researching and developing a new power module design for forced-air cooling systems for a power converter [8]. ETH Zurich University has published a number of studies on this topic recently and is actively researching high-temperature, air-cooled power electronics for automotive and other applications. One of these papers found that, combined with a Peltier element, a high-temperature SiC automotive inverter could operate at a 120°C ambient [9]. Another reports the possibility of using extremely high-temperature SiC devices (234°C and higher) to create an air-cooled electric-drive vehicle inverter with a power density of 51 kW/L and operating at 120°C ambient [10]. For aggressive, high-flux cooling of electric-drive vehicle inverters, Aqwest is investigating circulating liquid metal flow loops to enable forced-air cooling [11].

Approach

Project

- Use a system-level approach that addresses the cooling technology, package mechanical design, balance-of-system, and vehicle application requirements
- Research each of these areas in depth and apply findings to develop effective system-level designs
- Develop experimental and analytical/numerical tools and processes that facilitate high-quality and rapid research results
- Investigate the effect high-temperature power semiconductor devices have on air-cooled inverter design
- Work closely with industry, university, and national laboratory partners to ensure relevant and viable solutions.

The objective of this project is to assess, develop, and apply air-cooling technology to improve power electronics thermal management design and influence industry's products, thereby enhancing the ability to meet DOE technical targets for weight, volume, cost, and reliability. This research effort seeks to develop the necessary heat transfer technology and system-level understanding to eliminate the intermediate liquid-cooling loop and transfer heat directly to the air. The relative merits of air-cooled, high-heat-flux automotive power electronics thermal management systems and the influence of high-temperature, wide bandgap semiconductors on this design space will be quantified, evaluated, and demonstrated under steady-state and transient conditions. See previous reports for more detail on the overall project objectives [12].

In FY14, an optimized heat exchanger was down selected after modeling efforts examined various geometric configurations. Baseline and optimized sub-modules were fabricated and tested to validate dissipation of the target heat load. A module-level heat exchanger that took into account the desired electrical topology was fabricated and characterized.

Experimental Methods

A baseline air-cooled heat exchanger consisting of an aluminum heat sink with equally spaced rectangular channels was proposed [13]. Devices would be mounted to both sides to use the channel wall fins more effectively. The design incorporated nine modules for a full inverter with a 30-kW continuous and 55-kW peak (for 18 seconds) electrical power output. This design did not meet targeted 12-kW/L power density and 12-kW/kg specific power requirements, proposed as 2015 targets by the U.S. DRIVE Electrical and Electronics Technical Team [14]. For this inverter size and number of devices, the total power loss to heat was conservatively estimated to be 2.7 kW (using device loss information and analytical equations) [12].

Through a parametric computational fluid dynamics study, the heat sink was optimized for weight and volume by varying geometric parameters, including channel height, length and width, and device location. A constant heat flux was simulated for the devices, and the maximum allowable junction temperature for any device was set at 175°C. Two heat fluxes were investigated: one for an inverter with nine modules, and a higher flux for an inverter with six modules (lower weight and volume, but higher current and losses in each device). From this study, an optimized design was selected that met the specific power and power density targets [12].

Sub-module heat exchangers, which represent one-sixth of a full module, were prototyped for the baseline and optimized geometries from 6063 aluminum using wire electrical discharge machining (see Figure 3-130). A module-level heat exchanger was fabricated after sub-module testing and interaction with the electrical component layout. For mass manufacturing, final module-level heat exchangers could be manufactured using extrusion methods.

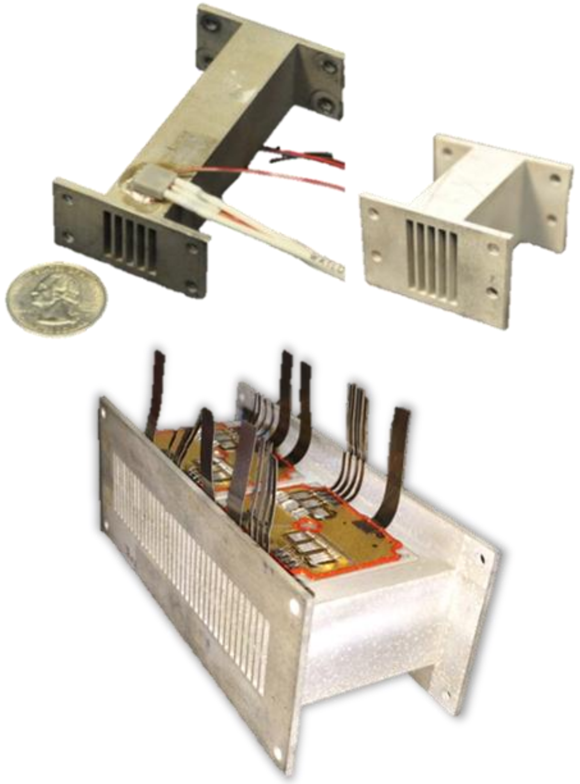

Figure 3-130: Baseline sub-module (top left), optimized (top right) sub-module, and module-level (bottom) heat exchangers fabricated from 6063 aluminum. Heaters are mounted on the top and bottom of the test section, one near the inlet edge and the other farther back. The flanges are for experimental convenience. The module-level heat exchanger shows electrical components mounted (tested by ORNL). Photo credit (bottom): Madhu Chinthavali, courtesy ORNL.

For the sub-module heat exchanger, channels for both baseline and optimized configurations were 2 mm wide with 1-mm-thick fin walls. The baseline channels were 15 mm tall and 74 mm long. The optimized channels were 21 mm tall and 40 mm long. The material thickness between the channels and the devices was 2.8 mm, calculated to nearly match the thermal resistance of a direct-bond-copper or direct-bond-aluminum substrate layer.

For the module-level heat exchanger, the channel and fin thicknesses were the same as the sub-module heat exchangers. The channels were 21 mm tall and 52.7 mm long. The material thickness between the channels and the devices was 4.0 mm to allow for electronic component attachment.

The test bench for this project (see Figure 3-131) used compressed air that was dried with a desiccant dryer to a dew point of -20°C or lower. The air was then passed through a 5-µm particulate filter and regulated at a pressure of 68 to 137 kPa. A mass flow controller provided the desired flow rates. A downstream laminar flow element was used to more accurately measure the flow rate and feedback to control the mass flow controller. The house air compressor was the limiting factor in maintaining the flow at adequate pressure throughout the experiment. Therefore, the maximum flow rate tested was 500 m^3/h for the module-level heat exchanger. The air passed through a plate heat exchanger for temperature control and entered the heat exchanger test section. The inlet temperature was set at 50°C, which is a conservative worst-case scenario for ambient air intake during vehicle operation.

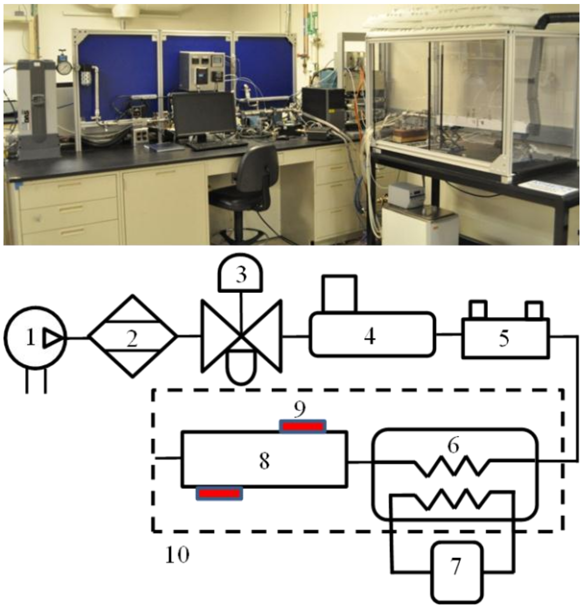

Figure 3-131: Air cooling test bench photo and schematic: (1) compressed air, (2) desiccant dryer, (3) filter/regulator, (4) mass flow controller, (5) laminar flow element, (6) plate heat exchanger, (7) temperature control bath, (8) fin test section, (9) ceramic resistance heaters, (10) isolation box.

Ceramic resistance heaters (8 mm × 8 mm) provided the heat load; power was adjusted to yield the desired junction temperature for each flow rate. A 0.5-mm-thick copper base plate with an embedded thermocouple was attached with thermal epoxy to the test section. Indium foil was placed between the copper base plate and the heater, topped with insulation, and held in place with a clamp (see Figure 3-132). The test section was wrapped in insulation. For more details of the experimental setup, see Waye et al. [12]. A similar setup was used for the module-level heat exchanger, as shown in Figure 3-133.

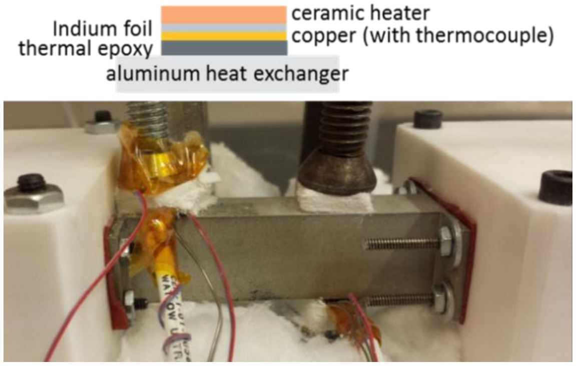

Figure 3-132: Heater stack-up and assembled sub-module (fin test section indicated by (8) and (9) in Figure 3-131).

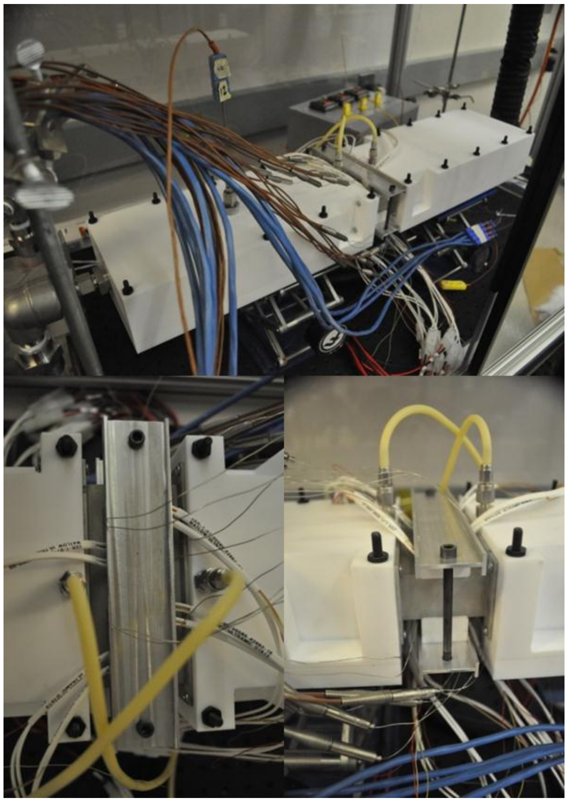

Figure 3-133: Module-level test setup (fin test section indicated by (8) and (9) in Figure 3-131). The top photo shows the inlet and outlet manifolds (white blocks) with the fin test section between them, shown in more detail in the bottom photos. The white wires are leads to heaters, clamped down with a small aluminum I-beam and rigid insulation. The yellow tubes are used for the pressure measurement.

Tests were conducted over a range of flow rates with a maximum junction temperature for any of the heaters. The power supplied to the heaters (dissipated as heat) and the pressure drop were measured for each flow rate. The heat dissipation and pressure drop results were extrapolated from the sub-module level to inverter scale; one module consisted of six sub-modules, and nine or six modules made up the entire inverter for the baseline and optimized configurations, respectively. To estimate the total inverter weight and volume, weights and volumes of the inverter components were combined with the heat exchanger assembly. The casing for each module was scaled for the heat exchanger geometry. The bus bars were assumed to be 0.088 kg per module. The capacitor was assumed to be 1.62 kg and 1.13 L. The gate driver and control board were assumed to be 0.42 kg and 0.88 L. Figure 3-134 shows the module-level heat exchanger and inverter assembly. An inverter casing was not included in the calculations.

The parasitic power of the system was of interest. Pressure drops across two production ducts (from other air intake systems) were combined to act as a surrogate inlet and exhaust ducting path for the air-cooled inverter system [12]. The total pressure drop of the system was calculated by using the flow rate through the heat exchanger.

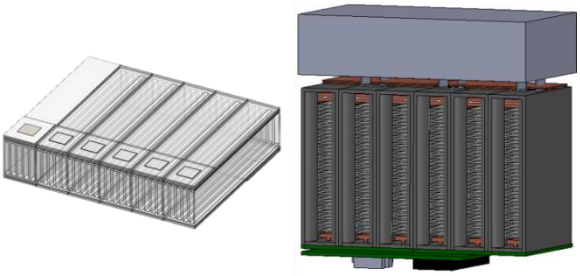

Figure 3-134: Schematic of module-level heat exchanger (left) with devices (six on top, six on bottom), and six-module inverter (right), including module casing, capacitor, bus bars, control board, and gate driver board. Computational fluid dynamics and experiments were conducted on the sub-module heat exchanger (opaque portion on far left of module-level heat exchanger).

Results

The heat dissipation for the baseline and optimized configurations is shown in Figure 3-135. Error bars represent 95% confidence levels. The target heat dissipation rate was 2.7 kW, which equates to an approximately 95% efficient inverter at peak power (55 kW).

Two production ducts for other applications were tested for pressure loss as a function of flow rate [12]. The ducting path would be designed for each vehicle platform and vary, so these ducts provide an estimate of the air intake and exhaust pressure losses. This pressure loss curve was combined with the pressure loss through the heat exchanger to provide an estimated system pressure drop, which is shown in subsequent plots and used in the calculation of the fluid power.

For the baseline configuration with nine modules, approximate air flow rates of 226, 100, and 70 m³/h [132, 56, 41 ft³/min] for 150°C, 175°C, and 200°C maximum junction temperatures, respectively, met the heat dissipation rate target. The power density and specific power for the inverter components are estimated at 10.1 kW/L and 8.9 kW/kg, respectively. The fluid power (the product of flow rate and pressure drop, a parasitic load) to maintain a maximum junction temperature of 175°C was approximately 4 W (40 W for 150°C and 1.5 W for 200°C).

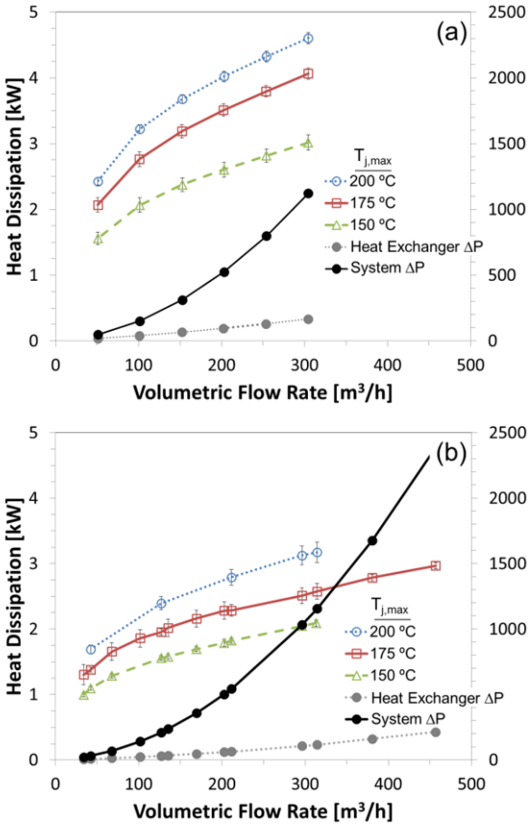

Figure 3-135: Heat dissipation curves and system pressure loss as a function of flow rate and maximum junction temperature for (a) baseline nine-module inverter*, and (b) optimized six-module inverter* configurations. The target heat dissipation is 2.7 kW. *Extrapolated to inverter level.

Reducing the number of modules reduces weight and volume, but also reduces the number of devices. To compensate and provide the same power, more current must run through the devices, which also increases heat dissipation. Using the optimized heat exchanger, 2.7 kW of heat was dissipated at approximate airflow rates of 384, 230, 79, 44, and 20 m³/h [225, 136, 47, 26, and 12 ft³/min] for maximum junction temperatures of 175°C, 200°C, 225°C, 250°C, 275°C, and 300°C, respectively. At 150°C, no flow rate tested could dissipate 2.7 kW of heat using the heat exchanger with the optimized design and six-module configuration. The power density and specific power of the inverter components rose to 14.5 kW/L and 13.2 kW/kg. The tradeoff of a more compact design is increased fluid power: approximately 183 W, 45 W, 3.5 W, and 0.5 W for the 175°C, 200°C, 250°C, and 275°C maximum junction temperature, respectively. As previously stated, at 150°C, no flow rate dissipated the target heat load. At 300°C maximum junction temperature, the lowest flow rate dissipated more heat than the target load.

For each case, a fan must be sized to provide the fluid power, and the fan efficiency must be considered. A typical air conditioning system blower or compressor fan uses up to around 150 W at peak demand.

The outlet temperature decreases with increased flow rate, as seen in Figure 3-136 for the optimized heat exchanger. The outlet temperatures for the optimized heat exchanger were also lower when compared to the baseline configuration for any given junction temperature. When the heat exchanger dissipated 2.7 kW of heat at 175°C maximum junction temperature, the outlet temperature for the baseline configuration was approximately 100°C. The optimized configuration outlet temperature was approximately 68°C.

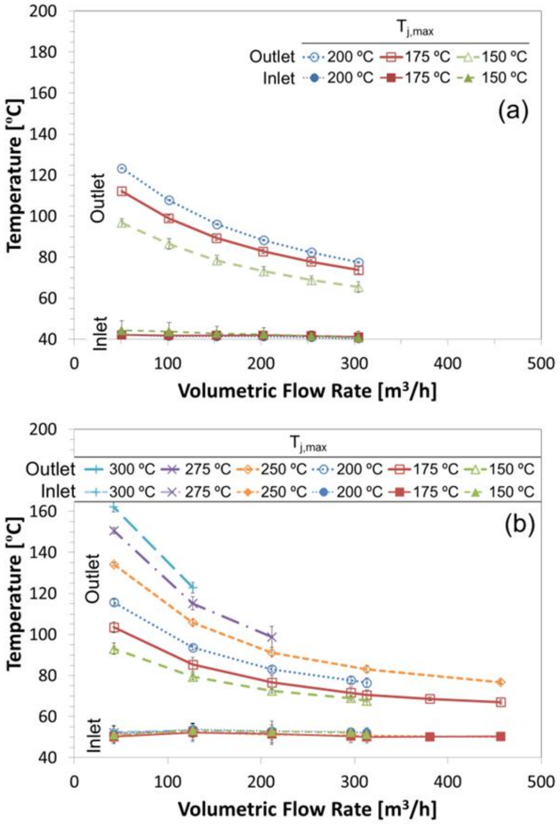

Figure 3-136: Inlet and outlet air temperatures as a function of flow rate and maximum junction temperature for the (a) baseline and (b) optimized sub-module heat exchanger.

For the baseline sub-module heat exchanger tests, the inlet temperature was approximately 45°C. For the optimized sub-module experiments, the inlet temperature was closer to

50°C. The effect of the inlet temperature was examined, as shown in Figure 3-137. For every 5°C increase in inlet temperature, the heat dissipation decreased by about 3% in the range tested.

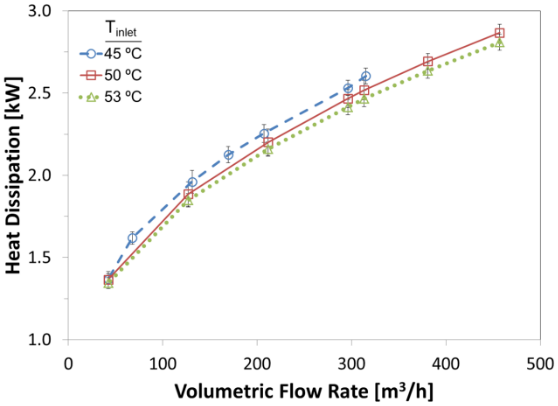

Figure 3-137: Inlet air temperature effect on heat dissipation for $T_{j,max}$ = 175ºC.

The design of the heat exchanger was iterated upon to meet electrical component layouts in collaboration with ORNL. Therefore, the design tested at the module level has lower thermal performance than the optimized geometry, but certain constraints had to be met to mount the electrical hardware. The layout tested is shown in Figure 3-138 (and the bottom picture in Figure 3-130), where there are four groups of transistor/diode device sets. In order to generate heat, two 8mm by 8mm ceramic resistance heaters were attached via the same method as previously addressed to each side of a module-level heat exchanger.

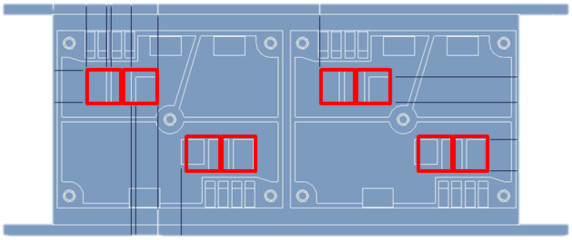

Figure 3-138: Location of ceramic resistance heaters overlaid on electrical design layout.

The heat dissipation at maximum junction temperatures from 150°C to 300°C is shown in Figure 3-139. The results are presented as a characterization of the single module heat exchanger. Thus, the results have not been extrapolated to a full inverter (six or nine modules). The module was initially designed to produce 10 kW of electrical power, but further design and analysis indicate that more power may be produced, which would improve weight and volume metrics. The pressure losses for the heat exchanger and for an extrapolated system (ducting pressure loss added) are shown on the same plot, using the right-hand axis.

For most tests, all sixteen heaters (eight on each side) provided the heat load. For a few experiments, heaters on only one side were turned on. These are designated as “1-side” in the plot under the maximum junction temperature at which they were run. All error bars represent 95% confidence levels.

The heat exchanger dissipates more heat with higher maximum junction temperatures, mostly due to the fact that there is a higher temperature difference, which drives the heat transfer. The curves are relatively flat, indicating that an increased flow rate is creating diminishing benefits of heat dissipation. The heat dissipated when the heaters on only one side are on is about 90% of the heat dissipated with both sides turned on. Therefore, the heat exchanger can be thought of as nearly single-sided for all devices, where the fins are being shared by all heat sources.

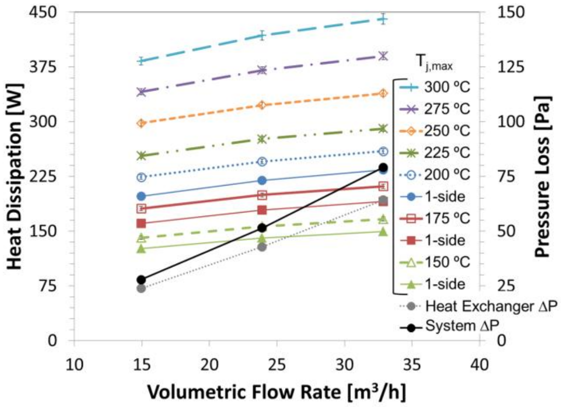

Figure 3-139: Heat dissipation curves and system pressure loss as a function of flow rate and maximum junction temperature for the module-level heat exchanger (not extrapolated to inverter level).

The inlet and outlet temperatures at the different maximum junction temperatures are shown in Figure 3-140. The temperatures are relatively low. Under-hood temperatures often rise to 140°C, so the exhaust heat from the inverter through the heat exchanger could be reasonably released under-hood or at another external location.

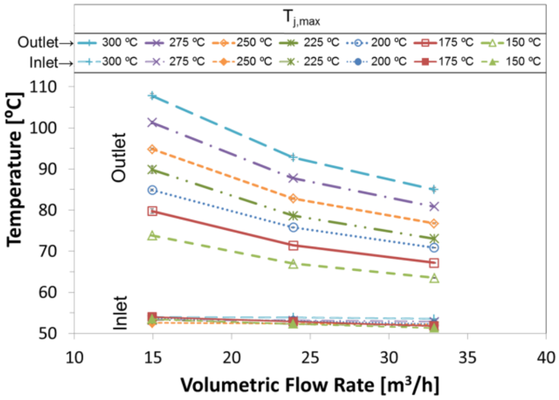

Figure 3-140: Inlet and outlet air temperatures as a function of flow rate and maximum junction temperature for the module-level heat exchanger.

The maximum temperature of the thin copper plate epoxied to the surface was set to be the maximum junction temperature being tested. All other temperatures were lower, depending on the local cooling effectiveness of the heat exchanger. The heater temperatures were slightly higher to produce the heat flux necessary to maintain this temperature.

The heat source temperatures were plotted to examine the distribution of temperatures on the heat exchanger (Figure 3-141). The low, medium, and high flow rates tested are shown for three maximum junction temperatures (150°C, 175°C, and 200°C). In the figure, the air would flow into the page. A front view of the heat exchanger is accompanied by a top and bottom view for each flow rate and maximum junction temperature.

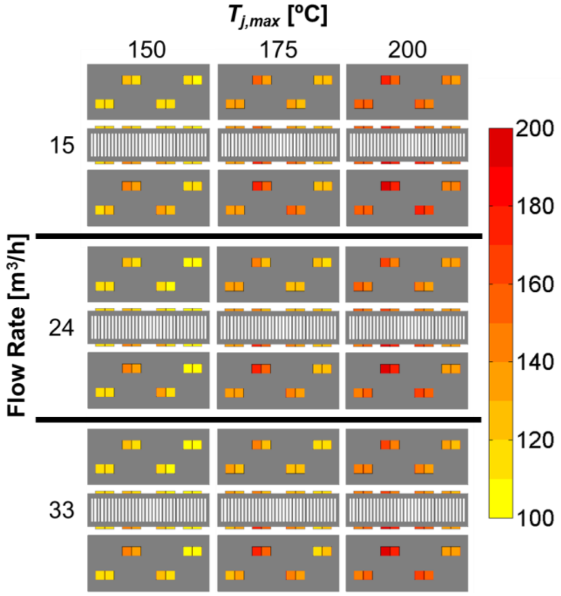

Figure 3-141: Temperature map for heat sources for three flow rates and maximum junction temperatures of 150°C, 175°C, and 200°C.

Several observations can be made from the thermal mapping of the heat sources. The temperature distribution is quite sensitive to the flow through the heat exchanger. The local heat transfer was sensitive to the air flow distribution, creating non-isothermal conditions and temperature distributions. During setup of the test section, there was a noticeable mal-distribution of air through the inlet manifold. A baffle and screen were put in place to create a pressure drop and to make the flow more uniform. The uniformity of the flow rate through the heat exchanger was measured to be above 90%. The areas that had slightly lower flow were the same locations in the thermal map that had the highest temperatures. Thus, those areas controlled the location of the maximum junction temperature. The temperatures scaled proportionally to the maximum junction temperature, as shown in Figure 3-142 (high flow rate for all the maximum junction temperatures)

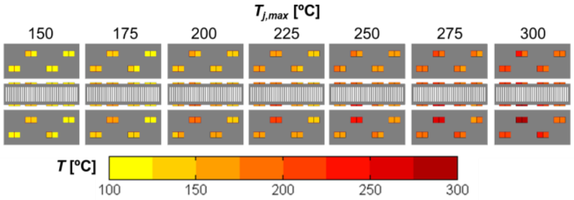

Figure 3-142: Temperature map of heat sources at high flow rate (33 m^3/h).

Conclusions

An air-cooled heat exchanger for power electronics inverter thermal management provides a potential technology for low cost, simple-to-manufacture option for high temperature devices. It would potentially eliminate the liquid-to-air coolant loop typically used in automotive applications. It would also provide potential solutions to cooling components with lower temperature limits (e.g., 85°C capacitor) while the desired liquid cooling temperatures are increasing.

In the current work, the thermal performance for baseline and optimized sub-modules was characterized. A module-level heat exchanger was characterized, and thermal performance metrics were presented. The parasitic power of the systems is projected to be in line with other vehicle components, such as an air conditioning fan or condenser, which was deemed acceptable.

Higher junction temperatures provide opportunities for increased heat transfer and greater feasibility of an air-cooled heat exchanger system. Heat dissipation was measured for up to 300°C maximum junction temperatures. Packaging remains a challenge for these elevated temperatures, and thermal interface materials and reliability concerns need to be addressed to fully take advantage of higher device temperatures.

Reducing the number of modules (with a penalty of increased heat generation from increased current and increased parasitic power) is beneficial for weight and volume considerations. Full inverter components (including housing) need to be considered for weight and volume targets. Further optimization of the heat exchanger within the thermal and electrical constraints could further reduce weight and volume. More advanced heat exchanger designs may improve heat transfer efficiency with tradeoffs in manufacturability and cost. This requires co-design of the thermal and electrical systems. Understanding the complete inverter system, including ducting pathways, inverter location, and fan requirements is important when comparing to currently used systems.

FY 2014 Publications/Presentations

1. Waye, S. "High Temperature Air-Cooled Power Electronics Thermal Design." Presentation, DOE Annual Merit Review; June 18, 2014, Washington D.C.
2. Waye, S. "High Temperature Air-Cooled Power Electronics Thermal Design." Presentation, EETT; August 27, 2014, Southfield, MI.
3. Waye, S.; Musselman, M.; King, C. "Air Cooling for High Temperature Power Electronics." Presentation, 2014 SAE Thermal Management Systems Symposium; September 23, 2014, Lakewood, CO.
4. Waye, S.; Lustbader, J.; Musselman, M.; King, C. "Air-Cooled Heat Exchanger for High-Temperature Power Electronics." 47th Symposium on Microelectronics: IMAPS 2014 – International Microelectronics Assembly and Packaging Society 2014, Oct 15, 2014, San Diego, CA.

Acknowledgments

The author would like to acknowledge the support provided by Susan Rogers and Steven Boyd, Technology Development Managers for EDT, Vehicle Technologies Office, U.S. Department of Energy Office of Energy Efficiency and Renewable Energy. The significant contributions of Matt Musselman, Charlie King, and Kevin Bennion (NREL) to the project are acknowledged. Collaboration with Madhu Chinthavali from ORNL has been important in balancing the electrical and thermal design and constraints. The author would also like to acknowledge SAPA Extrusions USA for providing aluminum fin block prototypes.

References

1. Staunton, R.H., Burress, T.A., Marlino, L.D. *Evaluation of 2005 Honda Accord Hybrid Drive System*. ORNL/TM-2006/535. Oak Ridge, TN: Oak Ridge National Laboratory, September 2006.
2. *Semikron Application Manual* 1998. Section 3.1. Accessed on July 7th, 2011.
3. Matsumoto, S. "Advancement of Hybrid Vehicle Technology." *European Conference on Power Electronics and Applications,* Dresden, Germany, September 2005.
4. Uesugi, T., Kachi, T. "GaN Power Switching Devices for Automotive Applications." CSMan Tech Conference, Tampa, Florida, May 2009.
5. Renken, F., Knorr, R. "High Temperature Electronics for Future Hybrid Powertrain Application," *European Conference on Power Electronics and Applications*. Dresden, Germany, September 2005.
6. Funaki, T., Balda, J., Junghans, J., Kashyap, A., Mantooth, H., Barlow, F., Kimoto, T., Hikihara, T., 2007, "Power conversion with SiC devices at extremely high ambient temperatures," *IEEE Transactions on Power Electronics*, 22-4, pp. 1321 –1329.
7. Chow, Y. (media contact). "AC Propulsion Partners with BMW to Build 500 Electric Vehicles." Press release. 2008. http://www.acpropulsion.com/pressreleases/11.20.2008%20BMW%20Press%20Release.pdf. Accessed July 6th, 2011.
8. Kodani, K., Tsukinari, T., Matsumoto, T., "New Power Module Concept by Forced-Air Cooling System for Power Converter." *IEEE 2010 International Power Electronics Conference*, Sapporo, Japan, July 2010.
9. Bortis, D., Wrzecionko, B., Kolar, J.W. "A 120°C Ambient Temperature Forced Air-Cooled Normally-Off SiC JFET Automotive Inverter System." *IEEE 26th Annual Applied Power Electronics Conference and Exposition (APEC)*, Fort Worth, TX, March 2011.
10. Wrzecionko, B., Biela, J, and Kolar J. "SiC Power Semiconductors in HEVs: Influence of Junction Temperature on Power Density, Chip Utilization and Efficiency." *IEEE 35th Annual Industrial Electronics Conference,* Porto, Portugal, November 2009.
11. Vetrovec, J. "High-Performance Heat Sink for Interfacing Hybrid Electric Vehicles Inverters to Engine Coolant Loop." *SAE World Congress.* Paper# T11PFL-0459, Detroit, MI, April 2011.
12. Waye, S., Narumanchi, S., Lustbader, J., Bennion, K., Smith, C. "Air-Cooling Technology for Power Electronics Thermal Management." FY2013 EERE Vehicle Technologies Office Advanced Power Electronics and Electric Motors Annual Report, April 2014.
13. Chinthavali, M. "Gas Cooled Traction Drive Inverter," U.S. Patent No. 8,553,414 B2, issued October 8, 2013.
14. "Electrical and Electronics Technical Team Roadmap." U.S. DRIVE. http://www1.eere.energy.gov/vehiclesandfuels/pdfs/program/eett_roadmap_june2013.pdf, June 2013.

3.10 Performance and Reliability of Bonded Interfaces for High-Temperature Packaging

Douglas DeVoto *(Principal Investigator)*

National Renewable Energy Laboratory (NREL)
Transportation and Hydrogen Systems Center
15013 Denver West Parkway
Golden, CO 80401
Phone: (303) 275-4256
E-mail: douglas.devoto@nrel.gov

Susan A. Rogers, DOE Technology Development Manager
Phone: (202) 586-8997
E-mail: susan.rogers@ee.doe.gov

Sreekant Narumanchi, NREL Task Leader
Phone: (303) 275-4062
Email: sreekant.narumanchi@nrel.gov

Start Date: FY14
Projected End Date: FY16

Objectives

- Investigate and improve the reliability of large-area sintered-silver bonded interfaces.
- Identify failure modes in sintered-silver interface materials, experimentally characterize their lifetime under known conditions, and develop lifetime estimation models.

Technical Barriers

In automotive power electronics packages, conventional thermal interface materials such as greases, gels, and phase-change materials pose bottlenecks to heat removal and are also associated with reliability concerns. The industry trend is toward high thermal performance bonded interfaces for large-area attachments. However, because of coefficient of thermal expansion mismatches between materials/layers and resultant thermomechanical stresses, adhesive and cohesive fractures could occur, posing a reliability problem. These defects manifest themselves in increased thermal resistance.

Technical Targets

Improved package reliability enables achievement of the U.S. Department of Energy (DOE) Electric Drive Technologies (EDT) Program power electronics targets for improved efficiency, performance, and lifetime.

Accomplishments

This research aims to investigate and improve the thermal performance and reliability of sintered-silver for power electronics packaging applications. This has been experimentally accomplished by the synthesis of large-area bonded interfaces between metalized substrates and copper (Cu) base plates that have subsequently been subjected to thermal cycles. A finite element model of crack initiation and propagation in these bonded interfaces will allow for the interpretation of degradation rates by a crack-velocity (V)-stress intensity factor (K) analysis. The experiment is described, and the modeling approach is discussed.

* * *

Introduction

In a power electronics module, a semiconductor device is typically attached by a bonded interface material (BIM), such as solder, to a metalized substrate. The substrate beneath this die attach layer is commonly composed of a ceramic bounded by Cu layers on either side and provides electrical isolation. This substrate is then mounted onto a base plate or directly to a heat exchanger, typically made of Cu or aluminum (Al) via a large-area BIM. A cross-section of a typical power electronics package is shown in Figure 3-143.

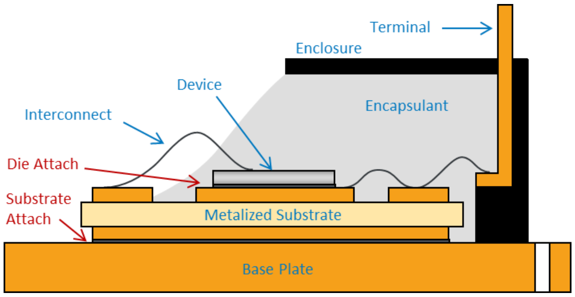

Figure 3-143: Traditional power electronics package.

A coefficient of thermal expansion (CTE) mismatch between the ceramic substrate and the Cu base plate, when paired with any temperature change, will impose stress that can initiate and propagate defects in the joining solder layer if the magnitude of that stress is sufficiently high. Lead-based solders had predominantly been used in the electronics packaging industry; however, the Restriction of Hazardous Substances Directive [1] mandated lead-free solutions. Initially, the industry focused on various tin (Sn), silver (Ag), and Cu (SAC) compositions as a suitable lead-free alternative, with Innolot ($SnAg_{3.8}Cu_{0.7}Bi_{3.0}Sb_{1.4}Ni_{0.2}$) proving to be a promising solution [2–3]. Research found that varying the composition of the Ag and Cu content in the SAC solders would help minimize creep strain. Despite these advances, the reliability under temperature cycling continues to be a concern with lead-free solders. The transition to wide-bandgap devices and junction temperatures of 200°C or higher also places packaging constraints on power electronics designs where temperatures would exceed reflow temperatures of many commonly used solder alloys.

To provide greater thermomechanical reliability under temperature cycling and to allow for higher temperature applications, sintered-silver material has been proposed as an alternative solution in power electronics packages [4–8]. However, to reduce synthesis temperatures to below 300°C, the concurrent application of pressure up to 40 MPa onto the package or sintered-silver BIM was originally advocated. However, this caused a higher complexity in the production process and more stringent flatness specifications for the substrates. Recently, several manufacturers have developed sintered-silver materials that require lower or even no bonding pressures.

Because large-area BIMs are promising [9–12], work has focused on assessing their thermal performance and reliability. Conclusions on thermal performance and reliability from the present effort are intended to directly assist incorporation of these materials into automotive power electronics designs. This research focuses on sintered-silver based on micrometer-sized Ag particles, and $Sn_{63}Pb_{37}$ solder as a baseline. The sample synthesis, characterization plan, experimental results, and interface modeling are described below.

Approach

Sample Synthesis

The assembly consisted of a 5-mm-thick Cu base plate attached to a 0.72-mm-thick active metal bonded substrate (0.32-mm-thick silicon nitride [Si_3N_4] with 0.2-mm-thick Cu foil on either side of Si_3N_4, 50.8 mm × 50.8 mm cross-sectional area footprint) via the bonding material. The Cu metallization layers were inset 1 mm from the perimeter of the Si_3N_4, for a 48.8 mm × 48.8 mm footprint. The corners were given a radius of 2 mm to minimize stress intensities. Before assembly, the Cu metallization layers in the substrate were plated with 4 µm of electroless nickel-phosphorus (Ni-P), 1 µm of palladium (Pd), and 0.3 µm of Ag to improve adhesion with the bonding material. The Cu base plate was electroplated with 5 µm of Ag. An assembled sample is shown in Figure 3-144.

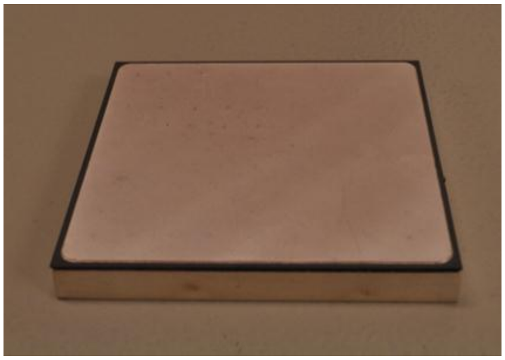

Figure 3-144: Representative metalized substrate/base plate assembly for sintered-silver and $Sn_{63}Pb_{37}$ solder (Photo credit: Doug DeVoto, NREL).

Bonded interfaces based on sintered-silver particles were synthesized by Semikron (Nürnberg, Germany). Corners of the Si_3N_4 substrate were rounded off to match the 2-mm radius of the Cu metallization layers. The sample assembly was placed in a hot press and raised to its processing temperature, after which pressure was applied. The specifics of the sintering temperature, schedule, and bonding pressure were not provided by Semikron.

As a baseline, a $Sn_{63}Pb_{37}$ bond was also synthesized between the substrate/base plate assembly. A 127-µm-thick stainless steel stencil with a five-by-five opening array (9-mm × 9-mm square openings with 1-mm separation) was used to apply solder evenly to the substrate and base plate surfaces. After the solder was applied, the assembled sample was placed in a vacuum solder reflow oven. The reflow profile ensured that flux was removed from the bond and that voiding remained less than two percent.

Initial Material Characterization

Degradation (e.g., cracks, voids, and delaminations) of the bonded interface can be non-destructively detected by scanning acoustic microscopy. After defect initiation, the thermal and electrical performances of the sample assembly degrade. The initial bonding condition of the samples was characterized using a C-mode scanning acoustic microscope (C-SAM). The interfaces were also characterized via the C-SAM after every 100 thermal cycles thereafter. Images showing the bonded interface within samples before accelerated thermal testing are shown in Figure 3-145. The circular bands visible in each sample are artifacts of the C-SAM representing top surface curvatures as 2-D images and are not indicators of bond quality. The $Sn_{63}Pb_{37}$ solder and sintered-silver both exhibited uniform bonds between the base plate and substrate samples.

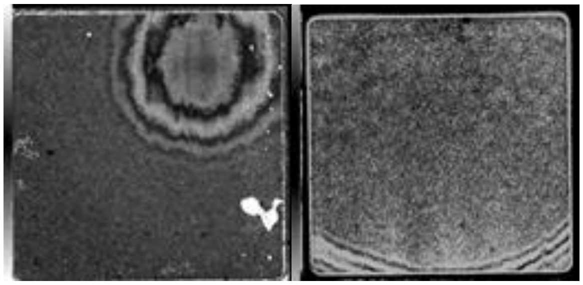

Figure 3-145: C-SAM images showing initial bond quality in $Sn_{63}Pb_{37}$ solder (left) and sintered-silver (right) (Photo credit: Doug DeVoto, NREL).

In addition to acoustic microscopy, the electrical resistance of the Si_3N_4 insulation layer was measured. In a high potential test, a high voltage is applied to an electronic device's current-carrying components. The quality of the insulation in the device is determined by measuring the presence of a leakage current. The presence of leakage current indicates that dielectric breakdown in the insulation layer has occurred [13]. A dielectric resistance tester was previously constructed based on the high potential testing process to detect when a crack in the Si_3N_4 has developed. A custom fixture contacts the top and bottom sides of a test sample, and a test voltage of 2.0 kV is applied for 20 seconds, which is sufficient voltage to cause an arc in the air through a defect or crack in the 0.32-mm-thick Si_3N_4 layer. Measurement of the leakage current from an arc indicates that damage occurred within the Si_3N_4 layer in the sample. The sample successfully passes the test if no current was measured over the analysis period. The results correlated with acoustic microscopy images, indicating that no initial samples exhibited defects within the Si_3N_4 layer.

The samples deformed as a consequence of their elevated temperature processing. Residual stresses due to CTE mismatches of the bonded constituents combined with the sample's geometry and cool-down to ambient temperature caused this deformation. These stresses can be sufficient to initiate and propagate cracks within the Si_3N_4, leading to failure of the layer's electrical insulating properties. Representative CTE parameters for materials common within a power electronics package and examples of package deformation conditions are shown in Figure 3-146. As a package cools from its strain-free temperature, the Cu base plate's higher CTE relative to the substrate and silicon die causes it to contract more and induce a bow into the package.

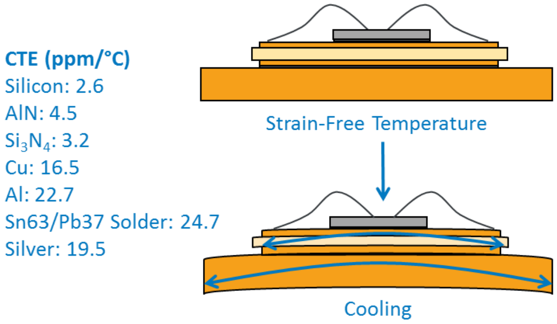

Figure 3-146: Power electronics package deformation caused by CTE mismatch under cooling condition.

The high pressure and temperature synthesis requirements for sintered-silver did not cause crack initiation within the Si_3N_4 substrate; however, package deformation was evident when samples were at room temperature. A laser profilometer was used to scan the top and bottom surfaces of sintered-silver samples for accurate measurements of these deformations. Figure 3-147 shows the top surface profile of one sintered-silver sample as well as a cross-section profile between two of the sample's corners. The maximum height variation across the sample was 166 µm. Surface profile measurements were also taken for $Sn_{63}Pb_{37}$ solder samples, but no significant permanent deflection was found.

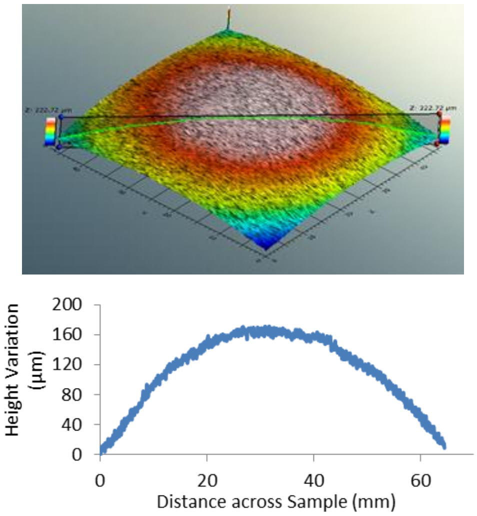

Figure 3-147: Surface profile of sintered-silver sample at room temperature.

Thermal Cycling

After initial characterization of the test samples, conditions were applied to create thermally induced stresses, leading to cracking, voiding, or delamination failures. Samples were cycled between –40°C and 150°C, a common temperature range for electronics testing, to evaluate the quality of the bonded interfaces [14–17]. Dwell periods of 10 minutes at the maximum and minimum temperatures were chosen to promote solder fatigue and creep [17]. Ramp rates for thermal cycling must be sufficiently low to avoid transient thermal gradients in the test samples; therefore, ramp rates were in the 5°C/min range. Each sample was planned to be cycled up to 2,500 thermal cycles or until degradation propagated to sufficient levels to separate the substrate from the base plate.

Sintered-Silver Modeling

The tracked ingress front of a delamination within a sintered-silver bonded interface (captured with C-SAM) can be linked to a corresponding modeled stress intensity factor to construct and interpret the V-K response. While this study's interpretation may be specific to the geometry selection and processing conditions employed, this analysis method could provide a logical way to interpret such damage in other interfaces. An identified V-K curve is important because it affords the possibility to pre-determine what sizes and shapes of sintered-silver interfaces can be used without causing delamination initiation, which has positive implications for future improvements in reliability with power electronic devices where the bonding of a relatively large area is desired.

Crack Modeling

The main objective of the computational modeling approach in this work is to calculate the values of stress intensity factor (K) using finite element analysis at various points along crack growth in sintered-silver BIMs. The 50-mm × 50-mm sample shown in Figure 3-144 was selected for modeling as the C-SAM images of the sintered-silver interface within the sample were already available. Stress intensity factor is a theoretical parameter whose magnitude determines the intensity or magnitude of stresses in the crack tip region. It depends on the sample geometry, size and location of the crack, and magnitude and distribution of the load. K is the single-parameter characterization of the crack tip stress field. Once computed, stress intensity factor values will be correlated with the crack velocities calculated from C-SAM images of delaminated sintered-silver. A three-dimensional linear elastic fracture mechanics-based crack initiation and propagation model of the sample shown in Figure 3-144 with sintered-silver interface is being developed to obtain the desired outputs.

The crack modeling feature in ANSYS is only available in version 15 or later. Crack size and location both need to be known before an analysis can be completed, otherwise, a linear analysis can be completed on the model geometry to find the locations of maximum equivalent stress and strain to locate where the crack is likely to initiate. The sample geometry was created in ANSYS DesignModeler, and a tetrahedral mesh was implemented, as shown in Figure 3-148. While a hexahedral mesh would provide more accurate results, the current capabilities within ANSYS are limited to performing crack modeling on a tetrahedral mesh.

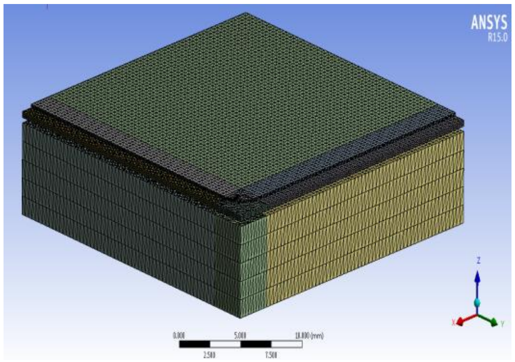

Figure 3-148: Quarter symmetry tetrahedral mesh of 50-mm × 50-mm sample.

A crack was then inserted at the far corner region within the sintered-silver using the “Fracture” feature in ANSYS Model, as shown in Figure 3-149. The crack takes a semi-elliptical shape and the major and minor radii are defined to create a crack of the desired size. After solving, stress intensity factor values can be obtained along the crack contour in the post-processing phase. If the maximum value of K exceeds a critical stress value (K_{crit}), which is unique for each material, it can be understood that crack would begin to propagate. However, crack propagation modeling is not currently available within ANSYS.

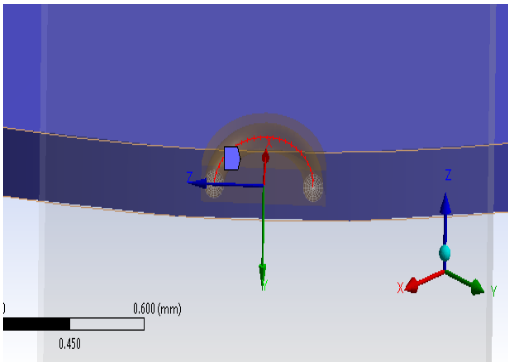

Figure 3-149: Crack inserted into the sintered-silver layer.

Preliminary stress intensity factor results have been obtained at the far corner region. Additional work such as mesh independence study is currently being conducted to confirm the validity of the obtained results.

Residual Stress Modeling

An accurate set of material properties for sintered-silver is required for the crack initiation and propagation models. Material characterization tests at various temperatures are planned for FY15 to extract stress-strain curves of sintered-silver, from which properties such as elastic modulus can be calculated. A parameter of interest is the amount of residual stress on the samples that would undergo material characterization tests. The temperature during the sintering process is typically between 250°C to 300°C; subsequently, samples are cooled to room temperature. This causes residual stresses to form due to the CTE mismatch of materials within the samples.

A geometric model of the sample that would undergo material characterization tests is shown in Figure 3-150. A parametric study was conducted using finite element analysis to optimize the sintered-silver geometry in the samples to keep residual stresses to a minimum. An ANSYS Parametric Design Language (APDL) code was developed that included model pre-processing, solver, and post-processing stages. The model geometry consists of a sintered-silver layer of 10-mm diameter bonded between two 12.7-mm × 12.7-mm direct-bond-copper alumina substrates. The thickness of the substrate was 1.2 mm; for sintered-silver, 25-µm- and 50-µm-thickness variations were considered. A quarter symmetry of the package was utilized in the modeling to save computational space and time.

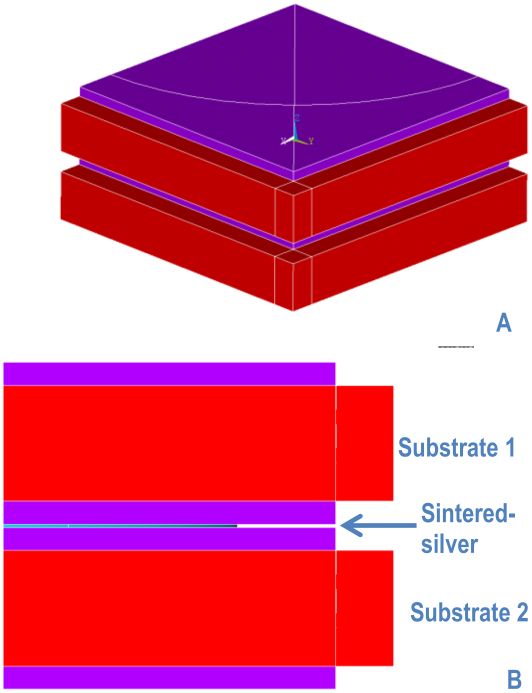

Figure 3-150: Quarter symmetry model (A) and layers in the sample (B).

Material properties were obtained from literature for the simulation [18] to explore general trends within the sintered-silver interface. After the geometry was constructed and material properties at room temperature applied, the model was meshed using SOLID185 hexahedral elements. Increased mesh density was achieved at the sintered-silver interface layer, as shown in Figure 3-151, through meshing operations like edge sizing and element sizing.

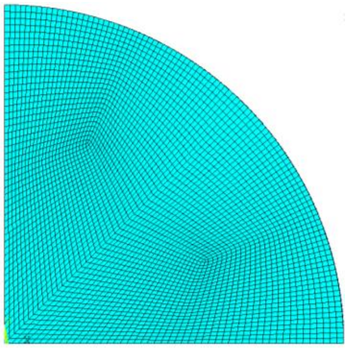

Figure 3-151: Sintered-silver joint (top-view).

Results

BIM Response to Thermal Cycling

A failure is defined here by any of the following: a crack in the Si_3N_4 substrate, a cohesive fracture within the BIM, or an adhesive/interfacial fracture between the BIM and either the substrate or base plate surface. A crack in the Si_3N_4 substrate could indicate loss of electrical insulation capabilities and the sample would immediately be considered failed. Cohesive or adhesive/interfacial fractures in the BIM would increase the thermal resistance of the power electronics package, eventually creating a thermal bottleneck that would elevate the operating temperature of a die above its maximum limit. For testing purposes, a fracture leading to 20% area delamination of the BIM is defined as a failure.

$Sn_{63}Pb_{37}$ solder samples were subjected to 1,500 thermal cycles. C-SAM images showed progressively increasing delamination up to 1,500 cycles, indicating a relatively poor performance of the large-area BIM (Figure 3-152). Light-shaded regions in the acoustic images indicate a void or defect while dark regions denote an intact bond.

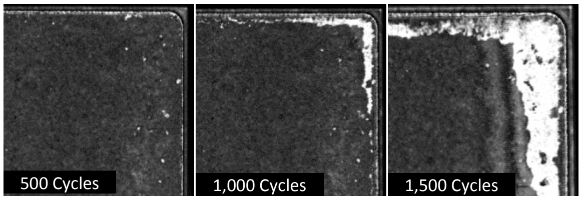

Figure 3-152: C-SAM images of $Sn_{63}Pb_{37}$ solder material after select number of thermal cycles
(Photo credit: Doug DeVoto and Paul Paret, NREL).

Sintered-silver samples completed 2,500 temperature cycles. The delamination rates were comparatively lower than $Sn_{63}Pb_{37}$ solder samples. This is observed in acoustic images of a corner region of the sintered-silver material after 1,000 temperature cycles, 1,500 cycles, and 2,500 cycles, as shown in Figure 3-153.

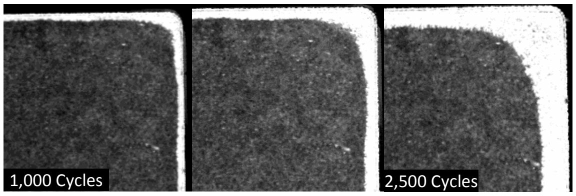

Figure 3-153: C-SAM images of sintered-silver material after select number of thermal cycles.
(Photo credit: Doug DeVoto and Paul Paret, NREL).

Measurements of the delamination percentage within the sintered-silver BIM were taken every 100 cycles from C-SAM imaging. Depending on the sample, this perimeter fracturing increased to 19%–32% of the initial 48.8 mm × 48.8 mm bonded area after undergoing 2,500 temperature cycles, as shown in Figure 3-154. Under these specific bonding and temperature cycling conditions, the sintered-silver samples remained defect free until approximately 300 cycles. A period of transient rate delamination occurred after defect initiation until approximately 1,000 cycles, after which a constant rate of delamination was observed to the conclusion of temperature cycling at 2,500 cycles.

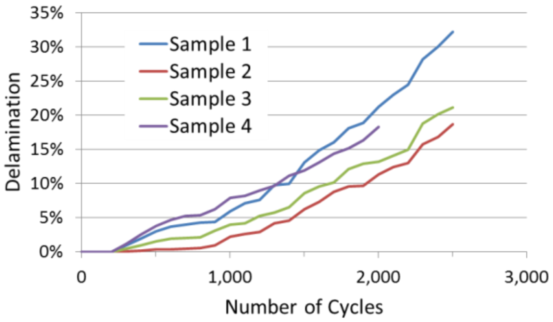

Figure 3-154: Perimeter delamination of sintered-silver BIM as a function of number of thermal cycles.

The fourth sample was cross-sectioned, and the bonded interface layer was imaged after 2,000 temperature cycles. The delamination observed in acoustic microscope images was the result of fracturing (i.e., cohesive failure) within the sintered-silver material. The cohesive fracturing is shown in Figure 3-155. After 2,500 cycles, additional cross-sectioning and imaging confirmed that cohesive fracturing occurred in the remaining three sintered-silver samples.

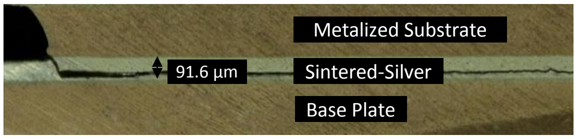

Figure 3-155: Cohesive fracture of the sintered-silver BIM after 2,000 temperature cycles.

The delamination percentage was calculated for the sintered-silver BIM and compared with the $Sn_{63}Pb_{37}$ solder material. After 1,500 cycles, cohesive fracturing within the solder material reached 21%–24% delamination. Observed delamination rates were higher in the solder samples than in the sintered-silver samples. Delamination rates of both interface materials are shown in Figure 3-156.

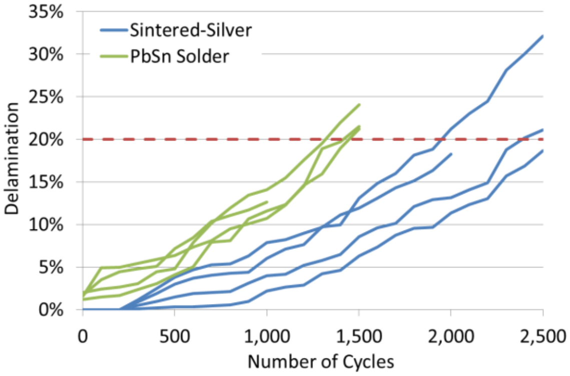

Figure 3-156: Perimeter delamination of sintered-silver and $Sn_{63}Pb_{37}$ solder as a function of number of thermal cycles.

Crack growth rates within the sintered-silver BIM were also determined as a function of number of thermal cycles. As with the delamination percentage, three characteristic regions of the delamination distance were observed. The delamination distance from the original corner in each quadrant for sample four is shown in Figure 3-157. No delamination occurred within the first few hundred cycles in any of the samples. Immediately after initiation, a region of transient increase in delaminated distance then occurred for the next few hundred cycles. Lastly, a constant or increasing rate of delamination distance occurred for the remainder of the testing.

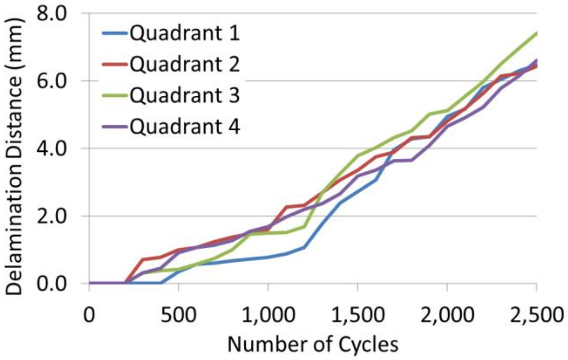

Figure 3-157: Delamination distance of sintered-silver BIM as a function of number of thermal cycles, or da/dN curves.

The observation of three such regions is consistent with those observed with the damage tolerant criterion (da/dN vs. K or ΔK) for fatigue [19] whose crack initiation and growth behavior follows a classic brittle fracture mechanics pattern. One such technique involves the study of crack growth rates (da/dN) or crack velocity (V) as a function of stress intensity factor (K). K is analytic for simple crack shapes and loading scenarios but can be obtained from three-dimensional finite element analysis for more complicated shapes and loadings. Stress intensity factor is a parameter that determines the intensity of the stresses in the crack tip region. Extensive crack initiation and propagation modeling will be conducted to obtain stress intensity factors, which will then be plotted against crack velocities to obtain a V-K curve. A typical V-K curve is shown in Figure 3-158.

Another supporting reason to consider such a V-K response for illustrating delamination response of sintered-silver interconnects is the cracking response in Figure 3-155 is consistent with cracking in a linearly elastic material. Conversely, delamination in a ductile or plastically deforming material, such as that that can occur in a solder, is better suited for representation by viscoplastic models such as Anand's.

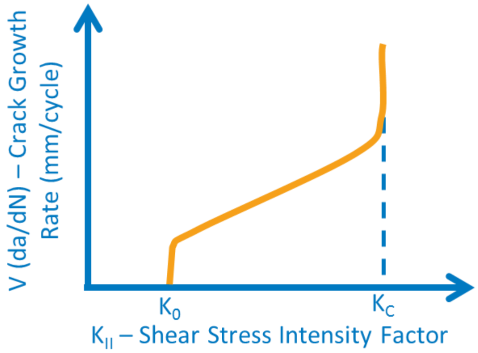

Figure 3-158: A typical V-K curve.

Physics of Failure Models

A total of six linear elastic simulations were performed incorporating variations in thickness and diameter of the sintered-silver joint. A contour plot of the von-Mises stresses in the sintered-silver interface layer is displayed in Figure 3-159.

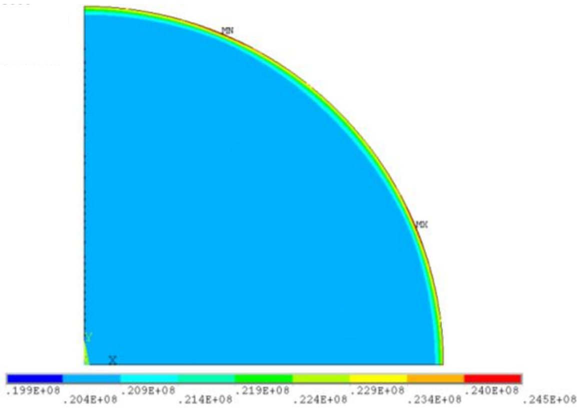

Figure 3-159: von-Mises stresses in the sintered-silver layer.

Results from the simulations are shown in Table 3-7.

Table 3-7: Maximum values of von-Mises stress

Thickness (µm)	Diameter (mm)	von-Mises Stress (MPa)
25	10	24.5
25	9	24.9
25	8	25.5
25	7	26.1
25	6	26.8
50	10	27.5

From the above results, it becomes clear that stresses increase with decrease in diameter of the sintered-silver joint for the same substrate size. Also, stresses increase with the thickness of the joint. Based on these results, a joint thickness of 25 µm and diameter of 10 mm will be chosen for the material characterization test samples.

Conclusions and Future Directions

A consistent framework has been implemented to establish the thermal performance and reliability of large-area bonded interfaces based on sintered-silver materials as compared to $Sn_{63}Pb_{37}$ solder. These large-area attachments are currently being considered in state-of-the-art power electronics packages for electric-drive vehicle applications. Results for bond quality after thermal cycling suggest that sintered-silver could be a promising alternative to solders. Perimeter fracturing within sintered-silver test samples increased to 19%–32% of initial bonded area after undergoing 2,500 temperature cycles. Future work will focus on capturing stress-strain data for the selected sintered-silver material and developing a crack initiation and propagation model to obtain stress intensity factor values. These values will be plotted against crack velocities to obtain a V-K curve. Additionally, a second round of test samples with sintered-silver BIM of different geometry will be made and subjected to accelerated tests. Crack initiation and propagation rates of these samples will be analyzed from C-SAM images to aid in generating the V-K curve. Based on this information, techniques to minimize the occurrence of cohesive fracturing by optimizing processing conditions will be evaluated.

FY 2014 Publications/Presentations

1. DeVoto, D.; Paret, P. “Reliability Challenges in Automotive Power Electronics Packages.” *IEEE Reliability Science for Advanced Materials and Devices (RSAMD),* Golden, CO, September 2014.
2. DeVoto, D.; Paret, P. “Performance and Reliability of Bonded Interfaces for High-Temperature Packaging.” *Presentation to the DOE Vehicle Technologies Office (VTO) Electrical and Electronics Technical Team,* Southfield, MI, June 2014.
3. DeVoto, D.; Paret, P. “Performance and Reliability of Bonded Interfaces for High-Temperature Packaging,” *2014 DOE VTO Annual Merit Review,* Crystal City, VA, June 2014.
4. DeVoto, D.; Wereszczak, A.; Paret, P. “Stress Intensity of Delamination in a Sintered-Silver Interconnection.” IMAPS High Temperature Electronics Conference (HiTEC), Albuquerque, NM, May 2014.
5. DeVoto, D.; Paret, P. “Performance and Reliability of Bonded Interfaces for High-Temperature Packaging.” *Advanced Power Electronics and Electric Motors FY14 Kickoff Meeting, DOE VTO,* Oak Ridge, TN, November 2013.

Acknowledgments

The author would like to acknowledge the support provided by Susan Rogers and Steven Boyd, Technology Development Managers for the EDT Program, Vehicle Technologies Office, U.S. Department of Energy Office of Energy Efficiency and Renewable Energy. The significant contributions of Paul Paret are acknowledged. The author would also like to acknowledge Christian Goebl (Semikron) for providing the sintered-silver bonded samples.

References

1. "Directive 2002/95/EC of the European Parliament and of the Council of 27 January 2003 on the Restriction of the Use of Certain Hazardous Substances in Electrical and Electronic Equipment." Official Journal of the European Union. February 13, 2003.
2. Dudek, R.; Faust, W.; Ratchev, R.; Roellig, M.; Albrecht, H.; Michel, B. 2008. "Thermal Test- and Field Cycling Induced Degradation and its FE-based Prediction for Different SAC Solders." *Proceedings of the ITHERM Conference*, Orlando, FL, May 28–31, 2008, pp. 668–675.
3. Wang, Q.; Johnson, W.; Ma, H.; Gale, W. F.; Lindahl, D.; 2005, "Properties of Lead Free Solder Alloys as a Function of Composition Variation," *Electronic Circuits World Convention (ECWC 10),* Anaheim, CA, February 22–24, 2005.
4. Klaka, S.; Sittig, R. 1994. "Reduction of Thermomechanical Stress by Applying a Low Temperature Joining Technique." *Proceedings of the 6th International Symposium Power Semiconductor Devices & ICs,* Davos, Switzerland, 1994, pp. 259–264.
5. Schulze, E.; Mertens, C.; Lindemann, A. 2009. "Low Temperature Joining Technique – a Solution for Automotive Power Electronics." *Power Conversion, Intelligent Motion (PCIM),* Nuremberg, Germany, May 12–14, 2009.
6. Lu, G.-Q.; Zhao, M.; Lei, G.; Calata, J. N.; Chen, X.; Luo, S. 2009. "Emerging Lead-Free, High-Temperature Die-Attach Technology Enabled by Low-Temperature Sintering of Nanoscale Silver Pastes." *International Conference on Electronic Packaging Technology & High Density Packaging (ICEPT-HDP)*, Beijing, China, August 10–13, 2009, pp. 461–466.
7. Schulze, E.; Mertens, C.; Lindemann, A. 2010. "Pure Low Temperature Joining Technique Power Module for Automotive Production Needs.*" 6th International Conference on Integrated Power Electronics Systems (CIPS),* Nuremberg, Germany, March 16–18, 2010.
8. Wereszczak, A. A.; Liang, Z.; Ferber, M. K.; Marlino, L. D. 2014. "Uniqueness and Challenges of Sintered Silver as a Bonded Interface Material." International Conference on High Temperature Electronics (HiTEC), Albuquerque, NM, 2014.
9. Chuang, R. W.; Lee, C. C. 2002. "Silver-Indium Joints Produced at Low Temperature for High Temperature Devices," *IEEE Transactions on Components and Packaging Technologies*, Vol. 25, No. 3, pp. 453–458.
10. McCluskey, P.; Quintero, P. O. 2007. "High Temperature Lead-Free Attach Reliability." *Proceedings of InterPACK, IPACK2007-33457*, Vancouver, British Columbia, Canada, July 8–12, 2007.
11. Wu, R.; McCluskey, F. P. 2007. "Reliability of Indium Solder for Cold Temperature Packaging." *Proceedings of InterPACK, IPACK2007-31456,* Vancouver, British Columbia, Canada, July 8–12, 2007.
12. Lei, T. G.; Calata, J. N.; Lu, G-Q.; Chen, X.; Luo, S. 2010. "Low-Temperature Sintering of Nanoscale Silver Paste for Attaching Large-Area (>100 mm^2) Chips." *IEEE Transactions on Components and Packaging Technology*, Vol. 33, No. 1, pp. 98–104.
13. Associated Research, Inc. 2011. "Exploring the Necessity of the Hot Hipot Test," http://www.asresearch.com/events-training/pdfs/HotHipot.pdf, Accessed May 2011.
14. JEDEC Solid State Technology Association. 2009. "JESD22-A104D Temperature Cycling."
15. Vandevelde, B.; Gonzalez, M.; Limaye, P.; Ratchev, P.; Beyne, E. 2007. "Thermal Cycling Reliability of SnAgCu and SnPb Solder Joints: A Comparison for Several IC-Packages." *Microelectronics Reliability*, Vol. 47, pp. 259–265.
16. Aoki, Y.; Tsujie, I.; Nagai, T. 2007. "The Effect of Ramp Rate on Temperature Cycle Fatigue in Solder Joints." *Espec Technology Report,* pp. 4–13.
17. Lu, G-Q.; Calata, J. N.; Lei, G.; Chen, X. 2007. "Low-Temperature and Pressureless Sintering Technology for High-Performance and High-Temperature Interconnection of Semiconductor Devices." *International Conference on Thermal, Mechanical and Multi-Physics Simulation Experiments in Microelectronics and Micro-Systems (EuroSime),* London, Great Britain, April 16–18, 2007, pp. 1–5.
18. Chen, X.; Li, R.; Qi, K.; Lu, G.-Q. 2008. "Tensile Behaviors and Ratcheting Effects of Partially Sintered Chip-Attachment Films of a Nanoscale Silver Paste." *Journal of Electronic Materials,* Vol. 37, No. 10, pp. 1574–1579.
19. Cameron, D. W.; Hoeppner, D. W. 1996. "ASM Handbook Volume 19, Fatigue and Fracture," ASM International, Materials Park, OH, pp. 15–26.

3.11 Reliability of Electrical Interconnects

Douglas DeVoto (Principal Investigator)

National Renewable Energy Laboratory (NREL)
Transportation and Hydrogen Systems Center
15013 Denver West Parkway
Golden, CO 80401
Phone: (303) 275-4256
E-mail: douglas.devoto@nrel.gov

Susan A. Rogers, DOE Technology Development Manager
Phone: (202) 586-8997
E-mail: susan.rogers@ee.doe.gov

Sreekant Narumanchi, NREL Task Leader
Phone: (303) 275-4062
Email: sreekant.narumanchi@nrel.gov

Start Date: FY11
Projected End Date: FY14

Objectives

- Investigate and improve the reliability of the ribbon bonds utilizing aluminum (Al) and copper (Cu)/Al-clad ribbon materials.
- Develop predictive lifetime models for ribbon bonds that can be used to design components and packages.

Technical Barriers

In automotive power electronics modules, standard packaging technologies have limited the advancement of insulated gate bipolar transistor (IGBT)-based power modules toward designs that promise higher performance and reliability. Increased power densities and larger temperature swings reduce lifetimes for traditional wire bond interconnects. Wire bonds can be replaced with ribbon bonding technology. The ribbon bond process promises a reduction in bonding time, lower loop heights (and correspondingly less heel fatigue), and higher current densities than wire bonds. However, as a newer technology, ribbon bond failure mechanisms are not well understood and thus do not have an accurate lifetime estimate.

Technical Targets

Improved package reliability is an enabler to achieve the U.S. Department of Energy (DOE) Electric Drive Technologies (EDT) Program power electronics targets for improved efficiency, performance, and lifetime.

Accomplishments

- Synthesized Al wire, Al ribbon and Cu/Al-clad ribbon electrical interconnects onto test substrates.
- Performed initial sample characterization via pull testing to quantify pull strength and failure modes.
- Subjected test samples to a series of accelerated tests, including temperature elevation, temperature cycling, high-temperature corrosion, and vibration testing.
- Repeated pull testing after accelerated testing to observe changes in pull strength and failure modes.

* * *

Introduction

The drive toward reduced cost, weight, and volume of components in electric drive vehicles has led to increased performance demands on power electronics modules. The trend toward higher power densities, current levels, and operating temperatures has shown that traditional packaging designs cannot meet the industry's reliability needs. Figure 3-160 shows an example of a power electronics package with electrical interconnects (wire or ribbon bonds), device (IGBT or diode), metalized substrate, and base plate components.

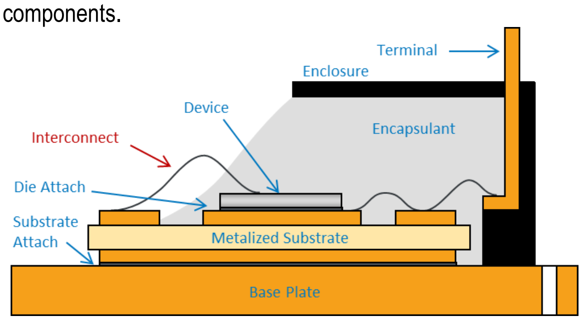

Figure 3-160: Traditional power electronics package.

Wire bonding technology is used to electrically connect devices to each other, to the top metallization layer within the substrate, or to lead frames for connections outside of the power electronics package. Gold, Cu, or Al has traditionally been used as the wire material, with each having tradeoffs in cost, current carrying capability, and mechanical strength [1]. For most common applications, Al has replaced gold and Cu because of its lower cost, but Cu is still selected for power module designs with high current requirements. In addition to material selection, the maximum current a wire can carry depends on its length and diameter; wire sizes are typically between 300 and 500 µm in diameter. If the maximum current level is exceeded, ohmic self-heating will cause the wire to fuse [2]. Heating from within the wire as well as from the devices creates large temperature fluctuations during operation. These temperature variations and mismatches in the coefficient of thermal expansion between the wire material and devices or metalized substrates cause failures in the heel of the wire through flexure fatigue as well as bond pad lift-off. Analytical models have been developed for both failure modes to estimate the mean number of cycles to failure. These common failure modes for wire and ribbon interconnects are shown in Figure 3-161.

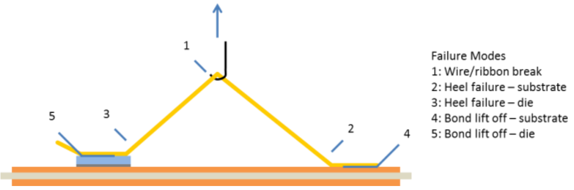

Figure 3-161: Wire and ribbon interconnect failure modes.

For high-current power modules, mechanical limitations to bonding a wire with a diameter larger than 500 µm have required multiple wires to be bonded in parallel. Adding more parallel wires is limited by a substrate's bond pad area and increases the time and cost of bonding. These limitations have generated interest in replacing wire bonds with ribbon bonding technology. Three Al wire bonds with diameters of 400 µm can be replaced on an equivalent electrical current basis by one ribbon bond with a cross section of 2,000 µm × 200 µm [3]. The single ribbon requires a bond width of 2 mm; the three wire bonds require a width of 2.5 mm. Bonding times for both technologies remain the same (300 ms per bond); therefore, the ribbon bonding time for a package can be reduced. For the same span distance, a ribbon bond allows for a lower loop height than a wire bond. This helps to reduce heel stress and ultimately flexure fatigue. Minimizing heel stress is necessary as desired IGBT operating junction temperatures continue to rise to 175°C or higher [4]. However, because of the ribbon's larger geometry, higher bonding energies and forces are required, and bond pad contact areas become larger. Damage initiated during the bonding process could be more likely under ribbon bonding, and coefficient of thermal expansion mismatches between the interconnect material and devices or the metalized substrate could cause failure under thermal cycling conditions.

The performance and reliability of conventional wire bonding are well understood; however, lifetime uncertainties of newer interconnect technologies remain barriers for those novel processes to be utilized by industry. The work at NREL focuses on providing a comprehensive reliability assessment of alternative interconnect technologies to wire bonds, beginning with ribbon bonding. Ribbon bonds are attached to a substrate using a variety of materials and geometries, and then are subjected to accelerated test conditions that highlight the same failure mechanisms found under normal operating conditions. Ideas unique to ribbon bonding will be evaluated, first with the selection of a Cu/Al-clad ribbon that allows the Al side to bond easily to device surfaces while providing the improved electrical performance of Cu [5]. The ribbon's rectangular cross-section geometry makes twisting to create forced angles more difficult than with wire bonding; therefore, bonds with forced angles will be attached to substrate samples [6]. The proposal to attach multiple ribbons over the same bond pad location will be explored as a stacked bonding technique [7]. In conjunction with accelerated testing, physics-of-failure models based on wire bond geometry will be validated for ribbon bonds.

Approach

Materials and Sample Synthesis

NREL chose several ribbon materials under various geometries for accelerated testing. The variations were as follows:

- Material – Al ribbon and a Cu:Al, 2:1 ratio, Cu/Al-clad ribbon.
- Ribbon cross-section – Two cross-sections suitable for current levels within a power module were chosen to be 2,000 µm × 200 µm and 1,000 µm × 100 µm.
- Ribbon span – 10-mm and 20-mm ribbon spans were selected. Corresponding loop heights were set at a ratio of 1:2.2, loop height to ribbon span.
- Number of stitches – Single and double stitches were bonded for 20-mm ribbon spans.
- Ribbon stacking – Stacking one ribbon pad above a second pad can minimize the bonding area on the top of a device but may create a weaker bond.
- Forced angle – Forcing a ribbon at various angles from its bond pad orientation would allow for offset pad locations, but may also create a weaker bond.
- Bond pad interfaces – One end of each ribbon was bonded to a silicon diode and the other end to a substrate's top Cu metalized surface.
- Bonding power – Two bonding powers were selected to evaluate the relationship between bond pad strength and long-term reliability.
- Tool Pattern – The geometry of the tool head affects the deformation shape of the ribbon pads.

The ribbon material and geometry variations cover a design space likely used within a power electronics unit if wire bonds were to be replaced with ribbon bonds. The interconnect variations are summarized in Table 3-8.

Table 3-8: Interconnect variations.

Criterion	Variation		
Bonding Material	Al Ribbon	Cu/Al-Clad Ribbon	Al Wire
Cross Section (µm)	2,000 × 200 Ribbon	1,000 × 100 Ribbon	300⌀ Wire
Ribbon Span (mm)	10	20	
Tool Pattern	Waffle	Three-Ridge	
Ribbon Stacking	Not Stacked	Stacked	
Forced Bond Angle (°)	0	20	
Bonding Power Level	Low	High	
Bond Pad Interface	Cu	Si (Al)	

A 140-mm × 190-mm test substrate design was obtained from Curamik and is constructed of a 0.635-mm-thick alumina layer sandwiched between two 0.203-mm-thick Cu metallization layers. The design of the etch mask for the top Cu layer configures four ribbon bonds electrically in series with multiple parallel paths. This layout was chosen for power cycling samples, but remains the same for all samples. Before the ribbon material was attached to the test substrate, Vishay 5-mm × 5-mm Schottky diodes were soldered in place. The selected diodes have a breakdown voltage of 100 V and can reach a maximum junction temperature of 175°C. The diode back side has a chromium/nickel/silver coating for good solderability; the top side includes a 3-µm layer of Al (1% Si) to be compatible with the ultrasonic bonding process. Each test substrate was imaged by acoustic microscopy to ensure that the solder attachment for each diode contained minimal voiding. The first end of each ribbon interconnect was bonded to the top Cu metallization layer of the test substrate; the second was bonded to the top surface of the diode.

Both Al and Cu/Al-clad ribbon materials were obtained from Heraeus Materials and were attached using an Orthodyne 3600 wedge bonder at Kulicke & Soffa. Dow Corning 3-4150 dielectric gel was used to protect the interconnects in silicone encapsulant. An example of a test substrate with a completed design layout is shown in Figure 3-162.

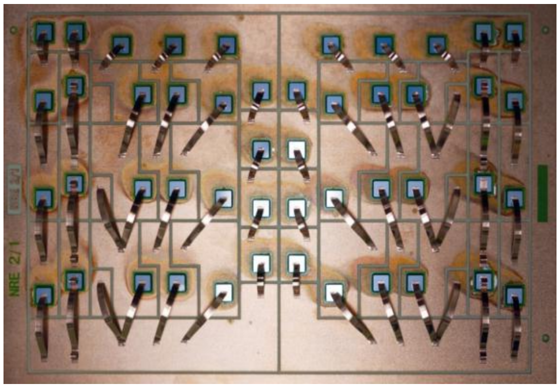

Figure 3-162: Test substrate showing ribbon layout (Photo credit: Doug DeVoto, NREL).

Multiple instances (material, span, angle, and stacked) of each ribbon configuration were arranged on the test substrates. The left and right sides of each substrate specified different bonding power levels for 1,000 µm × 100 µm ribbons while different tool patterns (wedge or three-ridge) were specified for 2,000 µm × 200 µm ribbons. The arrangement of the ribbon geometry instances is shown in Figure 3-163.

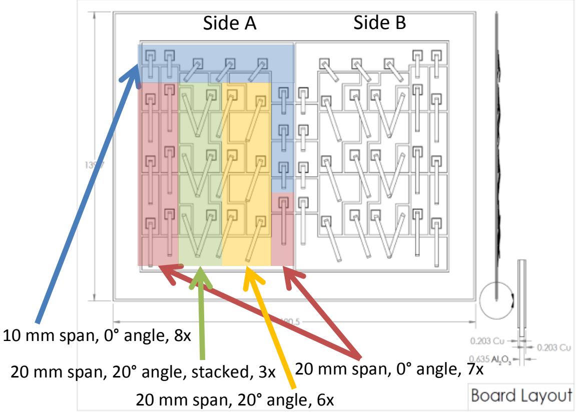

Figure 3-163: Wire and ribbon interconnect failure modes.

Ribbon Bonding Mechanical Characterization

An XYZTEC Condor 100-3 mechanical bond tester was used to measure the pull strength of the ribbon and wire bonds. As this was a destructive evaluation, one set of test sample substrates without any prior accelerated testing was selected to measure initial bond strength through pull tests. Silicone encapsulant was removed prior to pull testing with Digesil NCX de-polymerization compound. For the pull test, a hook was first positioned under the ribbon. At the initiation of the test, a constant velocity of 250 µm/s was applied to the hook and maintained for a travel distance of approximately 4 mm. Sufficient force was used to maintain this velocity against the tensile strength of the ribbon or wire material and strength of the bond pads. A test was completed when one of the five failure modes previously listed occurred, and the maximum force required for failure was recorded. This force was compared to minimum acceptable bond strengths as outlined in Method 2011.8 of the Department of Defense Test Method Standard 883H. The minimum acceptable pull force is a function of the interconnect's cross-section, as shown in Figure 3-164. The acceptable force ranges from 0.96 N for a 300-µm-diameter wire to 3.50 N for a 2,000-µm × 200-µm ribbon.

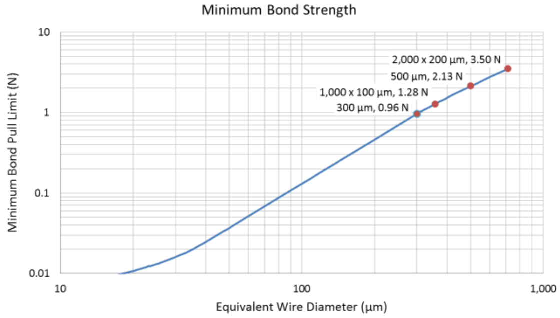

Figure 3-164: Minimum wire and ribbon bond pull strength limits.

In addition to recording the maximum tensile force, the failure mode was documented. Images showing the most common modes are shown in Figure 3-165. An interconnect with strong bonds may fail near the hook placement, as shown in the image to the left. Weakening of the heel of a ribbon can occur through repeated vibration or thermal cycling (center), while a bond lift-off (right) can indicate poor surface cleaning prior to bonding or inadequate bonding parameters.

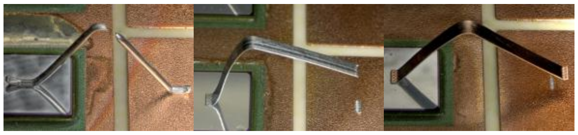

Figure 3-165: Failure modes from the left: wire break (left), heel failure from the substrate (center), and bond lift-off from the substrate (right)
(Photo credit: Doug DeVoto, NREL),

Accelerated Testing

Subjecting a component to accelerated test conditions identifies its failure mechanisms in a shorter time relative to normal operating stress conditions. Various accelerated tests were selected to evaluate likely failure mechanisms within ribbon interconnects and are shown in Table 3-9. These test procedures are based on standards for the microelectronics industry [8].

Table 3-9: Accelerated testing procedures.

Accelerated Test	Testing Condition	Duration
Temperature Elevation	150°C	500/1,000 hours
Temperature Cycling	–40°C to 150°C, less than 20 s transition time	1,500/3,000 cycles
Corrosion Testing	130°C, 85% relative humidity	96 hours
	110°C, 85% relative humidity	264 hours
	121°C, 100% relative humidity	96 hours
Power Cycling	25°C to 120°C, ~ two-second cycled DC bias	3,000 cycles
Vibration Testing	Highly accelerated life test (HALT)	Until interconnect fails

Accelerated test methods—humidity, thermal, power, vibration, or a combination of the four—are designed to highlight a particular interconnect's failure mode.

- Samples subjected to high-temperature storage testing highlighted thermally activated failure mechanisms. Ribbon bonds were stored at 150°C for 500 and 1,000 hours.
- Alternating temperature extremes test the ability of interconnects to withstand thermally induced mechanical stresses. Samples are being cycled from –40°C to 150°C for 3,000 cycles. A portion of the sample population will be pull tested after 1,500 cycles. Transition times between temperature extremes are completed in less than 20 seconds, and no dwell/soak times are held.
- Three humidity-based tests evaluated the corrosion resistance of the ribbons and their bond pads. Under a humidity test, ribbon interconnects were placed in a 121°C, 100% relative humidity environment for 96 hours. In two additional humidity tests, samples were subjected to an 85% relative humidity environment at either 110°C for 264 hours or 130°C for 96 hours.
- In power cycling tests, interconnects will be subjected to a periodically applied operating bias to thermally cycle them from room temperature to 125°C for 3,000 cycles.
- Random six-degree-of-freedom vibration and rapid thermal cycling stressed the ribbon bonds beyond their design specifications to quickly highlight predominant failure mechanisms and provided a qualitative comparison between geometries.

Temperature cycling tests were conducted in a Cincinnati Sub-Zero VTS Compact Thermal Shock Chamber to achieve rapid thermal changes. High-temperature storage testing was completed using ESPEC BTZ-175 bench-top temperature chambers. Samples were placed in an ESPEC Highly Accelerated Stress Test (HAST) chamber for humidity tests. Vibration testing following the HALT procedure was conducted in a Qualmark Typhoon chamber. Test samples were secured via custom fixtures to each corner region of the vibration table, as shown in Figure 3-166.

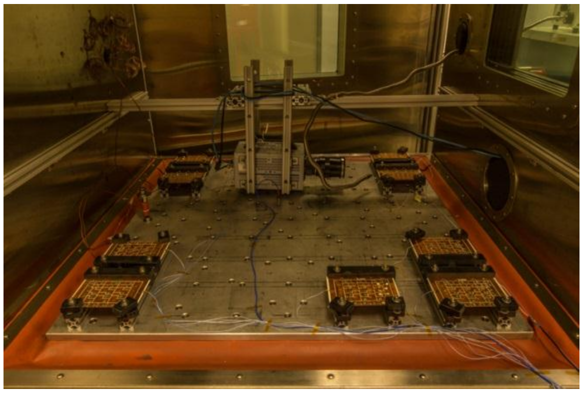

Figure 3-166: Test sample layout within Qualmark Typhoon chamber
(Photo credit: Doug DeVoto, NREL).

High-speed video capture and accelerometers mounted to each test board monitored the vibration response of the table, test boards, and individual wires and ribbons. Test sample measurements revealed acceleration levels four times higher relative to the table due to the fixtures and material properties of the test substrates. Eight consecutive tests were completed for HALT evaluation. Each test included three thermal cycles between the temperature extremes of –40°C to 150°C. Vibration conditions were incrementally increased from 5 G_{rms} to 30 G_{rms} over the eight tests. Table 3-10 summarizes the acceleration specified at the table for each test.

Table 3-10: Vibration test acceleration conditions.

Test Iteration	Vibration Condition (G_{rms})
1	5
2	10
3	15
4	20
5	20
6	20
7	25
8	30

After completion of each test, a Hioki RM 3544-01 resistance meter was used to determine if an interconnect was functional. An open circuit measurement indicated a heel or lift-off failure.

Results

Initial Results

The results from three accelerated tests are highlighted below. Table 3-11 summarizes these testing conditions and durations.

Table 3-11: Completed accelerated tests.

Accelerated Test	Testing Condition	Duration
Temperature Elevation	150°C	96 hours
Corrosion	121°C, 100% relative humidity	96 hours
Vibration Testing	HALT	Until interconnect fails

Before accelerated testing was initiated, pull tests established initial pull strength and failure modes for each wire and ribbon interconnect material. Figure 3-167 highlights the pull strength of 10-mm and 20-mm span, 1,000 µm × 100 µm interconnects with no forced angle or stacked bond pads.

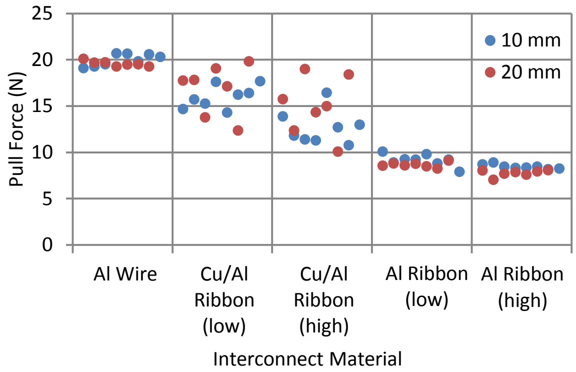

Figure 3-167: Initial pull strength for interconnect materials.

Al wire interconnects exhibited the greatest strength from the pull tests, closely followed by Cu/Al-clad ribbons. The strength of Al ribbon bonds was noticeably lower, but still strong enough to be considered successful. While the same synthesis technique was used for each interconnect material, a larger distribution in pull strength was observed for Cu/Al-clad ribbons. The key aspect to monitor is if the bond strength for each respective interconnect material significantly decreases after accelerated tests. The failure modes associated with the above pull test measurements are shown in Figure 3-168. Each interconnect material exhibited a different failure mechanism, with wire bonds failing within the material near the hook, Cu/Al-clad ribbons lifting off from their substrates and diodes, and Al ribbons failing within their heel region. Cu/Al-clad bond lift-off failures and the scatter of their pull strength may be an indication that their bonding force could have been higher. The failure mode potentially may then shift to heel failures or ribbon breaks and the scatter may reduce. However, a higher bonding force may damage the underlying Si devices so the parameters need to be balanced. It should be noted that the Cu/Al-clad ribbons still exhibit greater strength at their lowest data points relative to Al ribbons.

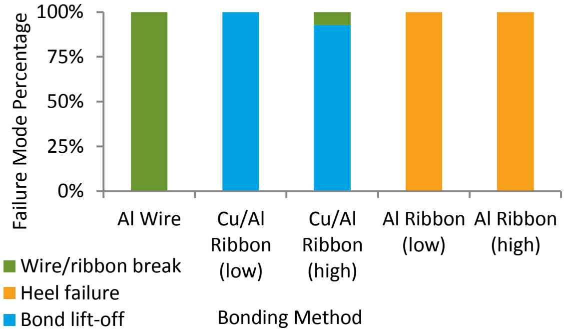

Figure 3-168: Failure modes for initial pull testing.

Accelerated Testing Results

Pull testing of the wire and ribbon interconnects after accelerated testing was completed to evaluate any reductions in bond strength. Figure 3-169 highlights the pull strength of 1,000 µm × 100 µm low-power Al ribbons after 500 and 1,000 hours of temperature elevation at 150°C. Results show a marginal decrease in pull strength after 500 hours with no change after 1,000 hours.

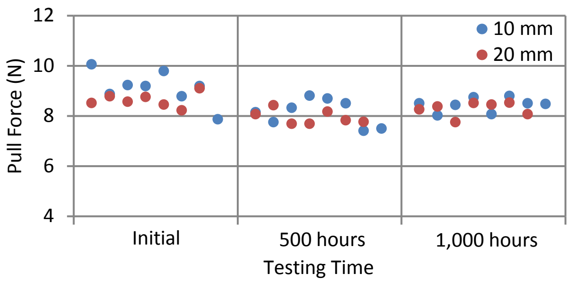

Figure 3-169: Pull strength for Al 1,000 µm × 100 µm low-power ribbon bonds after temperature-elevation testing.

Pull test results were also completed on Al ribbons that were bonded at high power levels, as shown in Figure 3-170. Results also showed a marginal decrease in strength after

500 hours with no change after 1,000 hours. This indicates that ribbon lifetime will not be severely reduced from high temperature operation.

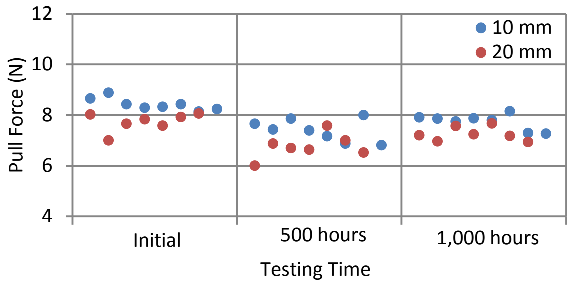

Figure 3-170: Pull strength for Al 1,000 μm × 100 μm high-power ribbon bonds after temperature-elevation testing.

Failure modes remained unchanged throughout the duration of the temperature-elevation testing at low-power bonding.

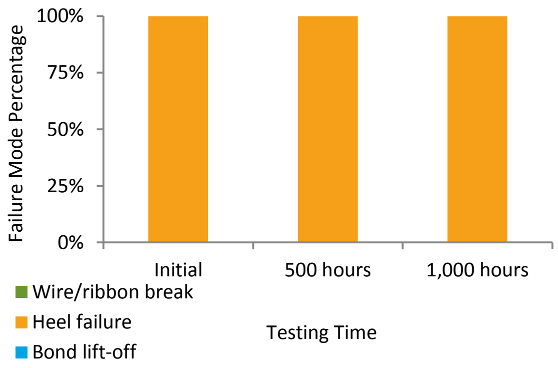

Figure 3-171: Failure modes for Al 1,000 μm × 100 μm low-power ribbon bonds after temperature elevation testing.

No change was observed with high-power bonded samples either, as shown in Figure 3-172.

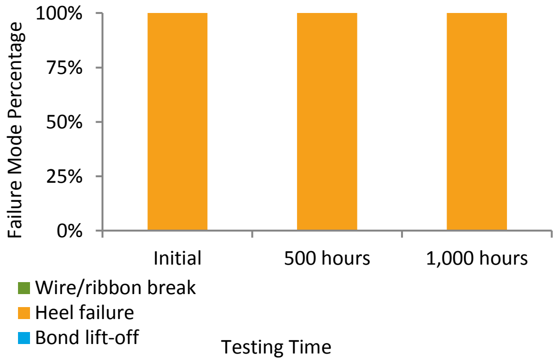

Figure 3-172: Failure modes for Al 1,000 μm × 100 μm high-power ribbon bonds after temperature-elevation testing.

Samples were subjected to corrosion testing at 121°C, 100% relative humidity for 96 hours. Pull strength testing indicated a slight decrease in Al wire strength with little change in strength of the ribbon interconnects, as shown in Figure 3-173.

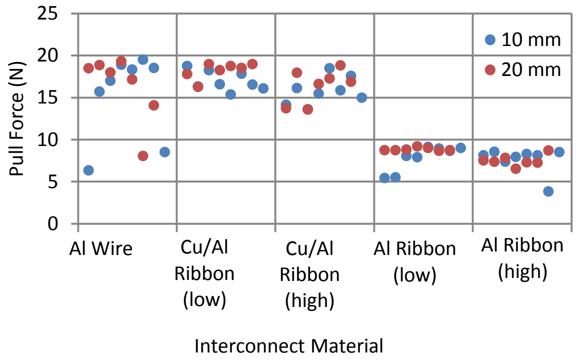

Figure 3-173: Pull strength for interconnect materials after corrosion testing.

Al wire failures shifted to include heel failures and bond lift-off failures while Cu/Al-clad and Al ribbons failure modes remained unchanged. The reduction in pull strength and change in failure modes indicates that Al wire is more susceptible bond weakening from moisture.

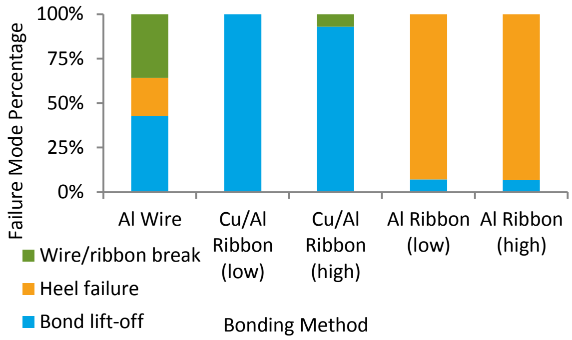

Figure 3-174: Failure modes for interconnect materials after corrosion testing,

Interconnects subjected to HALT profiles were evaluated under a different criterion compared to other accelerated life tests. The goal of a HALT evaluation is to identify the weakest mechanical component within an electronics package. While it is not intended to directly link to real-world operating conditions, it can be used to compare the reliability of packaging designs.in a short timeframe. After qualification of the fixtures and experimental setup, the eight test profiles were initiated in succession. Wire and 1,000 μm × 100 μm ribbon interconnects with 20-mm spans are summarized in Figure 3-175. Several observations can be made. Al ribbons failed at the highest rate, with all interconnects reaching failure by the end of the test profiles. The test board containing ribbons bonded at a higher power level exhibited failures more quickly than the test board with a lower bonding power level. Higher residual stress within ribbons bonded at the higher power level is likely the cause for the variance in failure times. Cu/Al-clad ribbons failed at a slower rate, but also indicated that the lower bonding power level was a more reliable design. Both ribbon interconnects failed at a more rapid pace than the baseline wire bonds. It should be noted that 10-mm-span wires and ribbons proved to be very durable under the HALT evaluation and would have required additional test profiles to initiate failures. For operational environments that include high vibration conditions, it is recommended to minimize ribbon span length.

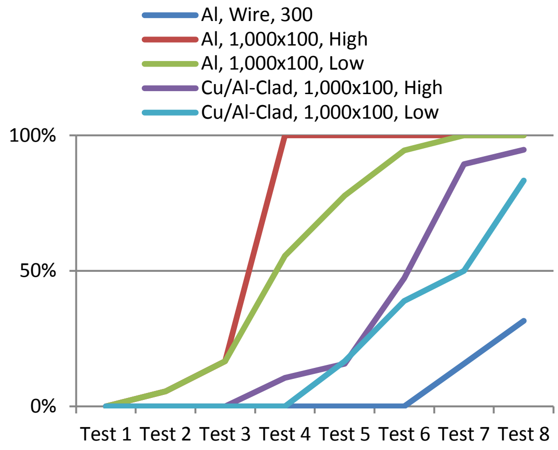

Figure 3-175: Percentage of 20-mm-span interconnects failed after each vibration test.

A similar evaluation was completed for 2,000 µm × 200 µm ribbon interconnects. While a distinction in reliability could previously be made for bond power level for 1,000 µm × 100 µm ribbons, there was no discernable benefit for selecting either a waffle or three-ridge tool pattern. Al ribbons again failed at a higher rate, but 2,000 µm × 200 µm ribbons proved to be more reliable than the smaller cross-section test samples. Ribbons again failed at higher rates than wire bonds, but 10-mm-span interconnects proved reliable under the testing procedure.

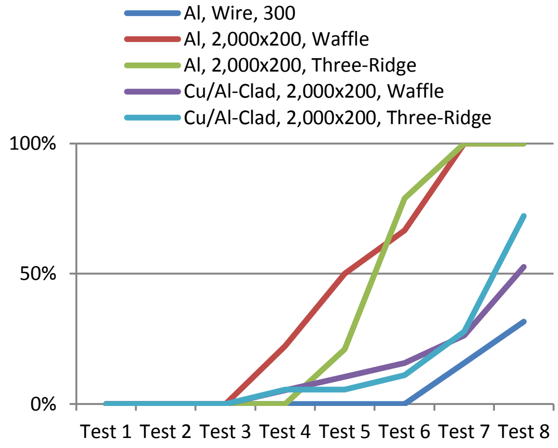

Figure 3-176: Percentage of 20-mm-span interconnects failed after each vibration test.

Interconnects that did not fail through HALT evaluation will be subjected to pull testing. Additional motion analysis of the ribbon and wire interconnects will be completed by analyzing high frame rate (10,000 fps) video.

Physics-of-Failure Models

Under temperature cycling loads, the coefficient of thermal expansion mismatch between the ribbon material and the silicon device or metalized substrate results in stress/strain reversals in the heel of the ribbon interconnect, gradually leading to its failure. Physics-of-failure models identify the root cause of this failure and then provide lifetime estimation based on material properties, geometry, and environmental conditions [9]. Using the theory of curved beams, the strain prediction on the upper side of the ribbon bond can be approximated using equation 1:

$$\varepsilon = \frac{r(\rho_f - \rho_i)}{\rho_i \rho_f} = r(k_i - k_f) \qquad (1)$$

where:

ε is strain induced

r is half the thickness of the ribbon

ρ_f is the radius of curvature of the ribbon heel after heating

ρ_i is the radius of curvature of the ribbon heel before heating

k_f is the curvature at the heel of the ribbon after heating

k_i is the curvature at the heel of the ribbon before heating.

This equation shows that the strain induced in the lower side ($[\rho_i/\rho_f]$+2r) will be lower compared to the strain in the upper side of the ribbon. Once the strain is calculated, the number of cycles to failure, N_f, can be determined using the Coffin-Manson equation:

$$N_f = C_r \varepsilon^{-m_r} \qquad (2)$$

where C_r and m_r are fatigue properties found through material tensile tests.

As the loop geometry plays a significant role in the prediction of strain values, the ribbon should be in a state of minimum potential energy. An energy-based cubic spline model is used to determine the geometry of the loop that achieves a minimum potential energy [9]. For a given span, the loop height is varied to find the least energy state, by equation 3:

$$d = \frac{Dh}{H}\left[1 - \sqrt{1 - \frac{H}{h}}\right] \qquad (3)$$

where

d is half the span

h is loop height

D is the total span of the ribbon

H is the height offset between bond pads.

This calculation was used to determine the least energy state for a ribbon interconnect to have a ratio of 1:2.2 between the loop height and span length.

A finite element analysis (FEA) model was developed to find the stress and strain values induced in an Al ribbon bond with a 10-mm span. The model geometry of a sample ribbon interconnect was created in SolidWorks and imported into ANSYS Workbench. A cross-section image of the sample ribbon was experimentally measured using a microscope to create a spline fit profile that could be imported into the FEA model. The plasticity model was specified as a multilinear kinematic hardening model to properly define the plastic behavior of the Al material, with stress-strain values at room temperature obtained from corresponding curves from literature [10]. A test case was run with a temperature cycle profile from 20°C to 160°C at a ramp rate of 5°C/min. A maximum deflection of 33.8 µm was observed at the top of the ribbon profile. Maximum von Mises stress values of 183.1 MPa and 193.9 MPa were found to be at the heel for the first and second bonds, respectively. The maximum deflection result from the model will be compared against experimentally obtained deflection results to validate the FEA model. The SolidWorks geometry showing the first and second bond locations and maximum von Mises stress are shown in Figure 3-177.

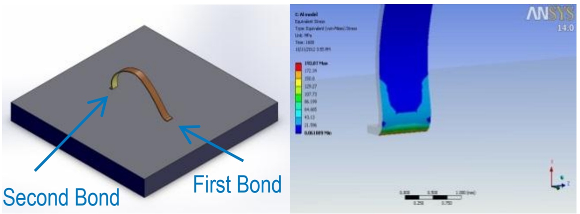

Figure 3-177: FEA model of 1,000 µm × 100 µm Al ribbon with 10-mm span (left) and maximum stress shown at heel location near second bond pad (right).

Future modeling results will be improved by including temperature-dependent material properties for Cu and Al, and will be expanded to include Cu/Al-clad ribbon geometries. Deflection, von Mises stress, and strain results will be compared to the failure modes observed in the experimental accelerated tests. Analytical and FEA results will be incorporated into the Coffin-Manson relation to predict the number of cycles to failure and validated with experimental test results for cycles to failure.

Conclusions and Future Directions

This comprehensive evaluation of the reliability of ribbon bond interconnects has resulted in several initial recommendations. To date, the impact of temperature elevation, humidity, and vibration on the interconnects has been investigated. Some key findings were that temperature elevation and humidity testing only marginally reduced the bond strength of Al wire, Al ribbon, and Cu/Al ribbon. Vibration testing highlighted the benefits of selecting shorter span lengths, lower bonding power levels, and Cu/Al-clad material. A variety of materials and geometries will continue to be tested under various accelerated testing conditions to highlight failure mechanisms. Combining experimental results with time-to-failure models will enable reliability predictions for ribbon interconnects.

FY 2014 Publications/Presentations

1. DeVoto, D.; Paret, P. “Reliability of electrical interconnects.” *Presentation to the DOE Vehicle Technologies Office (VTO) Electrical and Electronics Technical Team,* Southfield, MI, June 2014.
2. DeVoto, D.; Paret, P. “Reliability of electrical interconnects.” *2014 DOE VTO Annual Merit Review,* Crystal City, VA, June 2014.
3. DeVoto, D.; Paret, P. “Reliability of electrical interconnects.” *Advanced Power Electronics and Electric Motors FY14 Kickoff Meeting, DOE VTO,* Oak Ridge, TN, November 2013.

Acknowledgments

The author would like to acknowledge the support provided by Susan Rogers and Steven Boyd, Technology Development Managers for the EDT Program, Vehicle Technologies Office, U.S. Department of Energy Office of Energy Efficiency and Renewable Energy. The contributions of Paul Paret (NREL) to the project are acknowledged. The author would also like to acknowledge Christoph Luechinger and Tao Xu (Kulicke & Soffa) for providing substrates with the ribbon bonds.

References

1. Ménager, L.; Martin, C.; Allard, B.; Bley, V. (2006). “Industrial and lab-scale power module technologies: A review.” *IEEE 32nd Annual Conference on Industrial Electronics (IECON)*, Paris, France, November 7–10, pp. 2426–2431.
2. Ciappa, M. (2002). “Selected failure mechanisms of modern power modules,” *Microelectronics Reliability*, Vol. 42, pp. 653–667.
3. Farassat, F.; Sedlmair, J. (2007). “More performance at lower cost – heavy aluminum ribbon bonding.” F & K Delvotec Bondtechnik GmbH.
4. Guth, K.; Siepe, D.; Görlich, J.; Torwesten, H.; Roth, R.; Hille, F.; Umbach, F. (2010)., “New assembly and interconnects beyond sintering methods.” *Power Conversion, Intelligent Motion (PCIM),* Nuremberg, Germany, May 4–6, 2010.
5. Luechinger, C.; Loh, T.; Oftebro, K.; Wong, G. (2007). “Composite aluminum-copper ribbon bonding – heel reliability.” *Proceedings of IMAPS*, San Jose, CA, November 11–15, 2007.
6. Luechinger, C. (2007). “Ribbon bonding – A scalable interconnect for power QFN packages.” *IEEE 9th Electronics Packaging Technology Conference (EPTC),* Singapore, December 10–12, 2007, pp. 47–54.

7. Almagro, E.; Granada Jr., H. (2008). “Stack bonding technique using heavy aluminum ribbon wires.” *IEEE 10th Electronics Packaging Technology Conference (EPTC),* Singapore, December 9–12, 2008, pp. 976–981.
8. “Standards & documents search,” JEDEC, http://www.jedec.org/standards-documents.
9. Meyyappan, K. (2004). *Failure prediction of wire bonds due to flexure*, Ph.D. Thesis, College Park, MD: University of Maryland.
10. Tamarin, Y. (2002). *Atlas of stress-strain curves,* 2nd Edition. Materials Park, OH: ASM International.

3.12 Two-Phase Cooling of Power Electronics

Gilbert Moreno (Principal Investigator)

National Renewable Energy Laboratory (NREL)
Transportation and Hydrogen Systems Center
15013 Denver West Parkway
Golden, CO 80401
Phone: (303) 275-4450
E-mail: gilbert.moreno@nrel.gov

Susan A. Rogers, DOE Technology Development Manager
Phone: (202) 586-8997
E-mail: susan.rogers@ee.doe.gov

Sreekant Narumanchi, NREL Task Leader
Phone: (303) 275-4062
Email: sreekant.narumanchi@nrel.gov

Start Date: FY11
Projected End Date: FY14

Objectives

The overall project goal is to utilize the high-heat transfer capacity of two-phase cooling to significantly improve thermal management of automotive power electronics. Improving thermal management can enable achieving the U.S. Department of Energy (DOE) Electric Drive Technologies (EDT) Program power electronics technical targets. Specific FY14 project objectives are:

- Demonstrate a compact, inverter-scale passive two-phase cooling system capable of dissipating automotive power electronic heat loads.
- Increase the thermal performance (i.e., power density), coefficient-of-performance and reduce the weight and volume of the cooling system by using a passive two-phase cooling system.

Technical Barriers

Two-phase cooling is well known to provide very high heat transfer coefficients as compared to other forms of cooling [1]; however, concerns regarding reliability and cost of two-phase–based cooling systems hinder their implementation within automotive-based applications. In this project, we attempt to demonstrate a two-phase cooling solution for automotive power modules based on a passive and indirect cooling strategy. The indirect cooling strategy eliminates direct contact of the refrigerant with the electronics and thus eliminates material compatibility issues. Moreover, this approach also eliminates electrical feed-through penetrations that may pose a refrigerant leakage potential. The passive approach (i.e., no compressor or pump) simplifies the system, which has implications for reduced cost and increased efficiency. Although not the conventional method of cooling automotive power electronics, passive two-phase cooling solutions have been used to cool power electronic components (Gate-Turn-Off thyristors) in mining haul trucks and high-speed trains [2–4].

Technical Targets

This project aims to enable achieving the DOE EDT Program power electronics targets listed below by significantly improving thermal management:

- Power density
- Specific power
- Efficiency
- Cost.

Accomplishments

- Increased the device (e.g., insulated gate bipolar transistor) heat density by 139% (aluminum evaporator) to 189% (copper evaporator) using a passive and indirect two-phase cooling system that incorporates a novel evaporator design.
- Reduced the weight of the inverter coolant system by 41%. The estimates consider the majority of the coolant system components (radiator, inverter cold plate, and coolant). Moreover, the two-phase cooling system reduces the total aluminum weight by 17%. Additional reductions to the weight and also the volume can be obtained if the two-phase system is designed to operate at higher temperatures (>80°C).
- Increased efficiency combined with a reduction of the thermal resistance increases the coefficient-of-performance by 127%.
- Demonstrated that the cooling system can dissipate at least 3.5 kW (3.5 kW of heat is a conservative estimate on the heat dissipation from a 55-kW inverter) of heat with only 0.18 L (180 cm^3, 240 grams) of HFC-245fa refrigerant. For comparison, the coolant volume on a typical vehicle inverter coolant system can be several liters. The 2010 Toyota Camry utilizes 510 grams of refrigerant and 139 grams of refrigerant oil for the air conditioning system.

✧ ✧ ✧ ✧ ✧

Introduction

An efficient thermal management strategy can be an effective means of reducing the size and cost of electronics as well as improving performance and reliability. In this project, we are evaluating two-phase heat transfer as a means of cooling automotive power electronics. The high heat transfer rates and isothermal characteristics of two-phase heat transfer allow for increased power density and specific power, which may enable achieving the DOE EDT Program power electronics technical targets. The intent is to demonstrate superior thermal performance, increased efficiency, reduced weight, and reduced volume with the two-phase cooling system(s) developed. Passive (pump-less) two-phase systems with an air-cooled condenser will be developed due to their inherent efficiency and simplicity.

Approach

In this project, we performed both fundamental and system-level research to evaluate two-phase (boiling/evaporation) heat transfer as a potential power electronics cooling solution. Initial research efforts were focused on characterizing the pool boiling performance of novel coolants/refrigerants as well as investigating promising boiling enhancement techniques. HFO-1234yf and HFC-245fa are the two refrigerants being considered for automotive power electronics cooling applications. HFO-1234yf is qualified for automotive use and has a low global warming potential (GWP = 4). HFC-245fa is a lower-pressure refrigerant that has a higher critical temperature and is non-flammable.

The fundamental research results then fed into the design of the system-level components. The system-level study was focused on developing a prototype passive two-phase cooling system capable of dissipating automotive power electronic heat loads. Small-scale experiments were first conducted to understand and improve the performance of a passive two-phase cooling system (i.e., evaporator and condenser). Recent research efforts were focused on demonstrating an inverter-scale passive two-phase system for automotive power modules (Delphi's discrete power switches).

Experimental Apparatus

A schematic of the cooling system tested is provided in Figure 3-178. Two different evaporator design were tested—a copper cold plate-based design and an aluminum-based design. Both evaporators were designed to cool six Delphi discrete power modules/switches. The six power modules represent a voltage source inverter system required to power an automotive electric machine/motor. Details of the various evaporator designs tested are provided in the Results section.

Two condensers were tested, one with plain tubes and one with rifled tubes. The rifled features, shown in Figure 3-179, were evaluated as a means of enhancing condensation heat transfer. Per the manufacturer, the condensation-side surface areas were 1,190 cm^2 and 1,250 cm^2 for the plain and rifled condensers, respectively. The two condensers were finned-tube, air-cooled type heat exchangers. The fins were louvered and fabricated from 0.15-mm-thick aluminum sheets(Figure 3-179). The total air-side surface area was calculated to be approximately 29,000 cm^2. Twenty 0.95-cm (3/8-in.)-outer-diameter copper tubes were arranged in two rows (see Figure 3-178). Two tubes, one from each row, were connected at the top via U-bend fittings. A manifold header connected all tubes at the lower end.

Heat from the system was rejected to air by means of a 17.8-cm (7-in.)-diameter automotive axial fan mounted to the condenser. The fan operates on 12 V and consumes 38 W of power, calculated by voltage and current measurements. Two 2.54-cm-inner-diameter tubes connected the condenser manifold to the evaporator. The tubes were sized large enough to prevent falling liquid from restricting/blocking the rising vapor.

The system was designed with a maximum operating pressure of 1.03 MPa (150 psi). Finite element structural analysis was used to design the evaporators to allow for elevated-pressure operation. The condensers were purchased and had a 2 MPa pressure rating. Once the condensers and evaporators were assembled, hydrostatic pressure-tests were conducted to verify the system's pressure rating.

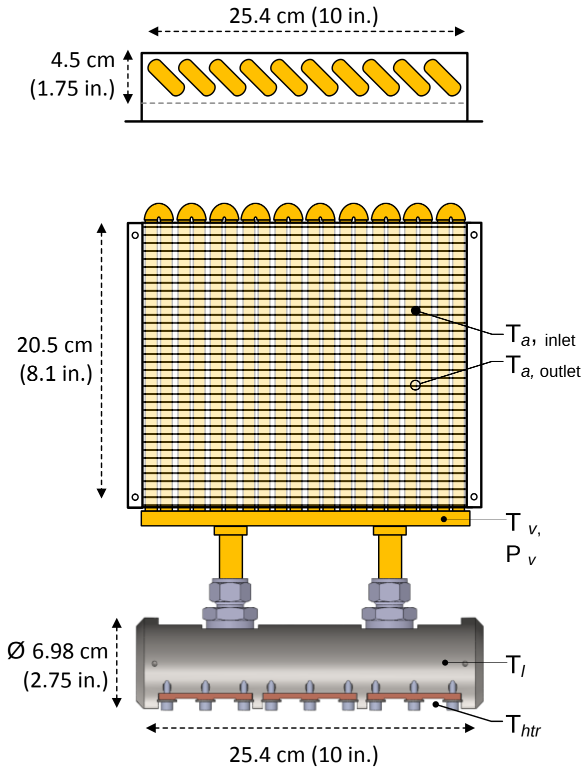

Figure 3-178: Schematic of the passive, two-phase cooling system. The initial, copper cold plate evaporator design is depicted in this schematic.

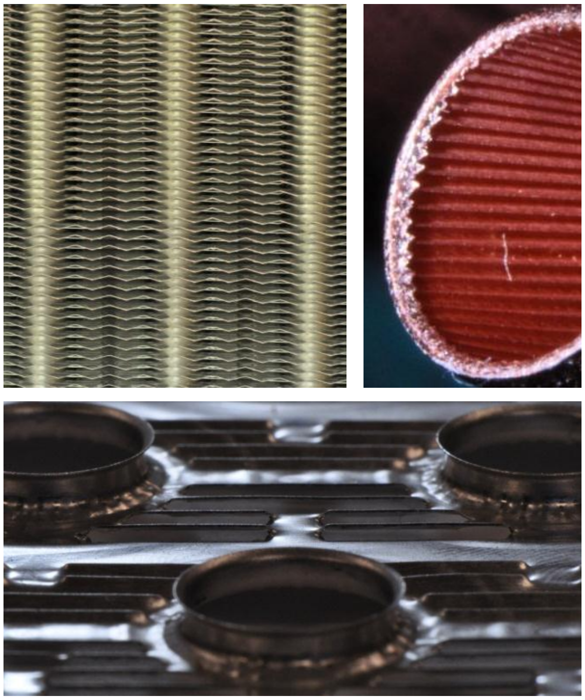

Figure 3-179: Images of the finned-tube condenser (top-left), rifled tube (top-right), and louvered-fin design (bottom). Photo credit: Gilbert Moreno (NREL).

The cooling system was instrumented with sensors to measure system pressure and temperatures. System vapor pressure was measured using a calibrated absolute pressure transducer. System temperatures were measured using calibrated K-type thermocouples for the inlet-air, outlet-air, liquid, vapor, and heater temperatures.

Experimental Procedures

Six Watlow ceramic heaters were used in place of the Delphi power modules. The dimensions of the ceramic heaters (25 mm × 15 mm × 2.5 mm) were similar to those of the Delphi modules. Each heater generates up to about 580 W of heat (total power for six heaters: 3,500 W). The ceramic heaters were externally attached to the evaporators using thermally conductive grease as the thermal interface material. The temperatures of the heaters were measured via thermocouples embedded within the ceramic heaters.

After the heaters were attached to the evaporator, the system was charged using a transfer tube that contained a measured amount of saturated, oil-free refrigerant. Prior to charging the system with the refrigerant, the air in the system was removed using a vacuum pump. Pressure within the system was allowed to decrease to about 2 Pa to ensure that most of the air was evacuated. A valve between the transfer tube and the system was then opened, allowing the refrigerant to drain into the system. Once the refrigerant was transferred, the valve between the transfer tube and the system was closed, and the transfer tube was disconnected from the system. Measurements of the vapor temperature and pressure confirmed saturated conditions, verifying that no air was present within the system.

Experiments were initiated after saturated conditions were verified. First, the fan was powered to pull ambient air (T_a inlet = 25°C) through the condenser. The six heaters were then powered using two Agilent direct current power supplies. Heater loads ranged from 250 W to 3,500 W. The system was allowed to reach equilibrium conditions (about 15 minutes) at each power level before increasing the power. Measurements of the system and heater temperatures combined with heat load measurements were used to compute the evaporator and condenser thermal resistances at various power levels.

Uncertainty Analysis

Analysis was conducted to quantify the uncertainty in the measured experimental values according to the procedures outlined by Dieck [5]. The procedure consisted of gathering systematic and random uncertainties in all measured variables. The propagation-of-error equation was then used to estimate the uncertainties in the calculated values. The uncertainty for the thermal resistance values is estimated to be approximately ±9%. After calibration, the uncertainty in a thermocouple was conservatively estimated at ±0.1°C, while the uncertainties in the heat measurements were estimated to be ±1%. All stated uncertainties were calculated at a 95% confidence level.

Results

Experiments were conducted to measure the thermal performance of a passive two-phase cooling system. This included measuring the thermal resistance of the condenser and evaporator. The thermal performance data combined with the volume, weight, and parasitic power requirements of the two-phase cooling system were then compared with equivalent metrics of a conventional, water-ethylene glycol-based (WEG) cooling system.

Experiments were conducted to measure the thermal resistance of two evaporator designs—a copper cold plate-based design and an advanced all-aluminum-based design. The evaporator's specific (area-weighted) thermal resistance was defined per Equation 1.

$$R''_{th,\ evaporator} = \frac{(\overline{T_{htr}} - T_l)}{Total\ power} \times A_{htr} \qquad (1)$$

where $\overline{T_{htr}}$ is the average temperature of the six ceramic heaters as measured by the thermocouples embedded within each heater, and T_l is the refrigerant liquid temperature. The *total power* is the total heat dissipated by the system and A_{htr} is the total surface area of the six heaters (22.5 cm^2).

Evaporator Thermal Performance (Concept 1)

The initial copper cold plate design consisted of a steel cylinder and three copper cold plates and was charged with 250 cm^3 of refrigerant (Figure 3-180). This evaporator's flexible design also allows testing of different boiling/evaporation enhancement techniques (e.g., boiling enhancement coatings and finned surfaces). The copper cold plates were machined with 4-mm-tall fins, each of which has a wetted surface area of about 55 cm^2. Because two-phase cooling provides high heat transfer rates, the fins are not expected to have a significant effect on the evaporator thermal resistance. However, the fins were included as a means of increasing surface area in an attempt to delay dry-out.

The specific thermal resistance of the copper cold plate evaporator is plotted versus the total heat dissipated in Figure 3-181. Results for refrigerants HFC-245fa (330 grams) and HFO-1234yf (280 grams) are provided. As shown in Figure 3-181, the heater-to-liquid resistances for both refrigerants decrease with increasing heat dissipation. This effect is associated with an increased contribution from two-phase heat transfer (i.e., boiling/ evaporation) at higher power levels, which improves thermal performance. Tests were performed with increasing and decreasing heat fluxes to evaluate for hysteresis effects. Results showed that using an increasing or decreasing heat rate had little effect on the thermal performance of the system.

With 250 cm^3 of HFC-245fa, the system was capable of dissipating 3.5 kW of heat under steady-state conditions without reaching dry-out (i.e., critical heat flux). The refrigerant-volume-to-heat-dissipated ratio, at maximum heat load, was 71 cm^3 / kW, which is less than the 100 cm^3 / kW estimate by Barnes and Tuma [6]. At 3.5 kW, the heaters are at their maximum allowable power rating, thus it was not possible to test to higher heat loads. The 3.5 kW of heat dissipation is noteworthy because it is a conservative estimate on the inverter heat dissipation requirement for a 55-kW electric traction-drive system. With HFO-1234yf, tests were limited to lower heat loads due to HFO-1234yf's higher operating pressures. At 1.25 kW of heat dissipation, HFO-1234yf's saturated temperature reached 42°C, which corresponds to a pressure of about 1.1 MPa—the maximum operating pressure of the system. Increasing the heat dissipation with HFO-1234yf requires increasing the condensing and/or pressure capacity of the system. Compared at the same heat loads, HFO-1234yf produced thermal resistance values that were 22%–47% lower than those produced with HFC-245fa. In a prior study [7] we showed that compared at the same saturated temperature, HFO-1234yf provides higher heat transfer coefficients as compared with HFC-245fa. HFO-1234yf's higher heat transfer coefficients allow it to outperform HFC-245fa.

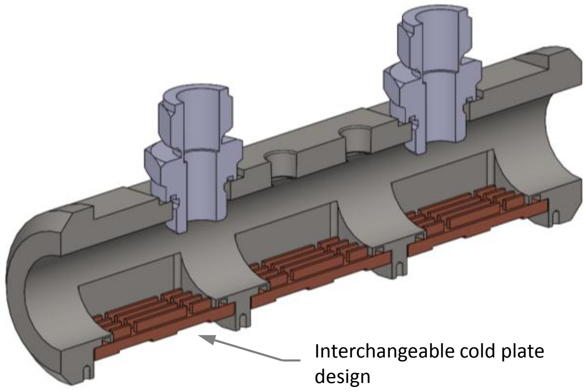

Figure 3-180: Cross-sectional view of the evaporator that incorporates an interchangeable cold plate design.

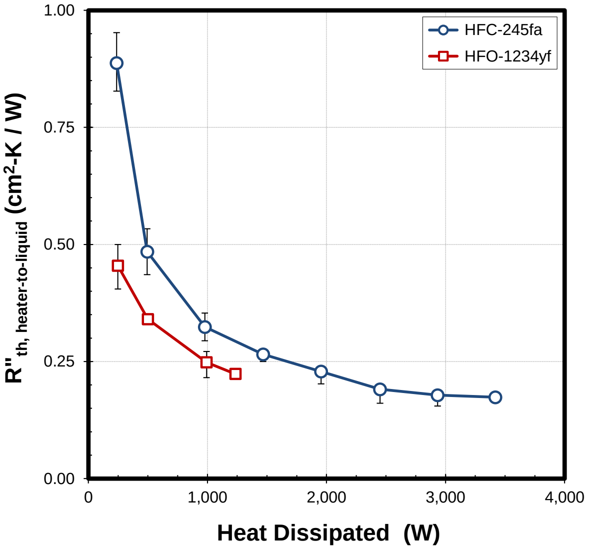

Figure 3-181: Averaged evaporator (heater-to-liquid) specific thermal resistance values versus the heat dissipated for HFO-1234yf and HFC-245fa. No enhanced surfaces were used. The error bars indicate maximum and minimum values.

Evaporator Thermal Performance (Advanced Design)

Features to improve the evaporator's performance and reduce its size were identified and incorporated into an advanced evaporator design. The features are intended to reduce the evaporator thermal resistance while utilizing low-cost fabrication techniques and materials (e.g., aluminum). The advanced evaporator concept uses an indirect cooling approach to be compatible with conventional power electronic packages (i.e., silicon on ceramic substrate). A simple schematic of the advanced evaporator design is shown in Figure 3-182. To protect potentially sensitive intellectual property, certain evaporator features are omitted from the figure. The evaporator was designed to cool six Delphi discrete power switches. The advanced design reduces the refrigerant volume to 180 cm^3 (HFC-245fa = 240 grams, HFO-1234yf = 200 grams). For comparison, the 2010 Toyota Camry requires 510 grams of refrigerant (HFC-134a) for the cabin's air-conditioning system [8]. Also, typical automotive inverter coolant systems utilize several liters of WEG (i.e., antifreeze). Reducing the refrigerant quantity is an effort to reduce system cost, weight, and size. As shown in Figure 3-182, the advanced design is more compact as compared with the previous copper-based design.

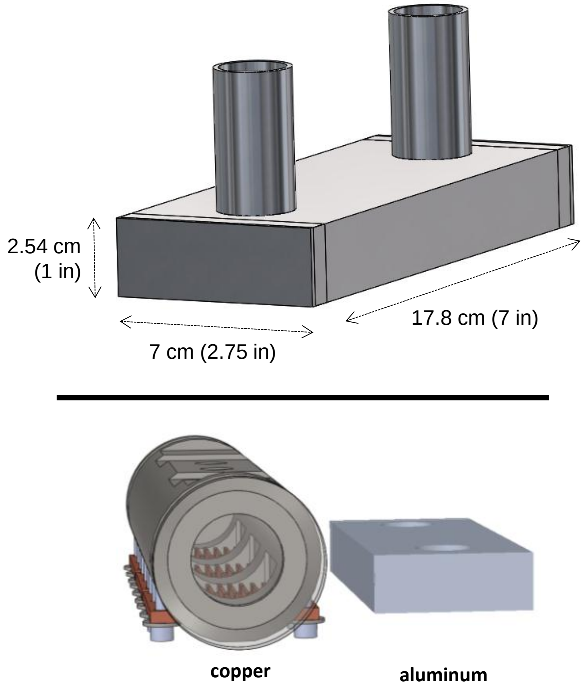

Figure 3-182: CAD drawing of the advanced evaporator design with dimensions (top) and a side-by-side size comparison of the advanced evaporator design and the initial, copper cold plate design.

The specific thermal resistance of the advanced evaporator design is compared to the thermal performance of the previous copper cold-plate design in Figure 3-183. The performance curves shown in this figure were obtained using HFC-245fa. The results demonstrated that the advanced design can dissipate automotive-scale power electronic heat loads (3.5 kW) with only 180 cm^3 of refrigerant. Additionally, the unique features of the advanced evaporator design allowed the aluminum evaporator to provide equal or lower thermal resistance values as compared with the initial evaporator design that utilized copper cold plates. Further reductions to the thermal resistance can be obtained if the advanced design is fabricated entirely out of copper. However, in an effort to reduce cost and weight, the use of aluminum is seen as a more practical option.

At higher heat loads (≥ 3 kW), fluctuations in the pressure and temperature were observed for tests with the advanced evaporator design. These fluctuations resulted in an increase in thermal resistance. The fluctuations are believed to be associated with the compact size of the advanced evaporator design that restricts vapor from exiting the evaporator. Applying microporous coatings to the evaporator's boiling surface may reduce or eliminate the fluctuations. Prior module-level experiments have demonstrated that microporous coatings can eliminate pressure–temperature fluctuations. Microporous coating structures provide passive refrigerant transport via wicking and may reduce the amount of vapor generation and these effects are believed to suppress pressure–temperature fluctuations in passive, two-phase systems.

It is important to note that the thermal performance results provided in Figure 3-181 and Figure 3-183 were obtained using ceramic heaters attached via thermal interface material. These heaters were used as a substitute for actual power modules attached via bonded interface materials (e.g., thermoplastics, solder). Therefore, the thermal resistance values are not necessarily indicative of the thermal performance in actual applications. Also, the thermal performance results provide in Figure 3-181 and Figure 3-183 were obtained using non-coated evaporator surfaces. The use of boiling enhancement coatings such as 3M's copper microporous coating [9] within the evaporator will enable both increased heat dissipation and lower thermal resistance values. The high temperatures required to fabricate the 3M microporous coating onto samples restrict their applicability to aluminum and thus were not utilized.

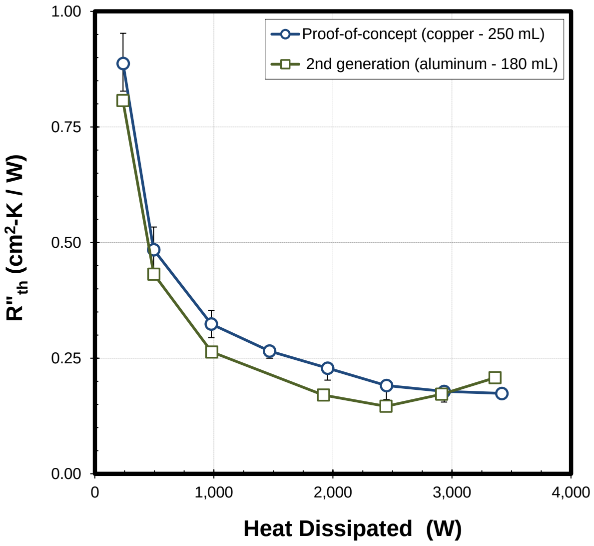

Figure 3-183: Evaporator specific thermal resistance (heater-to-liquid) versus the heat dissipated. The performance of the advanced evaporator design and the initial, copper cold plate design are compared. No enhanced surfaces were used.

Power Module Cooling Implications

The junction-to-liquid thermal resistance of the advanced evaporator design was simulated through finite element analysis (FEA). A computer-assisted design (CAD) model of the Delphi power modules bonded to the advanced evaporator design was first developed. The CAD model incorporated all the thermal resistance interfaces within the module stack, including the solder layers within the module and a thermoplastic-type bonded interface between the module and the evaporator. The model was then imported into ANSYS

Workbench for thermal analysis. The FEA imposed heat transfer coefficient boundary conditions to simulate boiling heat transfer from enhanced surfaces within the evaporator. In a prior studies [7,10] the boiling heat transfer coefficients for HFC-245fa and HFO-1234yf were experimentally measured with enhanced surfaces (3M microporous boiling enhancement coating) at various saturated temperatures. In those studies, the measured heat transfer coefficient values exceeded 100,000 W/m^2-K within a wide heat flux range. Moreover, the performance of the two refrigerants was found to be similar for boiling on microporous-coated surfaces. Because uniform boiling may not occur with the evaporator surfaces, a conservative estimate on the heat transfer coefficients was imposed (50,000 W/m^2-K) for these simulations.

The specific thermal resistance results (junction-to-liquid) as predicted by FEA are provided in Table 3-12. The insulated gate bipolar transistor's area and maximum temperature (i.e., junction temperature) combined with the refrigerant temperature were used to calculate the thermal resistance values. Two evaporator designs were analyzed— aluminum-based and copper-based. The aluminum fabrication is the more practical design while the copper fabrication is more of an idealistic concept aimed at reducing the package stack resistance. For comparison, the thermal resistance (junction-to-liquid) of the 2008 Lexus Hybrid double-sided and liquid (WEG)-cooled power module is also shown in Table 3-12. The thermal resistance value of 0.33 cm^2-K/W listed for the double-sided-cooled module was calculated using performance data from Sakai et al. [11] and the module's insulated gate bipolar transistor footprint as reported by Burress et al. [12]

The FEA-predicted thermal resistance values of the aluminum (0.14 cm^2-K/W) and copper (0.12 cm^2-K/W) evaporator modules are about 58% and 65% lower, respectively, than that of the double-sided, WEG-cooled 2008 Lexus system. (The 2013 Toyota Camry Hybrid uses a similar power modules and cooling system.) These thermal resistance reductions translate to a 139% and 189% increased heat flux capacity. Experimentally measuring the thermal resistance of the advanced evaporator with a power module was not possible due to equipment power limitations.

An immersion cooling (two-phase) strategy may allow for even greater thermal enhancements. However, an indirect cooling approach was used in this case to allow for its use with more traditional power modules and to alleviate some reliability concerns associated with immersing electronics in a refrigerant.

Table 3-12: The FEA-estimated evaporator (junction-to-liquid) thermal resistances for aluminum and copper evaporators. Performance data for an automotive cooling system are provided for comparison.

	R''_{th} (cm^2- K/W)	% R''_{th} reduction
Lexus Hybrid (2008) double-side cooled modules	0.33 [11,12]	–
Two-phase: aluminum baseplate (finite element analysis results)	0.14	58%
Two-phase: copper baseplate (finite element analysis results)	0.12	65%

Condenser Thermal Performance and Analysis

The unit-thermal resistances for the condensers are provided in Table 3-13 for both refrigerants. The vapor-to-air resistance includes the condensation-side and the air-side resistances and was defined per Equation 2.

$$R''_{th,\ condenser} = \frac{(T_v - \bar{T}_a)}{Total\ power \times Condenser frontal\ area} \qquad (2)$$

where T_v is the refrigerant vapor temperature and $\bar{T}_a$ is the average inlet air temperature as measured by two thermocouples just upstream of the condenser. The stated condenser performances are for a passive condenser design cooled via an automotive axial fan. The total fan parasitic power was measured to be 38 W. An estimate of the air flow rate was calculated by imposing an energy balance on the air-side (i.e., inlet and outlet to the condenser) and the total heat dissipated. Assuming steady-state conditions and incorporating the appropriate air thermal properties, the estimated air volumetric flow rate is 0.12 m^3/s (250 ft^3 per minute).

Table 3-13: Condenser thermal resistance values calculated using Equation 2.

Refrigerant	R''_{th} (cm^2- K/W)		
	Plain	Rifled	Rifled enhancements
HFC-245fa	9.30	7.58	18%
HFO-1234yf	8.12	6.06	25%

Condensation-side enhancements from the rifled tubes were found to reduce the overall condenser thermal resistances by 18% and 25% for HFC-245fa and HFO-1234yf, respectively. The results show that the rifled structures are more effective at enhancing condensation heat transfer with HFO-1234yf. Moreover, better performance is achieved with HFO-1234yf. For the plain tube condenser, HFO-1234yf yielded thermal resistance values that were about 13% lower than those with HFC-245fa. For the rifled tube condenser, HFO-1234yf yielded thermal resistance values that were about 20% lower than those with HFC-245fa.

An analysis was conducted to estimate condenser size based on operating conditions, a maximum allowable cooling system temperature (i.e., vapor and liquid), and the experimentally measured condenser thermal resistance values provided in Table 3-12. The operating conditions used for this analysis were: 3.3 kW of steady-state heat dissipation (estimated requirements for a 55-kW traction drive inverter) and 43°C inlet air temperature. The estimated condenser frontal area (i.e., frontal footprint) requirements are plotted versus the system temperature in Figure 3-184. In the figure, the lower system temperature of 65°C, used for this analysis, corresponds to the coolant (i.e., WEG) temperature typical of existing automotive power electronics systems. The solid line curves for both refrigerants are the sizing requirements for the finned-tube condenser per the performance data reported in Table 3-12. The T_j curve in Figure 3-184 represents the maximum junction temperature and was calculated using the thermal resistance data for an aluminum evaporator and a six power module/switch system configuration.

Because typical automotive condensers are constructed using a brazed, folded-fin design, a simplified analysis was conducted to estimate the sizing requirements for a folded-fin type condenser. For this analysis, the ratios of the air-side surface area to frontal surface area were measured for finned-tube and folded-fin condensers. The air-side-to-frontal-surface-area ratios were calculated to be 55.5 mm^2/mm^2 for the finned-tube and 86.7 mm^2/mm^2 for folded-fin condensers, assuming a condenser thickness of 4.5 cm for both cases. The folded-fin frontal area requirements were estimated by matching the air-side surface area for the folded-fin design to those of the finned-tube design at the various system temperatures. The folded-fin frontal area requirements were then calculated via the surface area ratio (86.7 mm^2/mm^2) and the results are shown Figure 3-184. This simplified analysis assumes that the air-side is the dominant thermal resistance, and air velocities are similar to those provided by the fan used in this study. For reference, the performance of a folded-fin condenser operating in a thermosyphon configuration, as reported by Barnes and Tuma [6], is provided in Figure 3-184. In that study, a condenser thermal resistance of 4.6 cm^2-K/W was reported using a hydrofluoroether fluid and an air velocity and pressure drop of 2.2 m/s and 44 Pa, respectively. The estimated condenser sizing requirements, per the performance reported by [6], are similar to the results predicted for HFC-245fa.

The size requirements of the condenser can then be estimated using Figure 3-184 and a maximum allowable system temperature. For low-temperature applications typical of existing automotive power electronics coolant temperatures and conventional silicon devices, the use of HFO-1234yf is recommended because it provides better performance. At a system temperature of 80°C and with HFO-1234yf, the condenser frontal size requirements are estimated to be about 325 cm^2 with a maximum T_j of about 125°C. HFC-134a may also be considered in this case because it is a refrigerant currently used in automotive systems and because prior studies [7,10] have shown that its heat transfer performance (boiling and condensation) is similar, if not slightly better than, that of HFO-1234yf.

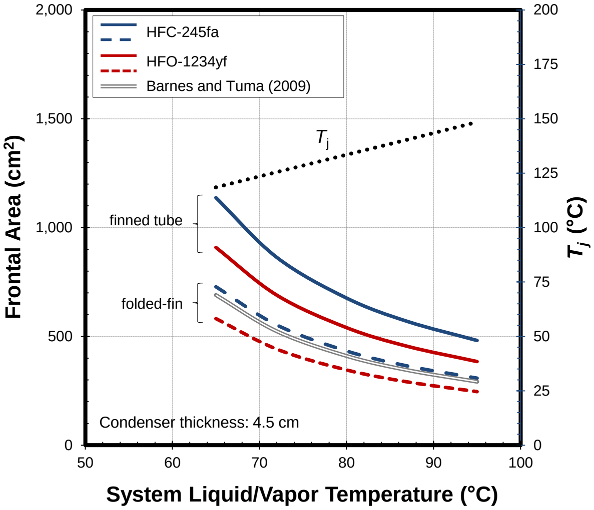

Figure 3-184: Condenser sizing requirements at various system temperatures. Barnes and Tuma data from [6].

Operating at higher system temperatures has advantages because it allows for a more compact condenser. However, higher temperature operation may be dependent on the development of higher temperature auxiliary electronic devices (e.g., capacitors) that are packaged within the inverter. With this in mind, if higher system temperatures are practical, HFC-245fa is recommended due to its higher critical temperature (T_C= 154°C) and lower operating pressures. At a system temperature of 95°C and a T_j= 148°C, the condenser size requirements would decrease to about 310 cm^2.

Two-Phase and Baseline Cooling Metric Comparisons

Analysis was conducted to compare the coefficient of performance (COP), volume, and weight of a passive two-phase cooling system with that of a conventional automotive WEG-based (single-phase) power electronics cooling system.

Passive Two-Phase Inverter Cooling System Metrics

The condenser, evaporator, and refrigerant were included in the volume and weight metrics for two-phase cooling system. The metrics for an aluminum evaporator were directly measured from the prototype that was fabricated and tested. The condenser metrics were estimated based on the condenser finned-frontal-area requirements from Figure 3-184 assuming 80°C (HFC-245 assumed) maximum system (liquid and vapor) temperatures. The additional volume of the headers/manifolds and specific weight (weight/volume) of an automotive condenser was measured and used to compute the total volume (finned and headers) and the weight of the condenser for the passive two-phase cooling system. The 240 grams (HFC-245 assumed) of refrigerant was included in the total system weight. The refrigerant volume was not included in the total volume measurement because the refrigerant is contained within the evaporator and thus its volume is accounted for in the evaporator volume. The thermal resistance of an aluminum evaporator (from Table 3-12) combined with the total parasitic power of the system (38-W fan parasitic power) was used to compute a COP value per Equation 3.

$$COP = \frac{1}{R''_{th} \times Parasitic\ power} \qquad (3)$$

The volume and weight of the fan and associated piping (connecting the evaporator to the condenser) were not included in the total volume and weight calculations.

Baseline, WEG-based Inverter Cooling System Metrics

Conventional automotive WEG-based inverter cooling systems consists of a cold plate to directly cool the inverter, radiator, pump, fan, WEG, and associated piping. Estimating the metrics for a baseline, the WEG-based automotive inverter cooling system is not a straightforward procedure because these systems are also designed to cool the electric motor. Therefore, the radiators in these inverter cooling systems are sized to dissipate the combined heat loads of the inverter and the electric motor. Because the proposed two-phase cooling system only considers cooling the inverter, analysis was conducted to size a radiator to dissipate heat loads for the inverter only, per the procedures outlined by Kargilis [13]. The radiator was sized to dissipate 3.3 kW of heat with a maximum inlet air temperature of 43°C—the same conditions used to size the two-phase condenser. Additionally, a 10 L/min WEG flow rate was assumed within the radiator. From this analysis, the finned radiator volume, fan pressure drop and flow rate, and pump pressure drop were estimated. The additional volume of the headers/manifolds and specific weight (weight/volume) of an automotive radiator was measured and used to compute the total volume (finned and headers) and the weight of the inverter-only radiator. The air-side pressure drop and flow rate were used to compute the fan parasitic power assuming 20% fan efficiency.

The 2012 Nissan Leaf inverter (80-kW motor) cold plate/heat exchanger was used to compute the volume, weight, and WEG pump parasitic power metrics for the inverter cold plate. The volume of the cold plate was directly measured and then scaled down by the ratio 55 kW / 80 kW (80 kW for the Nissan Leaf and 55 kW for the two-phase cooling system). The weight was computed assuming the density of aluminum (6061) and a 60% cold plate void space (i.e., WEG channels).

Experiments were conducted to measure the parasitic power required to circulate WEG (10L/min flow rate and 60°C) through the 2012 Nissan Leaf inverter cold plate. The power required to circulate WEG through the inverter cold plate and radiator was used to compute the total pump parasitic power requirements assuming a 60% pump efficiency. The COP of the baseline system was calculated per Equation 3 using the total parasitic power (fan and pump) and the specific thermal resistance (junction-to-liquid) of the 2012 Nissan Leaf as reported by Liang [14]

The volume of the WEG, contained within the Nissan Leaf cold plate was measured and doubled in an attempt to account for the total WEG volume in both the cold plate and radiator. The total WEG volume was computed to be approximately 1.6 L. The WEG's volume was not used when computing the overall volume of the system because the WEG is contained within the system components and thus its volume is accounted for in the cold plate and radiator volume. However, the WEG volume was used to compute the WEG weight via the specific weight properties of WEG. The weight of the WEG was then utilized to compute the overall baseline system weight. The volume and weight of the fan, pump, tubing, and WEG within the tubing were not included in the total volume and weight calculations for the baseline cooling system.

As shown in Table 3-14, utilizing a passive two-phase cooling system can reduce the weight by an estimated 41% and increase the COP by an estimated 127%. The volumes of the two cooling systems are nearly identical; however, more components were excluded from the baseline system (i.e., fan, pump, piping, and additional WEG volume and weight) as compared with the two-phase system (i.e., fan and piping) and thus reductions to the volume are also likely. The majority of the reductions to the system are associated with reducing the amount of coolant/refrigerant and reducing the size of the inverter/power module heat exchanger (Figure 3-185). The advanced aluminum evaporator is 23% the volume and 33% the volume of the scaled-down (by 55 kW / 80kW) 2012 Nissan Leaf cold plate. Moreover, the two-phase cooling system contains about 17% less aluminum (by weight) as compared to the WEG-based cooling system.

Table 3-14: Percent reductions to the volume and weight and percent increases to the COP and heat dissipation using a passive two-phase cooling system.

Volume reduction	Weight reduction	COP	Heat dissipation increase
-2%	41%	127%	139%

It should be noted that the size of the condenser can be reduced and the volume and weight reductions listed in Table 3-14 would increase, if the two-phase coolant system is allowed to operate at higher temperatures (Figure 3-184). In this analysis, the maximum two-phase temperatures (vapor and liquid) were kept below 85°C to enable the use of low-temperature capacitors.

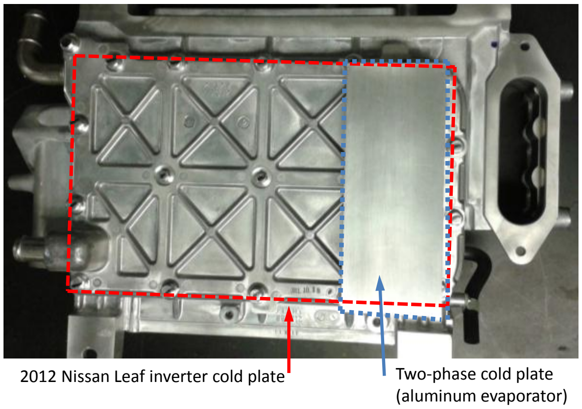

Figure 3-185: Picture of the advanced aluminum evaporator placed on the 2012 Nissan Leaf inverter cold plate. The two-phase aluminum evaporator is approximately 23% the volume and 33% the weight of the Nissan Leaf cold plate. Photo credit: Gilbert Moreno (NREL).

Conclusions and Future Directions

Future Directions

This is the final year for this project, and thus no further experiments are planned. However, we will seek out collaborations with industry to develop a two-phase cooled inverter.

Conclusions

Experiments and analysis have been conducted to evaluate the use of two-phase cooling (passive) for automotive power electronics. The following summarizes the major results from this work:

- We designed and fabricated a passive two-phase cooling system that can cool six Delphi discrete power modules. We demonstrated that the system can dissipate 55 kW inverter-scale heat loads (~3.5 kW) with only 180 mL of refrigerant.
- The proposed passive and indirect two-phase cooling approach can reduce the junction-to-liquid thermal resistance by 58% to 65%. These reductions to the thermal resistance translate to a 139% to 189% increase in the device heat dissipation capabilities.
- Analysis indicates that using a passive two-phase cooling approach can reduce the weight (by 41%) and significantly improve the COP (by 127%) of the inverter thermal management system. Additional improvements can be obtained if the two-phase cooling system is allowed to operate at higher vapor-liquid temperatures.

Nomenclature

A	area
P	pressure
R''_{th}	area-weighed/unit thermal resistance, cm^2-K/W
T	temperature, °C
Subscripts	
a	air
htr	heater
l	liquid
j	junction

FY 2014 Publications/Presentations

1. Moreno, G., Jeffers, J. R., and Narumanchi, S., 2014, "Effects of Pressure and a Microporous Coating on HFC-245fa Pool Boiling Heat Transfer," *Journal of Heat Transfer*, 136(10), pp. 101502–101502.
2. Moreno, G., Jeffers, J. R., and Narumanchi, S., 2014, “Passive Two-Phase Cooling of Automotive Power Electronics,” 30th SEMI-THERM Symposium, San Jose, CA, USA.
3. Moreno, G., Jeffers, J., and Narumanchi, S., 2014, “Inverter-Scale, Passive Two-Phase Cooling for Automotive Power Electronics,” Presentation at the SAE Thermal Management Systems Symposium, Denver, CO, USA.

Acknowledgements

The author would like to acknowledge the support provided by Susan Rogers and Steven Boyd, Technology Development Managers for the EDT Program, Vehicle Technology Office, U.S. Department of Energy Office of Energy Efficiency and Renewable Energy. The significant contributions of Jana Jeffers (NREL) and Charlie King (NREL) to the project are acknowledged. The author also thanks Phil Tuma (3M) for providing samples of the microporous copper coatings and Mary Koban (DuPont) for providing the HFO-1234yf refrigerant.

References

1. Mudawar, I., "Assessment of High-Heat-Flux Thermal Management Schemes," *IEEE Transactions on Component and Packaging* Technologies, (24:2), 2001; p. 122.
2. Brown, G. M., Elbacher, B. J., and Koellner, W. G., "Increased Productivity with AC Drives for Mining Excavators and Haul Trucks," *IEEE Industry Application Conference,* 2000; pp. 28–37.
3. Koellner, W. G., Brown, G. M., Rodriguez, J., Pontt, J., Cortes, P., and Miranda, H., "Recent Advances in Mining Haul Trucks," *IEEE Transaction on Industrial Electronics*, (51:2), 2004; pp. 321–329.
4. Tantolin, C., Lallemand, M., and Eckes, U., "Experimental Study of Immersion Cooling for Power Components," *IEE International Conference on Control*, 1994; pp. 723–727.
5. Dieck, R. H., *Measurement Uncertainty: Methods and Applications* ISA. Research Park Triangle Park, NC, USA, 2007.
6. Barnes, C. M., and Tuma, P. E., "Practical Considerations Relating to Immersion Cooling of Power Electronics in Traction Systems," *IEEE Transactions on Power Electronics*, (25:9), 2010; pp. 2478–2485.
7. Moreno, G., Jeffers, J. R., and Narumanchi, S., "Effects of Pressure and a Microporous Coating on HFC-245fa Pool Boiling Heat Transfer," *ASME Journal of Heat Transfer*, (136:10), 2014; pp. 101502–101502.
8. "2010 Toyota Camry SE 3.5L EFI DOHC 6cyl | Specifications | A/C System Refrigerant Capacity | AutoZone.com" [Online]. Available: http://www.autozone.com/autozone/repairinfo/specifications/specificationsMain.jsp?childCatName=A/C+System+Refrigerant+Capacity&childCatId=23201221&categoryNValue=23299999&categoryNameForTitle=Specifications&categoryName=SPECIFICATIONS&childCategoryNameForTitle=A/C+System+Refrigerant+Capacity. [Accessed: 03-Oct-2014].
9. 3M, 2009, "3M Microporous Metallic Boiling Enhancement Coating (BEC) L-20227."
10. Moreno, G., Narumanchi, S., and King, C., "Pool Boiling Heat Transfer Characteristics of HFO-1234yf on Plain and Microporous-Enhanced Surfaces," *ASME Journal of Heat Transfer*, (135:11), 2013; pp. 111014–111014.
11. Sakai, Y., Ishiyama, H., and Kikuchi, T., "Power Control Unit for High Power Hybrid System," *SAE Technical Paper*, 2007; p. 0271.
12. Burress, T. A., Coomer, C. L., Campbell, S. L., Wereszczak, A. A., Cunningham, J. P., Marlino, L. D., Seiber, L. E., and Lin, H. T., "Evaluation of the 2008 Lexus LS 600H Hybrid Synergy Drive System," Oak Ridge National Laboratory Report, 2009.
13. Kargilis, A., *Design and Development of Automotive Engine Cooling Systems*, ALKAR Engineering Company, Southfield, MI, USA, 2008.
14. Liang, Z., "Power Device Packaging." Electrical and Electronics Technical Team Presentation, 2012.

4.0 Electric Motors R&D

4.1 Scalable Non–Rare Earth Motor Development

Tim Burress (Principal Investigator)

Oak Ridge National Laboratory
National Transportation Research Center
2360 Cherahala Boulevard
Knoxville, TN 37932
Phone: (865) 946-1216; Fax: (865) 946-1262
E-mail: burressta@ornl.gov

Burak Ozpineci, ORNL EDT Program Manager
Phone: (865) 946-1329; Fax: (865) 946-1262
E-mail: burak@ornl.gov

Susan A. Rogers, DOE EDT Program Manager
Phone: (202) 586-8997; Fax: (202) 586-1600
E-mail: Susan.Rogers@ee.doe.gov

Start Date: October 2013
Projected End Date: September 2016

Objectives

- Develop low-cost non–rare earth motor solutions while maintaining high power density, specific power, and efficiency.
  - Develop or utilize new materials.
  - Perform fundamental research to improve motor modeling accuracy.
    - Evaluate impacts of factory stamping upon magnetic properties and motor performance.
    - Develop advanced modeling algorithms.
  - Employ high performance computational tools and resources.
  - Design unconventional motor technologies that address DOE 2022 targets.

Technical Barriers

- Even without using rare earth permanent magnet (PM) materials, 2022 DOE cost targets are challenging.
- Power density, specific power, and efficiency targets are difficult to meet with alternative motor technologies such as induction, synchronous reluctance, switched reluctance, non–rare earth PM, and field excitation.

Technical Targets

- DOE 2022 motor targets:
  - Power density: 5.7 kW/L
  - Specific power: 1.6 kW/kg
  - Cost: 4.7 $/kW.

Accomplishments

- Machine design and development:
  - Originated and designed two different novel machines (with several sub-designs of each).
  - Identified brushless field excitation (BFE) and synchronous reluctance motor designs through modeling as high-potential candidates to meet targets.
  - Selected a novel synchronous reluctance machine for fabrication.
- Material research and development (R&D):
  - Continued research on electrical sheet steel with high silicon (Si) content (>6%).
    - Confirmed capability for ingot-based processing vs expensive chemical vapor deposition (CVD) process.
    - Developed and confirmed a novel processing technique to reduce brittleness; otherwise, the workability of high-Si steel is not suitable for mass production of motor laminations.
  - Developed new magnetic material characterization systems for innovative analysis of electrical steel magnetic properties.
- Advanced modeling:
  - Incorporated findings from research on soft magnetic materials properties, using the new characterization system, into electromagnetics modeling.
  - Developed detailed micromagnetics code and a corresponding simulation environment to study the fundamental behavior and impact of various conditions upon the magnetization and loss characteristics of electrical steel.
- Proof-of-principle fabrication and bench top testing:
  - Fabricated a proof-of-principle prototype and began benchtop testing to verify basic parameters of the electromagnetic model.

✧ ✧ ✧ ✧ ✧

Introduction

The electric motor is one of the main components of electrified drivetrains; therefore, improving its efficiency, performance, and cost-effectiveness is crucial to the hybridization and electrification of vehicles. PM motors are not easily surpassed in terms of efficiency, power density, and specific power; that is why almost all hybrid electric vehicles (HEVs) and electric vehicles (EVs) use them. However, the cost of rare-earth PM materials accounts for at least 40% of the entire motor cost; and in the past decade, there has been significant volatility in the price and availability of the rare-earth materials used in PM motors. As a result, automotive manufacturers around the world are seeking alternative non-rare earth motor technologies that facilitate cost-effectiveness as the HEV and EV markets continue to expand. Therefore, the development of alternative non–rare earth motor technologies has an important role in the future of economic stability, clean energy, and energy independence.

Approach

The primary objective of ORNL's motor R&D is to develop low-cost non–rare earth motor solutions with high power density, specific power, and efficiency. The overall structure of the efforts in the project is described by the diagram in Figure 4-1. A key task for FY 2014 is motor design and optimization with conventional tools and optimization algorithms, which includes commercial electromagnetic finite element analysis (FEA) packages as well as other design tools developed by ORNL on previous projects.

Many novel electric motor concepts were considered. After candidates with high potential were selected, design optimization algorithms were applied to optimize machine designs with respect to DOE's 2020 power density, specific power, efficiency, and cost targets. For the second level of optimization, beginning in FY 2015, the development process will use feedback from advanced materials research, which will implement the advantages of new materials and improved modeling techniques.

Additionally, as a part of second level of optimization, ORNL is expanding upon its work in the area of high performance computing and parallel processing, using resources ranging from PC/workstation platforms to computational clusters and ultimately to large-scale supercomputing resources at ORNL. Fabrication and dynamometer testing of full-size prototypes will be carried out when motor designs are ready for prototyping. One proof-of-principle prototype was fabricated in FY 2014. Advanced materials research on the project includes the investigation and development of new materials (e.g., low-loss steel) and/or new processes to facilitate the incorporation of high-efficiency materials in electric motors. Another important part of the materials research effort is the characterization and analysis of electrical steel and other materials used in electric motors. Feedback from these characterizations will help improve the fundamental understanding of electrical steel magnetization and loss characteristics, which are critical for accurate motor modeling and development.

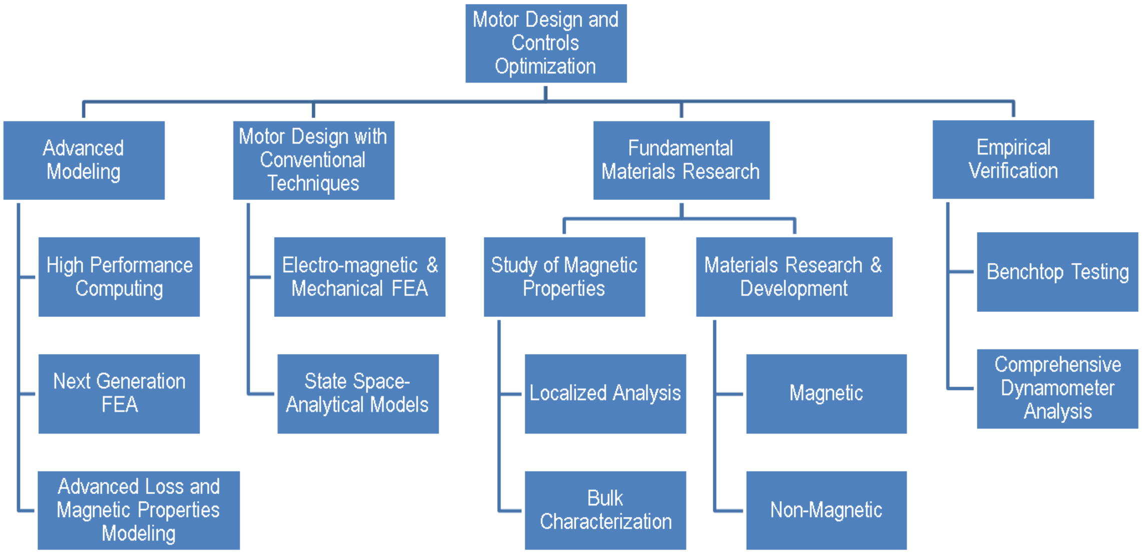

Figure 4-1: Block diagram of project structure, approach, and technical focus areas.

Results

Motor design optimization in FY 2014 was conducted with commercial FEA packages, in combination with other software packages, for external parametric optimization algorithms as well as state space simulations. The progress and results in the area of motor design are discussed after the following sections describing the parallel efforts in materials R&D. These parallel efforts are ultimately in support of improving motor designs by developing or facilitating the use of more efficient materials and by conducting fundamental research to improve the modeling accuracy of electrical steel characteristics. Findings from this research will begin to be incorporated into new modeling tools in FY 2015.

Materials Research and Development—6.5% Silicon Steel

ORNL is developing ways to facilitate the use of electrical steel with high Si content. Conventional electrical steel has about 2–3% Si content, and there are some expensive products with 6.5% Si content. A higher amount of Si increases resistivity and therefore reduces eddy current and hysteresis losses. The comparison in Figure 4-2 indicates that an increase from 3% to 6.5% Si yields an average core loss reduction of about 35%. This reduction of core loss is nearly indirectly proportional to resistance; thus the specific resistance of the 3% Si steel (labeled "Non-oriented SiFe") is about 44% lower than the specific resistance of 6.5% Si (labeled "JNEX-Core"). The loss reduction holds true for the various frequencies and flux density levels indicated.

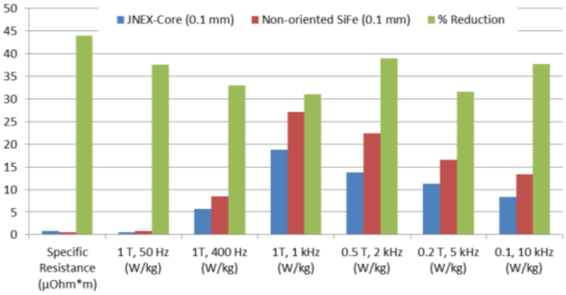

Figure 4-2: Comparison of electrical steel core losses: 6.5% Si vs 3% Si.

Currently, 6.5% Si is commercially available, but it is expensive because it is made by an intensive CVD process. Silicon steel is rolled into sheets with thicknesses of about 0.1 to 1 mm, depending on application requirements. The CVD process is used because conventional 6.5% Si steel is so brittle that it cannot be rolled and mechanically worked with conventional methods. Therefore, 6.5% Si sheet processing begins with 3% Si sheets, and the CVD process is used to increase the Si content to 6.5%. It remains a challenge to produce motor laminations from conventional 6.5% Si sheet steel since a stamping process is used for mass-produced motors. The brittle 6.5% Si sheet steel is difficult to stamp consistently without undesirable fracturing, and stamping tool lifetime is also reduced because the material is harder.

Research on this project aims to facilitate the production of 6.5% Si sheet steel from ingot form using processing techniques that are similar to conventional methods. Trace elements can be added to enhance strain softening behavior. This phenomenon was confirmed with experimental measurements as samples were prepared with trace amounts of various materials, including boron. Results confirmed that ductility can be recovered during warm rolling, in which certain crystalline phase ordering is destroyed.

In addition to developing methods to produce 6.5% Si from ingots, ORNL is developing processing techniques to facilitate the rolling process, as well as lamination production. This is a critical part of the development, because lamination quality control and tool lifetime are key considerations for motor production. Hardness measurements confirm that ORNL's new processing method softens 6.5% Si to a level similar to the softness of 3% Si without significant modification of conventional processing methods.

Near the end of FY 2014, this effort began to be a joint project with the Propulsion Materials Program of DOE's VTO. Plans for the joint project in FY 2015 include molecular dynamics simulations to determine the impact of various compositions of trace elements, analysis to gain a better understanding of ordering/disordering, and more experimental results to further validate novel processing techniques.

Materials Research and Development—Characterization Of Electrical Steel

Advanced materials characterization was conducted to facilitate improved modeling of magnetization and loss characteristics in conventional electrical steel (~3% Si) and to aid in the development of new materials and processes. A custom magnetic characterization tool was developed to observe localized properties in electrical steel. The measurement stage of the characterization system, shown in Figure 4-3, includes excitation coils that apply a magnetic field on a single sheet sample as the local magnetic field on the surface of the sample is measured. Conventional motor simulation techniques assume that the material properties are homogeneous for the bulk of the material. However, many things can impact magnetic properties, such as residual stress from stamping or laser cutting. Additionally, stamped or laser-cut edges are near the air gap, which is a critical location for the magnetic circuit and operation of the motor.

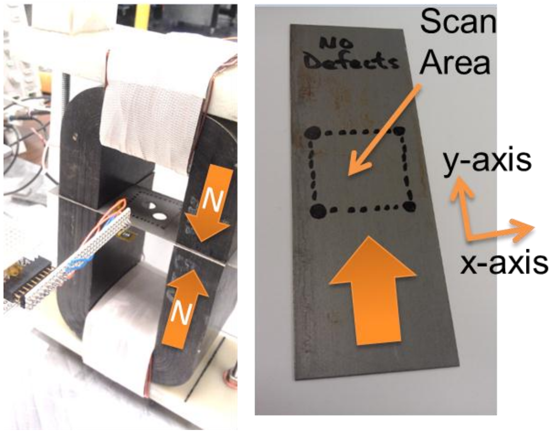

Figure 4-3: Measurement stage of magnetic characterization system.

This characterization tool provides the capability to observe the correlation between various deformations and disturbances and the non-homogeneity of magnetic properties in a sample. For example, results from scanning an unmodified sample at a flux density of 1.4 Tesla are shown in Figure 4-4, in which considerable variations in the magnetic field are observed, even in an undisturbed sample.

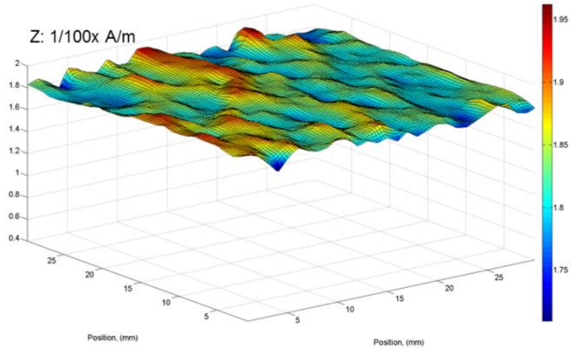

Figure 4-4: Magnetic field results from unmodified control sample.

The plot in Figure 4-5 shows the resulting magnetic field with a flux density of 1.4 Tesla after a brief application of laser pulses in five different areas of the sample. Although the disturbed areas are barely visible on the physical sample, five distinct areas are visible in the plot of the scanning results where the magnetic properties are significantly impacted.

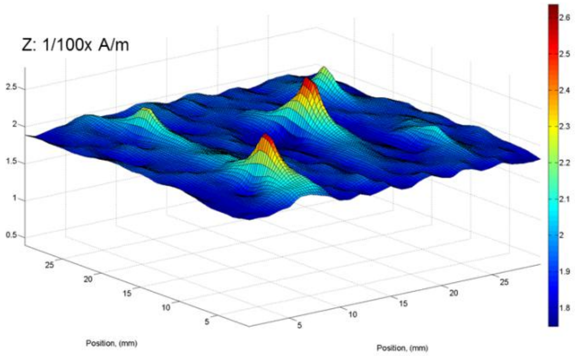

Figure 4-5: Magnetic field results after brief application of laser pulses.

A more significant deformation was applied to the sample shown on the left in Figure 4-6, in which two large holes were made with a punching tool. The results, shown on the right, clearly indicate the impact upon the magnetic field—levels of variation near the deformation zone are up to 3.5 times those in undeformed areas of the sample.

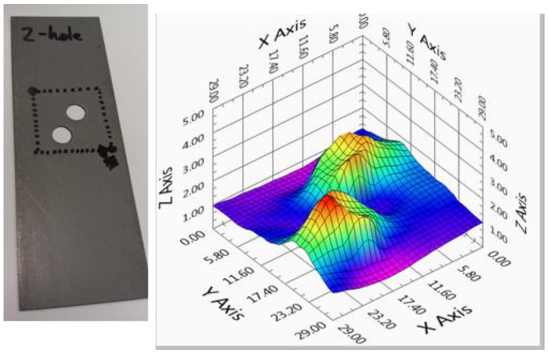

Figure 4-6: Magnetic field results after punching of two large holes.

Many types of deformations were applied and corresponding analyses were conducted. One of the more interesting and perhaps more meaningful studies in regard to electric motors involved shearing and rejoining a sample, as shown in Figure 4-7; the magnetic flux was forced across the deformation zone, which extends the entire width of the sample. Researchers were careful not to leave any noticeable air gap between the rejoined pieces, so the nonuniformities in the magnetic field in Figure 4-7 are due to residual stresses in the material. The magnetic field is up to five times higher at the deformation zone than it is at undisturbed areas of the sample. In other samples, it is more difficult to determine the impact upon permeability because the localized flux density changes across the area of the sample; but in this case, permeability can be more readily determined since the deformation extends across the sample in a direction that is perpendicular to the magnetic flux. Therefore, the local magnetic flux density is also consistent across the sample. Similar results were received regardless of whether the sheared edge or two laser cut edges were joined together. Additionally, short-term annealing of the sample was conducted for 15 minutes at 840°C and no significant changes were noticed in the magnetic field measurements.

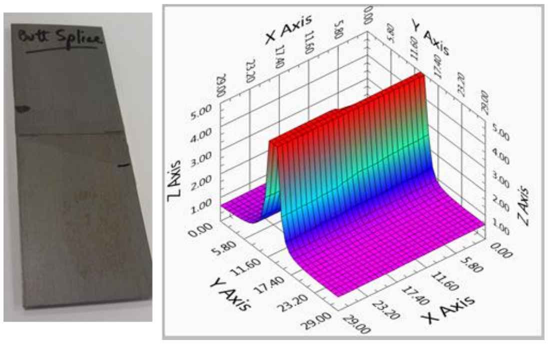

Figure 4-7: Magnetic field results after shearing and rejoining.

Samples were prepared for analysis with a scanning electron microscope (SEM) to identify the extent of the deformation zone by observing damage to the crystal lattices of the grains within the electrical steel microstructure. A back-scatter analysis method was used to visually represent where damaged areas are located. Normal grains should have a uniform color, as is shown for many of the grains on the left in Figure 4-8. However, near the edge (which is the point of deformation by laser cutting), discoloration within the grains is noticeable. This discoloration directly correlates with the amount of deformation within the grain. The image on the right in Figure 4-8 shows the amount of deformation: blue grains indicate normal undisturbed lattice, and green, yellow, and red coloration indicates the level of damage and dislocations within the lattices of the grains. A qualitative value of intra-grain stress can be determined by observing the misorientation spread, which is directly associated with the deformation within each grain. The graph in Figure 4-9 shows the misorientation spread vs the distance away from the laser cut edge (into the sample). According to this technique, the intra-grain residual stress reaches nominal levels within 150 µm.

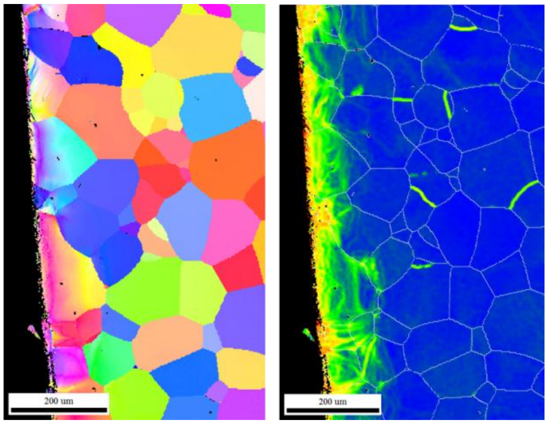

Figure 4-8: Electrical steel microstructure and intra-grain residual stress.

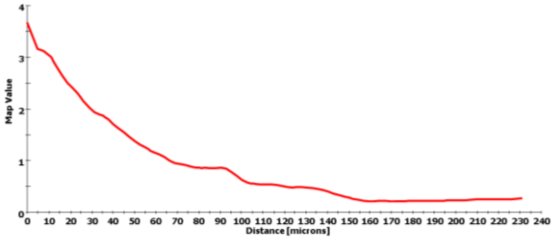

Figure 4-9: Misorientation spread representing residual stress within grains versus distance from cut edge.

It is important to realize that this technique provides a qualitative measure of intra-grain residual stress, but it does not include stresses that occur between the grains. Even if intra-grain stress is the only contributor to reduced magnetic performance, it is easy to see how it could impact electric motor operation, considering that air gaps in electric motors are on the order of 500 to 1000 µm. In comparing these results with findings from the magnetic characterization tool, where impacts upon magnetic properties are found to be on the order of millimeters, it appears that much of the degradation is caused by residual stress that is maintained at and throughout grain boundaries.

Magnetic domains were observed with a magnetic force microscope in the same samples and deformation areas that were observed with the SEM. To begin to identify correlations between deformation and magnetic domain behavior, domain images were superimposed on the deformation images, as shown in Figure 4-10. Domain behavior should be somewhat consistent within an undisturbed grain, but it is clear that the behavior within the deformation zone is not very consistent. This phenomenon is more noticeable in Figure 4-11, where magnetic domain patterns are more consistent within grains away from severe deformation zones, and patterns are more erratic near the edges of the sample. The patterns shown in Figure 4-12 indicate the rough correlation between magnetic domain pattern and crystal lattice orientation in undamaged grains. There is some variance, but the orientations of the magnetic domains correlate with the lattice structure. Although these observations are mostly qualitative, they are key indicators of the impacts of residual stress upon magnetic characteristics. Furthermore, techniques are being implemented to quantitatively determine magnetic properties through domain observation.

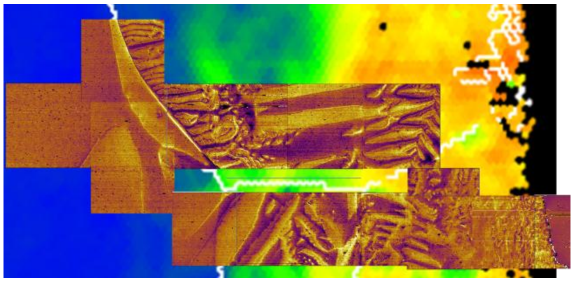

Figure 4-10: Electrical steel magnetic domain images of area near damage zone.

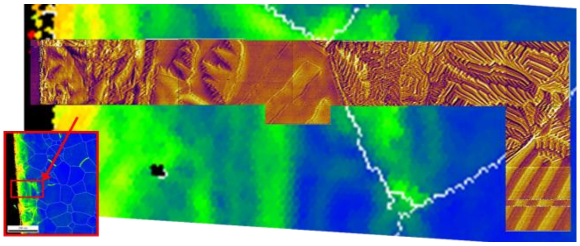

Figure 4-11: Electrical steel magnetic domain images of area near damage zone.

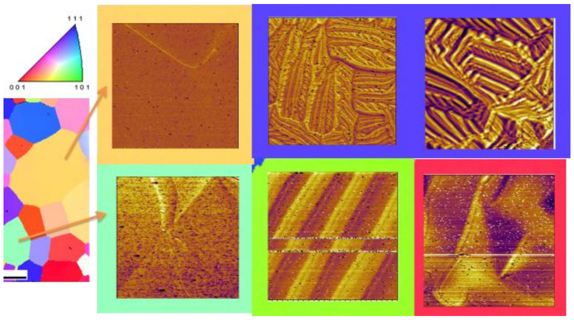

Figure 4-12: Association between crystal lattice and magnetic domains.

Materials Research and Development —Modeling of Electrical Steel

The fundamental behavior of magnetic domains in non-oriented Si steel is an area that has not been thoroughly explored or defined. Monte Carlo (MC) simulations are being conducted to examine some of these fundamental behaviors, and ultimately feedback will be provided for models that are being developed on a much larger scale. In ferromagnetic materials, the interaction energy between the magnetic moments is given by the following micro-magnetics equations.

$$E_{ext} = -H.M \qquad [1]$$

$$E_{exch} = J_1 \sum_{n1=1}^{6} Ma_i a_{n1} + J_2 \sum_{n2=1}^{6} Ma_i a_{n2} + J_3 \sum_{n3=1}^{12} Ma_i a_{n3} + J_4 \sum_{n4=1}^{6} Ma_i a_{n4} \qquad [2]$$

$$E_{dip} = M^2 \sum_{j=1}^{n} \sum_{k\neq j}^{n} \frac{(a_i a_k - 3a_j e_{jk} a_k e_{jk})}{4\pi\mu_0 r^3} \qquad [3]$$

$$E_{an} = K_1(a_1^2 a_2^2 + a_2^2 a_3^2 + a_1^2 a_3^2) + K_2 a_1^2 a_2^2 a_3^2 \qquad [4]$$

In Eq. (1), *H* is the external magnetic field strength, *M* is the magnetic moment of the atoms in the crystal, and E_{ext} is the energy due to the presence of the external field. According to Eq.(1), the energy is minimized when the magnetic moments are parallel to the magnetic field. In Eq. (2), E_{exch} is the spin exchange energy for each atom *i* where a_i is the magnetic moment vector of each atom and a_{n1} to a_{n4} are the magnetic moment vectors of atoms in the first through the fourth nearest neighbors of the atoms. J_1 through J_4 are the exchange coefficients. In the present work, exchange coefficients were used that correctly reproduce the Curie temperature of BCC iron.

The spin exchange energy is responsible for the spontaneous magnetization of ferromagnetic materials. In Eq. (3), E_{dip} is the dipole-dipole interaction energy where *a*'s are the magnetic moment vectors, e_{jk} is the unit vector of the displacement that connects an atom *i* with atom *k*, and μ_0 is the permeability of space. The formation of the magnetic domains is due to a balance between E_{exch} and E_{dip}. When the particle size is small, the E_{exch} contribution dominates and the entire particle exists as a single domain. As the particle size increases, the contribution from E_{dip} increases. E_{dip} specifically increases at the surfaces normal to the moments. This is the origin of the demagnetizing field that raises the system energy. This allows for the moments to align in directions away from those dictated by E_{exch}, resulting in the formation of various types of domains separated by the domain boundary.

In the current MC simulations, the total system Hamiltonian is the sum of these four energy contributions. The simulation domain is aligned with the global x, y, and z directions. The simulation volume can be a single crystal, a bicrystal, or a polycrystal. The local direction within each grain is defined by three Euler angles, ψ, θ, and ϕ. The magnetic moment vectors for sites within each grain are defined with respect to the local grain orientation. The MC move is a random rotation attempt of the magnetic moment of a randomly picked single atom keeping the orientation of the particle constant. The change in energy ΔE is calculated and the move is accepted with a probability of exp($-\Delta$E/kT) when ΔE > 0.0 and 1.0 when $\Delta E \leq 0.0$. The system size was scaled by replacing the atoms in the BCC crystal structure by a collection of BCC unit cells placed in a BCC arrangement. By computing the exchange energy as a function of the size of the lattice site, it was shown that the scaling factor for the exchange energy K_{exch} followed the empirical equation

$$K_{exch} = 6.810 - 11.587\, K_{size} + 5.776\, K_{size}^2 \qquad [5]$$

where K_{size} is the size factor. The effective lattice parameter due to scaling, LP_{size} is given by

$$LP_{size} = LP_1 2^{K_{size}-1} \qquad [6]$$

where *LP* is the lattice parameter of the BCC unit cell. The effective magnetic moment at each lattice site, a_{size}, in the scaled lattice is given by

$$a_{size} = \begin{matrix} a & K_{size} = 1 \\ 2a & K_{size} = 2 \\ 2a2^{3(K_{size}-2)} & K_{size} > 2 \end{matrix} \qquad [7]$$

Figure 4-13 shows the grain structure with superimposed tangent vectors of the magnetic domain in a random x, y, and z plane. The image on the left shows the magnetic moment vectors in the absence of external field. The image at the right shows the magnetic moments in the presence of a 0.25 T magnetic field in the z direction.

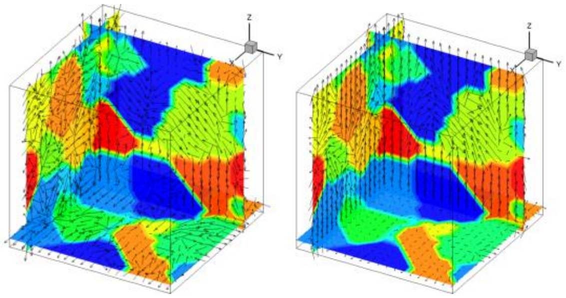

Figure 4-13: Three-dimensional grain structure with magnetic moment vectors indicating random orientation without magnetic field (left) and alignment with magnetic field (right).

It is clear that the application of the magnetic field causes some alignment of the magnetic moments, although the alignment is not very effective in certain grains. This indicates that the magnetic field intensity required to align the moments depends on the local grain orientation, which is well known.

Figure 4-14 shows the same simulation results as in Figure 4-13 but with the grain structure replaced by the magnetic domains obtained by a contour plot based on one of the direction cosines of the magnetic moment vector. These plots help with the visualization of magnetic domain growth as external fields are applied.

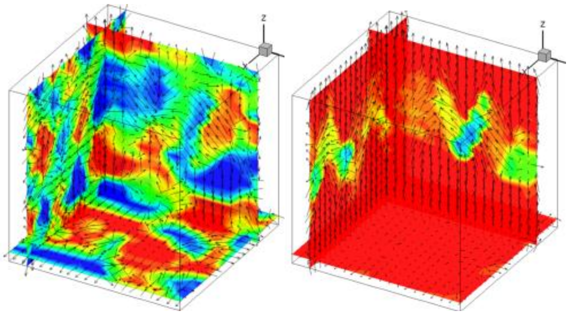

Figure 4-14: Domain structure and magnetic moment vectors from polycrystalline simulations without magnetic field (left) and the growth of the domains with external field (right).

The MC simulations are able to minimize the total energy of the system by reorienting the magnetic moments. Figure 4-15 and Figure 4-16 show the total energy and the relative magnetization, respectively, as functions of the simulation time. The total magnetization in the absence of the field is negligible, although there is a clear indication of magnetic domains within the grain structure as shown in Figure 4-14. However, application of the 0.25 T field has a significant effect on the magnetization, which relates to the unbalanced domain structure shown in Figure 4-14. The graph in Figure 4-15 shows that the total energy of the system decreases with simulation steps, although with the magnetic field, the reduction is much higher as a result of the contribution from Eq. (1).

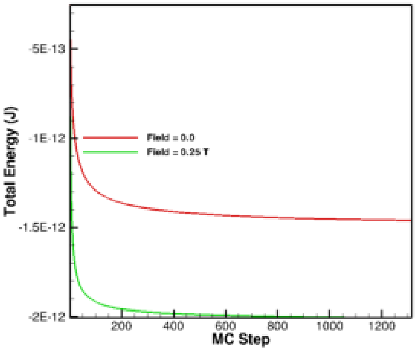

Figure 4-15: Total energy as a function of the MC simulation step with or without a superimposed 0.25 T field in the z-direction.

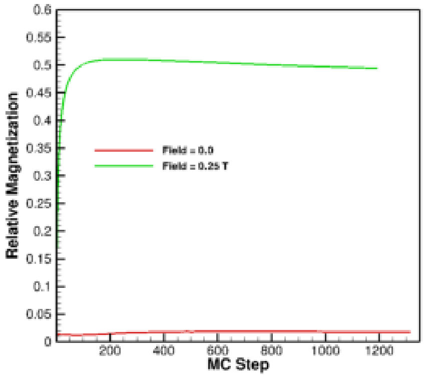

Figure 4-16: Relative magnetization as a function of the MC simulation step with or without a superimposed 0.25 T field in the z-direction.

Motor Design and Modeling

The development of unconventional motor technologies was accomplished by improvising upon promising technologies from previous work and initiating work on novel motor concepts. Previous research includes the design of various motor types, including the induction motor, switched reluctance motor, hybrid excitation motor, and flux coupling/field coil machines, with the latter two displaying the most potential. Novel motor designs were conceived and simulated, with consideration of various machine types such as switched reluctance, hybrid PM excitation, synchronous reluctance, and field coil excitation.

ORNL used advanced optimization algorithms to optimize machine design and controls. Electromagnetic FEA tools were used to implement basic models to determine performance and operational characteristics of new machine designs. Analytical models were used to determine additional performance metrics and associated control methods. A BFE motor without PMs, shown in Figure 4-17 and Figure 4-18, was developed during a previous research project at ORNL. The motor includes auxiliary coils that provide a magnetic field similar to what PMs provide in conventional PM motors. A new design was developed in FY 2014 in which the excitation coils are integrated more effectively with the primary motor components, thereby greatly reducing the volume of the auxiliary coils. Among many design choices, another leading ORNL design is a novel type of sinusoidally driven synchronous reluctance (SDSR) motor. Unlike switched reluctance motors, SDSR motors can be driven by a conventional three-phase inverter and have much less torque ripple.

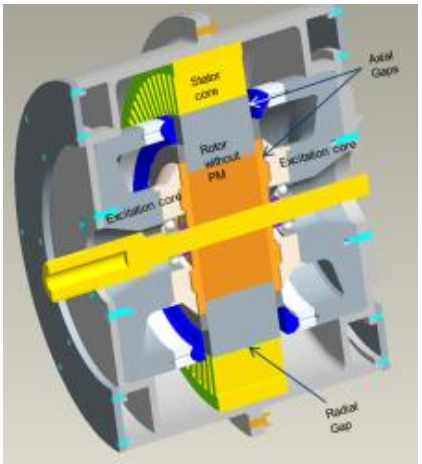

Figure 4-17: First-generation BFE cross-section overview.

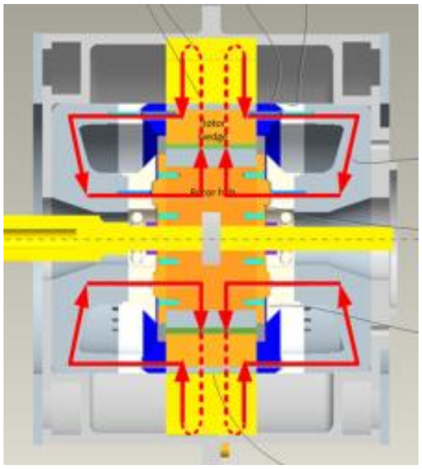

Figure 4-18: First-generation BFE cross-section side view.

Performance results for the new BFE and SDSR motor designs are summarized in Figure 4-19 and Figure 4-20. In Figure 4-19, the peak torque operation curves of the BFE and SDSR ("SyncRel") are compared with that of the 2010 Prius. To facilitate straightforward comparisons, the BFE and SDSR motors were designed so that they occupy the same volume as the 2010 Prius. It can be seen that the torque production capability of the SDSR is only slightly lower than that of the Prius, and the BFE peak torque production is just slightly lower than that of the SDSR. A more clear comparison can be made by observing the peak power capability shown in Figure 4-20. Note that these performance characteristics represent designs that have been only coarsely optimized. Therefore, the slight performance discrepancy from that of the 2010 Prius is reassuring, especially in light of the absence of PMs. Detailed design optimizations in FY 2015 will yield higher performance.

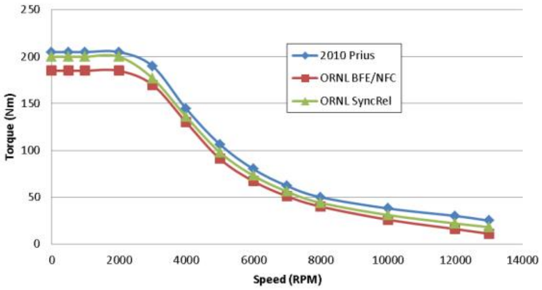

Figure 4-19: Comparison of simulated peak torque of various machines.

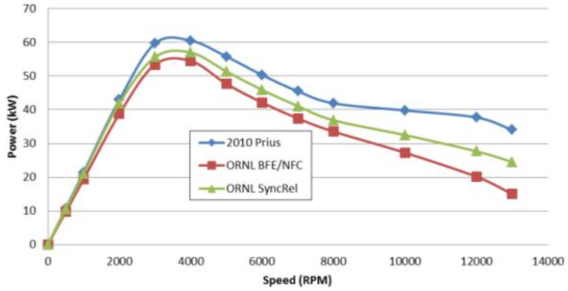

Figure 4-20: Comparison of simulated peak power of various machines.

The peak torque and power performance of the new BFE design is lower than that of the Prius and SDSR largely because of the additional current that is required for the field winding. Compounding the matter is the requirement that the field cross two additional air gaps in addition to the two crossings experienced in conventional electric motors. This inherently reduces the power density, specific power, and efficiency of the BFE design in comparison with a conventional PM motor. The simulated efficiency map of the BFE design with the highest field excitation current is shown in Figure 4-21.

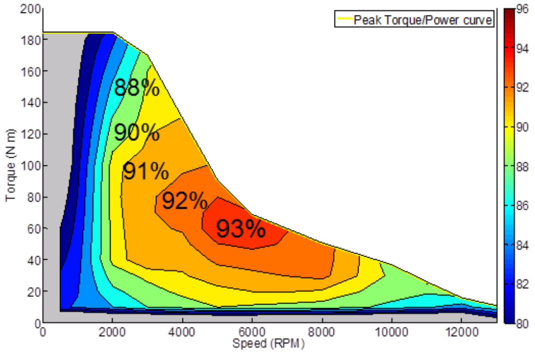

Figure 4-21: Simulated efficiency map for 2nd generation BFE with high field excitation level.

Simulated efficiency maps for medium-high, low-medium, and low field excitation levels are shown in Figure 4-22 and Figure 4-23. Although the peak efficiency and overall efficiency levels of the BFE design are lower than those of the Prius and SDSR motors, the adjustable field level has the effect of shifting the operation region in which the peak efficiency occurs. For example, the motor efficiency at 2000 rpm and 10 Nm is about 87% for high auxiliary field excitation currents. For low field excitation currents, shown in Figure 4-23, the efficiency is above 91%, compared with an efficiency of about 88% for the Prius at the same operation point. PMs have high residual fields even at low and moderate operation points where the high fields are not required, and so the core losses associated with these residual fields can yield low efficiencies for these regions. Some motors without PMs may have higher efficiencies than PM motors at low and moderate loads and high speeds as a result of this phenomenon.

The addition of auxiliary field control increases the potential for higher efficiencies at low and moderate loads and high speeds. This is particularly important because low and moderate operation points are frequented throughout common driving cycles, as shown in Figure 4-24. These data, recorded by Argonne National Laboratory, indicate the tractive force vs vehicle speed associated with various driving cycles for the Nissan LEAF. This is a direct drive powertrain, so the operation map directly relates to the torque vs speed efficiency maps that were just discussed. It can be seen that low-efficiency regions of the PM machine are encountered frequently for all drive cycles. This phenomenon highlights the potential for non-PM and adjustable field motors to have higher overall efficiencies than PM motors, as efficiency is averaged over the entire drive cycle.

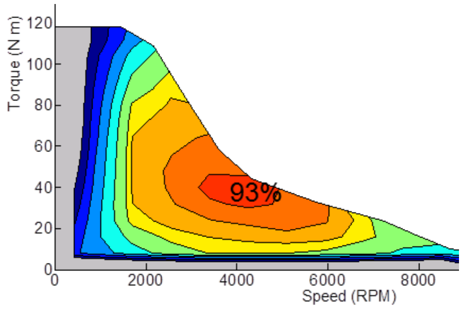

Figure 4-22: Simulated efficiency map for second-generation BFE with medium-high field excitation level.

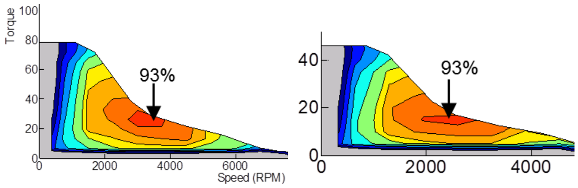

Figure 4-23: Simulated efficiency map for second-generation BFE with low-medium (left) and low (right) field excitation levels.

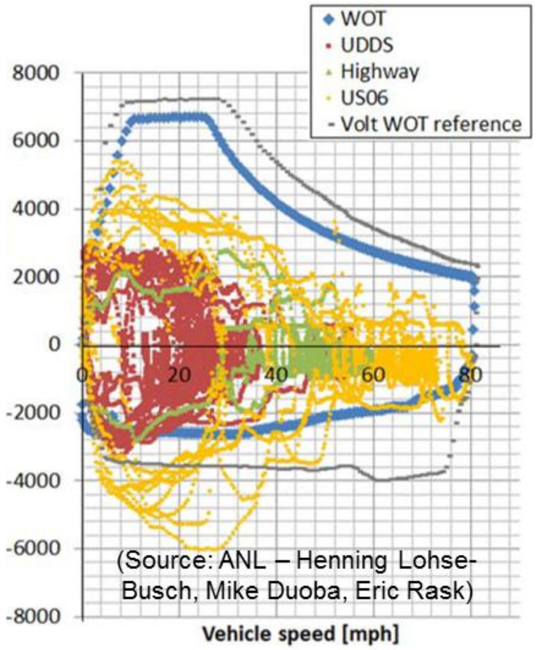

(Source: ANL – Henning Lohse-Busch, Mike Duoba, Eric Rask)

Figure 4-24: Required tractive force for Nissan LEAF measured for various drive cycles.

After coarse optimizations were performed on several designs that were validated in preliminary simulations, the design with the highest potential for success was selected for fabrication. The SDSR motor was selected based on its potential for higher power density and specific power and its simplicity of fabrication and assembly. Invention disclosures are being filed so details of the design can be discussed in the future. Fabrication and assembly of the novel SDSR was completed in FY 2014; images of the proof-of-principle prototype are shown in Figure 4-25. Unforeseen difficulties often arise during fabrication and assembly prototype motors, but the assembly process of the SDSR motor was accomplished without significant difficultly, which is a positive sign for manufacturability.

Figure 4-25: Proof-of-principle prototype assembly of novel synchronous reluctance motor.

Conclusions and Future Directions

Electrical steel with 6.5% Si has about 35% lower core losses than conventional electrical steel with 2–3% Si; therefore, the use of high-Si steel can increase peak motor efficiency by up to 2–5% and increase efficiency in other operation regions by 5–15%, particularly at high speeds. ORNL confirmed proposed methods and developed additional techniques to facilitate low-cost production of 6.5% Si sheet steel. A key factor in making it feasible to use 6.5% Si sheet steel for motor laminations is the implementation of softening techniques that allow the sheets to be rolled to the appropriate thicknesses and the laminations to be stamped. It is most common for the rolling operation to be carried out by the steel manufacturer, while stamping and other related processes are carried out by the motor manufacturer. ORNL's proposed methods address the need for two separate processing locations. These methods have been confirmed in simulations and with hardness testing on small samples. Future work on 6.5% Si steel will include simulations to determine the impacts of various compositions of trace elements, analysis to gain a better understanding of ordering (which causes brittleness), and more experimental analysis to further validate novel processing techniques.

Characterization of the impact of residual stress upon magnetic properties has revealed significant degradation near areas that have sustained mechanical deformation. The primary reason for interest in this phenomenon is to increase the understanding and model the impact of residual stress upon magnetization and core losses. An MC simulation environment has been developed to study the fundamental behavior and determine how a wide range of variables can impact the magnetization and loss mechanisms in electrical steel. A custom characterization system has been developed to perform large-scale assessments of these behaviors, and implementation of a system to perform detailed analyses on the magnetic domain scale is under way. These systems not only will help with the analysis of the impact of residual stress but also will advance the understanding of other factors that impact magnetization and loss behavior, such as rotational losses and the impact of pulse width modulation excitation. These areas will be included in efforts for FY 2015.

Motor modeling tools are under development to include the phenomena related to the advanced characterizations mentioned. When possible, advanced techniques will be implemented with commercial FEA packages and detailed optimization will be conducted with leading motor designs. Additionally, characterization of the proof-of-principle prototype will serve as an important feedback mechanism for model verification.

FY 2014 Publications/Presentations

1. T. Burress, "Scalable non-rare earth motor development," presented at the DOE VTO APEEM Kickoff Meeting, November 2013.
2. T. Burress, "Scalable non–rare earth motors," presented at the DOE VTO Annual Merit Review and Peer Evaluation Meeting, June 2014.
3. T. Burress, "Electric motor research for electric vehicles," presented at the IEEE Energy Conversion Congress and Exposition, September 2014.

4.2 Alternative High-Performance Motors with Non-Rare Earth Materials

Ayman EL-Refaie (Principal Investigator)

General Electric Global Research Center
1 Research Circle
Niskayuna, NY 12309
Phone: (518) 387-6660; Fax: (518) 387-6675
E-mail: elrefaie@research.ge.com

Francis Johnson, Materials Tasks Leader
General Electric Global Research Center
1 Research Circle
Niskayuna, NY 12309
Phone: (518) 387- 5087; Fax: (518) 387-6232
E-mail: johnsonf@research.ge.com

Start Date: September 2011
Projected End Date: December 2016

Objectives

- Design, build and test advanced traction motors that reduce or eliminate the use of rare-earth materials while meeting the DoE 2020 specifications.
- Develop advanced materials to open up the design space for the new motors.

Technical Barriers

- The specifications for hybrid vehicle motors are challenging in terms of power density, efficiency and cost. This requires a comprehensive approach to advance the state of the art, including novel concepts to push past barriers.
- High speed is key to high power density.
- High speed leads to higher electrical frequency.
- Higher stator core and rotor losses.
- On top of all these challenges, eliminating rare-earth permanent magnets makes the problem an order of magnitude more challenging.
- Scaling up materials processing to level needed for motor insertion.

Technical Targets

The goal of the project is to develop traction motors that reduce or eliminate the use of rare-earth materials and meet the DoE specifications summarized in Table 4-1 and Figure 4-26.

Table 4-1: Motor Specifications.

Items	Specification
Max. Speed	14,000rpm
Peak Power	55kW @ 20% speed for 18sec
Maximum Current	400Arms
Cont. Power	30kW @ 20~100% speed @ Vdc=325
Efficiency	Refer to target efficiency map
Operating Voltage	200~450V (325V nominal)
Back EMF	<600Vpk line-to-line @ 100% speed
Torque Pulsation	<5% of Peak Torque @ any speed
Characteristic Current	< Maximum Current
Weight	≤35kg
Volume	≤9.7L
Cost @100k	≤$275
Ambient (outside housing) Operating Temperature	-40~140°C
Coolant inlet	105°C, <10LPM, 2psi drop, <20psi inlet
Minimum isolation impedance-phase terminal to GND	1Mohm

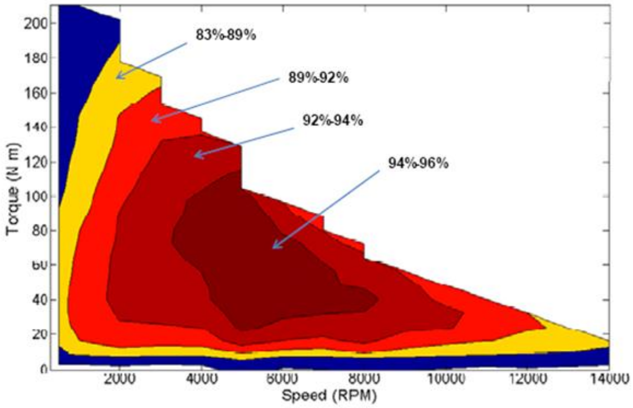

Figure 4-26: Motor Required Efficiency Map.

Accomplishments

(A) Motor accomplishments:

- Continue to evaluate more motor topologies (more than 10 evaluated so far).
- Down-selected the first 4 topologies:
  - First prototype has reduced rare-earth content (built and fully tested)
  - Second prototype has non-rare earth magnets (built and fully tested)

  - Third prototype has no magnets and includes one of the advanced materials (currently being built and testing will start in 2014)
  - Fourth prototype is a scaled-down version that has no magnets and includes another advanced material (construction will be initiated in 2014).

(B) Materials accomplishments:

- Applied advanced manufacturing methods to non-rare earth permanent magnet materials and quantified. processing factor dependence of key magnetic properties
- Completed first microstructural investigation GE-synthesized non-rare-earth Permanent magnets at Ames Laboratory.
- Demonstrated higher tensile strength soft magnetic laminates with magnetic properties approaching those of Si-Steel.
- Demonstrated stability of high temperature insulation materials at temperatures > 250°C.
- Performed initial studies on scalability of new materials for sub-scale prototype motor builds.

✧ ✧ ✧ ✧ ✧

Introduction

Electric drive systems, which include electric machines and power electronics, are a key enabling technology for advanced vehicle propulsion systems that reduce the petroleum dependence of the transportation sector. To have significant effect, electric drive technologies must be economical in terms of cost, weight, and size while meeting performance and reliability expectations.

The objective of the GE Global Research “Alternative High-Performance Motors with Non-Rare Earth Materials” program is to develop a higher power density traction motors at a lower cost while simultaneously eliminating or reducing the need for rare-earth materials. Successful completion of this program will accelerate the introduction of hybrid electric vehicles into the U.S. road vehicle fleet and bring the added benefits of reduced fuel consumption and environmental impacts.

(A) Motor Development:

- Develop advanced motor concepts including electromagnetic, mechanical, and thermal concepts.
- Build proof-of-principle machines to verify the design process as well retire the key risks.
- Design and build 55kW/30kW machines that meet the DoE specifications.
- Develop cost model to estimate the advanced motors cost based on 100,000 units/year.
- Investigate the scalability of the developed concepts by evaluating 120kW/65kW machines.

(B) Materials Development:

The objective of the materials development tasks is to develop non-rare-earth containing component materials that enable non rare-earth containing motor designs that meet project performance goals. In the first phase of research, the capability for improvement of four classes of materials are is being studied:

- Improving the coercivity of an existing non-rare-containing permanent magnet composition to enable operation at temperatures above 150°C.
- Improving the tensile strength of electrical steel to enable high speed motor operation with low iron loss.
- Improving the ability of motor laminates to control magnetic flux distribution.
- Improving the ability of dielectrics to withstand operating temperatures in excess of 280°C.

Approach

(A) Project Uniqueness:

- The project proposes a very comprehensive approach in terms of identifying the technologies that will meet the required performance.
- The project will explore various motor topologies; some include no magnets at all and some include non-rare earth magnets.
- Some of the motor topologies use only conventional materials while others will be enabled by advanced materials that will be developed under the project.
- Advanced materials including magnetic as well as electrical insulating materials will be developed to enable the motors to meet the required set of specifications.
- Advanced motor controls and thermal management techniques will also be developed.
- By evaluating the wide range of motor topologies and advanced materials, down-selected topologies/materials are expected to meet the required set of specifications.

(B) Approach:

Motor Development:

- Perform tradeoff study of various motor topologies.
- Identify promising scalable materials and produce coupons showing the expected properties.
- Down-select promising topologies/materials.
- Design/build/test 2–3 proof-of-principle motors.
- Down-select final motor topology.
- Design/build/test 3 identical motors as the key project deliverable(s).
- Develop cost model for the final motor.

Materials Development:

The materials development approach for the project is to develop the structure/processing/properties relationships of four categories of motor components being made with novel materials. The materials tasks will produce and characterize samples of the new materials and will culminate in the selection of materials for scaled-up production sufficient to produce a prototype motor.

- The microstructure of the non-rare-earth containing permanent magnet alloy is being refined through the application of modern casting and annealing technology. A series of designed experiments is being conducted to probe the capability of these technologies to increase coercivity while maintaining energy product. Magnet post-processing and characterization is being performed at Arnold Magnetic Technologies. Atom-scale structural characterization is being performed in collaboration with Ames laboratory to produce in-depth structure/processing/properties relationships.
- A novel processing route is being applied to conventional silicon steel alloys to improve the tensile strength by while retaining comparable power loss. The approach relies on understanding and controlling the trade-off between coercivity (and hence power loss) and tensile strength. The processing technology is being developed to form the new material into sheets suitable for motor laminates.
- Novel processing technology is being developed to enable improved control of magnetic flux contained within motor laminates. This approach requires the development of new alloys that are operable with this processing method and the demonstration of scalable processing at dimensions specified by the motors teams.
- High temperature dielectrics are being developed that maintain high dielectric strength with resistance to degradation by oxidation. This requires the selection of suitable materials components, production of sample films, and verification of electrical and mechanical properties as a function of time at temperature.

Results

(A) Motor Development:

The first prototype built and tested is a flux-switching machine using Dy-free magnets. The stator is shown in Figure 4-27 while the rotor is shown in Figure 4-28. Figure 4-29 shows a comparison of the machine predicted and measured back emf at 3000 rpm. It can be seen that there is good agreement between both results. The measured short-circuit current as a function of speed is shown in Figure 4-30.The short-circuit current is very close to the machine rated current which is a good infication of flux-weakening capability as well as fault-toelrance. There were no signs of demagnetization after the short circuit test, which si one of the key risks of Dy-free magnets. Figure 4-31 shows measured and 2D precidted torque as a function of rms current. The discrepancy between the results at higher current levels is attributed to 3D effects which were already accounted for during the design process. As can be see, the machine is able to provide 200 Nm at 400 Arms which is higher than the required peak torque of 187.6 Nm. Also there wer no signs of demagnetization after the peak torque testing. Figure 4-32 and Figure 4-33 show the machine performance during the 18 seconds peak-power operation. It can be seen that the machine can deliver 56.5 kW with a modest temperature rise of 16°C. Figure 4-34 and Figure 4-35 show the measured temperatures during heat runs at 2800 and 5000 rpm respectively. It can be seen that the machine is capable of producing more than the required 30 kW continuous ppower with modest temperature rises of around 25°C which is alos an indication of effective cooling. The machine full-load tested performance up to 10,000 rpm is summarized in Table 4-2. It can be seen that the prototype is capable of providing more than the required power within the voltage and current limitations and with good efficiencies.

Figure 4-27: Stator of first prototype.

Figure 4-28: Rotor of first prototype.

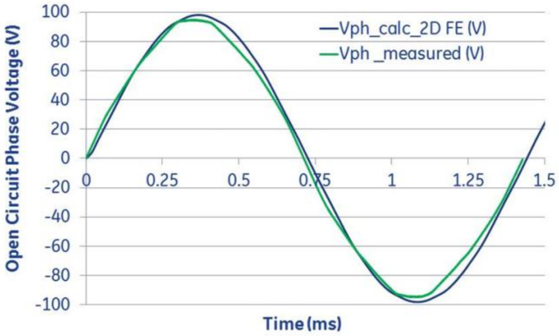

Figure 4-29: Measured and predicted back emf.

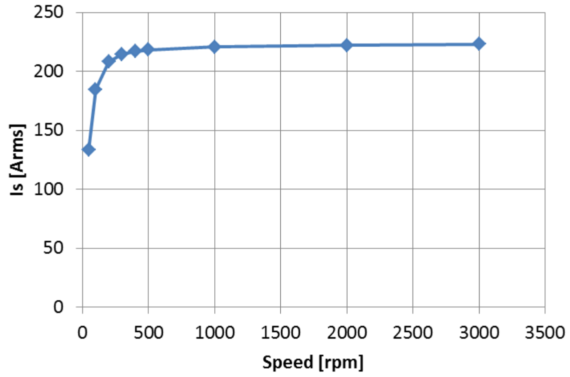

Figure 4-30: Measured short circuit current.

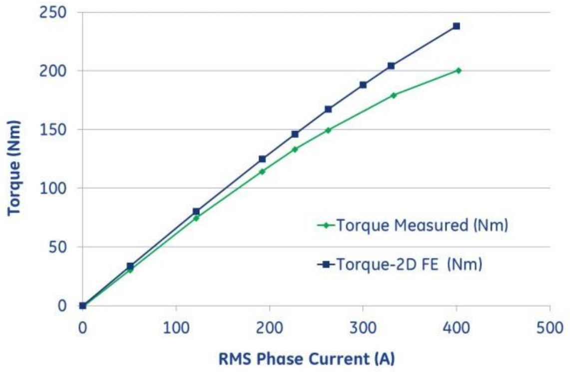

Figure 4-31: Torque vs. current.

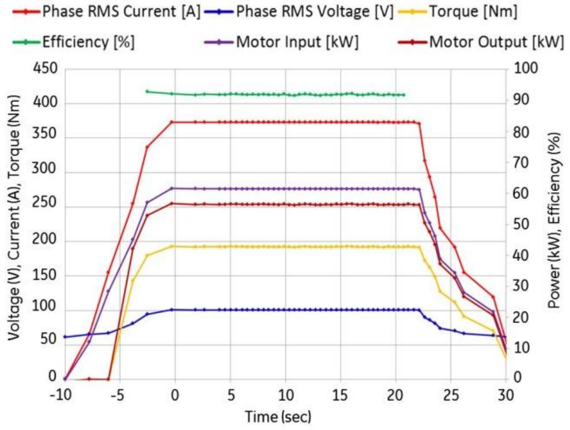

Figure 4-32: Measured Performance during 18 Seconds Peak Power Operation.

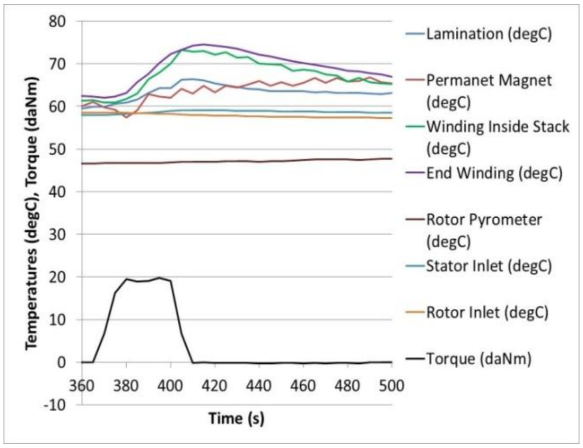

Figure 4-33: Measured Temperatures during a Heat Run for 18 seconds under 56.5 kW – 2800 rpm Peak Power Operation.

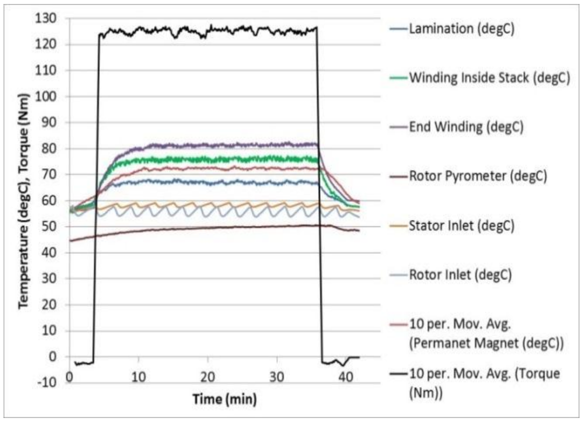

Figure 4-34: Measured Temperatures during a Heat Run under 36.7kW-2800rpm Continuous Operation.

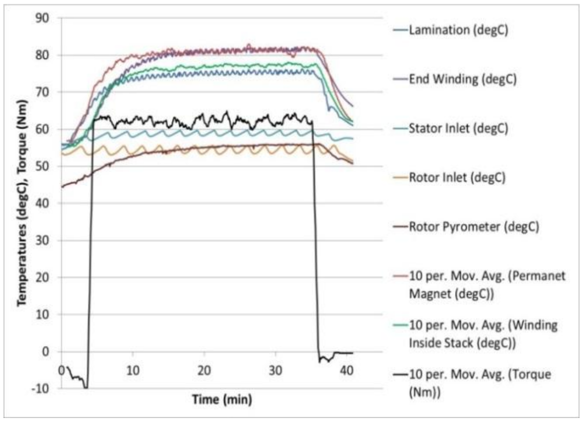

Figure 4-35: Measured Temperatures during a Heat Run under 32.3kW- 5000rpm Continuous Operation.

Table 4-2: First prototype full-load test results summary.

Speed [RPM]	Torque [Nm]	Pmec [kW]	Pelec [kW]	Eff [%]	Vph [Vrms]	Vll [Vrms]	Iph [Arms]	PF	Lo [k
2800	192.89	**56.54**	61.46	**91.99**	100.80	174.59	373.10	0.545	4.
2800	125.34	**36.72**	38.90	**94.40**	77.81	134.77	217.10	0.768	2.
4000	86.88	**36.37**	38.61	**94.20**	99.25	171.91	149.50	0.867	2.
5000	62.08	**32.49**	35.35	**91.91**	110.89	192.07	109.60	0.970	2.
6000	57.90	**36.38**	39.49	**92.12**	145.30	251.67	100.80	0.899	3.
7000	51.10	**37.49**	40.84	**91.80**	140.90	244.05	98.00	0.986	3.
8000	42.70	**35.79**	39.51	**90.60**	130.80	226.55	112.30	0.897	3.
9000	44.60	**42.02**	46.07	**91.20**	134.50	232.96	128.60	0.888	4.
10000	44.00	**46.12**	50.70	**91.00**	131.48	227.7	144.96	0.887	4.

The second protype built and tested is a spoke machine using ferrite magnets. The stator is shown in Figure 4-36 while the rotor is shown in Figure 4-37.

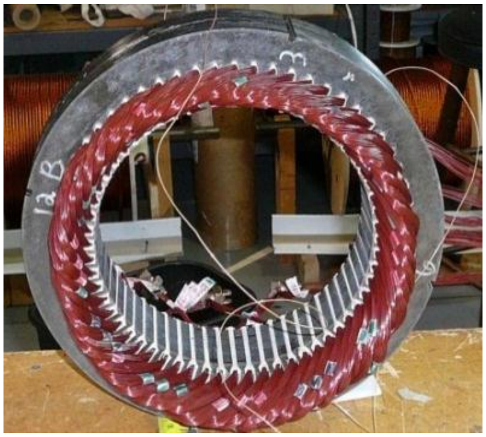

Figure 4-36: Stator of second prototype.

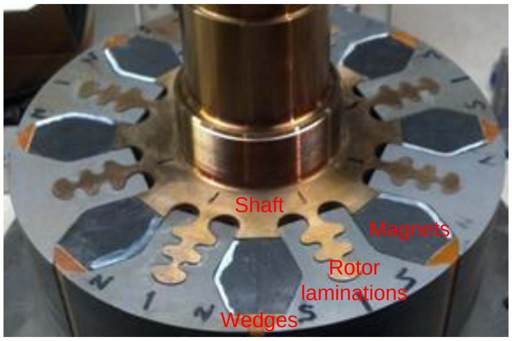

Figure 4-37: Stator of second prototype.

Figure 4-38 shows a comparison of the machine rpedcitse dand measured back ef at 2000 rpm and room temperature. It can be seen that there is good agreement between both results. The measured short circuit current was 48 Arms which is lower than the predicted 64 Arms. Further investigations showed that this difference is due to 3D effects which since then have been taken into consideration to modify the design. Figure 4-39 shows the measured torque ripple under rated torque condition. It can be seen that the peak-to-peak torque ripple is about 4.3% which is within the required specifications. This was accomplished by using fractional slot winding as well as rotor pole shaping. Figure 4-40 shows the machine performance under peak power loading. Figure 4-41 shows the full machine efficiency map while Figure 4-42 shows the machine partial load efficiency along the 20% rated torque trajectory. It can be seen that the machine has significant advantages in terms of partial load efficiency. Figure 4-43 shows the measured temperature rises inside the machine as a function of speed. It can be seen that the machine meets the design hotpsot with no active rotor cooling.

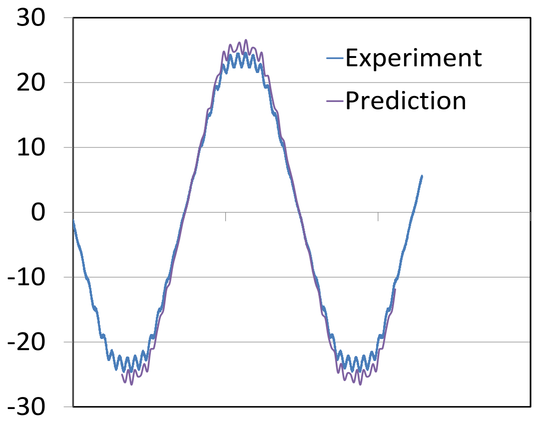

Figure 4-38: Back-emf: experimental vs. prediction at 2000 rpm and room temperature.

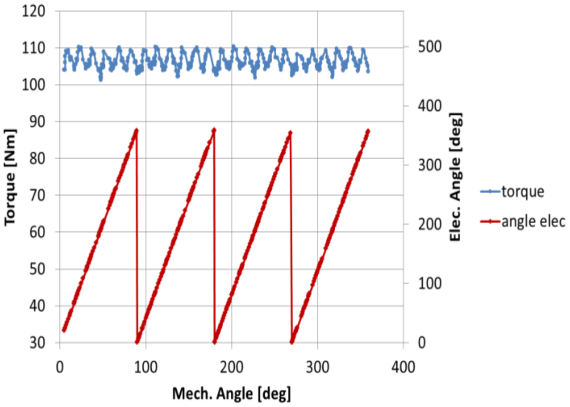

Figure 4-39: Measured Torque Ripple under rated torque shows that torque ripple is limited to 4.3%.

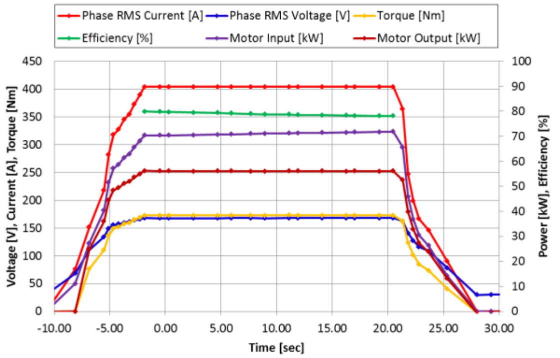

Figure 4-40: Machine performance under peak power for 20 seconds.

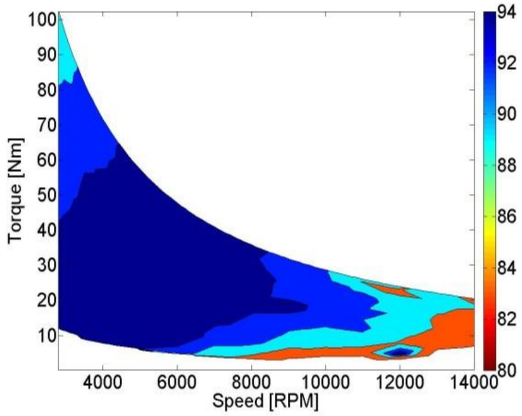

Figure 4-41: Machine efficiency map.

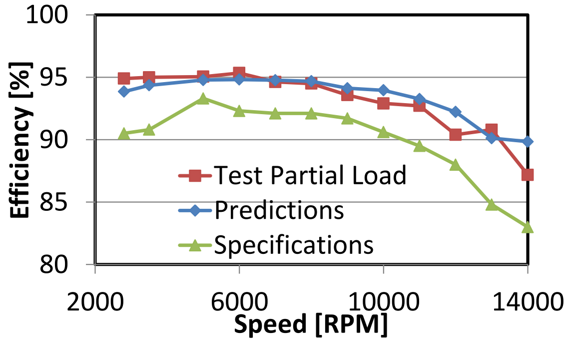

Figure 4-42: Machine partrial load efficiency along the 20% rated torque trajectory.

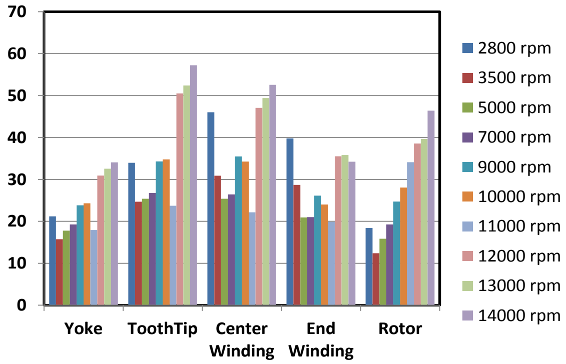

Figure 4-43: Measured Temperature Rise Inside The Machine as a Function of Speed Under Rated Power Testing.

(B) Materials Development:

a. Non-rare earth containing permanent magnets

The advanced manufacturing method explored during this project has been found to have the most effective in controlling the remanence of the non-rare-earth magnet material. Compositional variations were found that maintained that remanence while increasing coercivity. Further variations in composition and processing conditions were explored in an attempt to increase beyond that achieved in 2013. None of the compositions exceeded the best properties achieved in 2013. Table 4-3 and Figure 4-44 the properties of the best peforming materials to date. The utility of these properties in a motor design are presently under evaluation.

Table 4-3. Comparison of magnet properties of commercial non-rare-earth permanent magnets with best performing sample produced by GE to date.

Composition	Hci (kOe)	Br (kG)	$(BH)_{max}$ (MGOe)
Alnico5DG	0.73	1.3	6.5
Alnico8H	2.2	7.2	5.0
Alnico9	1.53	10.8	10.0
Best GE to date	**2.1**	**9.5**	**9.8**

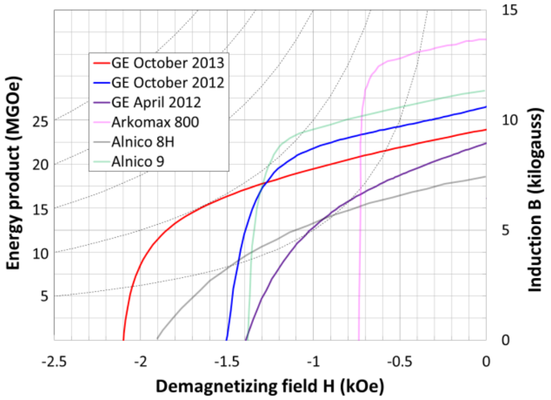

Figure 4-44: Improvement in magnetic properties for non-rare-earth permanent magnets cast via GE's advanced manufacturing method.Semi-transparent lines are commercially available Alnico type permanent magnets included for comparison.

b. High strength soft magnetic laminates

The power loss and magnetic properties of the higher strength soft magnetic laminates produced in 2013 were fully characterized. The best performing material had a tensile strength 15% greater than 3% Silicon Steel. However, the power loss was approximately 2X greater than that of Silicon steel in the frequency range used in electric machines. Additional efforts to reduce power loss were evaluated and judged to have a low likelihood of success. Further work on the high strength laminates was suspended.

c. Improved magnetic flux control

Further development was conducted on the manufacturing method down-selected in 2013. Aging tests at 180°C showed that processed material was stable for least 5000 hours. Mechanical properties were measured as a function of temperature. Finite element calculations were perfomed to verify that residual stresses would remain below tensile limits at all stages of processing. Design rules for motor laminate geometry were developed. A lithographic method was selected for developing the non-magnetic regions on the laminates. A spray-process was selected for applying a masking compound and efforts are now focused on developing methods to remove the mask after processing. Aging tests at 200°C and 220°C were started at the beginning of 2014 and will conclude by the end of December.

d. High temperature dielectrics

The inorganic-organic hybrid high temperature film has been developed and evaluated on its thermal performance since 2013. Weight loss percentage and tensile strength change of this film after isothermal aging at 320°C, 350°C and 400°C was significantly low in comparison to polyimide film. To mimic stator assembly, statorettes were built to evaluate the mechanical integrity of the hybrid film during manufacturing assembly. Dielectric performances of the hybrid films were measured after they were built into the statorettes with wiindings and varnish, AC hipot of 3kV was applied and passed after the statorettes subjected to thermal aging at 280°C for more than 2000 hours and subsequently at 300°C for more than 800 hours. HT film has shown no sign of any degradation.

To ensure the robustness of the hybrid film in machine assembly process and in service operation, we have further improved and developed film/fiber laminated composite sheet for the slot liner to improve the mechanical strength while maintaining the thermal performance. The roll to roll coating process for the hybrid film has been evaluated at the pilot machine for scale up capability.

Conclusions and Future Directions

There is significant progress made in terms of evaluating the various motor topologies. Some of them show promising performance both in terms of power density and/or efficiency compared to rare-earth IPM motors. The first prototype is a flux-switching machine that uses Dy-free magnet. It has been built and fully-tested. The second prototype is a spoke design with ferrites. This prototype has also been built and fully tested. Currently there are two more prototypes that do no use any permanent magnets under development. One of them is a full scale prototype and will include the high-temperature insulation system while the second one is a different topology scaled-down design where one of the advanced soft magnetic materials will be sued as a proof-of-concept demonstration.

Also significant progress made in terms of developing the advanced materials. Coupons have been produced and tested and some are showing promising results.

Significant progress has been made in developing advanced magnetic and dielectric materials for use as motor components. Structure/processing/properties relationships have been determined. Initial test coupons have been produced and characterized. Production of the high temperature dielectrics were scaled up in bacth process to support a motor prototype. The properties of a non-rare-earth containing permanent magnet were optimized. A motor laminate material capable of enhanced control of magnetic flux path was further developed. Work was suspended on high strength motor laminates due to high power loss exhibited in the processed material.In 2015 one or more of the material systems will be chosen for scaled-up processing to support a prototype motor build.

Future Direction

FY15

- Scaled manufacturing of selected materials
- Finsih building and testing the third and fourth prototypes
- Downselect final motor and initiate build and test

FY 2014 Publications/Presentations

1. Presentation at the 2014 AMR, June 2014.
2. James McFarland, Thomas Jahns, Ayman EL-Refaie, “Demagnetization Performance Characteristics of Flux Switching Permanent Magnet Machines”, ICEM 2014, September 2014, Berlin.
3. Tsarafidy Raminosoa, Ayman El-Refaie, Di Pan, Kum Kang Huh, James Alexander, Kevin Grace, Steven Galioto, Patel Reddy and Xiaochun Shen, “Reduced Rare-Earth Flux Switching Machines for Traction Applications” ECCE 2014, September 14–18, Pittsburgh, PA.
4. James McFarland, Thomas Jahns, Ayman EL-Refaie, “Analysis of the Torque Production Mechanism for Flux-Switching Permanent Magnet Machines” ECCE 2014, September 14–18, Pittsburgh, PA.
5. Patel Reddy, Steve Galioto and Ayman El-Refaie, “Effect of Magnet Types on Performance of High Speed Spoke Interior Permanent Magnet Machines designed for Traction Applications” ECCE 2014, September 14–18, Pittsburgh, PA.
6. James McFarland, Thomas Jahns, Ayman El-Refaie and Patel Reddy, ”Effect of Magnet Properties on Power Density and Flux-Weakening Performance of High-Speed Interior Permanent Magnet Synchronous Machines” ECCE 2014, September 14–18, Pittsburgh, PA.
7. Presentation to the APEEM EETT, October 2014.

4.3 Unique Lanthanide-Free Motor Construction

Josh Ley (Principle Investigator)
Subcontractor: UQM Technologies, Inc.

Alan T. Gilbert, Program Manager
UQM Technologies, Inc.
4120 Specialty Place
Longmont, CO 80504
Phone: (303) 682-4904
E-mail: agilbert@uqm.com

Subcontractor: N/A

Start Date: October, 1, 2011
Projected End Date: April 30, 2016

Objectives

- This project pursues new motor construction that eliminates, or significantly reduces the use of rare earth elements while maintaining the attractive size, weight and efficiency features of rare earth permanent magnet motors.
- The primary drivers for this work include:
  - Lack of transparency in the rare earth magnet supply market and its pricing structures
  - Significant rare earth price escalation in calendar year 2011
  - Need for small, lightweight, high efficiency, low cost motors for electric traction drives
  - New architectures and/or materials that eliminate rare earth materials while maintaining performance that is attractive for electrified vehicles.

Technical Barriers

The low coercivity of the AlNiCo magnets requires an unconventional rotor design for power density. This unconventional rotor design requires an innovative magnet retention system for high speed operation. The proof-of-concept (POC) rotor involves the use of retention bars, adhesive and fiber wrap to accomplish the retention.

A second item of concern is also related to the AlNiCo magnets and their characteristic of of de-magnetizing if not magnetically coupled with a conductive outer sleeve. This sleeve must be over the rotor any time it is not fully inserted in the stator. UQM has worked with the company magnetized the rotor to insure a sleeve can be designed to maintain the magnetization.

Technical Targets

- The DOE motor specifications that are targeted for this work include:
  - 55 kW baseline design
  - Scalable to 120 kW or higher.

Accomplishments

- Completed the full analysis and design and build of the POC motor, including:
  - Final magnet selection
  - Electromagnetic design, rotor geometry and magnet shape
  - 3D structural stress analysis of the magnet retention system
  - All other components of the POD motor.
- Completed design of tooling and fixtures:
  - Magnetizing fixture
  - De-magnetizing prevention sleeve “keeper”
  - Assembly tooling and fixtures.
- Completed assembly and testing of two (2) full POC motors (1 for delivery in operational condition, 1 spare for risk reduction):
  - POC1 and POC2 have been tested at UQM as described in the following sections.

✧ ✧ ✧ ✧ ✧

Introduction

Project Objective

This project pursues the development of a non-rare-earth permanent magnet motor architecture. It incorporates a novel rotor geometry that allows the use of lower energy Al-Ni-Co, Fe-Co-W, or other high flux, low coercivity magnet material. These materials are not currently adopted due to demagnetization within existing magnetic circuit designs, a problem that is overcome with this proposed design.

Project Description

Three unique design features of this motor architecture are proposed to enable the use of low coercivity magnet technology: magnet shape along with magnetization direction, a nonmagnetic support structure, and design features that reduce demagnetization fields. The project relies upon incremental improvement in the non-rare-earth magnet properties (collaboration with Ames Laboratory) and this is where the project starts. From there, UQM develops a motor design and integrates thermal technology in collaboration with the National Renewable Energy Laboratory. Finally, motors are built in years two and three (initial proof-of-concept motor followed by refined hardware). These will be tested at UQM and delivered to Oak Ridge National Laboratory for independent confirmatory testing. The project concludes with designs scaled to higher power and detailed cost estimating activities. Cost is key to the adoption of electrified vehicles, so substantial focus is placed on the tasks related to the detailed costing of the technology.

Project Impact: Benefits and Outcomes

The outcome of the technology development and the resultant scalable hardware will be motor designs that apply to a full range of vehicle electrification, from mild hybrid to heavy hybrid to fully electric vehicles. This unique permanent magnet motor technology has an efficiency advantage over wound-field or induction machines (no energy consumed to create the magnetic field), and therefore, will decrease petroleum consumption relative to other non-rare-earth motor technologies. Economically, the magnet material used for this program is one third the cost of NdFeB magnets on a per-pound basis, and therefore, supports lower cost if the material content can be maintained to be less than three times the amount of NdFeB for a given power level. UQM is confident that the total magnet cost of the proposed technology will be lower than the equivalent rare-earth motor. This will provide economic benefit to the end-use consumers (lower vehicle cost) and improve electrified transportation industry with products that compete more favorably with traditional petroleum engine driven vehicles.

Approach

- Pursue design that enables the use of low coercivity magnets:
  - Unique magnet and supporting rotor geometry
  - Stator and rotor design features that reduce demagnetization fields.
- Collaborate with FFRDC partners:
  - Ames Laboratory for incremental improvements in high flux, low coercivity magnet materials
  - National Renewable Energy Laboratory for thermal management
  - Oak Ridge National Laboratory for testing.
- Period 1 (10/2011 thru 4/2013) focused on the design of the electromagnetic circuit that will meet the DOE targets and be capable of manufacturing:
  - UQM's focus was the electromagnetic design with existing AlNiCo technology.
  - Ames Laboratory is pursuing increased performance of the AlNiCo material.
  - NREL will provide assistance in the thermal management of the motor design.
  - ORNL will provide testing of the motor.
- Period 2: Focused on the build proof-of-concept (POC) motor and test with standard three-phase inverter:
  - Tests at UQM showed the performance is achievable.
  - Unit submitted to ORNL to validate results.
- Period 3: Build and test proof-of-design (POD) motor:
  - Implement enhanced AlNiCo 8X magnet material developed by Ames in POD motor.
- Bill of materials with costs and higher power design at program completion.

Results

PROOF-OF-CONCEPT MOTOR DESIGN, BUILD AND TEST

The design of the motor was completed at the end of FY 2013. The design incorporated a unique architecture in order to keep the alnico from demagnetizing. With the completion of the design, the major focus of FY 2014 would be manufacturing and testing.

In manufacturing the motor there were several challenges that were overcome successfully. First, special tooling, refered to as a "keeper" was designed to ensure that the alnico did not demagnetize in a free pole state during assembly. This was accomplished by placing a steel keeper around the rotor, while outside of the stator. This ensured the presence of a complete magnetic circuit that maintained the magnet charge. The second issue delt with making special accomodations for AlNiCo9 magnets that experienced cracking in the magnet manufacturing process. Thus, a specification was developed to accept and reject parts in order to maintain structural integrity in the rotor.

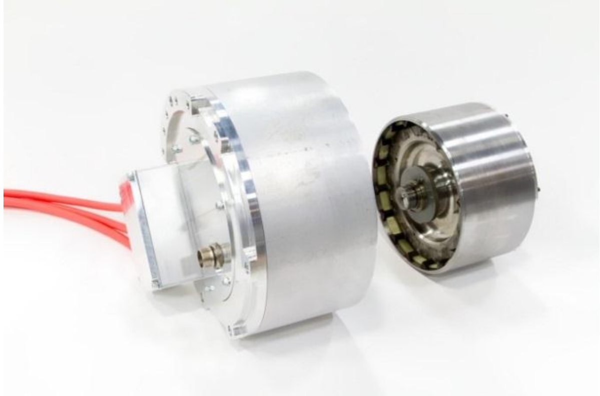

Figure 4-45: View of POC Motor Prior to Final Assembly.

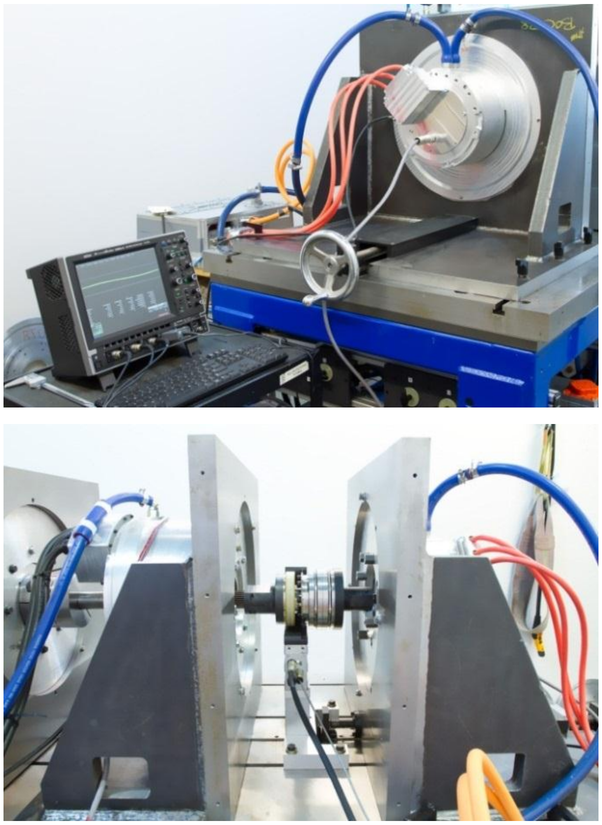

Figure 4-46: Dynamometer Testing Apparatus

Once key manufacturing problems had been addressed, the motor final assembly was completed and testing commenced. The motors were fixtured on the dynamometer testing apparatus to verify motor characteristics such as Back-EMF, Torque, and power. The initial tests on the dynamometer measured back EMF. The back EMF screen captures from the oscilliscope are shown below in Figure 4-47.

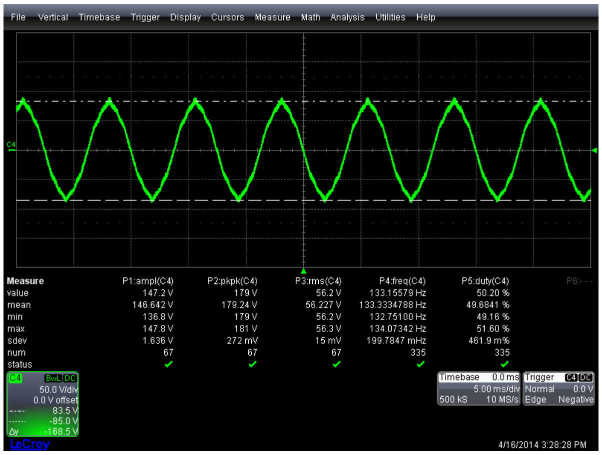

Measure	P1:ampl(C4)	P2:pkpk(C4)	P3:rms(C4)	P4:freq(C4)	P5:duty(C4)	P6:- - -
value	147.2 V	179 V	56.2 V	133.15579 Hz	50.20 %	
mean	146.642 V	179.24 V	56.227 V	133.3334788 Hz	49.6841 %	
min	136.8 V	179 V	56.2 V	132.75100 Hz	49.16 %	
max	147.8 V	181 V	56.3 V	134.07342 Hz	51.60 %	
sdev	1.636 V	272 mV	15 mV	199.7847 mHz	461.9 m%	
num	67	67	67	335	335	
status	✓	✓	✓	✓	✓	

Figure 4-47: Back EMF POC1 Before High Torque Test.

The above Figure 4-47 is a scope capture, illustrating the EMF waveshape. The back EMF amplidude measured 84.25 V/krpm Line-to-Line on POC1 motor before the high torque test. This was close to the 89.8 V/krpm value predicted and within the range of expected magnet property tolerance. The next step in the design verification process was to run an incremental torque test to deteriming maximum torque before demagnetization. The demagnetization analysis results from FY 13 were used to establish the methodology behind this test. The analysis predicted that the motor could partially demagnetize at near full torque. Therefore an incremental torque test was conducted by increasing current and torque in 10% increments and the EMF was measured after every point such that the point of demagnetization could be determined. The test results for EMF are shown in Figure 4-48 for EMF taken after the 100% torque test.

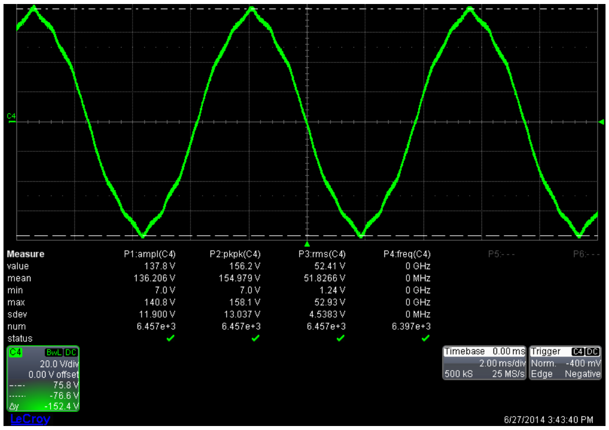

Measure	P1:ampl(C4)	P2:pkpk(C4)	P3:rms(C4)	P4:freq(C4)	P5:- - -	P6:- - -
value	137.8 V	156.2 V	52.41 V	0 GHz		
mean	136.206 V	154.979 V	51.8266 V	0 MHz		
min	7.0 V	7.0 V	1.24 V	0 GHz		
max	140.8 V	158.1 V	52.93 V	0 GHz		
sdev	11.900 V	13.037 V	4.5383 V	0 MHz		
num	6.457e+3	6.457e+3	6.457e+3	6.397e+3		
status	✓	✓	✓	✓		

Figure 4-48: EMF after 100% Torque POC1.

As, shown in Figure 4-48 results indicate the back EMF dropped to 76.6 V/krpm, indicating about 8% demagnetization. This was expected, since the demagnetization analysis indicated partial demagnetization given the loaded operating point fell on the knee of the B-H curve at 100% of full torque, see Figure 4-49. It was note that at 90% of full torque (235 Nm) no measureable demag occurred. Therefore, the demag point is somewhere between 90 and 100% of full torque. The torque data from the incremental torque test are shown in Figure 4-49.

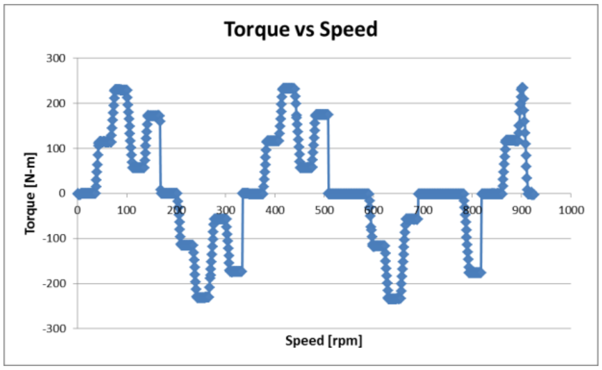

Figure 4-49: Torque vs Speed results for Maximum Torque Test.

Once design validation tests had been performed to determine the maximum torque before demag, power profile tests were performed on POC2, to measure the torque vs. speed and power vs. speed characteristics. The test involved validation of the motor's torque vs. speed curve up to 5000 [rpm]. The speed was limited to 5000 rpm due to durability concerns, given the cracked magnets. The torque was also limited to 85% of full torque, or 225 Nm, to ensure no demag occurs. The results of this test are shown, below in Figure 4-50 and Figure 4-51.

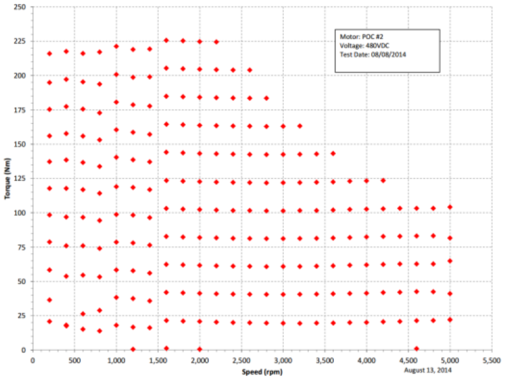

Figure 4-50: Torque vs Speed results for Power Profile Test.

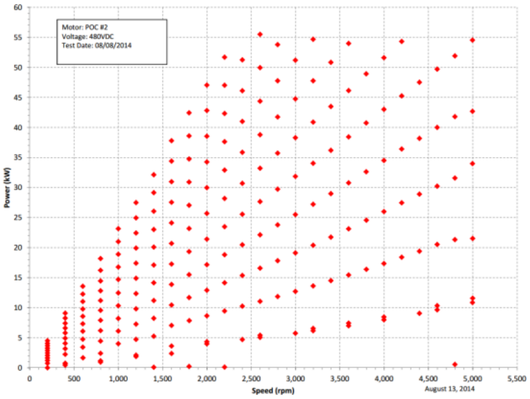

Figure 4-51: Power vs Speed results for Power Profile Test.

As can be seen from the results of this test, the motor was able produce the DOE Goal of 55 kW from 2000 rpm to 5000 rpm. Although the speed was intentionally limited as a precaution, POC1 did achieve 10 krpm in a separate test.

In conclusion, the test results verified the design EMF and reached the power goal of 55 kW. The design also proved capable of producing 90% of the torque goal 235 Nm relative to the goal of 262 Nm.

MAGNET IMPROVEMENTS:

During the period Ames Laboratory (Ames) focused on refining the AlNiCo material, AlNiCo 8 and 9 showed the most promise for improvement, due to their higher starting coercivity. This higher starting coercivity is believed to be the result of the elongated Fe-Co phase shape anisotropy. Using the in house gas atomizer, Ames produced a pre-alloy powder that had very spherical shape and a low content of satellite particles. Additionally, this powder had excellent flowability and powder packing. Sintering and compression molding, with a binder, were investigated as potential methods to form the powder into bulk magnet shapes. Compression molding was determined to be the preferred method for producing inexpensive bulk magnet shapes.

Additionally, Ames had very good success in determining the one of key paramenters, reduced spinodal spacing, which leads to increased coercivity. This reduction in spinodal spacing is a direct function of the time spent at a specific magnetic annealing temperature.

From these successes Ames has determined that an improved magnet composition (increased coercivity) can be produced for use in the POD motors for the next phase. This improved material will be a varation of AlNiCo 8.

In the next phase Ames will focus their efforts on producing an adequate quantity of the powder, molding into bulk shapes and the processing (annealing and final sizing).

THERMAL MANAGEMENT

In support of UQM's motor project "Unique Lanthanide-Free Motor Construction", NREL is providing thermal management analysis and design support. This report contains a summary of work performed at NREL during phase two of UQM's motor project. The summary covers the following areas:

Full stator cooling jacket flow and thermal analysis

Thermal parameter sensitivity study

Investigation of alternative cooling techniques

Stator-to-case thermal contact resistance measurements

In-situ motor testing.

Cooling Jacket Flow and Thermal Analysis

The phase two modeling work focused on verifying that the methodology developed during phase one to simplify the motor thermal analysis modeling was valid. The simplified thermal finite element analysis (FEA) model (Figure 4-45) developed during phase one focused on breaking the model down into a fundamental component in order to achieve a fast solving, efficient model. During phase two of the project NREL worked to verify the accuracy of the section FEA model and the process from which it was derived by running a full conjugate heat transfer model using computational fluid dynamics (CFD) (Figure 4-52) for the stator and cooling jacket to integrate the thermal performance and fluid flow.

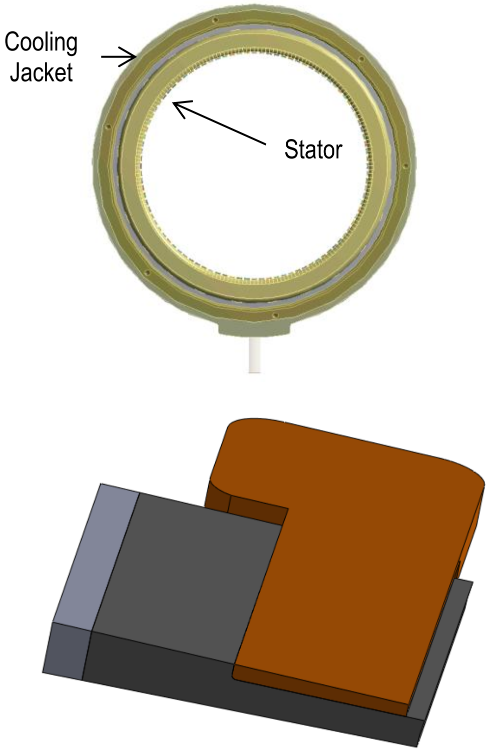

Figure 4-52: Full CFD model (top) and FEA section model (bottom).

Results showed that the section FEA model was accurate enough to be used in lieu of a full conjugate heat transfer CFD model for most analyses that focused on the motor stator. The section FEA model provided extra flexibility and quick turnaround time on design variations. The agreement between the full CFD model and the FEA section model confirmed the approach used to develop the FEA section model. The FEA model was used in a material sensitivity analysis detailed later in this document.

In the CFD model channel flow was also examined in detail to determine if any redesign was needed, and it was found that the stator and case provided enough heat spreading capacity to negate variation in flow between channels. Gravity was also examined and found to be negligible regardless of orientation.

Thermal Parameter Sensitivity Study

The results of the material and interface sensitivity study are shown in Figure 4-53. For the analyzed cooling configuration the most important properties were the in plane lamination thermal conductivity and the stator-case contact thermal conductivity or contact resistance. It is through these two parts that all the heat must flow out of the motor for the case cooled configuration.

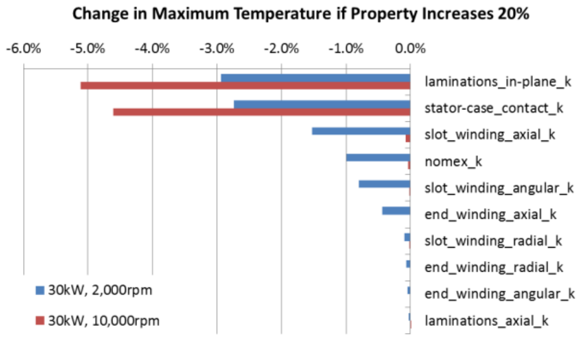

Figure 4-53: Summary of material sensitivity study.

Alternative Cooling Techniques

Two design alternatives were considered that focused on cooling the motor end windings. The justification of the designs was based on the observation that the hottest part of the motor was the end windings. All heat generated in the end windings is required to go through the entire motor assembly in order to be expelled from the motor. NREL evaluated the effect of encapsulating the end winding with a thermal potting compound and also directly cooling the end windings with oil.

The results of the FEA showed that encasing the end windings in a potting compound has potential for providing an effective means for cooling the end windings. For the high torque mode where maximum heat is generated in the winding the potting compound gives a 30% improvement in performance (Table 4-4). The results shown in Table 4-4 are preliminary but show that additional analysis and testing may be justified as a method to aid motor heat transfer. The use of oil or automatic transmission can be an effective method to cool the motor end windings; however it has challenges because of the potential added complexity of the oil fluid circulation.

Table 4-4: Summary of FEA Results Incorporating Potting Encapsulate for End Windings.

	Operating Point	30 kW; 2,000 RPM	30 kW; 10,000 RPM
Original Design	Max Winding T [°C]	153	170
Design with Potting Compound	Max Winding T [°C]	125	152
	change*	30%	16%

*winding to coolant, coolant at 60°C

Case-Stator Thermal Contact Resistance

As highlighted in the thermal sensitivity study, the lamination thermal conductivity and the thermal contact resistance between the stator and the cooling jacket case were identified as critical parameters in the motor thermal management. During phase two NREL worked to set up an experiment to measure both the lamination thermal conductivity and the thermal contact resistance between an electric motor stator and case. The technique relies on imposing a one-dimensional heat flux across a sample of interest and using the temperature gradient across the part to determine the thermal resistance. A schematic of the setup and the actual hardware are shown in Figure 4-54.

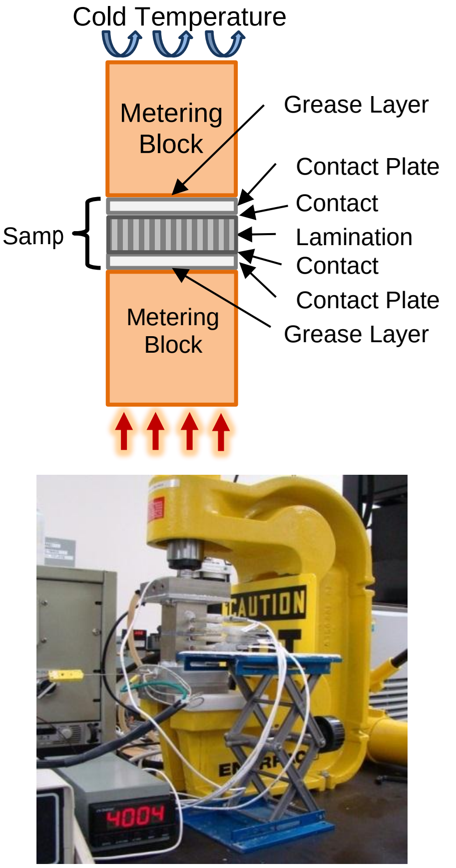

Figure 4-54: Schematic of ASTM setup (top) and test hardware (bottom).

By performing measurements with varying lamination heights the thermal resistance of the lamination stack can be separated from the contact resistance by curve fitting the data. During phase two sample material laminations were provided by UQM to NREL, and NREL has completed a preliminary set of tests designed to determine key factors affecting the measurements. The main set of experiments will be performed during phase three of the project.

In-Situ Thermal Testing

UQM will provide NREL with a motor stator to conduct in-situ thermal testing. The experiment will heat stator windings using a DC current to simulate winding losses. In addition, CFD and FEA models are being developed and will be validated against the experiment to improve thermal modeling for UQM's motor development efforts.

The test bench for the stator in-situ experimental setup is shown in Figure 4-55.The test bench repurposed existing equipment at NREL and improved the ability to thermally test electric motors cooled with water-ethylene glycol (WEG). The flow meters, piping, and flow control valves are installed behind the bench and are not visible in the figure. The developed WEG loop can work with NREL's existing automatic transmission fluid (ATF) thermal test bench to provide a combination of WEG and ATF thermal testing of electric motors. Both the WEG and ATF thermal test benches will be used to support future in-situ testing in support of UQM's motor research and development efforts.

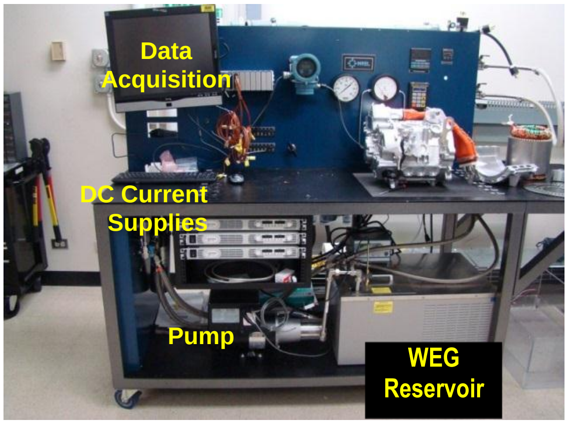

Figure 4-55: Motor stator thermal test bench.

Conclusion

During phase two NREL provided support in the analysis of motor thermal management in the context of UQM's motor development efforts. NREL's thermal analysis initially focused on thermal and fluid modeling, but during phase two the work transitioned to include a focus on experimental measurements to characterize important thermal parameters that can be used to improve future motor thermal modeling activities. The experimental work will continue into phase three of the project, and the results of the experimental work will be used to validate and improve the previously developed thermal and fluid models.

Conclusions and Future Directions

Based on the analysis and testing completed in the reporting period it was determined that the POC motor meets many of the DOE targets and will demonstrate compliance with the DOE targets in the next phase the program upon completion of the POD (proof of design motor) which will utilize improved magnet materials developed by AMES laboratories. A summary of the status for analysis and testing to DOE requirments follows:

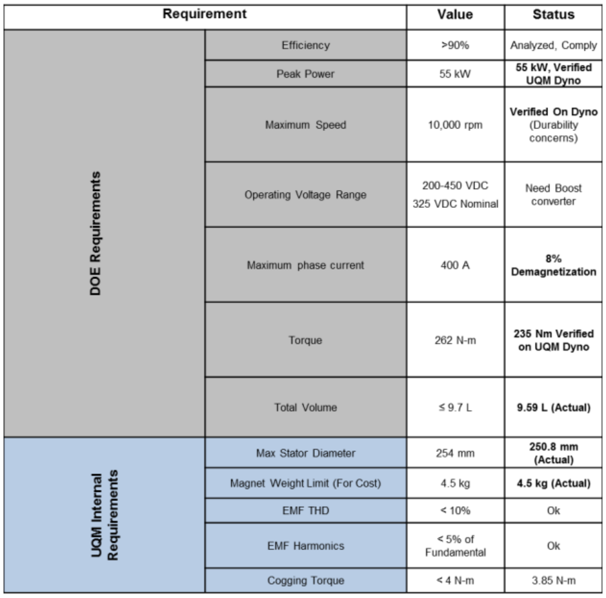

Requirement		Value	Status
DOE Requirements	Efficiency	>90%	Analyzed, Comply
	Peak Power	55 kW	**55 kW, Verified UQM Dyno**
	Maximum Speed	10,000 rpm	**Verified On Dyno** (Durability concerns)
	Operating Voltage Range	200-450 VDC 325 VDC Nominal	Need Boost converter
	Maximum phase current	400 A	**8% Demagnetization**
	Torque	262 N-m	**235 Nm Verified on UQM Dyno**
	Total Volume	≤ 9.7 L	**9.59 L (Actual)**
UQM Internal Requirements	Max Stator Diameter	254 mm	**250.8 mm (Actual)**
	Magnet Weight Limit (For Cost)	4.5 kg	**4.5 kg (Actual)**
	EMF THD	< 10%	Ok
	EMF Harmonics	< 5% of Fundamental	Ok
	Cogging Torque	< 4 N-m	3.85 N-m

The POC motors were constructed in FY14 and tested to confirm compliance with the above list specifications. Upon completion of in-housing testing a motor will be delivered to ORNL for independent testing and validation of performance.

Based on the successful demonstration and identified improvements from POC (Proof of Concept) analysis, design and testing a proof-of-design (POD) motor will be developed, built and tested in FY15.

FY 2013 Publications/Presentations

DOE Vehicle Technologies Office FY14 Kickoff Meeting (11/4–6/2013).

4.4 Permanent Magnet Development for Automotive Traction Motors:
Beyond Rare Earth Magnets (BREM)

Iver E. Anderson (Principal Investigator)

Ames Laboratory (USDOE)
Iowa State University
Ames, IA 50011
Phone: (515) 294-9791
E-mail: andersoni@ameslab.gov

Susan A. Rogers, Program Manager
Advanced Power Electronics and Electric Motors
Phone: (202) 586-8997
E-mail: *Susan.Rogers@ee.doe.gov*

Subcontractors:
Univ. Nebraska-Lincoln, ORNL, Univ. Maryland,
Arnold Magnetic Technologies, Inc.

Start Date: August 2001
Project End Date: September 2014

Objectives

- Develop the materials and processes needed to fabricate high performance permanent magnets (PM) that can be used for advanced traction drive motors with an internal PM rotor design.
  - Meet APEEM goals for enhanced performance at elevated temperature (180–200°C) and reduced cost.
- Anisotropic magnets should be developed to satisfy the need for magnets with maximum magnetic energy density and minimum content of valuable materials.
  - Improved magnet forming processes and mechanical properties also should be developed to further reduce motor manufacturing costs and extend lifetime in service.
- Market factors of rising RE demand, uncertain RE cost, and near total foreign control of RE supplies dictate that alternative non-RE magnets must be developed.
  - Magnet materials meeting the technical specifications are currently achieved using rare earth (RE) permanent magnets.

Technical Barriers

High energy density permanent magnets (PM) are needed for compact, high torque drive motors for HEV, PHEV, and EV. These drive motors should have reduced cost and be highly efficient, which requires PM of high energy density that are made in net shape (preferably) by simple mass production methods. Although PM made from RE elements are currently used in electric drive motors, the recent history of drastically rising prices of RE elements, a nearly singular source for RE supplies, the uncertain future RE prices, and a looming shortage of RE elements, especially Dy, provides motivation for research into alternative PM materials. Alternative permanent magnets must have high temperature tolerance and long life in harsh vehicle environments.

Technical Targets

- High energy density permanent magnets (PM) needed for compact, high torque drive motors (specific power >1.4kW/kg and power density >4.0Kw/L).
- Reduced cost (<$8/kW): Efficient (>94%) motors require aligned magnets with final-shape and simple mass production.
- Greatly reduce or eliminate RE elements, especially Dy.
- High temperature tolerance (150–200°C) and long life (15 yrs.) needed for magnets in PM motors.

Accomplishments

Results of preliminary cost analysis on SSHD method for consolidation of aligned magnetic microstructures from Zn (vapor) coated glassy MRE$_2$(Fe,Co)$_{14}$B flake indicated promise, but continuation dropped due to need for additional RE magnet alloy research effort or shared industrial development beyond project scope.

Initial characterization studies of commercial alnico indicated that the nano-phase assemblage (“mosaic tile”) and high magnetic phase (Fe-Co) anisotropy of alnico types 8 and 9, with highest coercivity, held most promise to pursue with advanced theoretical and experimental methods.

Confirmed by magnetic field strength variations in Lorentz microscopy mode in TEM that off-axis grains in alnico 8 had pinned submicron-sized domains around orthogonal regions of spinodal pattern, where comparisons with alnico 9 indicated that this feature may be a useful for enhanced coercivity.

Found that alnico 8 microstructures in bulk alnico magnet samples, either from pre-alloyed powder or from chill castings, could be successfully “reset” by a brief solution anneal and oil quenching, opening the processing window for development of low-cost powder processing methods for bulk magnets.

Demonstrated effective calorimetric method to identify preferred magnetic annealing temperature and produced improved magnetic properties over commercial levels in alnico 8.

First batch of newly designed low-Co (40% less Co) version of alnico 8 pre-alloyed powder was inert (Ar) gas atomized with high yield of fine, spherical powder (average powder dia.=32μm), close control (± 0.47wt.%) of final powder composition, and low oxygen content (190ppmw) in dia.<45μm powder to enable testing to begin.

The first net-shape alnico 8 bulk magnets were compression molded from previous pre-alloyed gas atomized powder in low-carbon binder and, after de-binding, were sintered to full density (1250°C) and magnetic annealed (840°C), in new processing developments.

Magnetic properties of molded magnets measured with new hysteresigraph showed that our best properties exceeded commercial sintered (unaligned) alnico 8HE, but the challenge remains to surpass energy products of aligned cast alnico 9 to gain benefit for advanced motors.

Discovered from microstructural analysis that abnormal grain growth during extended sintering (> 4h) of molded magnets resulted in partially aligned magnet microstructure with enhanced properties, indicating that control of grain growth is one processing path for improvement of remanence and energy product.

Identified by meso-scale analytical modeling another processing pathway for increased coercivity that involves development of methods that promote a significant decrease (about 3X) in the scale/spacing of the Fe-Co magnetic phase, which can more than double the coercivity, but this remains to be verified.

Simulated temperature dependence under equilibrium conditions of spinodal transformation of alnico 5-7 model system using improved Monte Carlo calculations with existing computer clusters and began exploration of composition gradients of alloy components at Fe-Co and NiAl phase interfaces.

Utilized theoretical predictions and combinatorial thin film synthesis results of stability range for hard magnetic phase of Co-Zr, along with prior knowledge of alloying with Mo, B, Si to synthesize desired single phase magnetic compound by melt spinning that showed significant permanent magnet properties with a coercivity of 9.6 kOe.

✧ ✧ ✧ ✧ ✧

Introduction

Understanding Phase Evolution in alnico

Permanent magnet alloys containing Al, Ni, Co (alnico) and Fe represent a class of functional nanostructured alloys that arise from spinodal decomposition. We show that the coercivity mechanism in alnico involves interplay of both size, chemistry and possibly stress at the interfaces, which is more complex than previously thought. The resulting phase separation is sensitive to chemistry and crystallographic orientation of the primary phase to an imposed magnetic field during decomposition. Atom probe tomography and advanced transmission electron microcopy techniques demonstrate that the morphology of the microstructure is strongly dependent on the Fe:Co content and the introduction of minor alloying elements, such as Cu and Ti. The saturation magnetization can be predicted by the Fe:Co in the magnetic bcc phase, the phase fraction of the bcc phase, and the degree of crystallographic alignment relative to the applied field during annealing. The theoretical energy density can rival best commercial Nd-based alloys above 200°C, but refining of the nanostructure to improve the coercivity will rely on understanding the delicate balance between the chemistry and the thermal history of the alloy.

Simulating Phase Selection and Ordering in alnico 5-7

Recent concerns about the supply and resource of rare earth (RE) metals strongly motivate the search for replacements for RE-based permanent magnets (PM). Alnico alloys has been considered as one of the promising candidates due to the abundance and low cost of constituting elements and the advantage of alnico PM at high temperature performance. It is believed that the coercivity of alnico can be improved much more from the current values. These improvements could be archived by optimizing the micro-scale morphology of alnico, i.e., size and phase spacing of the magnetic FeCo-rich rods to improve the shape anisotropy, and certainly the compositions of the decomposed phases, i.e., compositions FeCo-rich and NiAl-rich phases to improve the magnetization. In these regards, theoretical modeling and simulation can complement the experimental efforts in optimizing the structures of the material and accelerating the pace of technological advances in the development of high-performance alnico PMs. A comprehensive understanding of the atomistic and nano-scale structure of alnico also helps identify the atomistic origin of magnetic properties so that the composition of FeCo-rich phase can be optimized for PM performance. Such understanding at the atomistic and nano-scale also provides useful inputs into phase-field modeling to help mesoscale microstructure optimizations.

Improved Processing of Bulk alnico Magnet Shapes

From the findings thus far, the alnico 8 and 9 may have the most potential for improvement because of their starting advantage in coercivity, partially arising because alnico 8 and, especially, 9 have a very elongated Fe-Co phase shape anisotropy, thought to be the major coercivity source for alnico magnets. While anisotropic alnico 9 exhibits more uniformly extended α_1 rods, alnico 8 has a major processing advantage over 9, since it can be cast without directional mold cooling and, even, processed by a blended elemental/alloy powder metallurgy approach, producing isotropic magnets with equivalent (or higher) H_{ci}, albeit without the hysteresis loop squareness of aligned alnico 9. Therefore, experiments to test the apparent processing advantage for isotropic alnico 8 were performed, with an initial goal of improved coercivity. An alnico alloy was chosen close to the Arnold Magnetic Technology type 8 composition for production by gas atomization with parameters designed to produce a maximum yield of fine spherical powder with high purity with the intent of improved M_s by minimizing oxidation losses. Using this pre-alloyed alnico 8 powder, microstructure and magnetic properties of hot isostatically pressed (HIPed) alnico samples that were magnetic field annealed at different temperatures were analyzed in a recent study. Results indicated that the SD phase nano-metric morphology is very sensitive to the magnetic annealing (MA) temperature, where an optimum MA temperature selection can lead to increased coercivity that is accentuated by further "draw" annealing. Preliminary die pressing of near-final magnet shapes from the pre-alloyed alnico 8 powder were attempted in an effort to develop a processing method to mass produce bulk alnico magnets, but the as-solidified hardness of the powders prevented compressibility and further development. However, another widely practiced P/M forming process, compression molding, especially using a low residual contamination binder, appears to be a promising pathway to improved results.

Approach

Understanding Phase Evolution in alnico

Three commercial optimized alnico alloys, 5-7, 8, and 9, were supplied by Arnold Magnetic Technologies Corp (Table 4-5). Alnico 5-7 and 9 were directionally solidified with most of their grains aligned along the [001] direction, whereas alnico 8 was crystallographically isotropic. Each as-cast alloy cylinder was heat treated at ~1250°C to fully solutionize it and air-cooled to ~800°C. Starting from ~800°C, the alnico 5-7 and 9 cylinders were isothermally annealed with an applied magnetic field along their grain alignment direction or with the field applied along the cylinder axis for alnico 8, where all samples were cooled to room temperature. Depending on the type and grade, the alloys underwent extended (hours) 'draw' annealing cycles, holding at 650-580°C. The highest Fe content alnico 5-7 has highest B_r (13.5 KG), but lowest H_{ci} (740 Oe). The highest Co content alnico 8 has lowest B_r (8.2 KG) and highest H_{ci} (1860 Oe). Alnico 9 has the highest energy product of ~9-10 MGOe with a B_r (10.6 KG) and H_{ci} (1500 Oe), in between the other two alloys (Table 4-5).

Table 4-5: Commercial alnico alloy compositions.

	Composition in wt. %								
Alloy type	Fe	Co	Ni	Al	Cu	Nb	Ti	Br (kG)	Hci (Oe)
5-7	49.9	24.3	14.0	8.2	2.3	1.0	0.0	13.5	740
8	30.0	40.1	13.0	7.1	3.0	0.0	6.5	8.2	1860
9	35.5	35.4	13.1	7.0	3.2	0.5	5.0	10.6	1500

Transmission electron microscopy (TEM) analysis was performed on transverse (observation along the magnetic field direction during annealing) as well as longitudinal (observation perpendicular to the magnetic field direction during annealing) orientations. TEM samples with mm-long and micron wide electron transparent regions were prepared by mechanical wedge polishing followed by a short duration, low voltage Ar ion-milling in a liquid nitrogen cold stage. An FEI Titan G2 80-200 STEM with Cs probe corrector and ChemiSTEM ™ technology and an FEI Tecnai F20 (200kV, FEG) with Lorentz lens and biprism were used for microstructural characterization.

Atom probe tomography (APT) was performed with a LEAP 4000X HR in voltage-pulsed mode on samples prepared using a FEI Nova 200 dual beam focused ion beam (FIB) system. Samples were extracted from interior of grains (polished transverse sections) by standard lift-out technique to provide multiple interphase interfaces along the sample axis. Samples of the appropriate orientation were first located on the polished transverse sections using electron backscattered diffraction imaging, also known as orientation imaging microscopy (OIM), with an EDAX GENESIS system on an Amray 1845 field emission SEM. Two to three samples were characterized for each composition.

Simulating Phase Selection and Ordering in alnico 5-7

Alnico alloys consist of two alternating Fe-Co and NiAl-rich phases so that the phase boundary needs to be incorporated into the atomistic simulations at nano-scale. The supercell in these simulations should be very large containing thousands of or more atoms, making the first-principles total energy calculations not feasible for such studies. Empirical potential calculations can be very fast and scale well for large system size in parallel calculations, but the accuracy of empirical potential calculations is always questionable, particularly for multiple components systems such as alnico alloys. On the other hand, it is known from experiment that alnico alloys have a fixed underlying lattice of body-centered cubic (BCC). Giving a fixed underlying lattice and dealing only with the occupations of different chemical elements on the lattice sites, the cluster expansion (CE) method should be the most suitable energy model because of the following reasons: the energy of large system with thousands or more atoms can be calculated very fast and accurate and transferable CE coefficients can be obtained by fitting to energies of density functional theory (DFT) calculations for a selected set of small structures. With CE method for the energy model, it is very natural to use lattice Monte Carlo (MC) simulation to investigate the atomic structure of alnico alloys at nano-scale. MC simulations can determine the thermodynamic equilibrium atomic structure of a system under consideration at a given temperature.

Improved Processing of Bulk alnico Magnet Shapes

The Ames Lab experimental high-pressure gas atomizer (HPGA) was used to produce a pre-alloyed alnico 8 (prototype) powder composition of: 7.3Al-13.0Ni-38Co-32.3Fe-3.0Cu-6.4Ti (in wt.%). The elemental additions to the melting charge were all of high commercial purity (99.99%), with some of the additions pre-melted into master alloy buttons. The 4000g charge was melted, homogenized, and superheated to 1625°C before pouring and atomization with high purity Ar gas at 2.93 MPa (425 psi) of supply pressure.

Compression molding using a low residual trace element binder was developed as a method to produce a "green" compact in a near-final shape that can be extracted from a die and should be capable of sintering to a dense bulk magnet. The binder, QPAC 40® was selected as a commercially available polypropylene carbonate based product and was dissolved in acetone to form a solution that was blended with a bi-modal distribution of the pre-alloyed alnico powder, 90wt.% 32–38µm + 10wt.% 3–15µm. The polymer/powder compound was die-pressed at 1136 kgf to create "green bodies" of sufficient strength for removal from the cylindrical die (9.5mm dia.). Removal of volatile components was accomplished at a temperature of 300˚C to produce a "brown body" that could be handled for subsequent sintering. A vacuum (at 1 x 10^{-6}torr) sintering process with furnace cooling was utilized with a peak temperature of 1250˚C to promote diffusion and compact consolidation to a single B2 phase, approaching full density. A gettering material, either Ti or Zr, was employed in the sintering furnace to minimize possible contamination. Residual carbon impurity content of the sintered samples was measured by inert gas fusion with a LECO apparatus.

All as-sintered cylindrical samples were solutionized at 1250°C for 30min. in vacuum (1.3x10^{-4} Pa) and quenched into an oil bath. The samples were then magnetically annealed at 840°C for 10min., within an external applied field of 1T, followed by tempering at 650°C for 5h and 580°C for 15h to a "full heat treatment" (FHT) condition. The magnetic properties of the FHT samples (2.9mm dia. X 8mm length) were measured using a Walker Scientific AMH-1040 Hysteresigraph with a 12.7mm coil (using a non-magnetic concentric insert with an internal diameter of 3mm) and a maximum applied field of 10.0kOe at room temperature in a closed-loop setup. Since the final dimension of each sintered sample was about 9mm dia. X 10mm length, several smaller cylindrical samples (typically 3) were cut in a geometric pattern (without regard for microstructure) by electro-discharge machining (EDM) for obtaining duplicate hysteresigraph samples. Initial microstructural analysis of transverse sections of the as-sintered samples with a FE-SEM (from FEI, Quanta FEG 250 SEM) gave average grain size and a preliminary estimate of the spacing of the Fe-Co α_1 phase in some of the as-sintered samples. This FE-SEM was also fitted with electron backscattered diffraction (EBSD) mapping to provide an initial measurement of the principal axis of individual grain orientations on the transverse cross-section surface, specifically of the 8h-sintered sample.

Results

Understanding Phase Evolution in alnico

TEM provided a broader spatial dimension to the APT data, complimenting the detailed chemical analysis. High-angle-annular-dark-field (HAADF) scanning transmission electron microscopy (STEM) imaging, which emphasizes regions of high atomic number with brighter contrast because of greater electron scattering to large detector collection angles, clearly differentiated phase morphology in alnico alloys. A series of images along the transverse and longitudinal directions for the three alloys, clearly shows the morphological changes with alloy type. The 5-7 alloy shows a 'brick and mortar-like' structure when observed along the transverse direction, i.e., looking along the applied field direction (Figure 4-56a). The α_1 phase is slightly brighter due to its higher average atomic number. The dark "mortar" in between is the α_2 phase. The α_1 phase is in fact irregular elongated blocks when observed along longitudinal direction. The elongation was formed during annealing below the spinodal separation temperature, as a result of growth bias by the applied magnetic field (Figure 4-56b). The edges of the α_1 bricks are rounded. The somewhat more rectangular regions in Figure 4-56a most likely arise from regions that are branching as observed in the transverse micrographs (Figure 4-56b). The connectivity observed in the atom probe maps for the α_1 phase is also a reflection of this branching. The α_1 phase is ~40–60 nm in its narrower dimension and 100-300 nm in length, whereas the α_2 phase has a thickness between ~5–15 nm. The relationship of the morphology of the α_1 phase is represented schematically in Figure 4-56c.

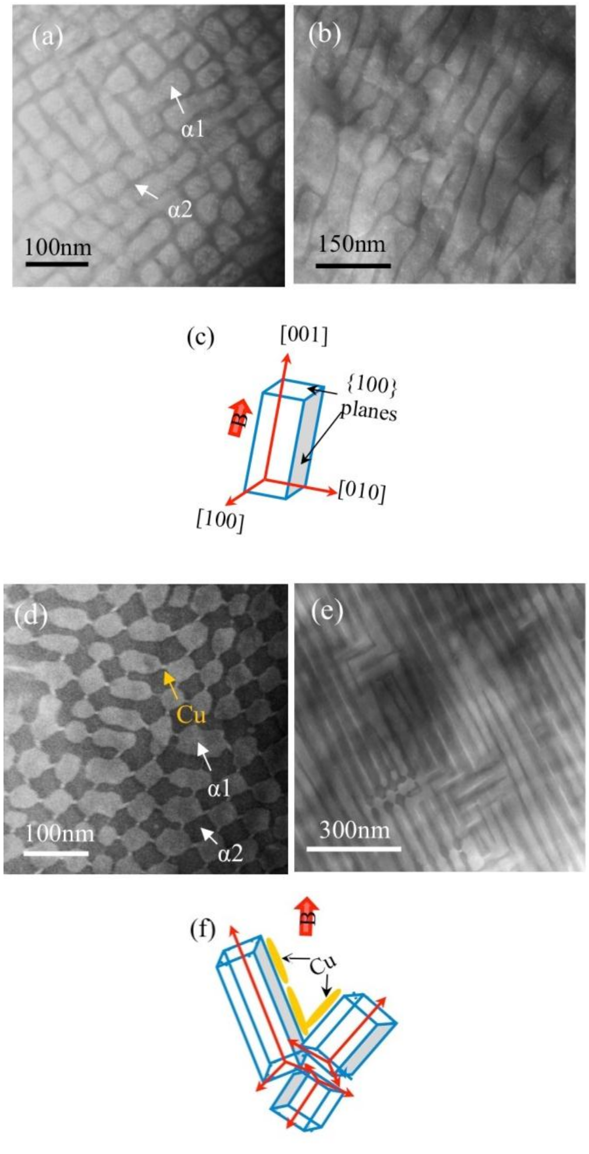

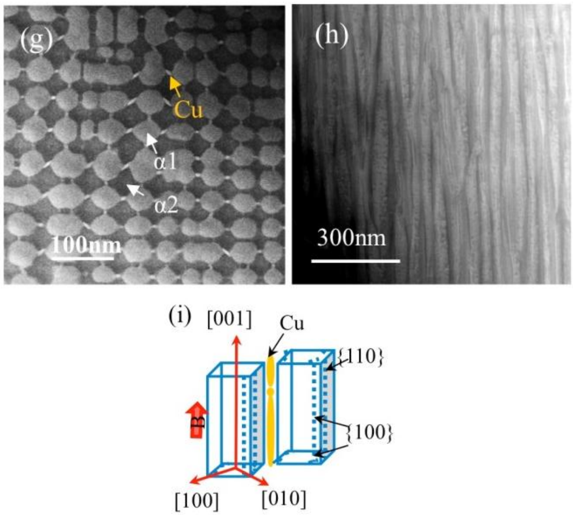

Figure 4-56: HAADF STEM images and schematic of α1 phase morphology of different alnico alloys. (a) alnico 5-7, transverse; (b) alnico 5-7, longitudinal; (c) model of α_1 phase in alnico 5-7; (d) alnico 8, transverse; (e) alnico 8, longitudinal; (f) model of α_1 phase in alnico 8; (g) alnico 9, transverse; (h) alnico 9, longitudinal; (i) model of α_1 phase in alnico 9.

A dramatic change in both morphology of the transverse section and the aspect ratio of the α_1 phase is observed in the 8 and 9 alloys (Figure 4-56d-Figure 4-56i). HAADF STEM image of alnico 8 along transverse direction shows a nanometer scale 'mosaic' structure of nearly similar sized 'tiles' ~ 35 nm across which are linked with the Cu-rich rods. The large bright tiles are the α_1 phase which tend to faceted on their {110} planes and less commonly on {100} planes. In comparison, the alnico 5-7 alloys show almost exclusively [100] facets. Cu-enriched rods (small bright dot, ~3-5 nm in diameter) are observed at the corner of two {110} α_1 phase facets and in α_2 phase. The lack of uniformity of the nanostructuring of the spinodal between grains is quite stark in the alnico 8 alloy along longitudinal direction and is clearly tied to the mismatch between grain's <100> crystallographic axis and the applied field direction during spinodal decomposition. Since there are three possible variants of the [100] in a cubic system, the degree to which one of the three <100> types will be elongated by the applied field is proportional to its correspondence to the applied magnetic field. This is demonstrated in Figure 4-56(e) where the α_1 phase is elongated in two orthogonal <100> which are bisected by the applied field (see schematic in Figure 4-56(e)). Detailed analysis on effect of orientation between grain and applied magnetic field during annealing on SD phase morphology showed that the length of α_1 phase depends on magnitude of the projected applied magnetic field on <100> directions. Given that the grains in alnico 8 are randomly oriented, the α_1 rods inside any given grain have a wide range a length from ~40nm to microns. Similar 'mosaic' transverse SD morphology as in alnico 8 was observed in alnico 9, as shown in Figure 4-56g. In both the 8 and 9 alloys, the α_1 rods were faceted on {100} and {110} planes. Observation of alnico 9 along longitudinal direction (Figure 4-56(h)) showed that in contrast to the alnico 5-7, the α_1 precipitate are very long (>400nm) and tend to have few orthogonal variants. They generally have a tapered ends with an aspect ratio >10. Branching was also commonly observed in the α_1 rods. The major difference between the 8 and 9 alloys is the uniformity of the mosaic nanostructure in the transverse orientation and its corresponding highly elongated grains along the longitudinal direction in alnico 9 (Figure 4-56d through Figure 4-56i).

Understanding the relationship between the SD phase morphology and micro-magnetic domain structure is necessary in order to optimize properties of alnico alloys by controlling its chemistry and processing. Of particular importance is determining what nanoscale features are giving rise to high coercivity and secondarily a quantitative measure of the remnant field in the magnetically active phase. Lorentz microscopy is a widely used TEM technique for direct observation of magnetic domain structure with high spatial resolution. Domains are revealed as a result of deflection of electron beam by magnetic field inside the TEM sample. Electron holography is a unique nanoscale phase-imaging TEM technique for electrostatic and magnetic fields' information. Quantitative field measurement can be achieved by related to the relative phase shift of the electron wave that has passed through the TEM sample with that has passed through the vacuum. In-plane magnetic induction map of the material can be extracted. Since the high coercivity in alnico alloys was believed due to the magnetic shape anisotropy of elongated α_1 particles, observation of micro-magnetic domain structure was only performed along longitudinal direction to minimize the possibility of cutting off part of the α_1 rods in thin TEM sample region (thickness <150 nm). Micro-magnetic domain structures inside alnico alloys were revealed by combination of Lorentz microscopy and off-axis holography.

Lorentz image of alnico 5-7 (Figure 4-57a) revealed domain walls as black and white line. Stripe shape domains with width between ~100-500 nm, and length >1 µm were observed. Color induction map obtained by mapping the phase gradient of a hologram of alnico 5-7 is shown in Figure 4-57b. The hologram was taken under field-free condition in Lorentz mode. The inset is a color wheel indicates in-plane induction direction as a function of hue. The green and magenta stripes are α_1 rods. The green rods indicates in-plane magnetic induction inside are along 7 o'clock direction, while magenta rods has their in-plane magnetic induction pointing towards 2 o'clock direction. It is obvious that the α_1 rods are single domains. Several of the α_1 rods couple with each other and form 180° micro magnetic domains with a size ~100-500 nm. The domain size and morphology in alnico 8 are determined by spinodal phase morphology, which is related to the relative crystallographic orientation of each grain to the applied external magnetic field direction. Lorentz image of a grain in alnico 8 (Figure 4-57c) shows block shape micro-magnetic domain structure. In-plane magnetic induction map of similar grains (Figure 4-57d) indicates that several parallel single domain α_1 rods coupled and formed 180º micro-magnetic domains, whereas, the orthogonal α_1 rods formed 90º micro-magnetic domains. Lorentz image of Alnico 9 taken from a grain with its [001] direction aligned very well with the applied external magnetic field direction (Figure 4-57e) showed stripe shape domains as wide as ~1 µm, and microns long. In-plane magnetic induction map of similar grains (Figure 4-57f) revealed that several α_1 rods coupled and formed 180º micro-magnetic domains.

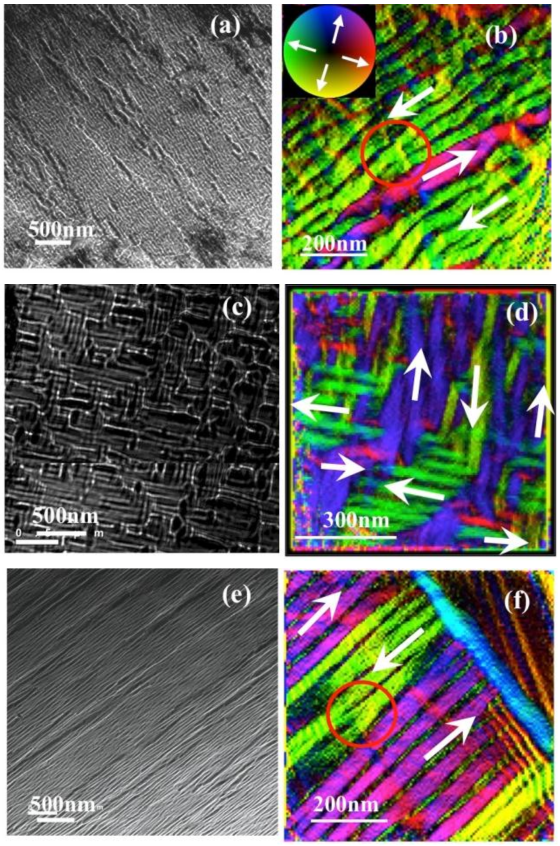

Figure 4-57: Lorentz images of alnico 5-7 (a), 8(c) and 9(e) along longitudinal direction. Color induction maps from holographic phase images of micro-magnetic domain morphology of alnico 5-7 (b), alnico 8 (d) and alnico 9(f) respectively. The in-plane magnetic induction direction in each alloy is indicated by white arrows. Interaction domains are indicated by red circles.

Simulating Phase Selection and Ordering in alnico 5-7

1. Cluster Expansion Model for alnico 5-7 Alloys

We fitted the CE coefficients for BCC Al-Ni-Co-Fe system up to 3rd nearest neighbor (NN) pair and triplet clusters and smallest tetrahedron clusters by ATAT code. In Figure 4-58 the formation energies of the reference structures used in the CE coefficients fitting obtained from the CE model are compared with those from DFT calculations. The DFT energies of reference structures were well reproduced by CE calculations with a small mean error of 9.7 meV/atom and a good cross-validation score of 13.6 meV/atom which is about half of the thermal energy at room temperature.

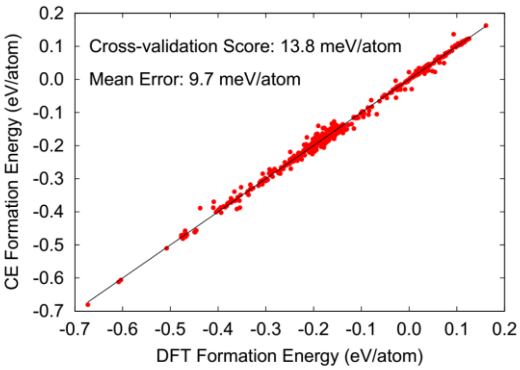

Figure 4-58: CE formation energies versus DFT formation energies of reference structures used in CE coefficients fitting.

In order to further validate the CE energy model for describing the phase selection and phase decomposition process in complex alloys, we performed MC simulations for a known BCC ternary: $AlNiFe_2$. The composition histograms of $AlNiFe_2$ ternary at different temperatures from our MC simulations are shown in Figure 4-59. We show that the ternary is in a B2 (AlFe, NiFe) single phase at high temperature and is decomposed into BCC Fe-rich and B2 NiAl-rich phases at low temperature. The results from the MC simulations are consistent with experimental observations except that the transition temperature from two phases to single phase is overeastimated in the simulations. This transition temperature offset can be corrected by calibrating with the experimental temperatures.

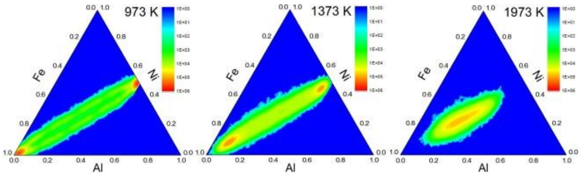

Figure 4-59: Composition histograms of $AlNiFe_2$ system at various temperatures.

2. Monte Carlo Simulation of alnico 5-7 alloys

a. Temperature dependent composition profiles

We used the overall experimental composition of alnico 5-7 in our simulations. The numbers of Al, Ni, Co and Fe atoms are 979, 749, 1267 and 2765, corresponding to an overall composition $Al_{0.17}Ni_{0.13}Co_{0.22}Fe_{0.48}$. We performed MC simulations for a wide range of temperature from 773 K to 2173 K starting with several different initial configurations for each temperature. At high temperature (1873 K), the composition histogram of each element shows only one symmetric peak at the corresponding overall compositions, which are 17%, 13%, 22% and 48% for Al, Ni, Co and Fe, respectively, indicating that the master alloy is homogenized at this temperature. When the temperature is decreased from 1873 K to ~ 1473 K, the peaks' shapes are changed from symmetric to more and more asymmetric and seem to have shoulders as well, except for the peak in the composition histogram of Co. Continue decreasing temperature to below

1373 K, all composition histogram peaks are separated into two distinct peaks (see Figure 4-60(c) and Figure 4-60(d)), showing that the master alloy has undergone phase decomposition from single phase into two phases. The positions of the peaks in the composition histogram determine the composition of each element in these two phases. The asymmetries and shoulders of Al, Ni, Fe composition histogram peaks in the temperature between ~1473 and 1873 K could be attributed to the strong local composition fluctuations in this phase transition temperature range. By analyzing the composition of each element in the two separated phases we found that the two phases are FeCo-rich and NiAl-rich phases. The decomposition of a homogenized master alloy into FeCo-rich and NiAl-rich phases upon lowering temperature obtained from our MC simulation is consistent with experiment.

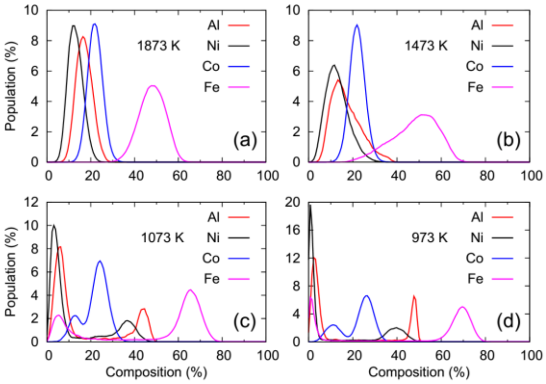

Figure 4-60: Composition histogram of alnico 5-7 from Monte Carlo simulation at different temperatures.

The details of composition changes in alnico as the function of temperature are summarized in Figure 4-61. We can see that as the temperature gets lower, the compositions of main constituents in the two decomposed Fe-Co and NiAl phases become higher. At the lowest temperature (773 K) in our simulations, the percentage of Fe in NiAl-rich phase and Ni or Al in Fe-Co-rich phase is already very small (less than 2%). These results suggest that Fe or Ni and Al could be extracted almost completely out of the NiAl-rich or Fe-Co-rich phase as the annealing temperature is lowered. In contrast, the concentration of Co in NiAl-rich phase remains at a quite high concentration of ~ 9% at 773K, indicating that Co is not easy to be extracted out completely from NiAl-rich phase just by lowering the annealing temperature. Because Co metal is much more expensive than other elements (Al, Ni and Fe) in alnico PM, there have been efforts to reduce the concentration of Co in NiAl-rich phase to reduce the price of alnico PM. The information we got here would be valuable to experiment that changing the annealing temperature and time could not help reduce the Co concentration in the NiAl-rich phase significantly below a saturated value, i.e., alloy substitution for Co is needed.

The compositions between 973 and 1273 K obtained from our MC simulation are quite close to those of the commercial alnico 5-7, especially, for the FeCo-rich phase. For NiAl-rich phase, the Ni and Al composition obtained from MC simulation is a little higher (~ 5% and 10% higher) and accordingly the composition of Fe and Co is lower than those of the commercial alnico 5-7. These composition differences could be traced back to the micro-scale difference in morphology of the commercial alnico 5-7 and our simulation model. The commercial alnico 5-7 is a quasi-2D system with “brick-and-mortar” micro-scale pattern while our simulation model is a quasi-1D system. The 2D system should have higher volume ratio of NiAl-rich “mortar” so that the compositions of Ni and Al should be lower. So a small difference in compositions between simulation and experiment results is expected because the overall composition in our MC simulations is the same as that in commercial alnico 5-7.

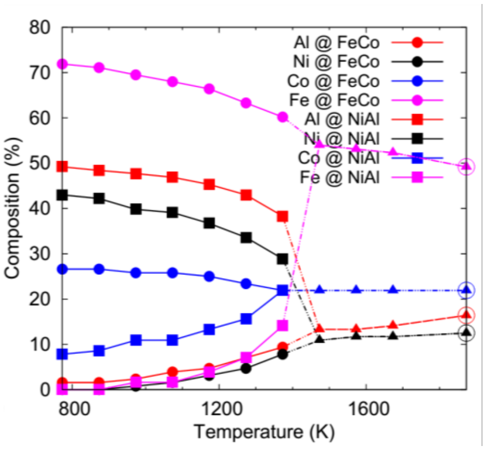

Figure 4-61: Compositions of FeCo-rich and NiAl-rich phases as function of temperature.

b. Ordering of Phases

Another interesting question for alnico systems is that what is the ordering of 4 chemical elements in the FeCo-rich and NiAl-rich phases. Experimentally, the ordering in NiAl-rich phase can be determined by X-ray scattering experiment due to the substantial difference in the scattering factors of Al and transition metals. However, Fe and Co are almost indistinguishable in X-ray scattering, making determination of ordering in Fe-Co-rich phase extremely difficult. Therefore, the ordering of Fe-Co-rich phase is still an open question. To investigate the orderings of NiAl-rich and Fe-Co-rich phases, we calculate the neighbor correlation matrices for these two phases at temperature from 773 to 1273 K (see Figure 4-62).

For NiAl-rich phase at low temperature, e.g., 872 K, there are almost no Al-Al, Al-Fe, Ni-Ni and Ni-Co NNs and there is a small fraction (5%) of Ni-Ni NN among the NNs of Ni, indicating that the NiAl-rich phase is in B2 ordering with Al and Fe on the α-site and Ni and Co on the β-site. In Fe-Co-rich phase there are no Al-Al NNs and there are small numbers of Al-Fe, Ni-Ni, Co-Co and Ni-Co NNs, indicating that the Fe-Co-rich phase is also in B2 ordering with the degree of order smaller than that of B2 NiAl-rich phase. For higher temperature, the above mentioned small fractions of Al-Al, Al-Fe, Ni-Ni, Co-Co, Ni-Co NNs are increasing but still smaller than those obtained from a totally random alloy, showing that there is tendency toward ordering in B2 structure for both NiAl-rich and FeCo-rich phases in the temperature range considered here.

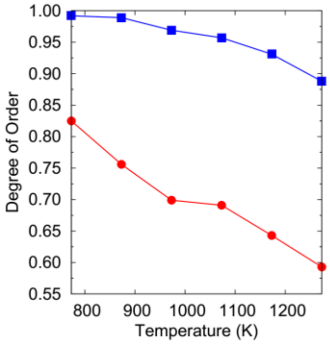

Figure 4-62: Degree of order of NiAl-rich and Fe-Co-rich phases versus temperature.

The degree of B2 order in these 2 phases can be estimated using the Bragg and William's model. The calculated results are shown in Figure 4-62. The degree of order of NiAl-rich phase is very high, almost 1.0 at 773 K and ~ 0.89 at 1273 K, confirming that NiAl-rich phase is indeed in a B2 ordering as observed in experiment. The Fe-Co-rich phase is also in a B2 ordering but the degree of order is smaller and decreases with rising temperature faster than that of NiAl-rich phase. Increase in temperature is expected to generate more anti-site defects, hence decrease the degrees of order in both phases. Recent experiment with latest advanced atomic-scale EDS mapping techniques showed that the Fe-Co-rich phase of commercial alnico 9 is in B2 ordering with the degree of order about 0.5. Our MC simulations suggest that the Fe-Co-rich phase in alnico 5-7 is also in a B2 ordering.

c. Phase boundaries

In Figure 4-63 we show the composition profile of alnico 5-7 at 873 and 1073 K along the long direction (z-direction) of supercell. The compositions of Al, Ni, Co and Fe at a given z-value were calculated as the average compositions over x- and y-directions. We can see clearly the phase separation of alnico 5-7 into FeCo-rich and NiAl-rich phases (right and left parts in each plot) along the z-direction. And for a wide range of temperature from 773 to 1273 K (not all shown in Figure 4-63), the boundaries between NiAl-rich and Fe-Co-rich phases are quite sharp with boundary width about 2 nm, which is about 8 times the BCC lattice constant. This result is consistent with experiment STEM EDS line scan results showing a sharp phase boundary of alnico 5-7.

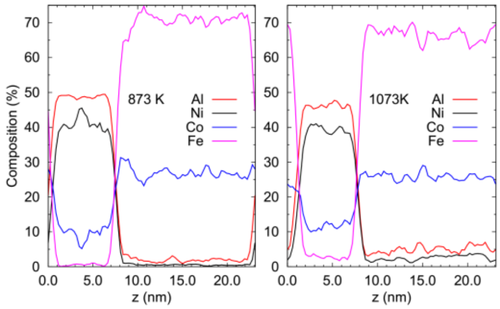

Figure 4-63: Composition profile along the decomposition direction of alnico 5-7 annealed at 873 K and 1073 K.

d. Magnetic Properties of Separated Phases

Finally, we investigated the magnetic properties of NiAl-rich and Fe-Co-rich phases. We used the site occupations obtained from degree of order calculations discussed above for the magnetic properties calculations within coherent-potential approximation (CPA) by SPRKKR code. The magnetic moments per B2 unit cell of NiAl-rich and Fe-Co-rich phases are shown in Figure 4-64. The magnetic moment of the magnetic phase (FeCo-rich) is decreasing with temperature, while that of NiAl-phase is increasing with temperature. These variations of the magnetic moments come mainly from the variations with temperature of Fe and Co compositions in Fe-Co-rich and NiAl-rich phases. The magnetic moment of Fe (or Co) is almost constant at **~** 2.58 (~ 1.76), ~ 2.37 (~ 1.65), or ~ 2.82 (~1.58) μ_B for each Fe (or Co) atom on the α-site, the β-site of Fe-Co-rich phase or the α (or β)-site of NiAl-rich phase in the temperature range considered here, except for very low temperature (773 K). At 773 K, there is almost no Fe in NiAl-rich phase and there are very dispersed Co atoms on the Ni-site of B2 NiAl-rich phase so that the Co is not spin-polarized, making the NiAl-rich phase non-magnetic. At 873 K, there is almost no Fe in the NiAl-rich phase as well. However, there are Co atoms on both Al-site and Ni-site of B2 NiAl-rich phase due to thermal induced anti-site defects, therefore the Co atoms are spin-polarized. The magnetic moment of Fe (or Co) on β (or α)-site (anti-site defect) of NiAl-rich phase varies stronger but the concentration of Fe (Co) on this anti-site defect site is small in NiAl-rich phase. The results in Figure 4-64 suggest that annealing alnico alloys at lower temperature could lower the concentration of Fe and Co in the NiAl-rich phase and enhance the degree of order in NiAl-phase so that magnetism of the NiAl-rich phase can be depressed. Because the coercivity of alnico PM comes from the shape anisotropy of Fe-Co-rich rods separated by NiAl-rich phase, the non-magnetism of NiAl-rich phase is crucial for high magnetic performance of alnico PM.

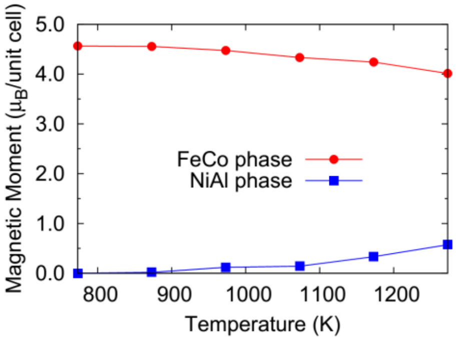

Figure 4-64: Magnetic moment of NiAl-rich and Fe-Co-rich phases at different annealing temperature.

Improved Processing of Bulk alnico Magnet Shapes

The micrograph in Figure 4-65 shows the resulting pre-alloyed alnico HPGA powder that had a very spherical shape and a low content of satellite particles, promoting excellent flowability and maximum loading in a polymer binder for compression molding.

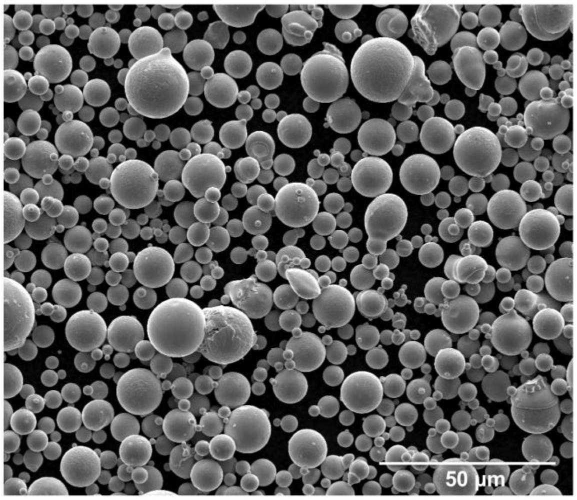

Figure 4-65: SEM micrograph of gas atomized pre-alloyed alnico 8 powder sieved to yield powders of dia. < 20µm.

A major benefit of the close-coupled HPGA method is the high yield of fine powder (dia. < 45µm) that results, which has enhanced sintering kinetics. Size distribution analysis by laser diffraction and by sieve analysis agreed that the average particle diameter (APD) for this batch was 30µm. Powder composition was measured with ICP-AES by an outside laboratory (NSL, Cleveland, Ohio) and the results showed an almost perfect correspondence between the nominal ("aim") composition and the resulting powder:

Aim: 32.3Fe-38.0Co-13.0Ni-7.3Al-6.4Ti-3.0Cu (wt.%) ≈ "8"

Result: 32.4Fe-38.1Co-12.9Ni-7.3Al-6.4Ti-3.0Cu (powder)

Compression molding was proven effective in creating magnets with near-final shape geometries. The rate of the de-binding process was found to be critical to the quality of the finished product. Heating too fast created a compact with non-uniform shrinkage and a lower final sintered density, so a debinding curve was developed that yielded brown bodies of sufficient handling strength, without excessive porosity. A suitable sintering cycle was developed subsequently that yielded bulk magnet shapes approaching ideal density. The preferred sintering cycle involved three isothermal hold temperatures at 250°C, 600°C and 1250°C, the peak sintering temperature, with a relatively slow cooling rate of 5ºC/minute to ambient. Sintering under these parameters yielded magnets close to 100% density, where the final density was a function of the holding time at 1250˚C (see Figure 4-66). The density was measured using Archimedes technique and validated qualitatively with SEM. An example of the final cylindrical shape of these samples is shown in Figure 4-67.

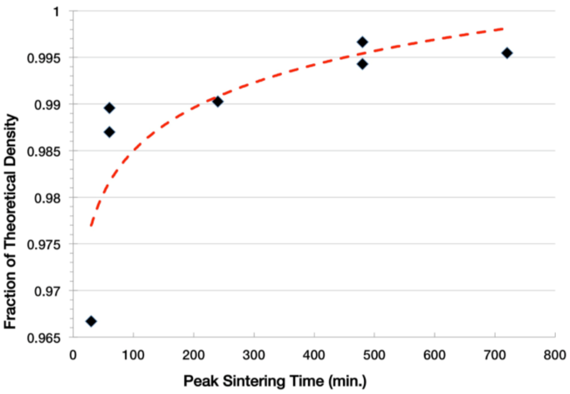

Figure 4-66: Summary of the densification curve for 1250˚C sintering of compression molded bi-modal powder of gas atomized pre-alloyed alnico 8.

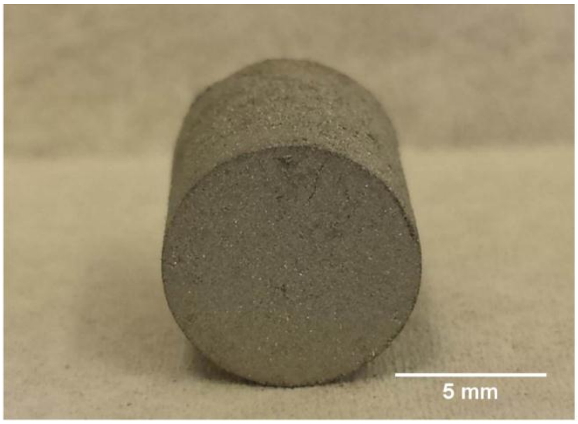

Figure 4-67: Fully de-bound and sintered bulk magnet sample produced by compression molding.

The modest cooling rate from the peak sintering temperature permitted formation (verified by X-ray diffraction and SEM) of the deleterious γ-FCC phase (5-7vol.%), as expected, during cooling of the sintered samples through its phase stability region, roughly 1100-700°C. Fortunately, a subsequent solution heat treatment at 1250°C for about 30 minutes, followed by an oil quench, was found effective for eliminating γ-FCC phase, producing essentially single-phase α-B2. The quench effectiveness at avoiding γ-FCC phase is helped by the low carbon content (100–200 ppmw) of the samples, since industry guidelines recommend <300ppmw of carbon to avoid stabilizing γ-FCC phase. This low carbon pick-up (base powder averaged 78ppmw C) was enabled by a polymer binder that was formulated to avoid residual carbon and by use of a getter to absorb contamination from the sintering atmosphere.

Grain size was one of the most interesting microstructural features in the as-sintered samples with less than 1% porosity, i.e., those sintered for 4h or longer at 1250°C. Since this sintering temperature is about $0.95T_m$ (absolute melting temperature), it is not surprising that the high diffusional mobility triggers abnormal grain growth at some time between 4 and 8 hours. This transition in grain size stability can be seen at the same magnification in Figure 4-68a and Figure 4-68b, where the approximate starting grain size (27µm for 4h sintered) grows only slightly (37 µm average) in a small (25–40%) vol.% of the 8h sintered microstructure, but the remaining 60–75 vol.% grew to an average of about 1mm. Preliminary density measurements on a 12h sintered sample were obtained recently, as shown in Figure 4-66, indicating that a maximum density of about 0.995 is possible with this sintering treatment. Microstructural and magnetic measurements will be reported on the 12h sintered sample when comprehensive results are available.

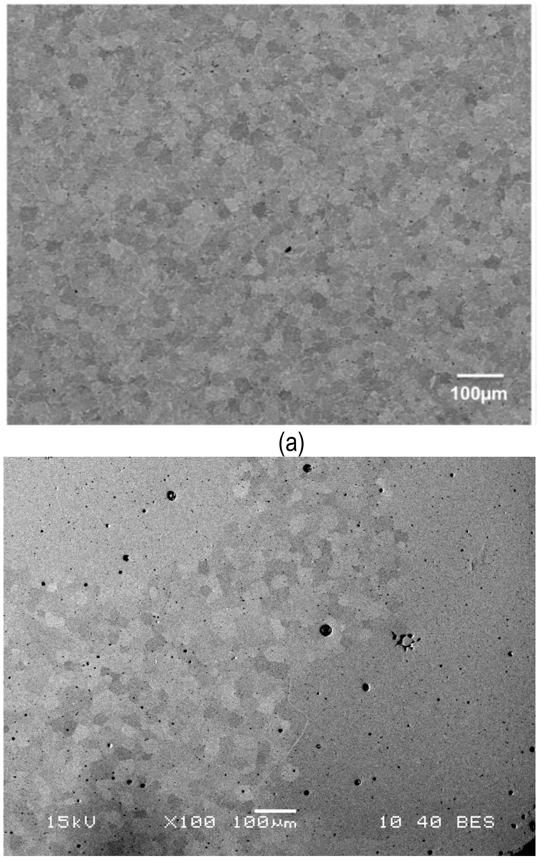

(a)

(b)

Figure 4-68: Representative SEM micrographs of the polished (un-etched) cross-sections of bulk pieces of alnico 8 alloy sintered at 1250˚C for a) 4h and b) 8h.

A large part of the interest in the effects of the sintering time that promoted pronounced grain growth after 8h sintering was motivated by analysis of the hysteresisgraph measurements that were made on the 3 sintered samples, thus far. As given in Figure 4-69, the second quadrant portions of the full hysteresis loops clearly show a remarkable difference in the 4h and the 8h sintered samples, in terms of the B_r, in particular. While the 1h and 4h sintered samples are nearly identical in their hysteresis loops and magnetic properties (see Figure 4-69 and Table 4-6), they also show average grain size values of 25µm and 27µm, respectively, from SEM observations. However, it appears that the grain growth between the 4h and 8h samples (seen in Figure 4-68) influenced the significant rise in B_r (and M_s, not shown), without much, if any, change in the coercivity.

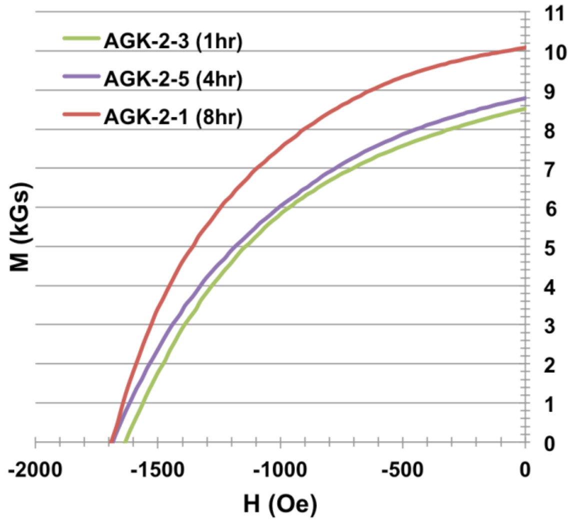

Figure 4-69: Summary of hysteresisgraph measurements, showing the results for quadrant 2 for samples sintered at 1250˚C for 1h, 4h, and 8h.

Table 4-6: Results of Hysteresisgraph Testing on Sintered Alnico 8 from Pre-alloyed Powder.

Sample	Br (G)	Hc (Oe)	Hci (Oe)	(BH)max (MGOe)	Hk (Oe)	Hk/Hci
AGK-2-3 (1h)	8,523	1,521	1,632	4.87	459	0.28
AGK-2-5 (4h)	8,789	1,569	1,685	5.04	483	0.29
AGK-2-1 (8h)	10,052	1,608	1,688	6.5	601	0.36

Thus, a polished section of the 8h sintered hysteresigraph sample was examined by EBSD mapping to observe any unusual grain orientation effects, since no attempt at grain alignment was made. Interestingly, the EBSD results (in Figure 4-70) show that large grains shared (111) or near-(111) orientation and were about 50% of the apparent volume of this sample, consistent with the measured B_r gain. In addition to the typical magnetic properties that are shown in Table 4-6, the ratio of H_k and H_{ci} (loop "square-ness") is interesting to note for these results. It is obvious that the hysteresis loop for the 8h sintered sample has a 24% gain in square-ness over the 4h sintered sample, consistent with improved alignment of a similar type of alnico microstructure, e.g., alnico 9.

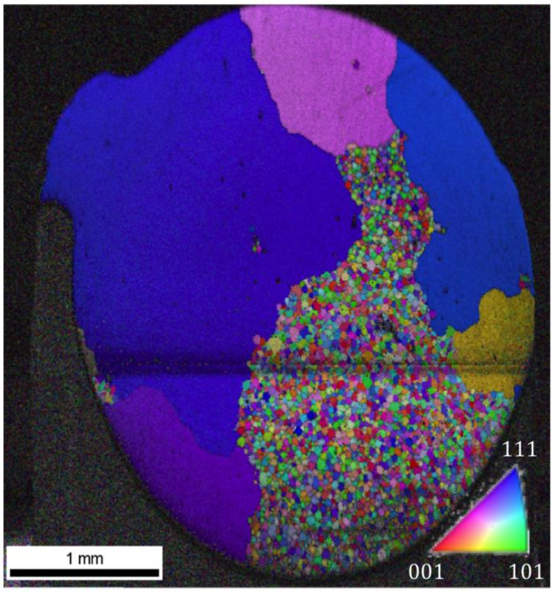

Figure 4-70: EBSD analysis of the full (transverse) cross-section of the 8h sintered hysteresigraph sample that is shown at higher magnification in Figure 4-59b.

While the 8h sintered sample does achieve a 29% increase in the energy product from this improved loop square-ness, the prime objective of the work, an increased coercivity, was not significantly enhanced. However, vacuum sintering (for at least 4h) of compression molded alnico pre-alloyed powder generated an excellent starting condition for additional magnetic annealing and draw annealing experiments, as well as more thermal-mechanical processing studies, to achieve extensive anisotropic grain growth. With these studies, a good potential exists for improving the nano-structure of the SD product phases in these sintered samples to improve coercivity, along with further improvement of the remanence. For use of these magnets in drive motors, the magnetic benefits of crystalline alignment from large grains should be balanced with the need for improved mechanical properties, especially fracture toughness, which is promoted by finer grains and/or a widely spaced distribution of spherical pores. Overall, the ability to produce as-sintered samples by compression molding with less than 1% porosity seems to satisfy a concern about the manufacturability of bulk alnico magnet alloys in near-final shapes and much further improvement in the magnetic properties should be possible with more work.

Conclusions and Future Directions

Understanding Phase Evolution in alnico

Three representative commercial grade alnico alloys with nanostructured SD phases were characterized by advanced techniques, including APT and TEMs, down to atomic scale. Comparison between alnico 5-7, 8 and 9 showed that the SD phase is very sensitive to alloys chemistry and processing condition. The SD phase has a "brick and mortar" structure in 5-7 and a "mosaic structure" in alnico 8 and 9. The α_1 phase is faceted on {100} planes in alnico 5-7, but on {110} and {100} planes in alnico 8 and 9. Addition of Ti transferred the α_2 phase from B_2 ordered structure in alnico 5-7 into $L2_1$ structure in alnico 8 and 9. Cu was pushed out of the α_2 phase and sit at corner of two <110> facets of the α_1 phase in alnico 8 and 9. The saturation magnetization can be predicted by the α_1 phase volume ratio, but prediction of coercivity is more complex, which may attribute to the large α_1 rods diameter and interaction domains. Reducing the spatial dimension of the domains appears to be the most promising route to increasing the coercivity in alnico.

Simulating Phase Selection and Ordering in alnico 5-7

In conclusion, we have developed an accurate and efficient energy model based on cluster expansion method for alnico 5-7 alloys and performed MC simulations to study the structures of alnico 5-7 at atomistic and nano scale as the function of temperature. The cluster expansion energy model describes well the phase selection and phase ordering in complex alloys containing three and four of Fe, Co, Ni, and Al elements. To our knowledge, cluster expansion model has never been developed for quaternary or more components alloys. By the MC simulations using the cluster expansion energy model, we observe phase decomposition of alnico 5-7 master alloy into FeCo-rich and NiAl-rich phases at low temperature. The phase boundary between these two phases is very sharp for a wide range of temperature. Both the NiAl-rich and the FeCo-rich phase are in B2 ordering with Al and Fe on the α-site and Ni and Co on the β-site, but the degree of order of NiAl-rich phase is much higher than that of Fe-Co-rich phase. The degrees of order in both the Fe-Co-rich and the NiAl-rich phases are reduced as the temperature gets higher due to the increase of anti-site defects. We also found that Fe in the NiAl-rich phase or Ni and Al in the Fe-Co-rich phases can be extracted almost completely at low temperature, but the concentration of Co in the NiAl-rich phase remains at a high level even at low annealing temperature. The magnetic moment of NiAl-rich phase approaches zero as the annealing temperature decreases, suggesting that the magnetic performance of alnico 5-7 could be improved by lowering the annealing temperature to diminish the magnetism of NiAl-rich phase. The results of our MC simulations are consistent with available experimental data.

Improved Processing of Bulk alnico Magnet Shapes

This study showed that alnico bulk magnets in near-final shape can be made by simple compression molding from spherical high purity gas atomized pre-alloyed powder. Dwell time at peak sintering temperature greatly affected grain size of the resulting magnet alloys, where the resulting (uncontrolled) anisotropic grain growth was demonstrated to be useful for gaining partially aligned magnetic properties and boosting energy product. While a route to increased coercivity was not identified by these experiments, manufacturability of bulk alnico magnet alloys in near-final shapes was demonstrated, permitting further processing and alloy modification experiments that can target higher coercivity and remanence.

FY 2014 Publications/Presentations

1. L. Zhou, M. K. Miller, P. Lu, L. Q. Ke, R. Skomski, H. Dillon, Q. Xing, A. Palasyuk, M. R. McCartney, D. J. Smith, S. Constantinides, R. W. McCallum, I. E. Anderson, V.Antropov, and M. J. Kramer, "Architecture and magnetism of alnico," Acta Mater 74, 224-233 (2014).
2. Y. Yu, K. Sun, Y. Tian, X-Z. Li, M.J. Kramer, D.J. Sellmyer, J.E. Shield, and S. Sun, "One-Pot Synthesis of Urchin-like FePd-Fe$_3$O$_4$ and Their Conversion into Exchange-Coupled L1$_0$-FePd-Fe Nanocomposite Magnets," Nano Lett. 2013, 4975-4979 (2013); DOI: 10.1021/nl403043d.
3. Y. Yu, A. Mendoza-Garcia, B. Ning, and S. Sun, “Cobalt-Substituted Magnetite Nanoparticles and Their Assembly into Ferrimagnetic Nanoparticle Array,” Adv. Mater. 2013, 25, 3090–3094.
4. D.J. Sellmyer, B. Balamurugan, W.Y. Zhang, B. Das, R. Skomski, P. Kharel, and Y. Liu, “Advances in Rare-Earth-Free Permanent Magnets,” The 8th Pacific Rim International Congress on Advanced Materials and Processing, Ed. F. Marquis (TMS, Wiley, 2013), pp. 1689–1696.
5. I.A. Al-Omari, W.Y. Zhang, L. Yue, R. Skomski, J.E. Shield, X.Z. Li, D.J. Sellmyer, “Hf Doping Effect on Hard Magnetism of Nanocrystalline Zr$_{18-x}$Hf$_x$Co$_{82}$ Ribbons,” IEEE Trans. Magn. 49, 3394–3397 (2013); doi: 10.1109/TMAG.2013.2245498.
6. B. Das, B. Balamurugan, P. Kumar, R. Skomski, V.R. Shah, J.E. Shield, A. Kashyap, D.J. Sellmyer, “HfCo$_7$-Based Rare-Earth-Free Permanent-Magnet Alloys,” IEEE Trans. Magn. 49, 3330–3333 (2013); doi: 10.1109/TMAG.2013.2242856.
7. L. Yue, I.A. Al-Omari, W.Y. Zhang, R. Skomski, and D. J. Sellmyer, “Magnetic Domain Structure of Nanocrystalline Zr$_{18-x}$Hf$_x$Co$_{82}$ Ribbons: Effect of Hf,” Mater. Res. Soc. Symp. Proc., Vol. 1557, (2013) Materials Research Society DOI:10.1557/opl.2013.1105.
8. W.Y. Zhang, X.Z. Li, S. Valloppilly, R. Skomski, J.E. Shield, and D.J. Sellmyer, “Magnetism of Rapidly-Quenched Rhombohedral Zr$_2$Co$_{11}$-Based Nanocomposites,” J. Phys. D: Appl. Phys. 46, 135004 (2013) (5 pp); doi:10.1088/0022-3727/46/13/135004.
9. R. Skomski, P. Manchanda, P. Kumar, B. Balamurugan, A. Kashyap, and D.J. Sellmyer, “Predicting the Future of Permanent-Magnet Materials,” IEEE Trans. Magn. 49, 3215–3220 (2013); doi: 10.1109/TMAG.2013.2248139.
10. B. Das, B. Balamurugan, R. Skomski, X.Z. Li, P. Mukherjee, G.C. Hadjipanayis, D.J. Sellmyer, “Structure and Magnetism of Dilute Co(Zr) Nanoclusters,” J. Appl. Phys. 113, 17B509 (2013); doi: 10.1063/1.4795318.
11. W. Tang, L. Zhou, K. W. Song, K.W. Dennis, M. J. Kramer, I. E. Anderson and R. W. McCallum, “Anisotropic Hot Deformed Magnets Prepared from Zn-coated MRE-Fe-B Ribbon Powder (MRE=Nd+Y+Dy),” J. Appl. Phys., Vol. 115, 17A725(2014).
12. Q. Xing, M.K. Miller, L. Zhou, H.M. Dillon, R.W. McCallum, I.E.Anderson, S. Constantinides, and M.J. Kramer, “Phase and Elemental Distributions in Alnico Magnetic Materials,” IEEE Transactions on Magnetics, Vol. 49, No. 7, July 2013, pp. 3314–3317.
13. A. Palasyuk, E. Blomberg, R. Prozorov, L. Yue, M.J. Kramer, R.W. Mccallum, I.E. Anderson, and S. Constantinides, “Advances in Characterization of Non-Rare-Earth Permanent Magnets: Exploring Commercial Alnico Grades 5–7 and 9,” JOM (2013) DOI: 10.1007/s11837-013-0618-z.
14. B. Balasubramanian, B. Das, R. Skomski, W.Y. Zhang, and D.J. Sellmyer, “Novel Nanostructured Rare-Earth-Free Magnetic Materials with High Energy Products,” Adv. Mater. 2013, vol.25, pp. 6090–6093.
15. Y. Yu, W. Yang, X. Sun, W. Zhu, X-Z. Li, D.J. Sellmyer, and S. Sun, “Monodisperse MPt (M = Fe, Co, Ni, Cu, Zn) Nanoparticles Prepared from a Facile Oleylamine Reduction of Metal Salts,” Nano Lett. 2014, dx.doi.org/10.1021/nl500776e.
16. R.W. McCallum, L.H. Lewis, R. Skomski, M.J. Kramer, and I.E. Anderson, “Practical Aspects of Modern and Future Permanent Magnets,” Annu. Rev. Mater. Res. (2014) 44:10.1–10.27, doi: 10.1146/annurev-matsci-070813-113457.
17. L. Zhou, M.K. Miller, H. Dillon, A. Palasyuk, S. Constantinides, R.W. McCallum, I.E. Anderson, and M.J. Kramer, “Role of the Applied Magnetic Field on the Microstructural Evolution in Alnico 8 Alloys,” Met. & Mat. Trans. E, Vol. 1e, March 2014, pp. 27–35.
18. P. Lu, L. Zhou, M.J. Kramer, and D.J. Smith, “Atomic-scale Chemical Imaging and Quantification of Metallic Alloy Structures by Energy-Dispersive X-ray Spectroscopy,” Nature.com/SCIENTIFIC REPORTS, vol. 4: 3945, (2014) DOI: 10.1038/srep03945, pp. 1–5.
19. X. Zhao, M.C. Nguyen, W.Y. Zhang, C.Z. Wang, M.J. Kramer, D.J. Sellmyer, X.Z. Li, F. Zhang, L.Q. Ke, V.P. Antropov, K.M. Ho, “Exploring the Structural Complexity of Intermetallic Compounds by an Adaptive Genetic Algorithm,” Phys. Rev. Lett. 112, 045502 (2014).

20. R. Skomski, E. Schubert, A. Enders, and D.J. Sellmyer, "Kondorski Reversal in Magnetic Nanowires," J. Appl. Phys. 115, 17D137 (1–3) (2014).
21. W.Y. Zhang, S. Valloppilly, X.Z. Li, Y. Liu, S. Michalski, T.A. George, and R. Skomski, "Magnetic Hardening of Zr_2Co_{11}:(Ti, Si) Nanomaterials," J. Alloys & Compounds 587, 578–581 (2014).
22. P. Kumar, A. Kashyap, B. Balamurugan, J.E. Shield, D.J. Sellmyer, and R. Skomski, "Permanent Magnetism of Intermetallic Compounds Between Light and Heavy Transition-Metal Elements," J. Phys. Cond. Matt. 26, 064209-1–8 (2014).
23. Y. Jin, W. Zhang, R. Skomski, S. Valloppilly, J.E. Shield, and D.J. Sellmyer, "Phase Composition and Nanostructure of Zr_2Co_{11}-Based Alloys," J. Appl. Phys. 115, 17A739 (1–3) (2014).
24. W.Y. Zhang, X.Z. Li, S. Valloppilly, R. Skomski, and D.J. Sellmyer, "Effect of Annealing on Nanostructure and Magnetic Properties of Zr_2Co_{11} Materials," Mat. Sci. & Eng. B, 186, 64–67 (2014).
25. L. Zhou, M.K. Miller, P. Lu, L. Ke, R. Skomski, M. McCartney, D. Smith, H. Dillon, Q. Xing, A. Palasyuk, S. Constantinides, R.W. McCallum, I.E. Anderson, V. Antropov, and M.J. Kramer, "Architecture and Magnetism of Alnico," Acta Materialia, (accepted).
26. A. Nelson, Y. Huh, P. Kharel, V. R. Shah, R. Skomski, and D. J. Sellmyer, "Structural, Magnetic and Electron Transport Properties of Mn3-xPtxSn (x = 0, 0.5, 1) Nanomaterials," J. Appl. Phys. 115, 17A923 (2014).
27. X.Z. Li, W.Y. Zhang, D.J. Sellmyer, X. Zhao, M.C. Nguyen, C.Z. Wang, K.M. Ho, "Orthorhombic Zr2Co11 Phase Revisited," J. Alloys and Compounds 611, 167–170 (2014).
28. B. Balamurugan, B. Das, P. Mukherjee, D.J. Sellmyer, "Development of Nanoparticle-Based Permanent-Magnet Materials: Challenges and Advances," Proc. REPM'14, Annapolis 2014, p. 429–432.
29. C.Z. Wang, X. Zhao, M.C. Nguyen, L.Q. Ke, W.Y. Zhang, M.J. Kramer, D.J. Sellmyer, X.Z. Li, V.P. Antropov, F. Zhang, K.M. Ho, "Predicting the Crystal Structures of Magnet Materials Using Adaptive Genetic Algorithm," Proc. REPM'14, Annapolis 2014, p. 446–449.
30. A. G. Kusne, T. Gao, A. Mehta, L. Ke, M. C. Nguyen, K. M. Ho, V. Antropov, C. Z. Wang, M. J. Kramer, C. Long, and I. Takeuchi, "On-the-fly machine-learning for high-throughput experiments: search for rare-earth free permanent magnets" Sci. Rep. 4, 6367 (2014).

4.5 Convective and Passive Stack Improvements in Motors

Kevin Bennion *(Principal Investigator)*

National Renewable Energy Laboratory (NREL)
Transportation and Hydrogen Systems Center
15013 Denver West Parkway
Golden, CO 80401
Phone: (303) 275-4447
E-mail: kevin.bennion@nrel.gov

Susan A. Rogers, DOE Technology Development Manager
Phone: (202) 586-8997
E-mail: susan.rogers@ee.doe.gov

Sreekant Narumanchi, NREL Task Leader
Phone: (303) 275-4062
Email: sreekant.narumanchi@nrel.gov

Start Date: FY13
Projected End Date: FY16

Objectives

Thermal management for electric motors will become more important as the automotive industry continues to transition to more electrically dominant vehicle propulsion systems. With the push to reduce component size, lower costs, and reduce weight without sacrificing performance or reliability, the challenges associated with thermal management for power electronics and electric motors increase. The transition to more electrically dominant propulsion systems leads to higher-power duty cycles for electric drive systems. Thermal constraints place significant limitations on how electric motors ultimately perform. As summarized by Thomas Lipo, "[a]n optimized thermal design can help increase machine rated power substantially, almost without any increase of its manufacturing costs." [1]. As thermal management improves, there will be a direct trade-off among motor performance, efficiency, cost, and the sizing of electric motors to operate within the thermal constraints.

The goal of this research project is to support broad industry demand for data, analysis methods, and experimental techniques to improve and better understand motor thermal management. Work in FY14 focused on two areas related to motor thermal management: passive thermal performance and active convective cooling. Passive thermal performance emphasized the thermal impact of materials and thermal interfaces among materials within an assembled motor. The research tasks supported measuring thermal contact resistances and orthotropic (direction-dependent) thermal conductivity within an electric motor. Active convective cooling focused on measuring convective heat-transfer coefficients using automatic transmission fluid (ATF).

Technical Barriers

The technical challenges to motor thermal management are summarized by Hendershot and Miller as follows: "Heat transfer is as important as electromagnetic and mechanical design. The analysis of heat transfer and fluid flow in motors is actually more complex, more nonlinear, and more difficult than the electromagnetic behavior" [2]. The primary technical challenges to the thermal performance of electric motors include:

- Orthotropic (direction-dependent) thermal conductivity of lamination stacks
- Orthotropic thermal conductivity of slot windings
- Orthotropic thermal conductivity of end windings
- Convective heat-transfer coefficients for ATF cooling
- Thermal contact resistance of stator-case contacts
- Cooling jacket performance.

Technical Targets

The DOE technical targets applicable to this research are the goals outlined in the "Electrical and Electronics Technical Team Roadmap" [3]. Specifically, the 2020 motor technical targets are $4.7/kW, 1.6 kW/kg, and 5.7 kW/L. Thermal management of electric motors supports improvements in each of the technical targets because of impacts on current density, material costs, and magnet costs (dysprosium). In addition, thermal management of an electric motor impacts efficiency and reliability.

Accomplishments

- Completed measurements of average convective heat-transfer coefficients for ATF jets impinging on target surfaces (with surface enhancements) showing a 10%–34% increase in the average effective heat-transfer coefficient relative to a plain surface compared to the tested flow rates.
- Designed and fabricated an experimental apparatus to measure the local variation in the convective heat-transfer coefficients of ATF jets.
- Completed measurements of thermal contact resistance between motor lamination steels and the orthotropic thermal conductivity of stacked motor laminations showing that the effective through-stack thermal conductivity is between 3%–9% of the bulk material thermal conductivity.
- Completed initial measurements for orthotropic thermal conductivity of wire bundles representative of motor slot windings.
- Developed a thermal test capability to measure thermal contact resistance for high-pressure thermal interfaces representative of the press fit between stator laminations and motor cooling jackets.

✧ ✧ ✧ ✧ ✧

Introduction

The ability to remove heat from an electric motor depends on the passive stack thermal resistances within the motor and the convective cooling performance of the selected cooling technology. Passive thermal design refers to the geometrical layout, material selection, and thermal interfaces that affect the heat-spreading capabilities within the motor. The ability for heat to spread through the motor affects the thermal temperature gradients within the motor. Active convective cooling technology is the cooling mechanism that ultimately removes the heat from the motor and transfers the heat to another location to reject the heat to the ambient environment. During FY14, work focused on these two areas.

Active Convective Cooling

Work during FY14 in the area of active convective cooling focused on using ATF jets to cool the end windings of electric motors. The advantage of cooling using ATF is it is possible to directly cool the motor end windings; however, no data related to the convective cooling performance of the ATF jets impinging on end windings is available in the public literature for motor designers to reference. For this reason, in FY14 NREL completed measurements of average heat-transfer coefficients of ATF jets impinging on target surfaces representative of motor end windings.

After NREL completed work on measuring the average heat-transfer coefficients, work focused on spatially mapping the ATF heat-transfer coefficient across a cooling surface. Jet impingement cooling provides high-heat transfer coefficients—higher than those of conventional channel cooling; however, the heat-transfer coefficients provided by an impinging jet are not uniform throughout the entire cooled surface. As shown in Figure 4-71 and Figure 4-72, jet impingement heat-transfer coefficients are highest at the stagnation zone (a result of a thin boundary layer) and decrease as the liquid flows radially outward. For motor cooling applications, the nonuniform heat-transfer coefficient results in nonuniform cooling on a motor's end windings (Figure 4-73). To better understand the effect of ATF jet impingement cooling, it is important to know the local variations of the jet impingement heat-transfer coefficients. For this reason, in FY14 NREL began work to spatially map the ATF jet heat-transfer coefficients.

The data provides motor designers with estimates of effective heat-transfer coefficients that can be applied to motor end windings when cooled using transmission fluid. In addition to being directly useful to the design and analysis of electric motors, the data provides a baseline against which improvements in using transmission fluid to cool motors can be evaluated.

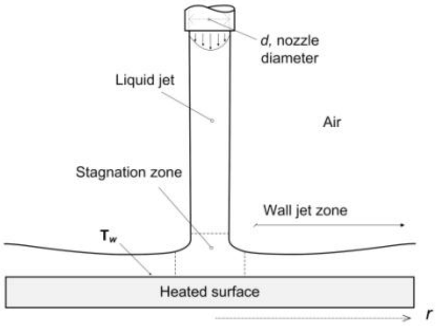

Figure 4-71: Schematic of jet impinging on heated surface.

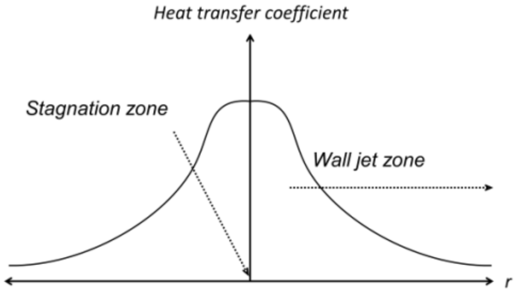

Figure 4-72: Schematic of heat-transfer coefficient variation of a typical fluid jet.

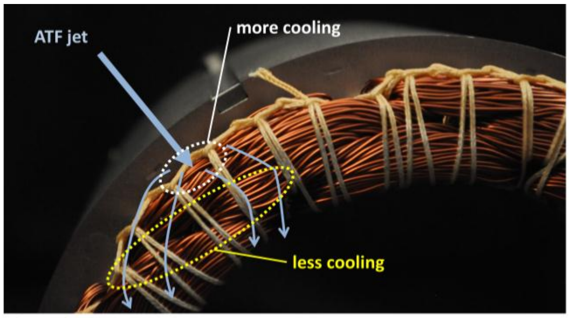

Photo Credit: Kevin Bennion, NREL

Figure 4-73: High-heat transfer is experienced on motor winding surfaces directly impacted by an impinging jet. Surfaces not directly impacted by the jet receive less cooling.

Passive Thermal Stack

Work during FY14 in the area of passive thermal stack focused on measuring thermal contact resistances and the orthotropic thermal conductivity of motor components. The work supports improved thermal models for motor design, but it also enables analysis to compare the potential impacts of new materials to enhanced thermal properties.

The stator and rotor lamination stacks are a significant portion of the thermal pathway for removing heat from the motor. The effective thermal conductivity is cylindrically orthotropic, as shown in Figure 4-74, so it is important to determine effective properties for both in-plane (shown in Figure 4-74 as the x-y plane) and through-stack (shown in

Figure 4-74 as the z direction) [4]. It is also important to know factors that affect these properties.

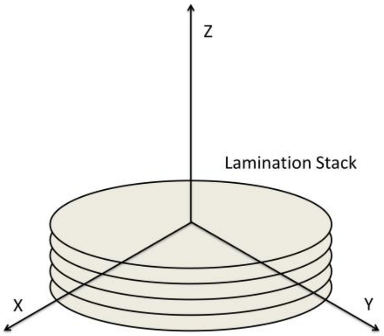

Figure 4-74: Orthotropic thermal property orientation for motor laminations. Through-stack conductivity is along the z axis, and in-plane thermal conductivity is along the x-y plane.

NREL experimentally measured effective thermal properties and interlamination contact resistance of different types of commonly used stator laminations. The information was used to calculate the effective through-stack thermal conductivity of lamination materials. Such nonbiased and consistent information is not available in the open literature. The data compares a range of lamination materials and demonstrates how the interlamination contact resistance is affected by contact pressure and the surface profile of the lamination materials that are in contact. The data quantifies the difficulty in extracting heat axially through the lamination materials within the motor, which has significant impacts, especially for cooling rotors used in permanent magnet motors.

In FY14, NREL also initiated work in collaboration with Oak Ridge National Laboratory (ORNL) to measure orthotropic thermal properties of windings used in electric motors. Figure 4-75 shows an example illustration of such a winding. The area of interest is to measure the effective cross-slot or cross-wire (along the x-y plane shown in Figure 4-75) thermal conductivity. The data will be used to validate modeling results and investigate improvements to insulation materials used in motor windings that could improve the effective cross-slot thermal conductivity of the motor windings.

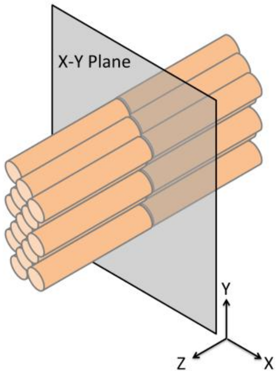

Figure 4-75: Orthotropic thermal property orientation for motor windings. Axial thermal conductivity is along the z axis, and cross-slot thermal conductivity is along the x-y plane.

In addition to the material thermal conductivity measurements, NREL also initiated work in FY14 to characterize the stator-to-case thermal contact resistance in electric motors. The stator-to-case thermal contact resistance can be a significant factor in the ability to remove heat from an electric motor [4].

Approach

The approach during FY14 was focused on two main areas: active convective cooling for electric motors and passive thermal stack of the electric motor. Each of these areas is discussed in more detail in the following sections.

Active Convective Cooling

Work in FY14 in the area of active convective cooling focused on completing measurements of average heat-transfer coefficients and validating the experimental setup used to obtain the results. The next step in the work is focused on measuring the local variation in the heat-transfer coefficients of ATF jets impinging on a target surface.

Average Heat Transfer

The experimental methods used to measure the average convective heat-transfer coefficients provide a reference for establishing confidence in the experimental results for ATF jet impingement and future work. To establish credibility of the average heat-transfer coefficients on target surfaces representative of motor end windings, it was necessary to compare data for the plain surface to available data in the literature under similar operating conditions. Ford Motor Company provided fluid properties for the Mercon LV transmission fluid used in the experiments. Although no data about the heat-transfer coefficients of ATF jets impinging on end-winding surfaces is available in the public literature, data does exist for fluids with high Prandtl numbers impinging on plain surfaces. The fluid properties for the tested ATFs were combined with existing correlations for fluids with high Prandtl numbers [5]–[7] to compare the results.

The setup for the measurement of average heat-transfer coefficients is shown in Figure 4-76. A detailed description of the setup was provided in the FY13 Annual Report, but the setup is summarized below. Fluid entered the test section through a tube at the top of the chamber. Fluid then flowed through a nozzle plate to generate an impinging jet onto the test sample. The nozzle consisted of a 2-mm diameter orifice. The test samples, fabricated from oxygen-free copper, had an impingement or cooled surface diameter (D) of 12.7 mm. Two calibrated K-type thermocouples were embedded within the sample to measure heat fluxes and to calculate surface/wall temperature. The sample was heated using a computer-controlled power supply that powered a resistance heater assembly attached to the lower side of the sample.

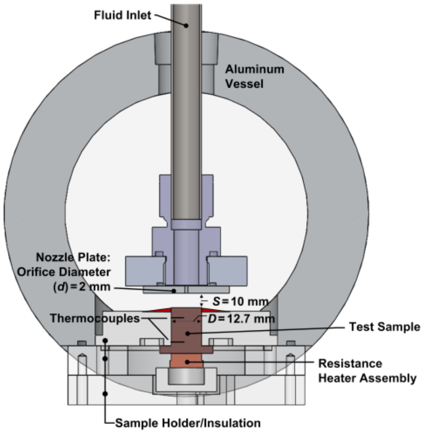

Figure 4-76: Experimental setup of apparatus used to measure average ATF jet heat-transfer coefficients.

The thermal performance of four test samples with different surface features were evaluated under jet impingement (free-jet) cooling conditions. The baseline sample was sandpaper-polished (600 grit) to create a smooth/plain impingement surface. The other three samples were fabricated (via wire electrical discharge machining) with surface features that were intended to simulate wire bundles found in electric motors. The features on these samples consisted of a series of parallel circular ridges running straight across the impingement surface. The radius of these ridges corresponds to the radius of the American wire gauge (AWG) (i.e., 18 AWG, 22 AWG, or 26 AWG) plus the thickness of the wire insulation based on Polyurethane-180 heavy-build insulation from MWS Wire Industries.

Spatial Mapping of ATF Heat-Transfer Coefficients

Work on ATF heat-transfer measurements in FY14 focused on the ability to measure local heat-transfer coefficients to spatially map the ATF heat-transfer coefficients over the target surface. A summary of the test setup developed during FY14 is given in Figure 4-77.

Encapsulated thermochromic liquid crystals (TLC) will be utilized to measure the temperature distributions on a heated surface. TLC's hue (color) changes in response to a change in temperature. When painted or spayed onto heated surfaces, TLCs can be utilized to the measure surface temperatures. The surface temperatures combined with the ATF fluid temperature and the imposed heat flux will then be used to spatially map the heat-transfer coefficients from the stagnation zone through the wall jet region, as shown in Figure 4-72.

Figure 4-77 shows a schematic of the test apparatus for these experiments. The apparatus consists of a vessel, 2-mm-diameter plain orifice nozzle, and a test article. The apparatus is connected to a flow loop that conditions and circulates ATF fluid. The test article consists of a thin metal foil, copper lead bars, guard heaters, and insulation/structural components. The thin (~50-µm) metal foil is spray-painted with TLCs on one side and then stretched across the two copper bars, as shown in Figure 4-77. The foil is heated by conducting a high current across it. The foil is then cooled via an ATF jet that impinges upon the upper surface of the foil. An optically clear path on the bottom side of the test article allows for visualization of the TLC with a camera. The camera images are combined with image-processing software to obtain the localized surface temperatures. Prior to conducting the experiments, the TLC's hue is calibrated to temperature.

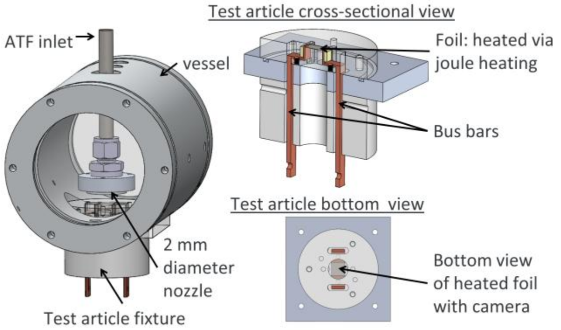

Figure 4-77: (Left) Design of the test vessel and (right) test article. TLCs are applied to the bottom side of the heated foil and provide localized temperature measurements of the ATF cooled surface.

Passive Thermal Stack

Work in FY14 in the area of passive thermal stack focused on measuring thermal contact resistances and orthotropic thermal conductivity of motor components that were shown to impact motor performance [4]. This included through-stack and in-plane thermal conductivity of lamination materials, cross-slot thermal conductivity of slot-winding materials, and stator-to-case thermal contact resistances.

All measurements used a setup similar to that shown in Figure 4-78, which is a test apparatus built in accordance with the ASTM 5470-12 steady-state technique [8], [9]. Figure 4-78 shows the sample being tested as the Lamination Stack, but as shown in the figure it is intended to represent any potential test sample in which it is desired to measure the orthotropic thermal conductivity in the vertical direction.

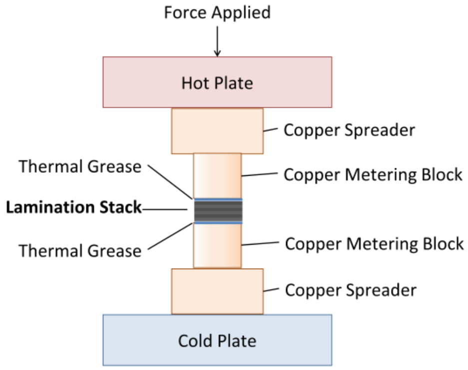

Figure 4-78: Steady-state setup for measuring orthotropic thermal conductivity values.

Lamination Through-Stack Thermal Conductivity

The effective through-stack thermal conductivity incorporates the lamination bulk material thermal conductivity and the thermal contact resistance between the individual laminations. Measuring the effective through-stack (Figure 4-74) thermal conductivity of the motor steel lamination materials was performed through a series of steps. The first step required measuring the bulk material properties for the motor lamination materials, including thermal conductivity, specific heat, and density. The necessary bulk material properties were measured directly. The density was measured by dividing weight by volume for the individual laminations and taking the average of 10 samples. Specific heat was measured using a differential scanning calorimeter, and bulk thermal conductivity was measured using a xenon flash transient technique.

The second step involved measuring the thermal contact resistance between lamination materials. The contact resistance is affected by clamping pressure, surface finish, and coating properties, all of which were analyzed. Measuring the thermal contact resistance of the lamination-to-lamination contact was performed by measuring the through-stack thermal conductivity of a stack of laminations and varying the number of laminations in the stack. The through-stack thermal resistance was measured using a test apparatus built in accordance with the ASTM 5470-12 steady-state technique [8], [9], shown in Figure 4-78. When the bulk materials properties and lamination-to-lamination thermal contact resistance were known, it was possible to calculate the effective through-stack thermal conductivity for a specific lamination material.

Four lamination materials were analyzed, including commonly used M19 lamination material in both 26 gauge (0.470 mm) and 29 gauge (0.356 mm). Two thinner lamination materials were also tested—HF10 (0.254 mm) and Arnon 7 (0.178 mm)—because these lamination materials reduce core losses and were of interest to industry collaborators [10]. All materials had the standard C5 coating used in electric motor lamination materials.

Each test was performed at four pressures between 138 kPa and 552 kPa (20 psi and 80 psi) based on industry feedback and equipment limitations. The total thermal resistance (R_{th}) of the stack measured by the ASTM setup can be described as a function of the number of interlamination contacts (N_C) in the stack using Equation 1, where R_C is the contact resistance between laminations, R_L is the lamination thermal resistance, and R_G is the total thermal resistance of grease layers used in the test setup.

$$R_{th}(N_C) = (R_C + R_L)N_C + R_L + R_G \tag{1}$$

Data from the different stack heights was fitted using a weighted curve fit [11]. The advantage to fitting a slope is its independence from any constant resistances present, such as R_G. Weighting was based on the systematic uncertainty in the measurements, which was found to be proportional to the stack height. The weighted curve-fitting method also provided uncertainty estimates in the measurements. After the slope of the curve fit was calculated, it was possible to calculate the lamination-to-lamination thermal contact resistance by subtracting the lamination thermal resistance. The measured contact resistance was checked using equations in published literature [12] for low-pressure contacts.

With the experiments, effort was made to quantify the uncertainty of the measurements. Five repetitions were performed at each stack height. Three stack heights were measured for each material (2, 5, and 8 laminations), except for the M19 29-gauge material, for which seven stack heights were used initially. Using the larger number of stack heights initially enabled a comparison to the same curve fit using three stack heights to confirm the number of experiments required to obtain accurate results. It is documented in the literature that thermal contact resistance will reduce with load cycling and thermal cycling [13]. For this experiment, only the first cycle was considered to minimize hysteresis. Also, the orientation and order of laminations in the stack was constant throughout every test. Finally, the 95% confidence interval was calculated for the results following established and recognized practices [14].

The through-stack thermal resistance is the sum of the resistances due to the laminations and contacts as described in Equation 1. The slope, m, (shown in Equation 2) is obtained through the weighted linear curve fit, and it is a function of the lamination resistance (R_L) and the lamination-to-lamination thermal contact resistance (R_C). Because R_L was known from the xenon flash measurements, R_C could be calculated. The thermal conductivity was determined as a function of N_L, as shown in Equation 3.

$$\frac{d}{dN_C}\big((R_C + R_L)N_C + R_L + R_G\big) = R_C + R_L = m \tag{2}$$

$$k(N_L) = \frac{t \cdot N_L}{R_C(N_L - 1) + R_L N_L} \tag{3}$$

As shown in Equation 3, the thermal conductivity changes with the number of laminations, because the ratio of laminations to contacts decreases. When a large enough number of laminations are stacked, the ratio approaches one and the effective thermal conductivity asymptotes to a specific value. Equation 4 gives the estimate of effective through-stack thermal conductivity.

$$k_{eff} = \lim_{N_L \to \infty} k(N_L) = \frac{t}{R_C + R_L} = \left(\frac{R_C}{t} + \frac{1}{k_L}\right)^{-1} \tag{4}$$

Lamination In-Plane Thermal Conductivity

Although the through-stack thermal conductivity measurements were the primary focus of the lamination measurements, the effective in-plane thermal conductivity of a lamination stack was also measured in collaboration with ORNL. ORNL provided the sample lamination materials for the testing, as shown in Figure 4-79. Assuming a high stacking factor for the laminations, the in-plane thermal conductivity should be very close to the bulk lamination material thermal conductivity. The samples provided by ORNL were tested in a setup similar to that shown in Figure 4-78. Figure 4-79 shows the samples in the test apparatus. The in-plane thermal conductivity is a factor impacting the cooling performance of electric motors [4].

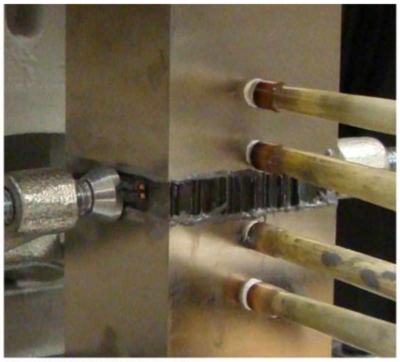

Photo Credit: Justin Cousineau, NREL

Figure 4-79: Test setup for measuring in-plane lamination thermal conductivity for lamination materials provided by ORNL.

Wire Cross-Slot Thermal Conductivity

Work also started in FY14 to measure the effective thermal properties across bundles of wire or cross-slot thermal conductivity, as shown in Figure 4-80. ORNL provided samples for the initial testing. The test setup was similar to that shown in Figure 4-78, and Figure 4-80 shows a picture of the wire bundle sample provided by ORNL is shown installed in the test. The axial thermal conductivity and cross-slot thermal conductivity of the wire bundle materials is a factor that impacts the cooling performance of electric motors [4].

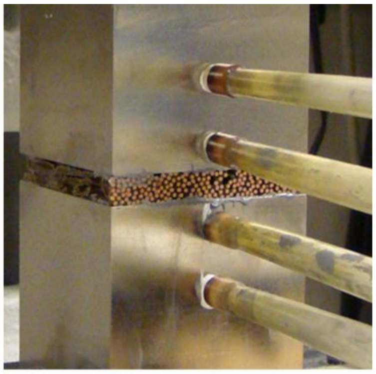

Photo Credit: Justin Cousineau, NREL

Figure 4-80: Test setup for measuring cross-slot wire bundle thermal conductivity with wire bundle sample provided by ORNL.

Stator-to-Case Thermal Contact Resistance

The case contact resistance is an important factor in the ability to cool electric motors that are primarily cooled with a cooling jacket surrounding the motor stator [4]. An example of such a motor and cooling system is shown in Figure 4-81 for an electric motor used in a commercial full-electric vehicle. The image on the left shows the rotor of the motor removed to show the stator, which is press fit into an aluminum cooling jacket that surrounds it [10]. The image on the right shows the same motor with a section of the cooling jacket removed. The capability to characterize the surface topography of the stator and cooling jacket interface surfaces was developed during FY14, as was the capability to measure thermal contact resistance under high pressures representative of press fits.

Photo Credits: Kevin Bennion, NREL

Figure 4-81: (Left) Example motor cooled with cooling jacket surrounding the motor stator. (Right) Image of motor with section of cooling jacket removed.

Results

The results are separated into the two main focus areas as described previously. The first section summarizes the progress for active convective cooling, with an emphasis on using ATF for cooling electric motors. The second section focuses on the passive thermal stack of the electric motor, with emphasis measuring thermal contact resistances and the orthotropic thermal conductivity of motor components

Active Convective Cooling

Work on active convective cooling focused on using ATF for cooling electric motors. Tests were completed for measuring the average heat-transfer coefficients, and the focus switched to mapping the spatial heat-transfer coefficient caused by an ATF circular jet impinging on a target surface.

Average Heat Transfer

Ford Motor Company provided fluid property data for the ATF used in the experiments conducted to measure the average effective heat-transfer coefficient of a jet impinging on target surfaces representative of motor end windings. In addition to running tests on the surfaces representative of wire bundle end windings, tests were performed on plain target surfaces. The plain target surfaces provide a baseline for comparing the experimental results. Although no data is available for ATF impinging on representative end-winding surfaces, data is available on fluid jets with high Prandtl numbers impinging on plain surfaces. Using the fluid property data proved by Ford Motor Company, it was possible to compare the measured data on the plain surface to existing heat-transfer correlations in the literature. The comparison of the measured data to available literature correlations is shown in Figure 4-82. Convective heat-transfer correlations are generally used with the assumption of some potential error or uncertainty in the final result because of the potential variation in operating conditions and fluid properties; however, as shown in Figure 4-82, the measured data is mostly in line with the results obtained from the correlations in the literature. Given the potential uncertainty of operating conditions and fluid properties, it was determined that the results provided confidence in the experimental setup used to measure the average heat-transfer coefficients.

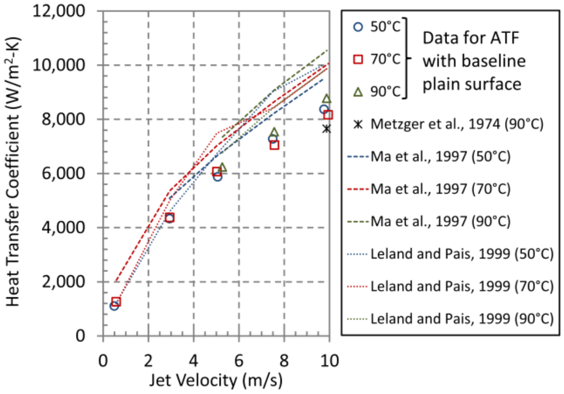

Figure 4-82: Comparison of measured data to predictions from the literature correlations for jet impingement cooling with high-Prandtl-number fluids.

Figure 4-83 shows a sample of the results comparing the impact of the target surface on the average jet impingement heat-transfer coefficient. In the illustrated case with the inlet ATF temperature at 50°C, the larger wire sizes resulted in a higher average convective heat-transfer coefficient as the jet velocity increased when compared to the baseline plain surface. The increase in the average heat-transfer coefficients corresponded to the increase in the wetted surface area of the target surface impacted by the ATF jet. Tests were also performed at higher temperatures than those illustrated in Figure 4-83, and detailed results are expected to be submitted for publication during FY15.

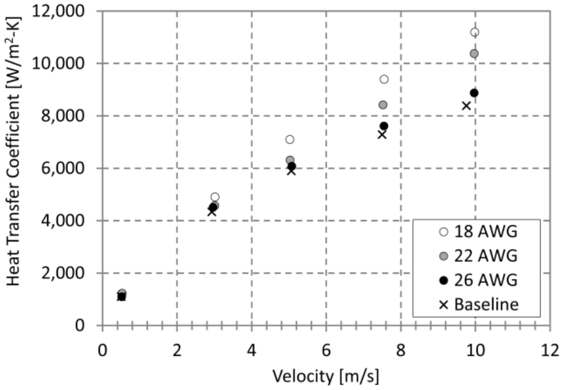

Figure 4-83: Comparison results for ATF impingement on target surfaces with an ATF inlet temperature of 50°C.

Spatial Mapping of ATF Heat-Transfer Coefficients

As illustrated in Figure 4-71 and Figure 4-72, the local heat-transfer coefficient form an impinging circular jet is not uniform across the cooled surface. During FY14, NREL initiated work to develop an experimental technique to measure the local variation of the heat-transfer coefficient caused by an impinging circular ATF jet on a target surface. Electrothermal finite element analysis (FEA) simulations that included resistive heating from the electric current were utilized to design the test article. The simulations were conducted using a one-quarter CAD model of the test article (Figure 4-77). As shown in Figure 4-84, electrically heating the metal foil resulted in a nonuniform temperature distribution on the foil's surface. The range of temperature distribution is on the order of 46°C. This effect is due to the highly thermally conductive nature of the copper bars on either side of the foil.

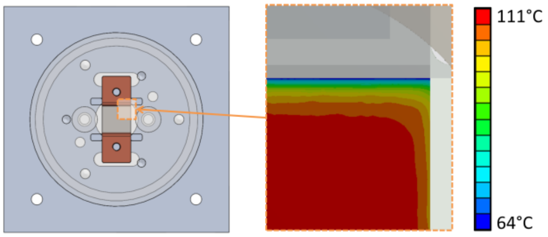

Figure 4-84: Electrothermal FEA-generated temperature contours of the heated foil surface. The copper leads act like heat sinks and create large temperature gradients on the heated foil surface.

To remedy the issue caused by the large copper bus bars, guard heaters were utilized to prevent heat from being conducted to the copper bars. FEA simulations incorporating a guard heater on the copper bars indicated a more uniform temperature distribution across the foil surface (Figure 4-85). The temperature distribution reduced to 6°C when using the guard heater. Because the surface temperature of the foil surface with the TLCs is known, it is possible to calculate the local heat-transfer coefficient over the surface of the foil heater and quantify the variation in heat-transfer coefficient.

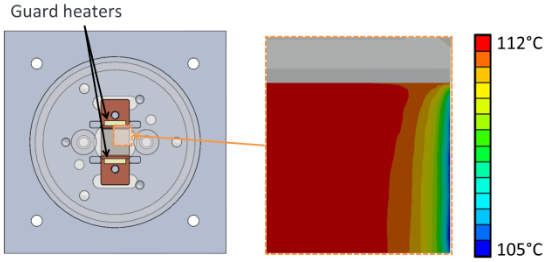

Figure 4-85: Electrothermal FEA generated temperature contours of the foil surface. Attaching guard heaters to the copper lead bars reduces foil surface temperature variations.

Passive Thermal Stack

The results of the work focusing on characterizing and improving the passive thermal stack in an electric motor are summarized below.

Lamination Through-Stack Thermal Conductivity

As described in the approach for measuring the lamination through-stack thermal conductivity, the first step in the analysis was to measure the lamination-to-lamination thermal contact resistance. The lamination-to-lamination thermal contact resistance was estimated from a curve fit as shown in Figure 4-86 and described by Equation 2. An example fit for the M19 29-gauge lamination material is shown in Figure 4-86. Error bars in the figure indicate the systematic uncertainty with a 95% confidence interval. The results for interlamination thermal contact resistance are shown in Figure 4-87, following the previously outlined approach for calculating the interlamination thermal contact resistance from the slope of the weighted curve fit. Figure 4-87 shows that the lamination-to-lamination thermal contact resistance decreases with pressure, but not all the samples showed the same dependence on pressure. The impact of pressure was found to be dependent on the lamination surface topography which is described in more detail below. The results provide an appropriate range for the lamination-to-lamination thermal contact resistance.

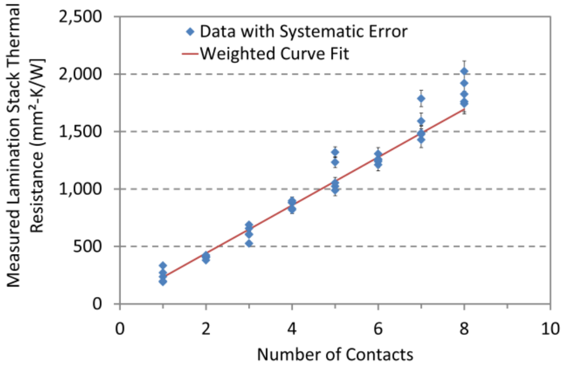

Figure 4-86: M19 29-gauge 138-kPa data set with weighted curve fit.

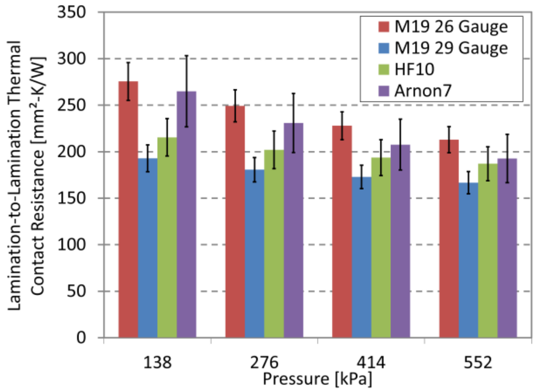

Figure 4-87: Summary of measured interlamination contact resistance for materials tested at the four pressures. Error bars represent a U_{95} confidence interval.

The through-stack thermal conductivity of a lamination stack was calculated from Equation 3, and the results for the M19 29-gauge material are plotted in Figure 4-88 as an example. The thermal conductivity changed with the number of laminations, because the ratio of laminations to contacts decreases. If the through-stack thermal conductivity were taken directly from the total thermal resistance measurement of a stack of less than 10 laminations, the result would be an overprediction of the effective through-stack thermal conductivity through a large number of laminations as used in motor applications. When a large enough number of laminations are stacked, the ratio of laminations to contacts approaches one and the effective thermal conductivity asymptotes to a specific value.

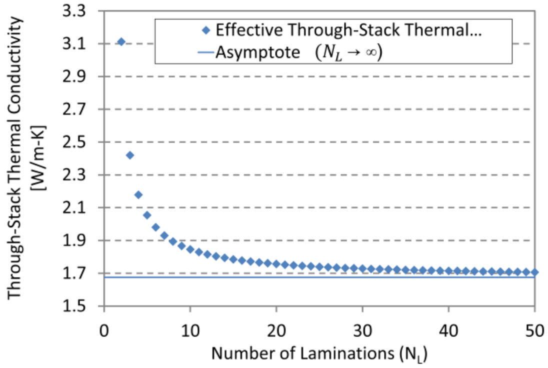

Figure 4-88: M19 29-gauge through-stack thermal conductivity at 138-kPa compared to the number of laminations and asymptote.

Equation 4 gives the estimate of effective through-stack thermal conductivity for a large number of laminations when the through-stack thermal conductivity reaches an asymptote. The results for each of the tested materials are shown in Figure 4-89. The through-stack thermal conductivity values shown in Figure 4-89 would be appropriate to use in a motor thermal model for the lamination stack. The through-stack thermal conductivity depends on the lamination-to-lamination thermal contact resistance, the lamination bulk material thermal conductivity, and the lamination thickness. The impact of lamination thickness is most visible in Figure 4-89 with thinner laminations in general showing a lower through-stack thermal conductivity.

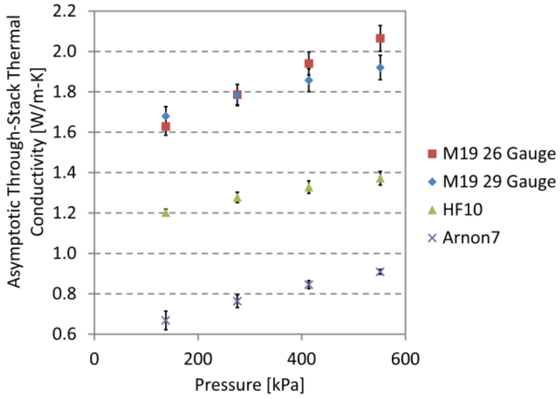

Figure 4-89: Asymptotic through-stack thermal conductivity for lamination stacks.

In addition to contact pressure, other factors affecting contact resistance include the surface topography and hardness of the contacting materials, which can be affected by the surface coating [15]. The remaining task was to determine the factors accounting for the differences among the different materials to better understand factors affecting contact resistance and better predict contact resistance.

Surface Coating

The laminations were all coated with a C-5 coating to provide electrical resistance among them. The purpose was to minimize eddy current formation within the steel, which would otherwise cause additional thermal loading and decreased efficiency. ASTM standards define a C-5 coating as inorganic or mostly inorganic with ceramic fillers to maximize electrical insulating ability [16]. The coating will withstand stress-relief annealing up to 840°C and burn off treatments of 320°C–540°C (as encountered during motor rebuilds). ASTM standards state that it can be applied to one or both sides of the laminations; they do not define a specific material composition, process, or coating thickness; and they do not specify a specific electrical resistance, stating only that it will be higher than C-4 or C-2, and noting that the exact electrical resistance is at the discretion of the manufacturer. Thermal performance, in the context of thermal contact resistance and thermal conductivity, is not taken into consideration.

Information about the sample coatings was collected to help identify whether the coatings were different for the materials tested. NREL utilized a scanning electron microscope (SEM) with focused ion beam (FIB) capability to determine the presence of the C-5 coating on one or both sides of the sample laminations as well as the coating thickness. FIB works by depositing a protective layer of platinum on the surface and bombarding it with gallium ions. The process produces very accurate cross sections that can be used for measuring thin layers. The images for the M19 29-gauge material are shown in Figure 4-90.

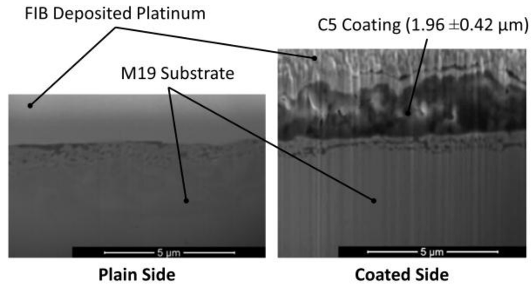

Photo Credits: Adam Stokes, NREL

Figure 4-90: SEM cross sections of M19 29-gauge lamination material.

There was some variability in the measured coating thickness, and the coating thickness was reported as an average. The variation in coating thickness was measured along the approximately 10-µm cross section. In some cases, there was uncertainty about the exact edge of the coating, because there was some penetration of the layer into the substrate. The results of the measurements are given in Table 4-7. The materials listed had a coating present on only one side. Results for the M19 26-gauge material were inconclusive.

Table 4-7: C-5 Coating Measurements.

Material	Average Coating Thickness (µm)	Coating Thickness Variation (µm)
M19 29-gauge	1.96	0.42
HF10	2.10	0.46
Arnon7	1.83	0.64

No correlation existed between the average coating thickness and thermal contact resistance. Further, the variation in coating thickness showed substantial overlap among samples. Because no significant difference among the samples existed, it was determined that the coating did not have a significant impact on the variation in the measured thermal contact resistance.

Surface Topography

The surface topography of the materials was different among the materials tested. Some of the samples were observed to have a ridged or striped pattern on one side of the laminations. The ridges are a side effect of the manufacturing process of the M19 29-gauge and HF10 materials and are present on one side. They have a roughly sinusoidal shape with a wavelength of 1.0 mm–1.3 mm and amplitude of 1.3 µm–1.5 µm. To measure the surface topography, a two-dimensional discreet Fourier transform was performed on the data taken from a surface profile scan of the samples using a laser profilometer. The scan data was imported into a custom MATLAB script to provide a spatial frequency spectrogram. Surface spatial frequency spectrograms were processed for both sides of each lamination material. Figure 4-91 shows the processed surface profile data for a sample lamination material that shows the striped pattern.

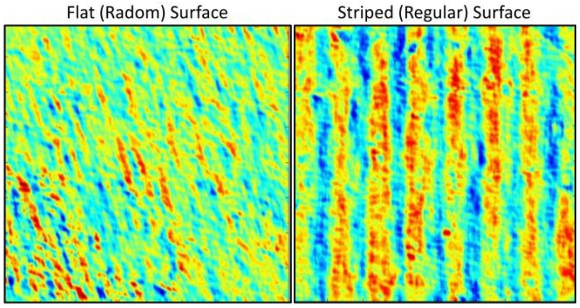

Figure 4-91: Surface data for both sides of the M19 29-gauge material.

The tested samples showed a correlation between surface topography and thermal contact resistance. The samples that had the striped (regular) pattern showed a lower thermal contact resistance and less variation with respect to pressure. These materials included the HF10 and the M19 29-gauge samples. The samples with flat surfaces (random contacts) on both sides showed a higher thermal contact resistance and more sensitivity to increasing pressure. The flat samples included M19 26-gauge and Arnon7. It is important not to imply that HF10 and M19 29-gauge will always have regular contacts and Arnon7 and M19 26-gauge have random contacts, only that the tested materials do have these characteristics. Differences in manufacturing techniques will yield different surface finishes. The striped pattern reduced the contact resistance by approximately 24% at the lowest tested pressure and by 13% at the highest tested clamping pressure, when comparing the average thermal contact resistance of the striped surfaces to the average thermal contact resistance of the flat surfaces.

Lamination In-Plane Thermal Conductivity

The results for the in-plane lamination thermal conductivity are shown in Figure 4-92. The samples were provided by ORNL and tested as shown in Figure 4-79. Figure 4-92 compares the measured bulk thermal conductivity of the lamination material, the calculated in-plane thermal conductivity assuming a 99% stacking factor, and the measured in-plane thermal conductivity. The results confirmed that the in-plane thermal conductivity is close to the bulk material thermal conductivity.

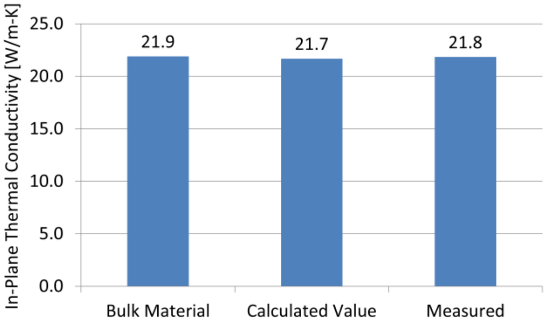

Figure 4-92: Comparison of bulk lamination thermal conductivity, calculated in-plane thermal conductivity assuming a 99% stacking factor, and measured in-plane thermal conductivity for M19 29-gauge laminations.

The results for the cross-slot wire bundle thermal conductivity are shown in Figure 4-93. The samples were provided by ORNL and tested as shown in Figure 4-80. Two samples were tested, each with a slightly different wire fill factor. Figure 4-93 compares the measured cross-slot thermal conductivity to model results of the wire bundle assuming a perfect fill between the wires leaving no air voids. The results were also compared using the same model, but assuming a voiding fraction within the filler material of approximately 50%.The voiding of the sample had a significant effect on the cross-slot thermal conductivity. More work is needed to experimentally test the impact of the voiding and wire-to-filler thermal contact resistance within wire bundle samples.

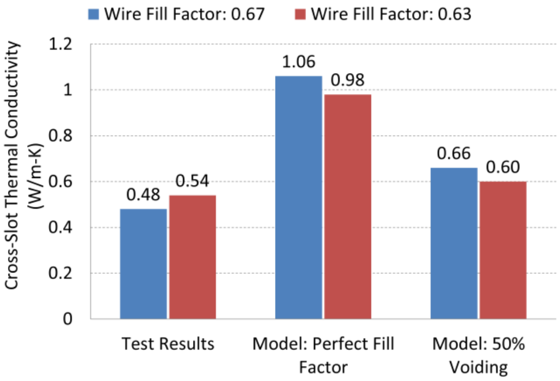

Figure 4-93: Effective cross-slot wire bundle thermal conductivity comparing test results to model results with perfect fill and 50% fill voiding.

Stator-to-Case Thermal Contact Resistance

Initial progress toward characterizing the thermal contact resistance between the motor stator and the aluminum cooling jacket is illustrated below. Figure 4-94 shows a cross section of an in-use commercial cooling jacket. Three distinct areas are highlighted: A, B, and C; B represents the surface in contact with the motor stator. Figure 4-95 shows a comparison of the surface profile and the amplitude spectrum of each of the highlighted surfaces. The surface profile shows a representation of the three-dimensional surface, and highlights the tooling marks on the case. The amplitude spectrum emphasizes the frequency content of the tooling marks. In Figure 4-95 three distinct frequencies are highlighted that correspond to the tooling marks on the case. The surface of B that is in contact with the motor stator is machined to be a smooth surface. Also, the contact pressure due to the press fit between the stator and cooling jacket is not so high as to cause the laminations to imprint the aluminum case.

Sample Case-Stator Contact Surface for Motor Cooling

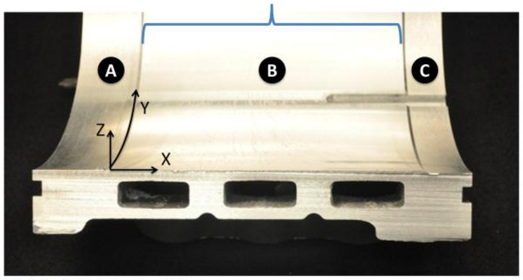

Photo Credit: Kevin Bennion, NREL

Figure 4-94: Example motor cooling jacket showing three distinct regions of the inner diameter. Surface B is in contact with the motor stator.

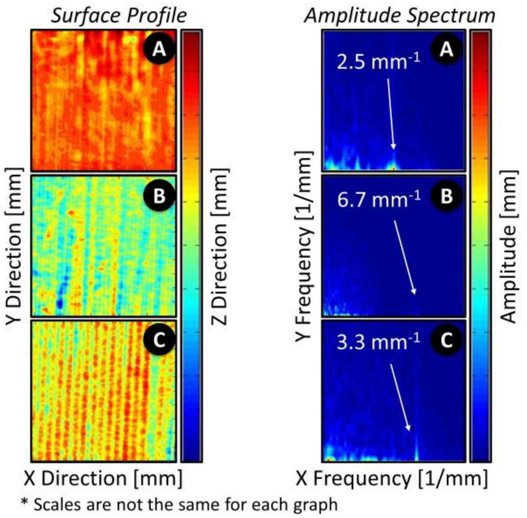

Figure 4-95: (Left) Surface profile data for three highlighted sections of the motor cooling jacket. (Right) Amplitude spectrums of the surface profile data showing tooling mark patterns.

The importance of the thermal interface between the motor stator and the cooling jacket led to the development of a new test capability, as shown in Figure 4-96. The capability makes it possible to measure thermal properties and thermal contact resistances under high pressures that are typical of press fits between the stator and aluminum case surrounding the motor. This test capability is being used to support industry-led motor development efforts to meet DOE 2020 targets.

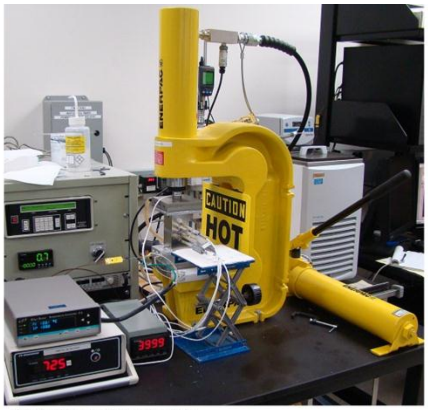
Photo Credit: Justin Cousineau, NREL

Figure 4-96: Stand for measuring thermal conductivity and thermal contact resistance under high pressure.

Conclusions and Future Directions

During FY14, work was completed in the areas of active convective cooling and passive thermal stack for electric motors. The focus in the area of active convective cooling emphasized a need for data on the effective convective heat-transfer coefficients of ATF jets impinging on motor end windings. The focus area for the passive thermal stack emphasized the need to quantify important orthotropic thermal properties and thermal contact resistances that impact motor cooling.

The data for ATF fluid jets impinging on representative motor end windings is the first data available in the open literature. The experimental results for the heat-transfer coefficients was compared to predictions from available literature correlations for fluids with high Prandtl numbers impinging on plain surfaces using fluid property data provided by Ford Motor Company. The results establish confidence in the experimental apparatus and in the test data for the textured surfaces representative of end-winding wired bundles. Future work in the context of ATF jet impingement on representative motor end-winding surfaces will focus on spatially mapping the variation in the convective heat-transfer coefficient.

Thermal properties of lamination stacks were measured with four materials commonly used in electric motors. Orthotropic thermal conductivity, density, and specific heat were measured for each material. Further analysis was performed to understand the physics of lamination-to-lamination thermal contact resistance to understand results and help predict contact resistance for unknown materials. The important conclusions of the work are as follows:

- For any practical application, it can be assumed that effective in-plane thermal conductivity and effective properties are the same as the bulk material.
- Through-stack thermal conductivity is highly dependent on lamination-to-lamination thermal contact resistance, which is dependent on pressure and surface topography.

This work will be used to improve NREL thermal models and will be published in the public literature to fill a current need for material property data to support electric motor design.

FY 2014 Publications/Presentations

1. K. Bennion, J. Cousineau, J. Jeffers, C. King, and G. Moreno, “Convective Cooling and Passive Stack Improvements in Motors,” 2014 DOE Vehicle Technologies Office (VTO) Annual Merit Review, June 2014.
2. K. Bennion, J. Cousineau, J. Jeffers, C. King, and G. Moreno, “Convective Cooling and Passive Stack Improvements in Motors,” Presentation to the DOE VTO Electrical and Electronics Technical Team, Southfield, MI, August 2014.
3. K. Bennion, J. Cousineau, J. Jeffers, C. King, and G. Moreno, “Convective Cooling and Passive Stack Improvements in Motors,” Advanced Power Electronics and Electric Motors FY14 Kickoff Meeting, DOE Vehicle Technologies Program, Oak Ridge, TN, November 2013.

Acknowledgments

The author would like to acknowledge the support provided by Susan Rogers and Steven Boyd, Technology Development Managers for the Electric Drive Technologies Program, Vehicle Technology Office, U.S. Department of Energy Office of Energy Efficiency and Renewable Energy.

The significant contributions from Justin Cousineau, Jana Jeffers, Charlie King, Mark Mihalic, Gilbert Moreno, Caitlin Stack, and Adam Stokes (NREL) to the project are acknowledged. The support, collaboration, and sample motor materials provided by Andrew Wereszczak and Tim Burress (ORNL) are also acknowledged.

References

1. Lipo, T.A. *Introduction to AC Machine Design.* 3rd ed. Madison, Wisconsin: Wisconsin Power Electronics Research Center, University of Wisconsin, 2007.
2. Hendershot, J.R.; Miller, T.J.E. *Design of Brushless Permanent-Magnet Motors*. Madison, WI: Magna Physics Publishing, 1994.
3. U.S. Drive. “Electrical and Electronics Technical Team Roadmap.” *Partnership Plan, Roadmaps, and Other Documents.* June 2013. Accessed September 10, 2013: http://www1.eere.energy.gov/vehiclesandfuels/pdfs/program/eett_roadmap_june2013.pdf.
4. Bennion, K.; Cousineau, J. “Sensitivity Analysis of Traction Drive Motor Cooling.” *IEEE Transportation Electrification Conference and Expo (ITEC) Proceedings;* 2012; pp. 1–6.
5. Metzger, D.E.; Cummings, K.N.; Ruby, W.A. “Effects of Prandtl Number on Heat Transfer Characteristics of Impinging Liquid Jets.” *5th International Heat Transfer Conference Proceedings*; 1974; pp. 20–24.
6. Leland, J.E.; Pais, M.R. “Free Jet Impingement Heat Transfer of a High Prandtl Number Fluid Under Conditions of Highly Varying Properties.” *Journal of Heat Transfer* (121:3), 1999; pp. 592–597.
7. Ma, C.F.; Zheng, Q.; Ko, S.Y. “Local Heat Transfer and Recovery Factor with Impinging Free-Surface Circular Jets of Transformer Oil.” *International Journal of Heat and Mass Transfer* (40:18), 1997; pp. 4295–4308.
8. Narumanchi, S.; Mihalic, M.; Kelly, K.; Eesley, G. “Thermal Interface Materials for Power Electronics Applications.” *11th Intersociety Conference on Thermal and Thermomechanical Phenomena in Electronic Systems (ITherm) Proceedings*; 2008, Orlando, FL; pp. 395–404.
9. D09 Committee. “Test Method for Thermal Transmission Properties of Thermally Conductive Electrical Insulation Materials.” ASTM International, 2012.
10. Sato, Y.; Ishikawa, S.; Okubo, T.; Abe, M.; Tamai, K. “Development of High Response Motor and Inverter System for the Nissan LEAF Electric Vehicle.” 2011-01-0350. Warrendale, PA: SAE International, Apr. 2011.
11. Kirkup, L. *Data Analysis with Excel: An Introduction for Physical Scientists*. Cambridge, MA: Cambridge University Press, 2002.
12. Jeevanashankara; Madhusudana, C.V.; Kulkarni, M.B. “Thermal Contact Conductances of Metallic Contacts at Low Loads.” *Applied Energy* (35:2), 1990; pp. 151–164.
13. Snaith, B.; Probert, S.D.; O’Callaghan, P.W. “Thermal Resistances of Pressed Contacts.” *Applied Energy* (22:1), 1986; pp. 31–84.
14. Dieck, R.H. *Measurement Uncertainty: Methods and Applications*. Research Triangle Park, NC: ISA, 2007.
15. Madhusudana, C.V. *Thermal Contact Conductance*. Springer Science & Business Media, 2013.
16. A06 Committee. “Classification of Insulating Coatings for Electrical Steels by Composition, Relative Insulating Ability and Application.” ASTM International, 2013.

U.S. DEPARTMENT OF ENERGY | Energy Efficiency & Renewable Energy

DOE/EE-1163 December 2014
Printed with a renewable-source ink on paper containing
at least 50% wastepaper, including 10% post consumer waste.

For more information
eere.energy.gov